Nanotechnology-Enhanced Near-Surface Mounted-Fibre Reinforced Polymers (NSM-FRP) Structural Retrofitting

By

Mohammad Ibrahim Al-Zu'bi

Department of Civil and Environmental Engineering

College of Engineering, Design and Physical Sciences

Brunel University London

A thesis submitted for the degree of Doctor of Philosophy

December 2023

To

The soul of my father, Maj. Gen. Ibrahim Al-Zu'bi,

my first teacher who always encouraged and supported me,

to embark on every adventure,

especially this one.

Abstract

The retrofitting of concrete structures using fibre-reinforced polymers (FRP) bonded with neat epoxy (NE) adhesives, while proven efficient, has faced challenges related to interfacial debonding at FRP-NE and/or concrete-NE interfaces. These debonding issues pose a threat to both structure performance and safety, since the occurrence of the interfacial debonding weakens the bond between the FRP and concrete, compromising the load transfer mechanism. This compromised bond diminishes the effectiveness of the retrofitting, potentially leading to structural failures, reduced load-bearing capacity and overall instability. From a structural safety perspective, these issues are deemed unacceptable as they can significantly undermine the reliability and safety of the retrofitted structures. Consequently, given the challenges posed by interfacial debonding, exploring advanced bonding technologies, such as nanomaterial-modified adhesives, holds promise for enhancing the long-term stability and performance of retrofitted structures.

The addition of nanomaterials to epoxy adhesives has proficiently overcome the drawbacks accompanied with using NE in retrofitting concrete members with FRP materials, by improving their mechanical and physical properties in addition to the interfacial bond strength. However, the use of nano-modified adhesives is currently limited to the application of the externally bonded reinforcement (EBR)-FRP strengthening systems, and there is no recorded application of these adhesives in the near-surface mounted (NSM)-FRP retrofitting techniques.

Therefore, this thesis addresses utilising the nanomaterial-modified epoxy adhesives (NMEAs) for the NSM-FRP retrofitting of concrete members. The NMEAs were produced by incorporating various carbon-based (i.e. carbon nanofibres (CNF), cellulose nanocrystals (CNCs) and graphite nano powder) and silicon-based nanomaterials (i.e. silica nano powder and MMT nano clay) into the NE at 0.5, 1.0 and 1.5% by weight.

First, inclusive chemical, physical and microstructural characterisations of the NMEAs were conducted to investigate the effect of incorporating different nanomaterials into neat structural epoxy adhesive (Sikadur®-30) on those properties. The NMEAs were also examined for their interfacial bond characteristics through testing the interfacial bond strength and characteristics of cement paste (CP)-adhesive joints bonded by NE or NMEAs. Afterwards, a comprehensive experimental programme was carried out to investigate the overall mechanical (i.e. flexural

capacity and ductility response) and bond (i.e. failure modes) behaviours of the NSM-FRP-retrofitted concrete prisms bonded by NE or NMEAs.

In regard with the NSM-FRP flexural retrofitting, a total of 68 concrete prisms were retrofitted for the purpose of investigating the effect of several parameters, mainly the types of bonding agents, on the performance of tested specimens. Results showed that using silica, clay and graphite NMEAs rather than NE enhanced the retrofitted concrete capacities by about 17%, 5% and 15%, respectively, while about 37% and 9% strength decreases, respectively were observed with using CNF- and cellulose-modified epoxies. Furthermore, it was found that the specimens bonded with silicon-based NMEAs had, on average, higher capacities than those bonded using carbon-based ones, which, on the other hand, showed more ductile behaviour. Also, using carbon-based NMEAs was able to prevent the interfacial debonding and switched the failure mode from shear to flexural, while slight debonding at the bar-adhesive interface was observed in the specimens retrofitted using silicon-based NMEAs accompanied with cohesive failure in the adhesive layer alongside minor concrete crushing.

This research establishes the potential for broader applications of nanotechnology-enhanced retrofitting in concrete structures, particularly in the NSM-FRP retrofitting technique. The enhanced mechanical properties and interfacial bond strength offered by NMEAs hold promise for improving the long-term stability and performance of retrofitted concrete members in various real-world scenarios. Beyond flexural retrofitting, future research could explore the application of NMEAs in shear and torsion retrofitting, as well as their performance under cyclic, fire and earthquake conditions. Additionally, considering the complex nature of concrete retrofitting, further investigations are warranted to comprehensively understand the efficiency of NMEAs-bonded NSM-FRP technique. This could involve exploring new nano-fillers, individually or in combination, to optimize adhesive properties. Furthermore, alternative types and geometries of FRP reinforcement, such as Aramid FRP (AFRP) or different strip geometries, could be studied to expand the applicability of NMEAs across diverse structural configurations.

Expanding the application of novel retrofitting techniques to large-scale concrete members, such as full-scale beams, columns or slabs, will provide valuable insights into the behaviour of retrofitted structures under realistic conditions. This includes assessing their performance under cyclic loads and extreme scenarios like fire and earthquake conditions, aligning with the latest NSM-FRP design guidelines provided by ACI. Additionally, the development of

analytical formulas based on these guidelines could facilitate the practical implementation of the developed retrofitting system, ensuring its adoption and integration within the construction industry.

Acknowledgement

First and foremost, I am very grateful and thankful to Allah, the most gracious and merciful, for guiding me to the right path and providing me with countless bounties and blessings through all the stages of my life.

I would like to express my profound and heartfelt appreciation to my supervisory team, consisting of the esteemed Prof Mizi Fan and the remarkable Dr Lorna Anguilano. Without their endless guidance and support, this thesis would not come to light. They served not only as supervisors but also as inspiring and motivating allies, making the journey truly enriching. Collaborating with them has been an immense privilege. Additionally, I would like to extend a special note of gratitude to Dr Elisa Bertolesi, whose invaluable expertise greatly contributed to the success of this research.

I'd like to give a big thank you to the technicians of the Civil Engineering Research Centre, Mr Charles Morrison, Mr Andrew Smith and Mr Nirvan Razaghi-kashani, for their highly-appreciated help and support during the experimental work. The staff members at the Experimental Techniques Centre (ETC), Dr Nicho Nelson, Dr Ashley Howkins and Dr Uche Onwukwe are also highly acknowledged for their guidance and assistance throughout the project.

I would also like to thank my faithful friends, Aziz Shwareb, Ammar Alhalaki, Hussien Alberawi, Ubada El Joulani, Ali Ali and Dr Mazen Al-Kheetan and Dr Musab Rabi, who have supported me during my journey.

Finally, I owe a huge debt of gratitude to my dear mother, Mrs. Huda Al-Zu'bi, as well as my brothers and sisters, for their constant support and encouragement. This work wouldn't have been achievable without their love and prayers.

Declaration

I hereby declare that the research presented in this thesis, which is based on research carried out at Brunel University London, United Kingdom, is my own work except where otherwise stated, and has not been submitted for any other degree.

Publications generated from this thesis

The work presented in this thesis has led to a list of journal and conference papers, as follows:

Journal articles

1. **Al-Zu'bi, M.,** Fan, M. and Anguilano, L., 2022. Advances in bonding agents for retrofitting concrete structures with fibre reinforced polymer materials: A review. *Construction and Building Materials*, *330*, p.127115. https://doi.org/10.1016/j.conbuildmat.2022.127115.

2. **Al-Zu'bi, M.**, Fan, M. and Anguilano, L., 2023. Parametric investigation of flexural performance of concrete prisms retrofitted with near-surface mounted FRP bars. Composites Part C: Open Access, p.100421. https://doi.org/10.1016/j.jcomc.2023.100421.

3. **Al-Zu'bi, M.,** Anguilano, L. and Fan, M., 2023. Effect of incorporating carbon-and silicon-based nanomaterials on the physico-chemical properties of a structural epoxy adhesive. *Polymer Testing*, p.108221. https://doi.org/10.1016/j.polymertesting.2023.108221.

4. **Al-Zu'bi, M.,** Fan, M. and Anguilano, L., 2024. Near-surface mounted-FRP flexural retrofitting of concrete members using nanomaterial-modified epoxy adhesives. *Journal of Building Engineering*, p.108549. https://doi.org/10.1016/j.jobe.2024.108549

5. **Al-Zu'bi M**, Fan M, Bertolesi E, Anguilano L. A review on retrofitting concrete members with near-surface mounted-fiber reinforced polymer composites. Structural Concrete. 2024. https://doi.org/10.1002/suco.202300382

Conference papers

Al-Zu'bi, M., Anguilano, L. and Fan, M., 2023. Carbon-Based and Silicon-Based Nanomaterials for Enhanced Structural Adhesives. https://doi.org/10.4028/p-cRQ0UD

In the 7th International Conference on Materials Sciences and Nanomaterials & 2023 6th International Conference on Advanced Composite Material. Cambridge, UK, July 11-13, 2023.

Table of Contents

List of Figures

List of Tables

List of Abbreviations

ATR-FTIR	Attenuated Total Reflectance-Fourier Transform Infrared
BFRP	Basalt FRP
CF	Carbon Fibre
CFRP	Carbon FRP
CNC	Crystalline Nano Cellulose
CNFs	Carbon Nanofibres
CNH	Carbon Nano Horns
CNTs	Carbon Nanotubes
COV	Coefficient of Variation
CP	Cement Paste
CSR	Core-shell Rubber
DPT	Direct Pull-out
EBR	Externally Bonded Reinforcement
EpCNT	Epoxy-functionalized CNTs
EVA	Ethylene Vinyl Acetate
FRP	Fibre Reinforced Polymers
GFRP	Glass FRP
GNP	Graphene Nano Platelets
GNS	Graphene Nano Sheets
GO	Graphene Oxide
GPa	Gigapascal
I_D/I_G	The peak intensity ratios of D-band to G-band
IPA	Isopropanol

KBr	Potassium Bromide
LP	Long Pot
LSS	Lap-shear Strength
LVDT	Linear Variable Differential Transformer
MMT	Montmorillonite
MPa	Megapascal
MWCNTs	Multi-Walled CNTs
NE	Neat Epoxy
NMEAs	Nanomaterial-modified Epoxy Adhesives
NSC	Normal Strength Concrete
NSM	Near-surface Mounted
OPC	Ordinary Portland Cement
PA6	Polyamide 6
PVA	Poly Vinyl Alcohol
RC	Reinforced Concrete
SSA	Specific Surface Area
w/c	Water-cement Ratio
Wt.%	Weight Percentage
XRD	X-ray Diffraction

Chapter 1: Introduction

1.1 Background

Concrete is the world's most consumed man-made material globally and the second most consumed material on earth, after freshwater. It has also been accepted for over 200 years for its long-lasting and dependable nature. In addition to durability and dependability, concrete has superior energy performance, is flexible in design, affordable and relatively environmentally friendly.

However, existing concrete structures are subjected, as time goes by, to several kinds of deterioration caused by aggressive environmental conditions, overloading and/or the poor structural detailing. Those structures are, therefore, in need of structural retrofitting/strengthening in order to ensure their durability, sustainability and, most importantly, safety to avoid material and human losses.

Fibre reinforced polymers (FRP) have emerged as very effective materials for many retrofitting applications as they can be an integral part of modern design of structures due to superior properties of FRP composites and their potential in developing structural systems that exceed those constructed by traditional materials. FRP systems are very versatile and easy to install which come in handy in flexural retrofitting applications, to name a few. The use of FRP composites for retrofitting concrete structures by means of externally bonded reinforcement (EBR) or near-surface mounted (NSM) techniques has gained considerable popularity worldwide and can produce confident retrofitting systems for existing concrete structures. It's worthy to note that the efficiency of FRP retrofitting applications greatly relies on the adhesive type and properties considered to bond the FRP reinforcement to the concrete substrate, as the adhesive layer is the responsible part to transfer and distribute stresses between those components.

1.2 Research significance and motivation

Amidst the escalating demands for enhanced performance in civil engineering structures and infrastructure, there exists a parallel imperative for prolonged service life without necessitating extensive rehabilitative interventions. Moreover, there is a growing need for efficiency in material utilisation and heightened resilience to cope with diverse environmental and anthropogenic challenges. Thus, retrofitting/strengthening of existing concrete structures is deemed essential not solely for the purpose of utilising them throughout their intended service

life, but also to ensure the safety and serviceability of the interconnected components and restore their strength and stiffness, thereby conforming to contemporary and future structural standards.

Moreover, since the costs for demolition and reconstruction are quite high, rehabilitation for the structure may be the best option to restore the loss of strength and to improve the serviceability of the structure. Therefore, the adoption of retrofitting methods over complete replacement of structures should be regarded as a prudent approach, taking into consideration its potential for being environmentally sustainable and economically advantageous. So, it would be more effective to approve the need for retrofitting at suitable intervals than build a maintenance-free structure under severe conditions for a long period.

The expenditure on the concrete rehabilitation processes is expected to grow to $2.7 billion by 2025 due to the increasing infrastructure development around the world [95]. Thus, there is urgent need to decrease those expenses through adopting novel retrofitting methods alongside those that would provide durable (longer lifespan) structures and would ultimately reduce their maintenance costs on the short and long run.

1.3 Knowledge gap

FRP composites, traditionally paired with neat epoxy (NE) adhesives, have been a mainstay in the retrofitting of concrete structures using the NSM technique for many years. However, the exclusive reliance on NE has laid bare deficiencies in bonding strength between the FRP and concrete, resulting in concerning instances of debonding at critical interfaces. These occurrences not only compromise structural durability but also raise significant safety concerns. Consequently, the imperative to develop modified epoxy adhesives stems from the pressing need to rectify these inherent shortcomings in NE usage, thereby fortifying bond performance at these interfaces.

The integration of nanoparticles into epoxy adhesives represents a promising avenue for boosting mechanical properties and augmenting interfacial bond strength. This innovation holds the potential to elevate the overall structural performance of the EBR-FRP-retrofitted members. However, despite notable advancements, comprehensive investigations into the application of these modified adhesives -termed Nanomaterial-Modified Epoxy Adhesives (NMEAs)- within the NSM-FRP framework for concrete retrofitting have been notably absent from the research landscape. It is against this backdrop that the present thesis assumes

significance, as it endeavours to unlock the full potential of NMEAs in facilitating high-performance NSM-FRP flexural retrofitting systems. Through a meticulous examination of their chemical, physical, and microstructural properties, this research seeks to elucidate the interfacial bond characteristics of these modified adhesives, thereby laying the groundwork for their effective utilization in concrete retrofitting applications.

It's noteworthy that the term "Nanomaterial-Modified Epoxy Adhesives (NMEAs)" is introduced for the first time in this thesis, marking a novel contribution to the field.

1.4 Aim and objectives

The research study mainly aims at interjecting the nanotechnology to create a novel NSM-FRP technique for flexural retrofitting of concrete members, through adopting the NMEAs for enhanced structural performance and mechanical behaviour. The primary aims of this study will be realised by accomplishing the following objectives:

- Conducting a thorough literature study of the existing research work carried out on the Nano-modification of epoxy adhesives, the potential of using the nanocomposites in the structural retrofitting highlighting the shortcomings and the potential challenges, mainly in the context of the NSM-FRP retrofitting of concrete members.

- Developing the structural behaviour of the NSM-FRP-retrofitted concrete members through improving the bond strength and characteristics at the concrete-adhesive-FRP interfaces in the retrofitted specimens in addition to their mechanical properties (i.e. overall capacities and ductility) through the development of novel (i.e. Nano-modified) epoxy adhesives that would provide outstanding bond performance over the pristine ones.

- Investigating the effect of incorporating the Nano-fillers on the chemical, physical and microstructural characteristics of the NE. The outcomes of the various analyses were interconnected to enable a comprehensive and efficient assessment. Furthermore, these findings were correlated with the interfacial bond strength and characteristics observed in the retrofitted concrete specimens.

- Providing a comprehensive understanding of NSM-FRP flexural retrofitting entails exploring further parameters, including FRP reinforcement and retrofitting design, to elucidate their impact on structural behaviour and capacity of tested specimens. This endeavour aims to establish a correlation between retrofitting parameters and structural

performance, thereby identifying optimal retrofitting systems for enhanced effectiveness and durability.

- Disseminating the findings of the present study to inspire and facilitate future experimental and/or numerical studies on the relevant topics, thereby enriching the scholarly discourse and advancing the boundaries of knowledge within the research community.

1.5 The outline of the thesis

This thesis consists of a total of nine chapters. The overview of the chapters is as the following: (The thesis outline is depicted in Fig 1.1).

Chapter 1: Introduction

This chapter provides a general background on retrofitting of concrete structures. The motivation to conduct this research in addition to the knowledge gap to be addressed are also included. The chapter also includes the aims and objectives of the current research study alongside the thesis structure/organisation.

Chapter 2: Literature review

This chapter gives a critical state of the art review of the relevant work conducted previously, and it aims to build a comprehensive database in the field of the current research and to identify the limitations of the work done so far. Three sections are considered to achieve that purpose: (I) concrete retrofitting with FRP composites and the techniques adopted for that, (II) the advances in the bonding agents used for the retrofitting purposes and (III) the characterisation of the polymer matrices reinforced by nanomaterials.

Chapter 3: Materials and methodology

This chapter presents the details of the materials used for the purpose of this study, their properties and the reasons why they were used. The methods of the materials characterisation and testing are also comprised. Three categories of methods were considered for: (I) the chemical, physical and microstructural characterisation of the NE and the NMEAs, (II) the Lap-shear Strength (LSS) of Cement Paste (CP)-adhesive-bonded joints and (III) the flexural testing of the retrofitted concrete specimens.

Chapter 4: Effect of incorporating carbon- and silicon-based nanomaterials on the physico-chemical properties of a structural epoxy adhesive

This chapter focuses on presenting the results of a comprehensive characterisation of both the NE and the NMEAs, encompassing chemical, physical, and microstructural aspects. It begins by detailing and discussing scanning electron microscopy (SEM) analysis findings concerning the microstructural characteristics, morphology and dispersion state of the Nano-fillers within the epoxy adhesive. The chapter also covers the analysis of porosity in the characterised samples. Subsequently, attention shifts to the examination of alterations in the physical structure of the NE due to nanoparticle integration, as indicated by changes in % crystallinity, determined through X-ray diffraction (XRD) analysis. Finally, the chemical characterisation and assessment of the selected samples are carried out, investigating changes in chemical composition, particularly bonding, within the NE as a result of nanomaterial incorporation, employing Attenuated Total Reflectance-Fourier Transform Infrared (ATR-FTIR) and Raman spectroscopies. It's noteworthy that the results from various investigations performed on the tested specimens were linked together to provide a more effective and inclusive investigation.

Chapter 5: Bond characteristics of the CP-adhesives-bonded joints

The results of the lap-shear test of the CP-adhesive-bonded joints are shown and discussed in this chapter. The analysis considers the effect of bonding the CP joints with different adhesives (i.e. NE and NMEAs) on the interfacial bonding strength in terms of the ultimate LSS of the tested specimens (i.e. joints) in addition to their failure modes.

Chapter 6: Effect of FRP reinforcement on the behaviour of the retrofitted specimens

In this chapter, the effect of the presence, type, position and number of the FRP reinforcement bars on the behaviour of the NSM-FRP-retrofitted specimens are shown and discussed. In which specimens' behaviour in terms of their overall flexural capacities and the displacement at maximum load (i.e. ductility) are considered, in addition to their modes of failure.

Chapter 7: Performance of the NSM-FRP-retrofitted specimens bonded using nanomaterial-modified epoxy adhesives

Several comparisons of the performance of the tested specimens bonded with different adhesives are included in this chapter. The effect of bonding the specimens with NMEAs rather than NE on their performance (maximum capacities and ductility and failure modes) are first considered. Afterwards, the behaviour of the specimens bonded with two different groups of the NMEAs (i.e. carbon- and silicon-based Nano-fillers) are compared to each other. Bonding

the specimens with NMEAs (i.e. graphite Nano-filler) with three different wt.% are also addressed.

Chapter 8: Influence of groove size on the efficiency of the NSM-FRP retrofitting

The influence of considering different groove dimensions on the specimens' behaviour are shown and discussed in this chapter. Three square grooves dimensions, which are 8x8, 10x10 and 12x12 mm with 1.33, 1.67 and 2.00 groove width or depth to the FRP bar diameter (b/d_b), respectively were utilised for this purpose.

Chapter 9: Conclusions and future work

This chapter contains the concise summary and conclusive statements established within this thesis. Recommendations for potential future work in the relevant research fields are also addressed.

Finally, the limitations/shortcomings of the study have been provided along with some proposed solutions.

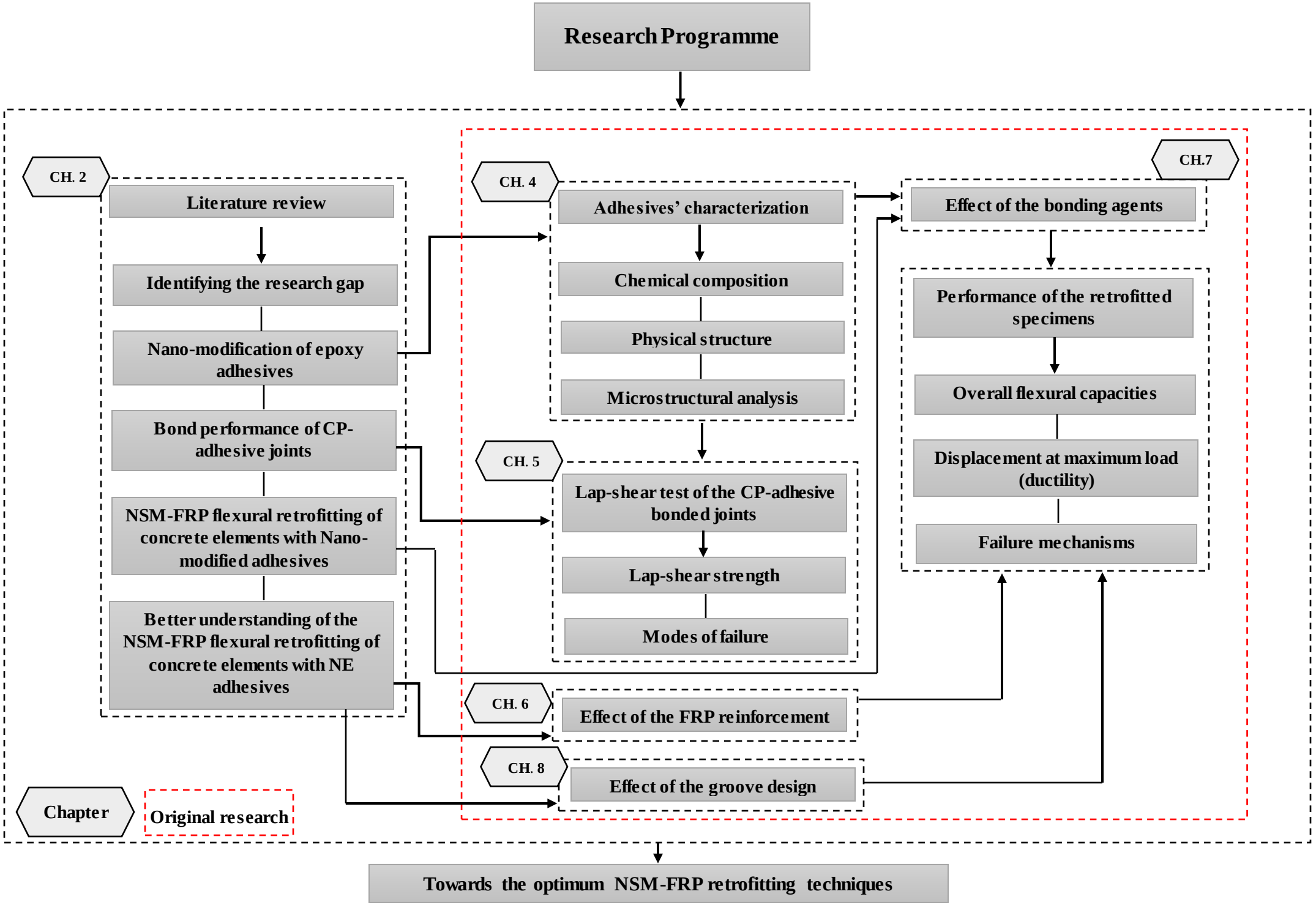

Fig. 1.1 Thesis outline.

Chapter 2: Literature review

This chapter mainly aims to provide engineers and research community with a solid database in the field of this research study through presenting the related work done in the literature. The chapter is divided into three main sections/parts, in which the first section includes a comprehensive review on the advances of retrofitting concrete structures through time, the application FRP composites for concrete retrofitting in addition to the techniques/systems considered for implementing the retrofitting processes. In the second part, the development of the bonding agents, in particular epoxy adhesives, used for the purpose of retrofitting concrete structures by means of EBR-FRP composites is also included. Where the improvement of the strength, ductility and bond performance of the retrofitted members through using nanomaterial-modified epoxy adhesives rather than the neat adhesives is addressed. The third part offers a review of the research conducted on the chemical, physical and microstructural characterisation of the polymer matrices reinforced by nanomaterials by means of Attenuated Total Reflectance-Fourier Transform Infrared (ATR-FTIR) and Raman spectroscopies, X-ray diffraction (XRD) in addition to scanning electron microscopy (SEM) analyses. Where the findings of the relevant research studies in terms of the changes happened in those properties of polymers as a result of incorporating Nano-fillers into them are also addressed. Additionally, the review encompasses the studies that investigated the effect of using nanomaterial-modified adhesives on the bond behaviour, particularly LSS, of the adhesive-bonded joints.

2.1 Retrofitting of concrete structures

2.1.1 Concrete structures

Concrete structures are the most widely applied structural materials worldwide due to their several advantages such as their low cost, easily obtainable ingredients and the possibility of incorporating within it waste products from other industrial process. Therefore, concrete is considered as a fundamental constituent of many existing structures designed to fulfil people needs, which would contribute to a considerable ease and convenience in their lives. Structures like buildings, bridges, dams, to name a few, are good examples of contributing concrete to people's daily lives.

Although there is a huge number of successful concrete structures, which are designed to serve for several decades, many structures have been impaired and become unsafe/ unsatisfactory for current specifications, because of corrosion of steel reinforcement, improper/insufficient

maintenance, severe environmental conditions, increase in the applied loads recommended by design codes and standards due to functional changes, and errors in the design/construction phase [1, 2, 6-8, 206]. All these reasons would negatively affect the durability, safety and serviceability of concrete structures and deteriorate their structural integrity. Therefore, the need for repair and rehabilitation of deteriorated concrete structure has become essential not only to extend the service lives of structures, but also to ensure their safety and serviceability and to keep the structural integrity.

Different methods have been adopted to rehabilitate those deteriorated structures, like concrete and/or steel jacketing, externally bonded (EB) steel plates, external post-tensioning and the addition of new extra members or replacement of degraded ones. Those traditional repair methods could effectively improve both strength capacity and stiffness of deficient concrete elements, however, they are time-consuming. Moreover, the materials used (i.e. concrete and steel) significantly increase the dead load of repaired structures. Thus, finding alternative materials and/or methods for repairing or strengthening existing deficient concrete members was essential [2].

FRP materials have been the most suitable alternative strengthening materials for structural rehabilitation, where they have been used in civil construction for more than three decades. This was due to continuing drops in the cost of those materials in addition to their many features over traditional strengthening materials, such as concrete, steel and wood. These advantages include their high strength-to-weight ratio (i.e. outstanding mechanical properties), low thermal conductivity, high durability (noncorrosive), electromagnetic neutrality, rapid execution with less labour and ease of handling, in addition to their lower installation cost and reduced maintenance cost, reduced mechanical fixing, excellent malleability, and unlimited availability in size (i.e. dimensions) and geometry. Hence, using FRP materials in construction industry has gained large popularity worldwide and could produce effective strengthening and retrofitting systems for existing RC structures [2, 9-12, 207].

2.1.2 FRP composites

Since the 1950s, FRP composites have been adopted and have continued to provide designers with the ability to deliver innovative and intelligent solutions in several applications, like the construction industry, aerospace, aeronautical, automotive manufacturing, and so many others [1-3], as shown in Fig. 2.1.

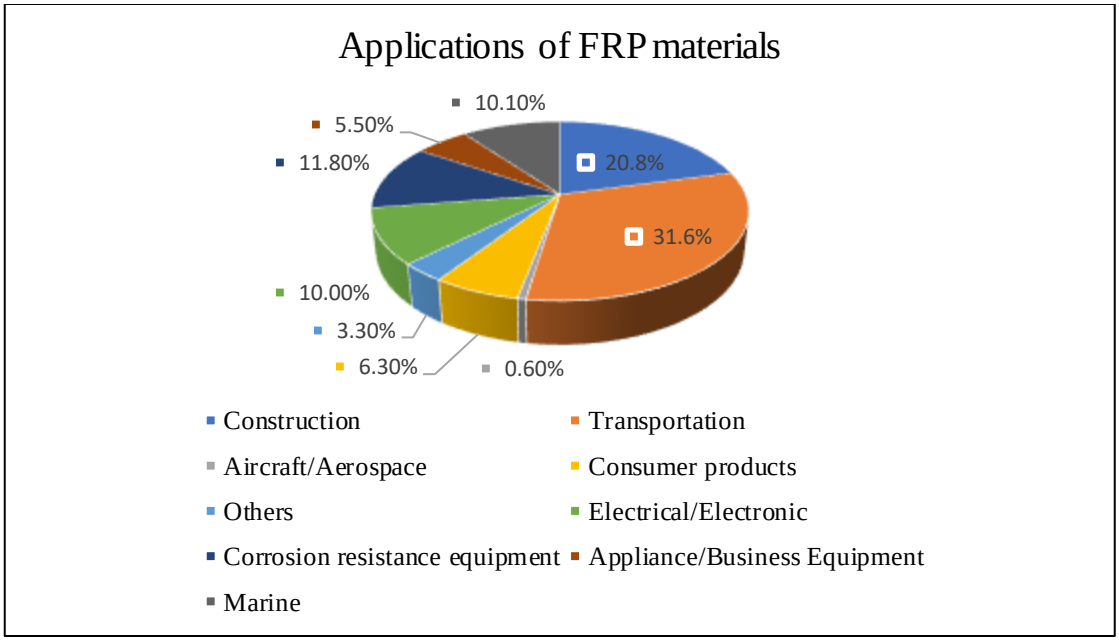

Fig. 2.1 Applications of FRP materials [3]

FRP composites in construction industry

FRP materials are a novel kind of construction materials that compose of raw fibres and polymer matrix [2], as shown in Fig. 2.2 The applied loads are carried by the fibres, which also provide the FRP composite with strength and stiffness, while the matrix is responsible to bind the fibres together, to transfer load/stress to the fibres and to keep them from damage throughout the manufacture process and against harmful environments. Two types of the polymer matrix are used in manufacturing the FRP composites, which are thermoplastic and thermosetting polymers. Therefore, the properties of FRP materials directly relate to their constituents [2]. The FRP materials used to produce the FRP composites are typically made of carbon FRP (CFRP), glass FRP (GFRP), basalt FRP (BFRP) and aramid FRP (AFRP), and they are available in different forms, e.g. strips, round bars and flexible sheets, as shown in Fig. 2.3.

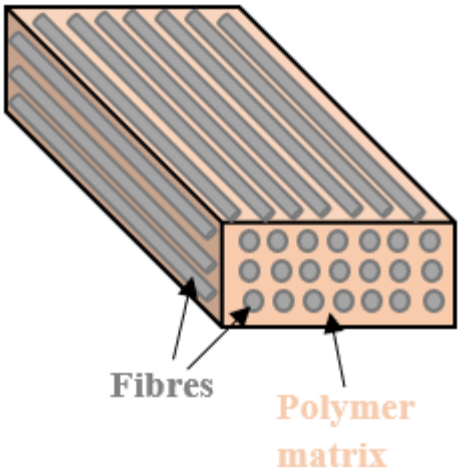

Fig. 2.2 FRP constituents [2].

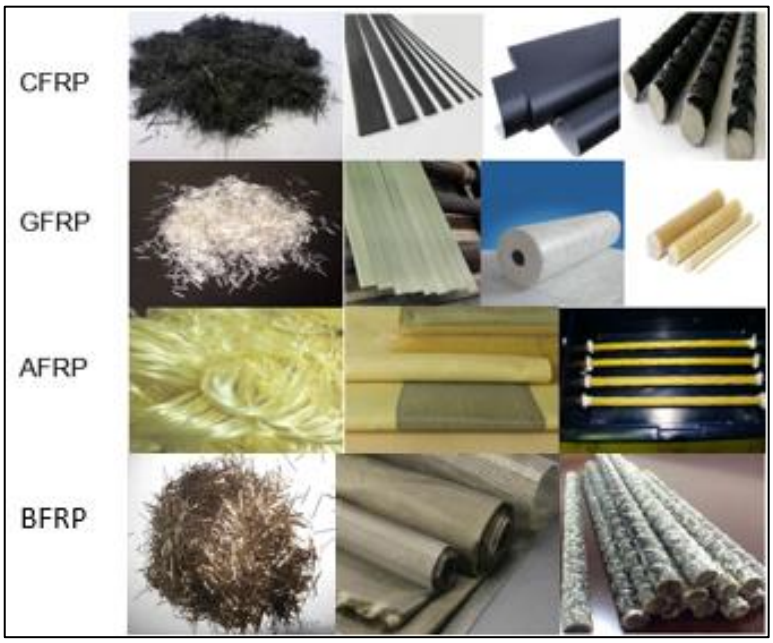

Fig. 2.3 Typical fibres and their FRP materials.

Generally, the selection process of FRP materials for strengthening and retrofitting purposes is dependent on several factors; including the types of materials used in the existing structure, strength requirements, environmental conditions, availability and cost. For instance, BFRP reinforcements are more suitable than CFRP counterparts because the former shows good strain control capability at failure. On the other hand, CFRP materials are preferable to GFRP for their high resistance to all forms of alkali, while the latter is highly vulnerable in alkaline environments given that it contains a high amount of silica. Also, CFRP has been selected over GFRP or AFRP to improve the strength and expansion resistance of concrete owing to its high stiffness, tensile strength, and elastic modulus, while GFRP and AFRP materials are more ductile than CFRP counterparts. It is noteworthy that CFRP materials are more expensive than

the other FRP materials [4]. The stress-strain curves for steel and some FRP composites are shown in Fig. 2.4. Also, Table 2.1 illustrates some properties of steel and FRP materials, while properties of thermosetting polymers used in construction are provided in Table 2.2.

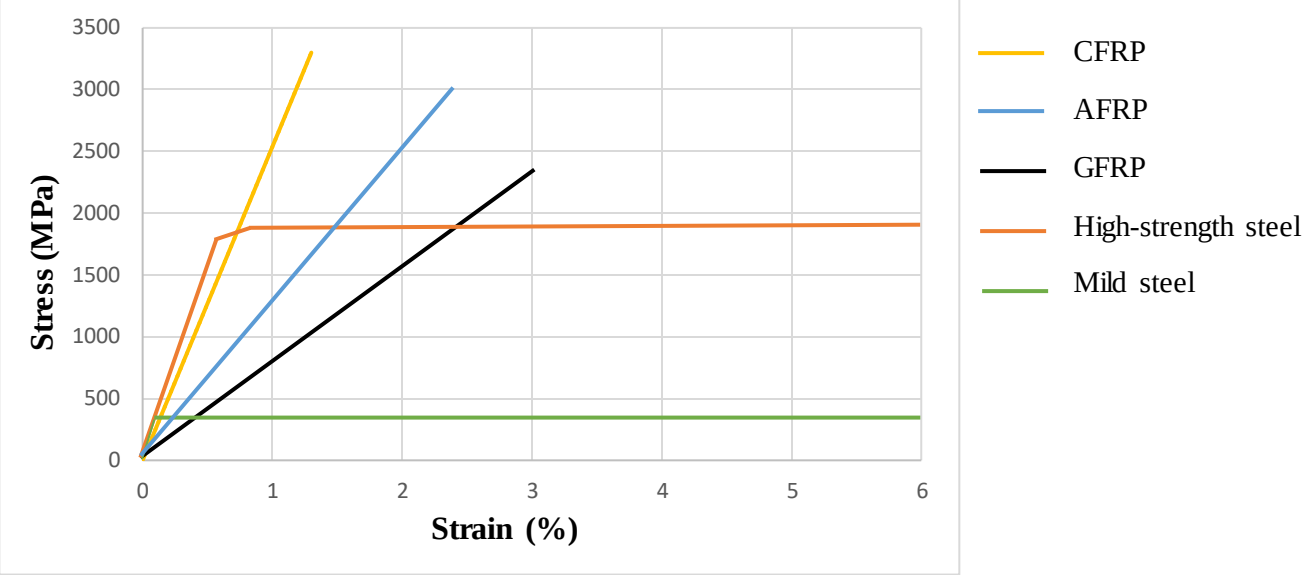

Fig. 2.4 Stress-strain curves of steel and some FRP composites [14].

Table 2.1 Properties of steel and FRP materials [3].

Properties / Material	Physical properties		Mechanical properties			
	Density (g/cm^3)	Specific gravity	Yield strength (MPa)	Tensile strength (MPa)	Elastic modulus (GPa)	Strain at break (%)
Steel	7.75-8.05	7.80	500	-	200	-
CFRP	1.55-1.76	1.0-1.10	1755-3600	1720-3690	120-580	0.5-1.9
GFRP	2.11-2.70	1.50-2.50	600-1400	480-1600	35-51	1.2-3.1
AFRP	1.28-2.60	1.38-1.39	1700-2500	1720-2540	41-125	1.9-4.4
BFRP	2.15-2.70	2.70-2.89	1000-1600	1035-1650	45-59	1.6-3.0

Table 2.2 Properties of the thermosetting polymer matrices used in construction [5].

Polymer	Specific gravity	Ultimate tensile strength (MPa)	Tensile elastic modulus (GPa)	Coefficient of linear expansion (10^{-6}/°C)
Epoxy	1.03	90-110	3.5	45-65
Polyester	1.28	45-90	2.5-4.0	100-110
Vinyl-ester	1.07	90	4.0	80

As the construction industry sector, as shown in Fig. 2.1, represents the second largest sector regarding contribution of FRP materials among several applications with about one-fifth of their contribution, it would be worthwhile to conduct an in-depth investigation about the important role that those materials play in the advancement of the construction sector, for instance, in terms of structural retrofitting.

2.1.3 Retrofitting techniques of concrete members using FRP composites

2.1.3.1 EBR technique

The EBR system is the most common strengthening/ retrofitting system of RC structures and has become a prevalent technique over the last two decades [13]. Its concept is invented from EB steel plate method for strengthening concrete structures. This technique has emerged as an alternative technique to conventional materials and construction manners used in the past; such as EB steel plates, steel or concrete jackets, and external post-tensioning. EBR technique has been adopted due to its many advantages such as quick and easy installation, low performing costs, immediate use of strengthened structures and no need for specific labour skills.

The EBR-FRP strengthening technique is based on attaching FRP materials to the external surface of concrete elements to be strengthened/repaired using a suitable adhesive. First of all, the weak surfaces of concrete element should be removed through grinding, sandblasting or high-pressure water jet. The EBR-FRP strengthening system is applied through either a wet lay-up or a pre-cured technique. In the wet lay-up system, the FRP materials are saturated using resin on site before attached to the surface of the concrete structures using an appropriate adhesive, while for the pre-cured system, the FRP materials are saturated using resin then cured out the site. After that, the FRP composites are delivered to site for application by attachment/adhesion to the external surface of the concrete structures using an appropriate adhesive [2]. EBR-FRP reinforcement can be used as flexural and shear reinforcements to strengthen the deficit RC beams, where vertical, inclined, side-bonding, U-wrapping, or full-wrapping can be applied, as shown Fig. 2.5.

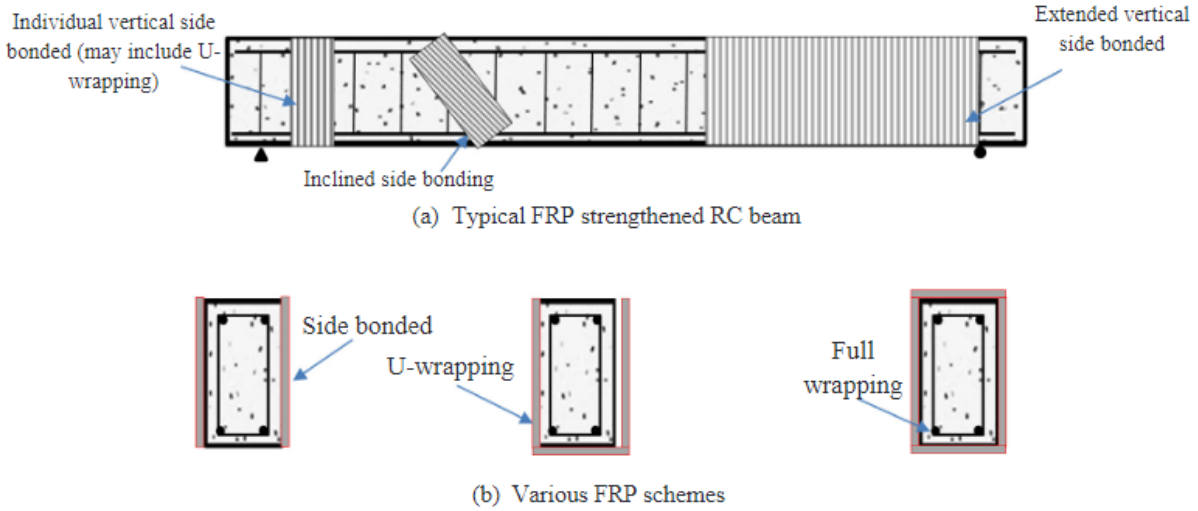

Fig. 2.5 EBR-FRP strengthening of RC beams [1].

Disadvantages of EBR-FRP strengthening system of concrete members

Although EBR-FRP reinforcement system could efficiently enhance the strength of concrete beams, it has a number of limitations/disadvantages. For example, the premature debonding of FRP composites from concrete surface, which is due to the fact that the FRP composites are susceptible to the risk of physical damage, fire and vandalism as a result of collision during stress transfer process, and humidity effect for being open to atmosphere. For instance, the EBR-FRP plates tend to debond at low strains, which eventually limits the ductility or moment redistribution to such an extent, leading to inefficient use of reinforcing material. The most common form of debonding is the intermediate crack (IC) debonding, which usually takes place in the regions of maximum moment when a crack in the RC section intercepts the plate. Such a failure mode (i.e. debonding) not only diminishes the strengthening potential of EB FRP plates but is also unacceptable from the structural safety perspective. Therefore, EBR technique is not able to develop full FRP's strength, as the whole capacity of FRP reinforcements cannot be utilised [15-17, 22-24]. The modes of failure associated with EBR-FRP flexural strengthening RC beams are shown in Fig. 2.6.

The earlier mentioned drawbacks of the EBR-FRP system (i.e. debonding failure) have led the researchers to adopt another strengthening/retrofitting system, to provide the retrofitted concrete members with better performance under harsh conditions. NSM technique was found to be the most appropriate alternative [82].

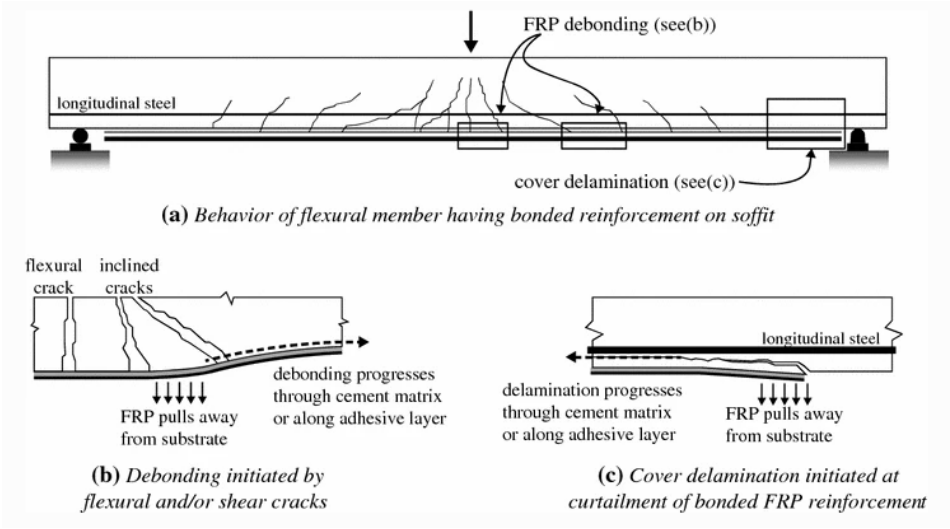

(a)

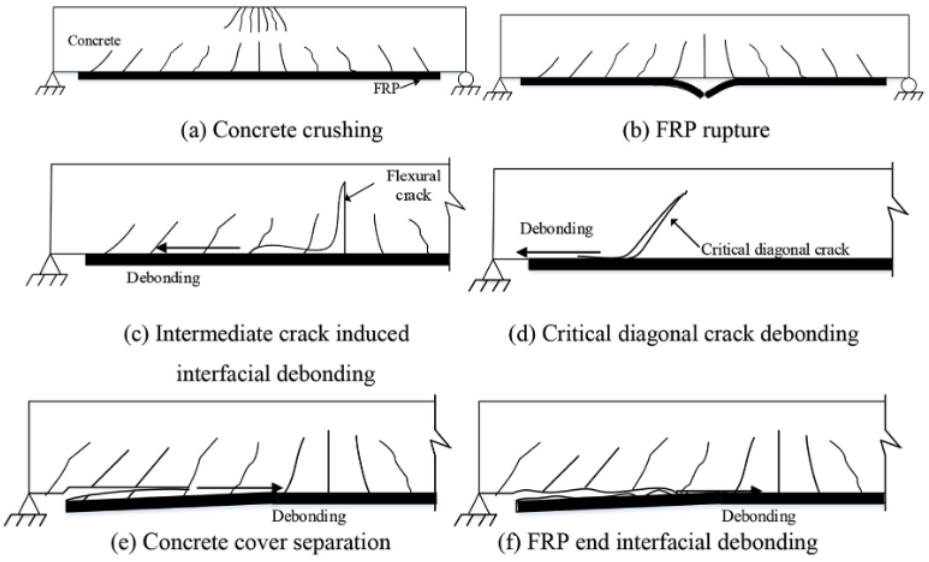

(b)

Fig. 2.6 Failure modes of EBR-FRP flexural-strengthened RC beams (a) [25] and (b) [26].

2.1.3.2 NSM technique

The concept of NSM strengthening system was invented in the 1940s in Europe by means of embedding steel bars into grooves cut into the surface of concrete elements to be strengthened/repaired using cement mortar as a bonding agent [29]. NSM-FRP technique is to use FRP materials of square, circular or rectangular cross-sections, which are embedded into slits cut onto the concrete surface using an appropriate adhesive, such as epoxy paste or cement grout [30, 33]. Fig. 2.7 shows the NSM-FRP strengthening process of RC beams.

(a) (b)

Fig. 2.7 NSM-FRP strengthening of RC beams for: (a) flexure [35], and (b) shear [7].

2.1.3.2.1 Configurations of NSM-FRP strengthening

NSM-FRP reinforcement has been used in several configurations (Fig. 2.8). The minimum groove dimensions for NSM-FRP strengthening system for FRP bars and strips were proposed by ACI 440.2R-08 [26], where a_b and b_b are the smallest and largest FRP strip dimension, respectively (Fig. 2.8 A). It has also been reported that other construction parameters could affect the bond behaviour and hence the structural performance of the strengthened elements [36], which are, for example, the nominal diameter of FRP round bar (d_b), the width/thickness and the height of FRP strip or rectangular bar, (t_f and h_f, respectively), the groove width (b_g) and depth (h_g), the net distance between two adjacent grooves (a_g) and the net distance between a groove and the beam edge (a_e) (Fig. 2.8 B).

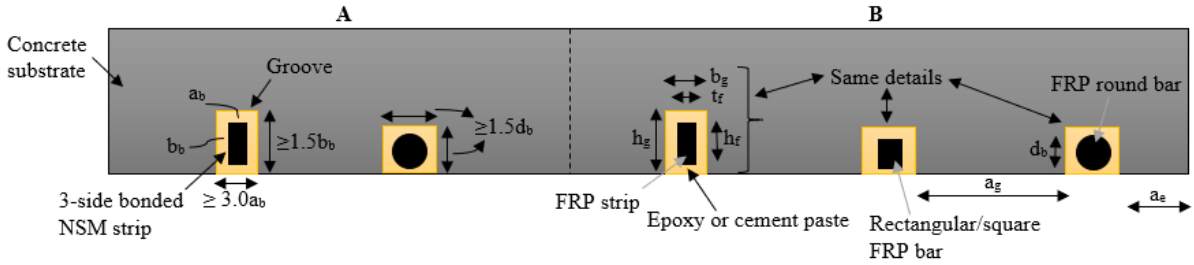

Fig. 2.8 Configurations of the NSM-FRP system, A [26] and B [36].

Kang et al. [27] suggested a minimum value of 40 mm for the spacing between adjacent NSM-CFRP laminates and the distance of the CFRP strips from the edge of the concrete member. This was to ensure that each CFRP laminate behaves independently without premature debonding failure and could prevent interference between adjacent FRP strips and bars, which would eventually lead to more effective NSM-FRP strengthening system, which was also confirmed in [2].

The bond test with square grooves ($b_g = h_g$) indicated that the minimum value of k ($k = b_g/d_b$) should be 1.5 for smooth or lightly sand-blasted round bars and 2.0 for deformed bars [37]. The bond tests on NSM-FRP strips showed that a minimum value of a'_e ($a'_e = a_e + b_g/2$) of

about 20 mm was required to avoid concrete splitting [38], and no concrete cracking was observed at bond failure for values larger than 30 mm. It was also suggested that a_e' should be no less than 30 mm or the maximum aggregate size, whichever is greater. The maximum aggregate size was suggested as a limit to avoid damaging the concrete during the cutting of the groove. a'_e affected the bond behaviour until the maximum value of 150 mm, beyond which no further influence was assumed. It was also proposed that the depth and width of the cut groove should be about 3 mm larger than the height and thickness of the corresponding FRP strip, respectively, in order to obtain an adhesive layer thickness of about 1-2 mm. Parretti and Nanni [39] suggested that both b_g and h_g should be no less than $1.5d_b$. For NSM strips, it was recommended that the minimum groove width to be no less than $3t_f$, while the minimum depth should not be less than $1.5h_f$. De Lorenzis and Nanni [40] stated that the optimum groove sizes appeared to be 19mm and 25mm for embedment of NSM-FRP deformed rods of 9.5mm and 13mm diameter, respectively. Hassan and Rizkalla [41] proposed a minimum clear spacing between the grooves of NSM-FRP bars of twice the diameter of the bars regardless of the groove width. Also, a minimum edge distance of $4d_b$ was recommended to diminish the edge effect for NSM-FRP bars.

2.1.3.2.2 Advantages of NSM technique over EBR technique

NSM technique was found to have many advantages over EBR counterpart. For instance, it requires no surface preparation work and, after cutting the thin slit, requires minimal installation time. As the NSM-FRP reinforcements are covered by concrete, that would protect the reinforcements against harm resulting from acts of vandalism, fire, mechanical damage, harsh environment and aging effects, which is not applicable in the case of EBR-FRP reinforcement, which are open to atmosphere. That would result in premature debonding of FRP composites from concrete surface. Such failure mode (i.e. debonding) not only diminishes the strengthening potential of EBR-FRP reinforcement but is also unacceptable from the structural safety perspective. Therefore, EBR technique is not able to develop full FRP's strength, as the whole capacity of FRP reinforcements cannot be utilised [14-17, 22-24].

Moreover, the NSM system was confirmed to tend to deliver a greater bond condition between the FRP reinforcement and the concrete substrate than that provided by the EBR technique, and consequently, the FRP materials are less prone to debond from concrete. Furthermore, the appearance/aesthetic of the NSM-FRP-strengthened elements is practically unaffected by the strengthening intervention [30, 31, 71].

It was reported that the NSM-FRP technique shows significantly better strengthening performance than the EBR-FRP system in terms of load-bearing capacity and bond characteristic of the strengthened elements [30, 33, 34, 63, 64, 69, 70, 74, 75]. For instance, the shear capacity of rectangular RC beams that were tested through four-point bending and strengthened with EB U-wrapped laminate was found to increase by 16% but that was 22%-44% for those strengthened with NSM-FRP reinforcement [33]. It was also noticed that the EB-FRP-strengthened beam failed by debonding of the CFRP laminate, while separation of the side concrete covers of the internal steel stirrups was the governing mode of failure for the NSM-FRP-strengthened specimens. Similar specimens were considered by Nurbaiah et al. [74], which found that the increase of the ultimate load over the control specimen was from 40% - 88% and from 8% - 16% for beams strengthened with NSM-GFRP bars and for those strengthened with EBR-CFRP sheets, respectively, while increase in stiffness was in the range of 55% - 85% for NSM beams and from 26% - 38% for EBR beams, which failed in flexure alongside debonding of CFRP sheets, while no debonding was observed in NSM beams. Similarly, Dias and Barros [34, 64] found that the EBR and NSM beams showed an increase in average load capacity of 54% and 83%, and increments in deflection of 77% and 307%, respectively, compared to the control beams. It was also reported that the failure modes of the NSM beams were not as brittle as those strengthened by the EBR technique.

T-section beams were tested through three-point bending by Dias and Barros [70]. Results showed that the values of load-carrying capacity and stiffness of the EBR-strengthened beams, after shear crack formation, were 34% and 59%, respectively, of the values obtained for those strengthened by NSM system. Similar findings were reported by the authors in [63, 70]. More details (i.e. improvement and failure modes) about the existing studies that considered NSM and EBR techniques for strengthening RC beams are summarised in Table 2.3.

Flexural strengthening of beams utilising EBR in grooves (EBRIG) method was also found to increase the load capacity and energy absorption of concrete members in comparison to those strengthened using EBR method. Moreover, shear strengthening of beams by those techniques significantly enhanced the load-displacement behaviour compared to those strengthened by EBR technique [92].

From bond behaviour perspective, Bilotta et al. [75] indicated that the RC beam strengthened with NSM-CFRP strips are less sensitive to debonding phenomena, however, they were less effective in increasing the stiffness than those strengthened with EBR-CFRP plates. Similar

observations were reported by Abdallah et al. [88], as the debonding strain in the NSM beam was found to be 51.5% higher than that strengthened using EBR system. In addition, the NSM technique was found to allow a higher moment redistribution values in the hogging region (i.e. +19.59% and +11.49%) at the ultimate state than that provided by the EBR counterpart (i.e. +13.87% and +1.48%). The corresponding values for the sagging region were -11.83% and -6.92% for the NSM beams and -8.32% and -0.89% for the EBR ones. Lim et al. [72] indicated that the ultimate tensile strains measured in the CFRP strips for the EBR beams were between 700-1200 $\mu\varepsilon$, while they were in the range of 3500-4500 $\mu\varepsilon$ in the NSM ones. Strains for the beam strengthened with combined NSM and EBR-CFRP strips were measured at around 3000 $\mu\varepsilon$.

Bond tests conducted by Blaschko and Zilch [58] showed that the strengthening technique "CFRP in concrete slits" has a greater anchoring capacity compared to CFRP strips glued on the surface of a concrete structure. It was also found that the strength of the beams strengthened by the latter system is less than half than those strengthened by the former one. Results of bond tests conducted by Bilotta et al. [69] showed that the tensile strength of the FRP materials is better exploited by the NSM technique with much higher utilisation factors (36–100%) than those attained in EBR systems (approximately 15%). Therefore, it was concluded that the NSM technique delays debonding, and hence FRP tensile strength to be better exploited. It was also confirmed by Kim et al. [73] that beams strengthened with NSM-CFRP strips dissipate more energy than those strengthened with EBR-CFRP sheets because of enhanced bond.

Table 2.3 Summary of available researches that applied both EBR- and NSM-FRP techniques.

Reference	**Specimen code**		**Increase in the load-carrying capacity (%)**	**Maximum displacement (mm)**	**Modes of failure**	
Dias and Barros [30, 63]	NSM	2S-4LV	11.1	7.14	All the tested beams failed in shear	Debond and concrete fracture
		2S-7LV	23.1	7.17		Separation of parts of the concrete cover
		2S-10LV	30.8	6.09		
		2S-4LI45	29.3	6.45		Debond and concrete fracture
		2S-7LI45	38.8	7.93		Separation of parts of the concrete cover
		2S-10LI45	47.0	6.76		
		2S-4LI60	27.2	6.90		Debond and concrete fracture
		2S-6LI60	29.8	7.87		Separation of parts of the concrete cover
		2S-9LI60	35.8	6.44		
		2S-4M	2.4	4.79		

	EBR	2S-7M (1)	7.0	5.99		Debonding of the wet lay-up CFRP sheets from the concrete
		2S-7M (2)	21.8	7.77		
Rizzo and De Lorenzis [33]	NSM	NB90-73-a	15.8	N/A	Separation of the side concrete covers of the internal steel stirrups	
		NB90-73-b	44.4			
		NB90-45-b	21.6			
		NB45-146-a	23.4			
		NB45-73-a	32.1			
		NS90-73-a	22.9			
		NS45-146-a	41.3			
	EBR	UW90	26.8			
η (%) = f_{fd} / f_{fu}, f_{fd} = P_{max} / A_f						
Bilotta et al. [69]	NSM (Three specimens of each configuration)	B-6-SC	87	N/A	E/C and T	
		B-8-SC	50		E/C	
		G-8-SW	63		B/E	
		G-8-RB	71		E/C	
		C-8-S	40		E-C and CL	
		C-10x10-S	36		(B/E + E/C) and E/C	
		C-1.4x10-S	106		T	
		C-2.5x15-S	48		E/C	
	EBR (Three specimens of each configuration)	C-1.30x60	13		DP-C and DB-C/E	
		C-1.60x100	19		DB-C/E and SP	
		C-1.20x100	14		DB-C and DB-C/SP	
		C-1.25x100	11		DB-C and SP	
		C-1.70x100	12		DB-C and SP	
		C-1.40x100	11		DB-C	
Bilotta et al. [75]	NSM	NSM_c_2 × 1.4 × 10_1	61	N/A	CDCD	
		NSM_d_2 × 1.4 × 10_1	55		SH	
		NSM_c_3 × 1.4 × 10_1	66		CDCD-CCS	
		NSM_d_3 × 1.4 × 10_1	47		SH	
	EBR	EBR_c_1.4 × 40_1	81		ED-ID	
		EBR_c_1.4 × 40_2	75		CDCD-CCS	
		EBR_d_1.4 × 40_1	63		ED-CCS	
		EBR_d_1.4 × 40_2	40		ED	
Dias and Barros [34]		A10_VL	58	12.86		
		A10_IL	57	30.96		
		A12_VL	102	6.70		
		A12_IL	125	11.75		

& Barros and Dias [64]	NSM	B10_VL	77	6.83	Formation of a shear crack before the yielding of the longitudinal tensile reinforcement	
		B10_IL	63	4.27		
		B12_VL	84	4.44		
		B12_IL	96	4.92		
	EBR	A10_M	22	3.75	Debonding and rupture of CFRP sheets	
		A12_M	54	4.91		
		B10_M	50	4.40		
		B12_M	89	3.52		
Dias and Barros [70]	NSM	2S-4LV	11.1	7.14	All the tested beams failed in shear	Debonding and concrete fracture
		2S-7LV	23.1	7.17		
		2S-10LV	30.8	6.09		
		2S-4LI45	29.3	6.45		
		2S-7LI45	38.8	7.93		
		2S-10LI45	47.0	6.76		
		2S-4LI60	27.2	6.90		
		2S-6LI60	29.8	7.87		
		2S-9LI60	35.8	6.44		
		4S-4LV	14.3	9.32		Separation of parts of the concrete cover
		4S-7LV	15.1	9.75		
		4S-4LI45	19.1	7.93		
		4S-7LI45	28.7	8.26		
		4S-4LI60	19.5	6.91		
		4S-6LI60	23.2	7.31		
	EBR	2S-4M	2.4	4.79		Debonding of the wet lay-up CFRP sheets from the concrete
		2S-7M (1)	7.0	5.99		
		2S-7M (2)	21.8	7.77		
Nurbaiah et al. [74]	NSM	A-1G	40.7	4.67	Crushing of concrete in a ductile flexural mode	
		A-2G	87.5	6.36		
	EBR	B-1L	7.78	4.76	Debonding rupture of CFRP sheet/s followed by of CFRP	
		B-2L	15.85	5.13		

DB-C = debonding in concrete; DB-E = debonding at plate/epoxy interface; SP = splitting of concrete. E/C = debonding at the epoxy-concrete interface; B/E = debonding at the bar-epoxy interface; CL = detachment of a concrete layer; T = tensile failure of FRP reinforcement. CC = concrete crushing, SY = steel yielding, SH = shear failure. ED = end debonding, ID = intermediate debonding. CDCD = critical diagonal crack debonding, CCS = concrete cover separation.

2.1.3.2.3 NSM-FRP flexural retrofitting of concrete members

Concrete members may repeatedly undergo bending action; therefore, there is a need to increase their flexural strength. It was found by several researchers that utilising NSM-FRP reinforcement is feasible for strengthening/repair of concrete structures, and it is very efficient in enhancing the flexural strength, stiffness and load-carrying capacity of RC beams [18, 19, 28, 32, 41, 83, 93].

Factors affecting the NSM-FRP flexural retrofitting of concrete members

Several factors were found to affect the flexural performance of the NSM-FRP-strengthened concrete members, as follows,

1) Percentage of NSM-FRP reinforcement

It was found that increasing CFRP, GFRP or BFRP bars increased the flexural capacity of the strengthened beams, in terms of yielding and maximum loads, in addition to their ductility. For instance, the yielding and maximum loads were found to increase by 25.6% and 7.5%, respectively with doubling the number of NSM-CFRP, and 11.7% and 13% when using NSM-GFRP bars [32]. The small percentage increment in the maximum load was mainly due to the separation of concrete cover. Similar observations were reported by Nurbaiah et al. [74], where strengthening beams with two GFRP rods rather than one was found to increase the ultimate load by 34%, but reduced the ultimate deflection by 41%. On the contrary, it was found in [87] that doubling the number of GFRP bars could increase both maximum load (30.7%) and mid-span deflection (15.2%). In similar manner, it was found in [83] that the ultimate load of the tested beams increased by about 32% with increasing the GFRP reinforcement ratio from 0.87% to 1.18%. However, about 7% reduction in the ultimate displacement was observed. Further study [90] indicated that tripling the CFRP reinforcement area resulted in 14.4% and 22% increase in the maximum load and the cumulative energy absorption, respectively, but reduced the maximum deflection by about 29%. Doubling BFRP bars also showed increment in the maximum load (26.4%) and the corresponding maximum moment (26.3%), however, 13.7% reduction in the mid-span deflection at maximum load was observed [84]. The increase in the maximum load with increasing the % of NSM-FRP reinforcement is shown in Fig. 2.9. It could be observed that the % increase in the ultimate load increased with the increase of the area (mm^2) of GFRP reinforcement, which yielded about 56% higher increase in the ultimate load compared to CFRP strengthening with increasing the FRP area by the same amount. While increasing the BFRP reinforcement area provided reasonable % increase in the ultimate load if compared with those strengthened with CFRP and GFRP bars.

In addition to what was found experimentally, the theoretical prediction done by Barris et al. [94], revealed that, for low values of concrete compressive strength (i.e. f_c = 25 MPa), doubling the CFRP reinforcement area resulted in a maximum increase in the flexural capacity of 27% and 34% for beams strengthened with CFRP strips with elastic modulus of 120 GPa and 180 GPa, respectively, but did not modify the mode of failure, which is concrete crushing.

Nevertheless, it was reported by Abdallah et al. [86] that increasing the ratio of the CFRP reinforcement to the tension steel reinforcement from 18% to 26%. led both the load-carrying capacity and ductility of the strengthened beams to decrease by 12.6% and 51.5%, respectively, compared to those of the control beam. Moreover, it was observed that the tensile strain of CFRP decreased and moment redistribution negatively affected by increasing the CFRP reinforcement.

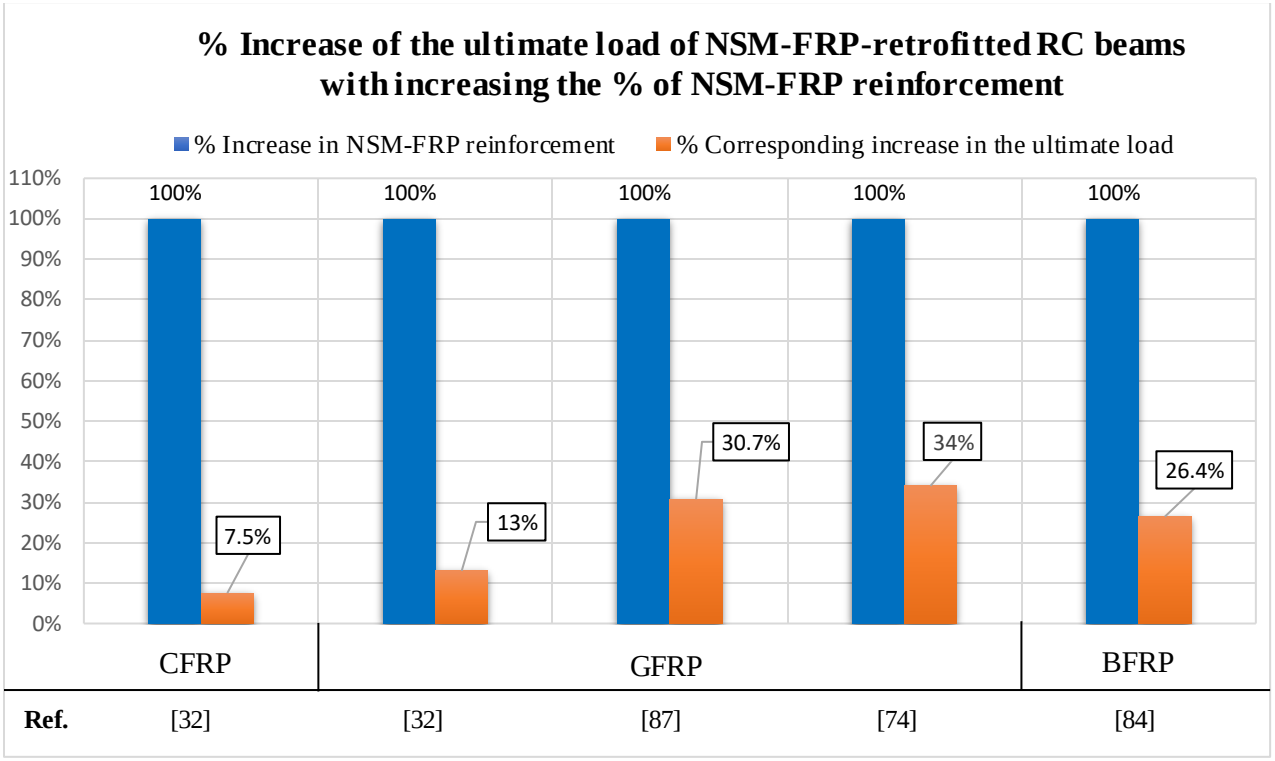

Ref.	[32]	[32]	[87]	[74]	[84]
FRP area increase	50.27	50.27	113.1	122.72	70.88

Fig. 2.9 The effect of % NSM-FRP reinforcement on the ultimate load of RC beams.

2) Size and type of NSM-FRP reinforcement

Al-Mahmoud et al. [18] reported that doubling the cross-sectional area of CFRP rods increased the ultimate bending moment of the specimens by about 12% - 24%. Strengthening beams with 12mm diameter NSM-GFRP bars showed 13.6% and 6.7% higher increase in the yielding and the maximum loads, respectively, than those strengthened by 8mm bars [32]. Moreover, it was also indicated that the RC beams strengthened by CFRP bars showed higher increase in the yielding and the maximum loads by 8.7% and 10%, respectively, over those strengthened by GFRP bars. However, it was found that increasing the area of the GFRP bars was more efficient in increasing the maximum load than increasing the area of CFRP bars. This was attributed to that the concrete cover mode of failure occurring in that case. Increasing the NSM-GFRP bar

diameter from 6mm to 8mm and from 8mm to 10mm resulted in 8% and 21% increase in the ultimate load, respectively [83]. It was also recommended to use FRP bars with diameter not more than half the depth and width of the groove, to avoid peeling failures.

Abdallah et al. [86] found that using NSM-GFRP bars improved ductility by about 24% compared with using CFRP bars. However, the load-carrying capacity of the NSM-GFRP-strengthened beams was about 77% of those strengthened with CFRP bars, which also achieved higher stiffness. It was found in [93] that the yield and ultimate loads of the CFRP-reinforced beams were found to be consistently higher than GFRP counterparts by 23% and 19.7%, respectively. However, the mid-span ultimate displacement and ductility factor dropped by 45% and 69%, respectively, which resulted in higher steel strains, indicating lower utilisation ratio of the FRP reinforcement. It was also found, according to the proposed finite element model, that increasing the axial stiffness (EA) of the NSM-FRP reinforcement, by increasing either its area, assuming enough concrete cover (25mm in that case), or its elastic modulus would increase the failure load and decrease the debonding strain levels. Further observation was that strengthening beams with GFRP bars achieved 30% and 158% higher maximum deflection, respectively, for bonded lengths of 24d and 48d (d is the CFRP rod diameter), and consequently higher ductility, than those strengthened using CFRP bars, which was attributed to the low modulus of elasticity of the GFRP bars compared to that of the CFRP bars.

3) Bonded length of NSM-FRP reinforcement

It was found that increasing the bonded length of NSM-CFRP bars by 10 % (i.e. from 270 to 300 cm) resulted in about 10% increase in the ultimate bending moment of the strengthened beams [18]. However, both beams failed by pull-out of the CFRP rods simultaneous with concrete splitting. other researchers [41] reported that increasing the bonded length of the NSM-CFRP bars from 150 mm to 550 mm led to increase the failure loads of the tested beams by about 20%. It was also recommended that the development length of the NSM-CFRP bars should not be less than 80 times the FRP bar diameter. Similarly, it was indicated in [85] that the failure load and the maximum mid-span deflection of the strengthened beams increased by 38% and 24%, respectively, by increasing the bond length of the CFRP strips from 1100mm to 1300mm, which was also reported by Carolin et al. [20]. On the other hand, decreasing the CFRP length from 2.0 m to 1.5 m caused 11.8% and 45.5% drop in the load-carrying capacity and ductility, respectively [86].

The failure loads of the beams with SL/BL ratio (the ratio between NSM-CFRP strengthening length SL and beam length BL) of 0.94 were about 9.1% and 12.6% greater than those of SL/BL ratio of 0.56, for beams strengthened using epoxy adhesive and mortar, respectively [89]. Further investigation [93] observed that the ultimate carrying capacity increases with the bonded length, but up to a certain limit, which is in the range of 48d, where increasing the bonded length from 24d to 48d increased the ultimate capacity by 29%, while only 3% increase in the ultimate capacity was observed with increasing the bonded length from 48d to 60d. No further increase in the capacity for any further increase in the bonded length beyond that limit (i.e. 48d) is expected to occur.

Additionally, the NSM-FRP reinforcement length was also found to affect the failure mode of the beams [86], where terminating the CFRP bars before the point of zero-moment was noticed to change the mode of failure from pull out of the FRP bars to premature peeling off of the concrete cover. Zhang et al. [83] reported that the analysis of the failure modes showed that the end anchorage of the NSM-FRP bars could effectively eliminate the premature debonding of the bars.

4) Groove-filling material

Although applied loads are mainly carried by the fibres the type of bonding agent plays a main role in success of the NSM-FRP strengthening processes, as the mechanical behaviour of FRP composites is highly dependent on the mechanical properties of the matrix used to bond the FRP composites to the concrete substrate [2]. Tang et al. [19] found that using epoxy with higher flexural strength (27 MPa to 49 MPa) increased both the failure load and ultimate moment by about 7%. However, 38% reduction in the maximum deflection was observed. Although both specimens failed by the rupture of NSM-GFRP bars, less splitting of epoxy paste was observed in the case of using epoxy with higher flexural strength. Using epoxy resin with about 39%, 36% and 22% higher elastic modules, compressive and tensile strength, respectively, could slightly increase the load-carrying capacity (2.3%) and deflection (7.7%) of the NSM-CFRP-strengthened beams. The effect was much less for the specimens strengthened with GFRP bars. Moreover, no influence on the beams' stiffness was observed [32]. It was reported in [41] that using high-strength adhesives and/or increasing the thickness of the epoxy cover layer would delay the epoxy split failure for CFRP bars.

On the other hand, using mortar as an adhesive for beams strengthening showed 21% lower maximum bending moment than those strengthened using epoxy resin. It was also found that

CFRP rods fixed using epoxy resin were better bonded to concrete. Using mortar instead of epoxy shifted the failure mode from debonding at the mortar-concrete interface to pull-out of NSM-FRP rods. Less amount of cracking was observed in the case of mortar-strengthened beams [18]. Similar observation was reported by Fathuldeen *et al.* [90], where replacing epoxy resin with cement-based adhesive resulted in 59% and 61% decrease in the ultimate load for monotonic and repeated loading, respectively. This was due to better bond properties provided by epoxy resin with CFRP strips. However, specimen strengthened using cement-based adhesive failed at a higher number of cycles.

The load capacity and the ductility of the beam strengthened using epoxy adhesive was found to increase by about 18.4% and 42.4%, respectively, in comparison with that strengthened using mortar, which had lower ductility and bonding strength at the concrete-adhesive interface [86]. It was also confirmed by Abdallah et al. [89] that the beam strengthened using epoxy adhesive showed 9.4% greater ultimate load than that strengthened using mortar. Furthermore, CFRP rods embedded using epoxy resin exhibited better resistance to the flexural bending than those embedded using mortar. More information on flexural strengthening of concrete structures using inorganic adhesives (i.e. mortar) can be found in [91].

5) Groove dimensions

The efficacy of the NSM-FRP strengthening technique was found to depend on the groove size, in addition to that the resistance to concrete split failure increases with the groove width [41]. It was also confirmed in [21] that embedding CFRP strips with a nominal width of 25 mm and a total thickness of 1.2 mm in 5 mm wide by 25 mm deep groove could prevent splitting of the epoxy cover. On the other hand, an inverse relationship between the bond strength of cement mortar-bonded NSM-FRP reinforcement decreases and the groove dimensions was also found in [91]. On the contrary, the load-carrying capacity of the strengthened beams was found to increase with the groove breadth and depth to FRP composite width ratio compared to non-strengthened beams. An inverse relationship was found when the groove depth to FRP width ratio exceeds 1.00 [92].

Using smaller groove width (i.e. 1.5*strip width (b_b) rather than 2.0b_b) resulted in higher load capacity (28%), ductility (44%), and energy absorption (84%) [90], which also delayed the debonding failure. Soliman et al. [93] found that the ultimate loads of the specimens strengthened with a groove size (i.e. depth) of 1.5d (d is the CFRP bar diameter) was on average 8.33% higher than those strengthened with 2.0d groove size. It was also stated that the smaller

groove size had insignificant effect on the strength, in terms of ultimate load, for bonded length greater than 24d.

Modes of failure associated with NSM-FRP flexural strengthening of concrete members

1) Ductile failures

Ductile failure can be categorised into two main modes, which are concrete crushing and the rupture of FRP reinforcement. Concrete crushing is a typical flexure mode in RC beams. It happens due to crushing of compressive concrete, next to mid-span, after tension steel reinforcement yields. This failure mode takes place by buckling of one or more compression steel bars with a gradual loss of the top surface of the RC beam, as shown in Fig. 2.10 (a).

The rupture of FRP reinforcement occurs by rupture of FRP reinforcement after yielding of tensile steel bars without failure of compressive concrete, due to good bond at concrete/adhesive/FRP interfaces. This mode of failure is recorded in specimens with sufficient NSM-FRP bonded lengths, as shown in Fig. 2.10 (b).

2) Brittle failures

RC beams could be failed in a brittle form through three main failure modes, including debonding failure, steel rupture and shear failure. Debonding failure occurs due to the loss of bond at FRP-adhesive-concrete substrate interface or by concrete cover separation. The failure of the FRP-adhesive-concrete interface takes place because of the intersection between flexural cracks and adhesive cover. When the maximum applied tensile and shear stresses reach the tensile strength of the adhesive, longitudinal splitting cracks start to appear in the adhesive cover parallel to the FRP reinforcement at the FRP ends or at mid-span, caused by stress concentration at the cut-off point or in the nearby flexural cracks. This mode of failure was noticed in specimens with inadequate NSM-FRP bond lengths, as shown in Fig. 2.10 (c-1).

Separation of concrete cover occurs because of the development of bond cracks on the beam's abdomen. These cracks transfer up on the beam's parts with approximately 45° slope inside concrete cover, they then spread horizontally by the side of tension steel bars, resulting in the separation of the concrete cover. In this mode of failure, NSM-FRP reinforcement remains attached to the concrete cover. This mode of failure is governed by the mechanical properties of concrete and adhesive, the ratios of tensile steel and FRP reinforcement and the geometry of FRP reinforcement, as shown in Fig. 2.10 (c-2).

Rupture of tensile steel reinforcement is considered as the most common failure mode of the NSM-FRP-strengthened RC beams and tested under low fatigue load ranges, followed by the failure mode of bond or FRP failure. Although the fatigue life of the RC beams strengthened using NSM-FRP system is controlled through the fatigue life of the tensile steel reinforcement rather than those of concrete or FRP reinforcement, the FRP reinforcement decreases the stress in the tensile steel bars, extending the fatigue life of the RC beams, which means that NSM-FRP-strengthened RC beams, which undergo to cyclic loads, may fail by tensile steel rupture before debonding of the FRP-concrete interface, which depends on the applied stress level in the tensile steel bars, as shown in Fig. 2.10 (d).

Shear failure is observed in beams made of high-density concrete and those reinforced with inadequate internal steel bars. The shear failure occurs due to formation of diagonal shear cracks in the shear span of concrete, which then propagate until reach the compression face causing the shear failure, as shown in Fig. 2.10 (e).

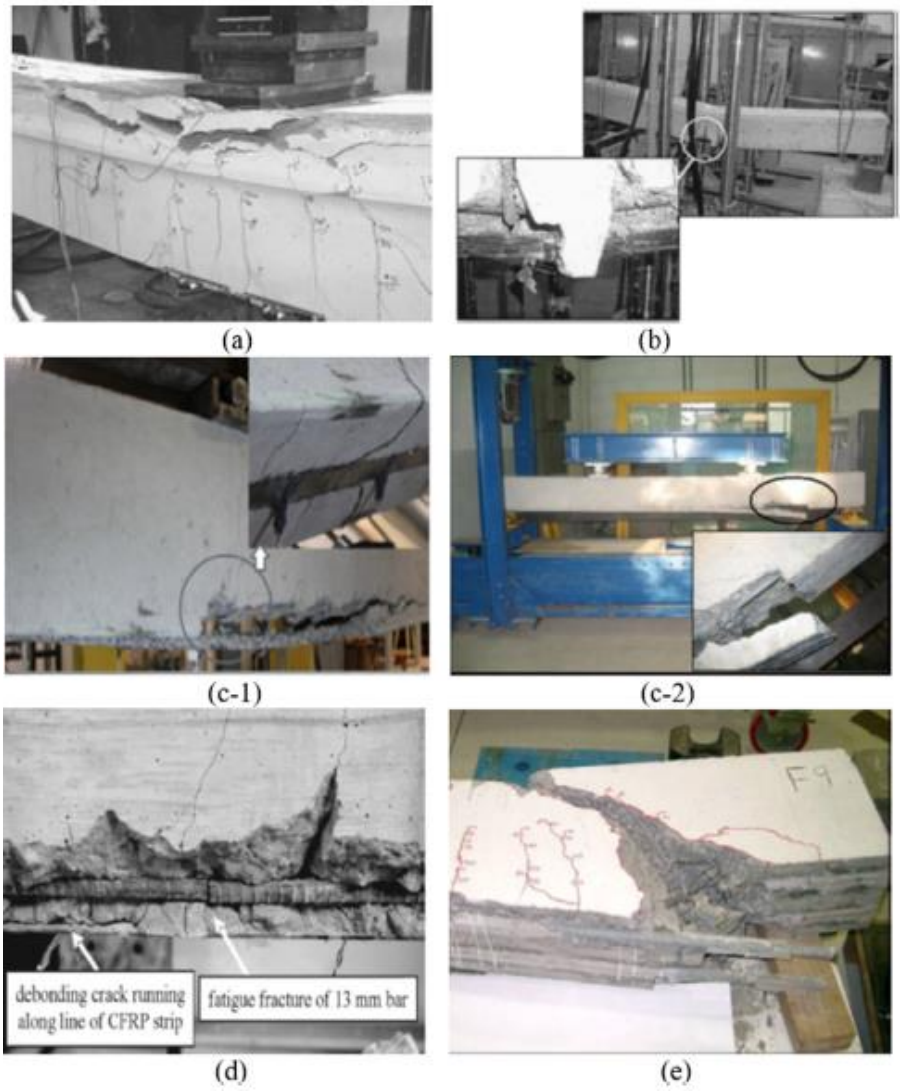

Fig. 2.10 Failure modes of NSM-FRP flexural-strengthened RC beams; (a) Concrete crushing, (b) FRP rupture, (c-1) Debonding failure due to failure of NSM-FRP-adhesive-concrete interface, (c-2) Debonding failure due to concrete cover separation, (d) Rupture of steel reinforcement and (e) Shear failure [2].

2.1.3.2.4 NSM-FRP shear strengthening of concrete members

As the shear mode of failure of concrete members is brittle and unpredictable, it should be avoided [10]. Several research studies confirmed that shear strengthening of RC beams with NSM-FRP reinforcement is very effective and it significantly enhances the shear strength/capacity and behaviour of the shear deficient specimens, in terms of maximum load and load-carrying capacity after formation of shear crack, in different manners [11, 31, 34, 59-61, 64, 66]. However, the performance of the NSM-FRP-shear- strengthened RC beams are influenced by many factors.

Factors affecting shear strengthening of concrete members

1) The percentage of steel shear reinforcement (stirrups)

It was noticed that there is an interaction between the percentage of steel stirrups and the behaviour of the NSM-FRP-strengthened beams. Where it was found that the effectiveness of the NSM-FRP system, in terms of the shear capacity of the strengthened beams, was higher in the beams with lower or no shear reinforcement [7, 10, 11, 59, 60, 62, 67]. For example, it was found by Ibrahim [7] that the specimen without steel stirrups showed an average of 7% and 9% higher load-carrying capacity and maximum deflection, respectively, than those with two stirrups. That was also confirmed in [59], where it was reported that an increase in capacity of only 35% compared to the control beam was obtained for the beams with steel stirrups while that value was 106% in absence of steel stirrups, which also showed 12-29% increase in beam capacity in further research study [62]. Other researchers [10] found that increasing the percentage of steel stirrups from 0.1% to 0.17% was found to decrease the load-carrying capacity by about 55%, which was 70% in another investigation [60]. However, it was found by Mofidi et al. [61] that the FRP shear contribution increased by about 14% in the beams with steel stirrups compared to those without stirrups, where the presence of steel stirrups was reported not diminish the shear contribution NSM-FRP reinforcement.

On the other hand, Rizzo and De Lorenzis [33] noticed that the presence of steel shear reinforcement influenced the modes of failure of the tested beams, as they stated that "the vertical legs of the steel stirrups create two vertical planes of weakness which facilitate the detachment of the side concrete covers".

2) The inclination of NSM-FRP reinforcement

It was found that, independently of other parameters (i.e. percentage of FRP and steel stirrups), the NSM-FRP shear strengthening with FRP rods/laminates inclined at 45°, 52°, and 60° with beam axis was more effective, in terms of enhancing load-carrying capacity, maximum load, stiffness and deformation at failure of the strengthened beams, than inserting them vertically (i.e. at 90°). This is because the total resisting bond lengths of FRP rods/laminates are higher in the case of using inclined laminates. It was also concluded that the debonding failure modes can be avoided by using inclined rods at an adequate close spacing [10-12, 30, 34, 59, 60, 62-65, 67, 70, 82].

For example, it was reported by Dias and Barros [10, 30] that strengthening specimens with 45°-inclined NSM-CFRP laminates rather than vertical ones showed a higher increase of 12% and 5% in the maximum load and maximum deflection, respectively [10], where these values were 16% and 39% in [30], while increased the shear capacity between 39.4% - 43.6% [59], which was because of 41.4% increase in the reinforcement in the case of inclined bars. A 6.4% - 11.3% increase in the shear resistance was also reported by Ali and Mezher [62], and it was also found that debonding of FRP rods can be prevented by using 45°-inclined rods, which showed in another investigation [82] an enhancement in the load-carrying capacity, ductility, stiffness and toughness by about 5.5%, 13.4%, 31.5% and 22.6%, respectively, compared to inserting them vertically. However, Rizzo and De Lorenzis [33] noticed that changing the angle of the NSM-CFRP bars from 90° to 45° led to 17% decrease in the shear capacity of the tested beams.

Other researchers [63, 70] found that the most effective inclination of NSM-CFRP laminates was 45°, regardless of the percentage of laminates. Where the beams strengthened with 45°-inclined laminates exhibited a 16% and 2% increase in the maximum loads compared with those strengthened with vertical and 60°-inclined laminates, respectively. Furthermore, laminates inclined at 60° showed about 15% higher increase in the maximum load than vertical laminates. On the other hand, another study [12] indicated that 22% and 13% increase in the maximum load and deflection, respectively, could be obtained when replacing the vertical laminates with inclined ones (i.e. at 52°).

As known, using inclined (i.e, at 45°) CFRP reinforcement rather vertical ones would result in increasing the length of the reinforcement. The corresponding increase in the shear capacity due to using inclined NSM-CFRP reinforcement instead of vertical reinforcement is shown in Fig. 2.11, considering the increase in the CFRP length.

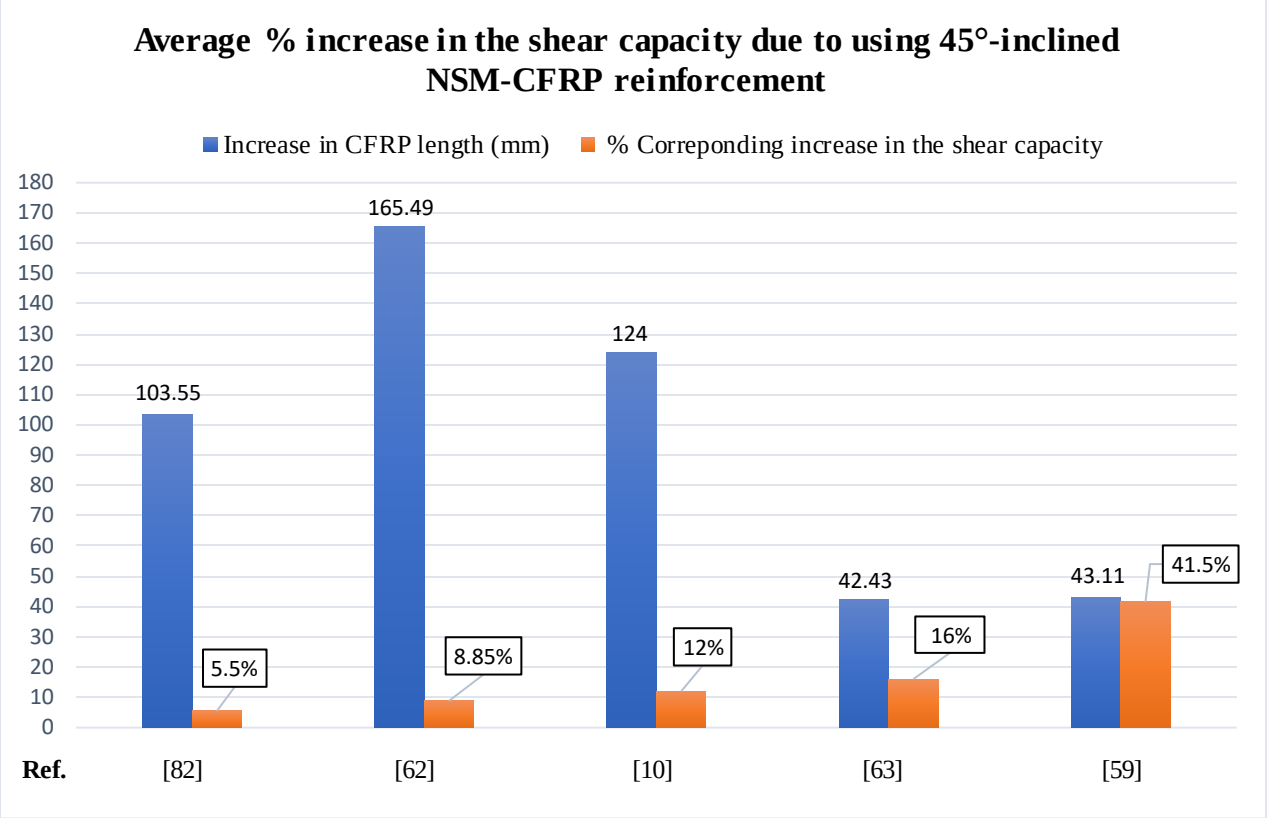

Fig. 2.11 Average % increase in the shear capacity of NSM-FRP-retrofitted RC beams due to using 45°-inclined NSM-CFRP reinforcement other than vertical reinforcement.

3) Percentage of NSM-FRP reinforcement

It was concluded that the increase of the CFRP percentage (in terms of the number of CFRP rods/ laminates) produced more efficient strengthening in terms of increasing the shear capacity of the strengthened beams [7, 10-12, 30, 31, 60, 63, 67, 70]. For instance, Ibrahim et al. [7] found that the specimens strengthened using four NSM-FRP strips exhibited an increase in the load-carrying capacity of about 4% and 12% compared to those strengthened with three and two strips, respectively. Doubling (i.e. from 1 to 2) and tripling the number CFRP rods showed about 4% - 6% higher ultimate loads, respectively [31]. Increasing the 60°-inclined CFRP reinforcement ratio from 0.07% to 0.11% enhanced the load capacity and the maximum deflection by about 5% and 7%, respectively [10], and by about 2% and 14%, respectively [60], while increasing the reinforcement ratio from 0.08% to 0.13% resulted in about 11% and 54% increase in the maximum load and deflection, respectively, for the beams strengthened with vertical laminates [30], while those values were about 7% and 23%, respectively for beams strengthened with 45°-inclined laminates [63, 70]. This means that increasing the NSM-CFRP reinforcement ratio was more effective in the case of using vertical laminates than in the case of applying the laminates at 45° inclinations. It was also concluded that, with increasing the

NSM-CFRP reinforcement ratio, the performance of the beams strengthened with 45°-inclined laminates was better than those strengthened with 60°-inclined laminates.

4) The spacing of NSM-FRP reinforcement

Several studies found that decreasing the spacing of the NSM-FRP rods enhances the shear capacity of the strengthened beams [12, 59, 62, 65, 67]. Dias and Barros [12] noticed that, for the beams strengthened with 45°-inclined laminates, decreasing the spacing between the laminates to the half (i.e. 350 mm to 175 mm) increased the maximum load and deflection by 23% and 36%, respectively, while in the case of vertical laminates, the maximum load enhanced by 18% but the maximum deflection dropped by 11%. Decreasing the spacing of the NSM-CFRP rods from 178 mm to 127 mm, which corresponds to 40% increase in the amount of FRP material, yielded 10.8% and 7.5% increment in the load-carrying capacity, respectively, when using vertical and 45°-inclined rods [59], while reducing the CFRP spacing form 150 mm to 100 mm led to 8% increase in shear capacity [62].

However, it was noticed that decreasing the spacing of the CFRP bars decreased their contribution to the shear resistance because that accelerated the formation of the debonding failure mode involving all the bars together [33, 66]. For instance, Rizzo and De Lorenzis [33] indicated that for the beams strengthened with 45°-inclined NSM-CFRP bars, decreasing the spacing of the bars from 146 mm to 73 mm resulted in about 7% drop in both shear and ultimate capacities. On the other hand, there was no enhancement neither in the shear capacity nor in the ultimate load by decreasing the spacing between the vertical bars. That was due to that decreasing the spacing led to an earlier formation of the debonding failure involving all the NSM-CFRP bars together. Tanarslan [66] found that decreasing the CFRP reinforcement spacing reduced the FRP contribution to the shear resistance by at least 32%. Dias and Barros [10, 11, 63] stated that "a limit exists for the spacing between laminates since for the maximum percentage (0.19%) of laminates a failure mode consisting of the detachment of the concrete cover of the beams lateral faces occurred, leading to a loss of effectiveness of the technique".

5) Geometry and dimensions of NSM-FRP reinforcement

Rizzo and De Lorenzis [33] found that the beams strengthened with NSM-CFRP strips have slightly lower maximum loads (2.2% to 4.4%) than those strengthened with NSM-CFRP round bars, while it was confirmed in [66] that the specimen strengthened with 9 mm diameter CFRP rods exhibited 29% and 12% higher strength and strain increments, respectively, compared to those strengthened with 6 mm diameter. Besides, specimens strengthened with larger CFRP

rods showed additional ductile behaviour accompanied by a reduced development of shear crack.

6) Groove-filling material

The type of filler was found to be of high importance in the strengthening process because it works as a medium to transfer load/stress from concrete to FRP materials and distribute them evenly through both concrete/adhesive and FRP/adhesive interfaces [95]. Two types of epoxy adhesives were considered by Rizzo and De Lorenzis [33] with direct tensile strengths of 18.6 MPa and 22.8 MPa and corresponding tensile elastic moduli of 4.15 GPa and 12.87 GPa. It was noticed that the beam strengthened using epoxy having lower tensile strength and elastic modulus failed at 19% higher load, and its FRP contribution to the shear capacity was more than twice that of the beam strengthened using the one with higher mechanical properties. On the other hand, Al-Mahmoud et al. [31] found that the beams strengthened using epoxy resin exhibited greater ultimate load by about 6% compared to those strengthened using mortar.

7) Depth of beams

Dias and Barros [12] found that shear strengthening with NSM-CFRP laminates is very efficient in RC beams of relatively large T-cross section height (h = 600 mm) in terms of enhancing the load-carrying capacity (between 21% and 83%) and assuring higher mobilization of the laminates' tensile capacity. By comparing the results of this study with the results of the experimental study conducted by Dias and Barros [11] with the same test setup but using RC beams of lower T-cross section (h = 400 mm), it was verified that the effectiveness of the NSM-CFRP shear strengthening technique increased with the height of the beam cross section, which was also confirmed by Dias and Barros [34]. However, Ali and Mezher [62] reported that NSM-CFRP strengthening system had a small effect (3%) on decreasing the mid-span deflection of deep beams (h=400 mm).

Modes of failure associated with NSM-FRP shear strengthening of concrete members

Multiple modes of failure associated with shear strengthening of RC beams have been recorded in the literature. For instance, debonding of one or more FRP rods due to splitting of the epoxy cover was observed by De Lorenzis and Nanni [59] and Ali and Mezher [62], while the shear failure was the governing failure mode of the beams tested by Barros and Dias [64]. Shear failure, flexural failure, and peeling-off of NSM-FRP layers were recorded by Wiwatrojanagul et al. [65]. Debonding failure (it was not pure debonding since parts of concrete were still adhered to the laminate, indicating that failure occurred due to debond and concrete fracture)

and separation of parts of the concrete cover were observed by Dias and Barros [10, 30, 60, 63]. Three modes of failure were recorded by Dias and Barros [11], which are rupture of the CFRP laminates, sliding of CFRP laminates at the CFRP-adhesive interface, and concrete fracture. All the tested beams by Dias and Barros [12] failed in shear in the shear span. All beams test by Al-Mahmoud et al. [31] failed by crushing of the compressed concrete, except one beam failed by shear. Mofidi et al. [61] found that the final failure was in shear because of splitting of the concrete cover, wherein two thick layers of concrete cover (including the NSM-FRP rods) split off from the beam sides. The beams tested by Rizzo and De Lorenzis [33] failed due to spalling of the bottom concrete cover of the steel longitudinal reinforcement, also by separation of the side concrete covers of the internal steel stirrups, while three different failure modes were observed in the beams strengthened and tested by Tanarslan [66], which are: (1) the typical shear failure, (2) the shear failure due to separation of concrete cover and (3) flexural failure followed by shear failure.

2.1.3.2.5 Bond behaviour of NSM-FRP-bonded joints

The bond between FRP reinforcement and concrete substrate plays a key role in the NSM-FRP strengthening system, therefore, to ensure an effective NSM-FRP strengthening, there should be an adequate bond between FRP reinforcement and concrete substrate, with a suitable adhesive material which works as a medium to transfer load/stress from concrete to FRP materials and distribute them evenly through both concrete/adhesive and FRP/adhesive interfaces, eventually resulting in a successful strengthening process. Thus, understanding the factors affecting the bond behaviour among the NSM-FRP reinforcement and concrete is of high importance.

Factors affecting the bond behaviour of the NSM-FRP joints

The factors affecting the bond behaviour of the NSM-FRP joints were found to be:

1) Groove-filling materials

As the groove-filling adhesives are responsible for the loads' distribution on the individual fibres, their type and properties have a great effect on the bond between NSM-FRP reinforcement and concrete, and they are considered as crucial for an efficient design and strengthening process. It was found that the use of groove-filling epoxy with higher modulus of elasticity and tensile strength caused the failure mode to shift from NSM-FRP bar-epoxy interface to splitting of concrete cover. A corresponding higher bond strength and load capacity, and lower slip at maximum pull-out force was also reported [44-46].

For instance, Galati and De Lorenzis [44] found that using epoxy resin with 23% and 210% higher tensile strength and elastic modulus, respectively, yielded about 65% increase in bond strength of NSM-CFRP joints, which showed in further study [45] about 8% - 20% increase in load capacities, when stiffer epoxy, e.g. 19.8%, 11.1% and 20.8% higher elastic modulus, tensile and compressive strengths, was used. Using stiff adhesive rather than flexible one resulted in 700% higher maximum pull-out forces and bond stiffness, and shifted the failure mode from a mixed failure mode combining debonding at laminate-adhesive interface and cohesive failure in the adhesive to debonding at laminate-adhesive interface or by CFRP rupture [46]. 20% increase in the failure load of NSM-CFRP bonded specimens was reported due to using epoxy resin with 22% higher tensile strength [77].

On the other hand, the ultimate pull-out loads of the specimens bonded using epoxy-filled grooves were always higher than those bonded using cement mortar. Debonding failure at the mortar-concrete interface was also observed [49, 50, 57]. For example, Al-Mahmoud et al. [49] reported that the ultimate load of the bonded joints in the case of the resin was in all cases about twofold that obtained with the mortar, which exhibited, in another investigation [50], 40% - 56% lower ultimate/pull-out loads than those with epoxy adhesive, which mainly failed by concrete tension accompanied with or without epoxy splitting, while adhesive splitting at the concrete-cement interface was observed to be the main mode of failure for the mortar-bonded specimens, which showed in [57] 70% lower maximum load than that of epoxy-filled specimens. This was due to the lower flexural tensile strength of the mortar (6.3 MPa) compared to the direct tensile strength of epoxy (28 MPa).

2) FRP bonded length

It was concluded that as the embedment length of the FRP reinforcement enhances the ultimate pull-out load, the corresponding strain, and the maximum displacement of the NSM joints increases, but the bond strength found to be approximately constant or tends to decrease due to the uneven distribution of the bond stresses along the bonded length. However, the failure modes are not affected by changing the bonded length [40, 45-48, 50-52, 54-57, 68, 77].

De Lorenzis and Nanni [40] noticed that the ultimate pull-out load increased by 15% and 40% with doubling the bonded length (i.e. from $6d_b$ to $12d_b$) for CFRP and GRFP-bonded specimens, respectively. However, the average bond strength was approximately unchanged with the bonded length for the CFRP-bonded joints, indicating a uniform distribution of bond stresses along the bonded length at ultimate. While it was found to decrease by about 43% for

GFRP-bonded specimens. Increasing the CFRP bonded length in the same manner as previous resulted in 83% increase in failure/pull-out load. However, about 9% drop in the average bond stress was observed, which was due to the uneven stress distribution in the case of longer bonded length [50]. Similar findings were reported by Merdas et al. [52], as doubling (40 mm to 80 mm) and tripling (40 mm to 120 mm) the bond length of the CFRP rods increased the maximum pull-out load by 37% and 102%, respectively. However, a corresponding decrease of 46% and 49% in the bond stress was observed. The doubling and tripling the CFRP bonded length (i.e. from 150 mm to 300 mm and 450 mm, respectively) could significantly increase the ultimate loads of the joints by 71% and 168%, respectively [68], while the average bond strength was found to be approximately constant, which was ascribed to the uniform distribution of bond stresses along the bonded length at ultimate. Similarly, increasing the bonded length by threefold (i.e. from $4d_b$ to $12d_b$) produced a 103% increase in the maximum load of the NSM-CFRP joints, but a 10% drop in the average bond strength was noticed.

42%, 46%, and 21% average increase in the load capacity, respectively with increasing the CFRP-bonded length from $12d_b$ to $24d_b$, $12d_b$ to $30d_b$, and $24d_b$ to $30d_b$ was found by Torres et al. [45]. Bonding specimens with 100 mm long CFRP laminates rather than with 80 mm and 60 mm led to about 14% and 32% higher ultimate loads, respectively, but the corresponding average shear bond strength decreased by about 9% and 26% [46]. Similar observations were reported by Novidis et al. [48], where increasing the bonded length of CFRP rods from $3d_b$ to $5d_b$ and to $10d_b$ produced an increase of about 113% and 144% in development capacity of the joints (in terms of total load carried), respectively, while a reduction of the average bond strength after a critical bonded length was observed, which was attributed to the non-uniform distribution of the bond stresses along the bonded length. 22% - 25% increase the in the maximum load of the bonded joints with increasing the CFRP bonded length by 50% (i.e. from 150 mm to 275 mm) was reported by Gómez et al. [51] for specimens with 7.5 mm and 10 mm groove thickness, respectively, keeping the failure mode at concrete-adhesive and FRP-adhesive interfaces, respectively.

An increase in the maximum pull-out loads by 52% and 49%, respectively with increasing the bond length of CFRP strips from 40 mm to 60 mm and to 80 mm were found by Barros and Sena-Cruz [55, 56], while the corresponding displacements increased by 69% and 124%. A marginal increase (i.e. 1%) in the corresponding bond strength was observed by increasing the bonded length from 40 mm to 60 mm. However, doubling the bonded length decreased that

value by about 35%. Results obtained by Sharaky et al. [77] indicated that increasing the bond length of the NSM-CFRP bars by 25% ($12d_b$ to $15d_b$) enhanced the failure load of the NSM joints by about 17 % without forming splitting cracks on either the surface of the epoxy paste or the concrete. A marginal difference in average bond stress was observed. Fig. 2.12 shows the effect of increasing CFRP bonded length on the capacity of NSM-CFRP bonded joints. It could be noticed, generally, that the % corresponding increase in joints' capacity increases with the CFRP bonded length.

On the other hand, it was reported by Seracino et al. [17], which considered bonded lengths between 100 mm and 350, that the maximum load-carrying capacity could be achieved with a minimum bonded length of 200 mm, while bonded lengths between 25 and 350 mm were used by Zhang et al. [53] to test CFRP-NSM-strengthened concrete members. Results revealed that the experimental effective bonded lengths for the different specimens were between 150 mm and 175 mm.

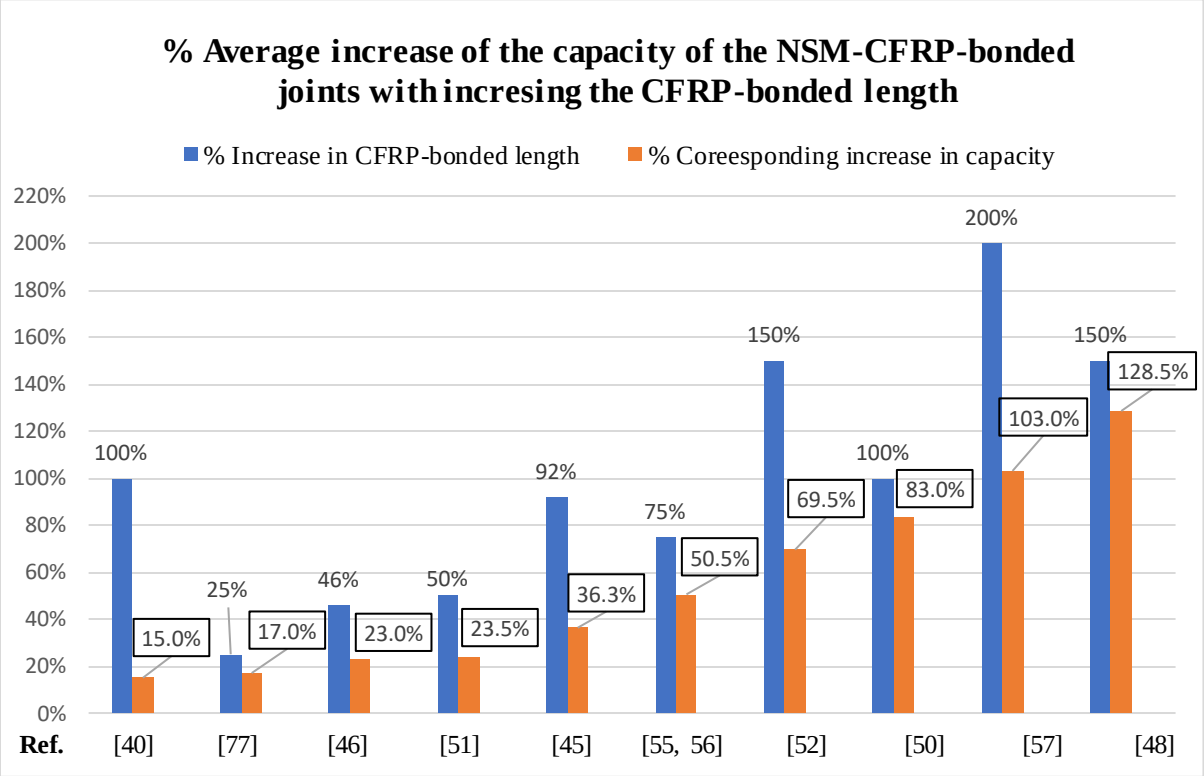

Fig. 2.12 The effect of increasing the CFRP-bonded length on the capacity of the NSM-CFRP-bonded joints.

3) Type of FRP reinforcement and its surface texture

It was found by Torres et al. [45] that using CFRP instead of GFRP yielded 5% increase in the maximum loads of the NSM joints and shifted the failure mode from either detachment of

concrete cover, bar-epoxy interface failure, or bar damage to failure at bar-epoxy interface and concrete cracking. Similarly, the CFRP-bonded specimens were found to fail at 17% higher maximum load compared to those bonded with GFRP bars [77]. It was also noticed that the CFRP-bonded specimens failed at bar-epoxy interface, while failure due to epoxy splitting followed by concrete detachment was noticed with those bonded with GFRP bars. It was reported by Coelho et al. [47] that the maximum pull-out force installed in the FRP increases when moving from BFRP to GFRP and from GFRP to CFRP bars, which was due to increasing stiffness from basalt to carbon. In contrast, Soliman et al. [50] reported that the specimens bonded by GFRP bars showed 36% and 73% higher ultimate load and average bond stress, respectively, than those strengthened with CFRP bars. However, the failure mode of FRP bar slip was not affected.

On the other hand, the surface texture of the FRP reinforcement was also found to influence the bond performance and the failure modes of the NSM joints [36, 40, 47, 57, 96]. For example, De Lorenzis and Nanni [40] reported that the deformed CFRP rods exhibited a greater tendency to induce splitting failure than the sandblasted ones and were more efficient in terms of bond performance, while the dominant failure mode for both spirally wound and ribbed CFRP bars was found to be at the concrete-epoxy interface [57]. Bonding specimens with CFRP bars with textured surface exhibited about 34% higher failure load over those bonded with smoother surface bars, which could be due to the effect of the surface treatment and bar size [96].

4) FRP size and geometry

Differences in either FRP reinforcement dimensions or cross-section geometry would influence the bond performance between FRP reinforcement, adhesive and concrete substrate. It was found that using CFRP laminates with larger cross-section achieved a higher maximum pull-out load, due to the higher contact area at the laminate-adhesive and adhesive-concrete interfaces. It was also found that using CFRP strips with larger aspect ratios (width/thickness) resulted in more effective bond behaviour. However, the loaded end slip at the maximum pull-out force was found to be higher in the specimens bonded with the smaller CFRP laminates, while the bond stress development at laminate-adhesive interfaces is independent of the CFRP cross-sectional dimensions. It was also confirmed that, in terms of exploring the FRP capacity, the rectangular bars are more efficient than round bars as the former explore better the surface to cross-section area ratio [17, 46, 47, 50, 52, 77].

Cruz et al. [46] found that specimen bonded by CFRP laminate with 20 mm width showed about 80% higher pull-out force than that bonded with 10 mm wide laminate, which exhibited 40% increase in the loaded end slip. Increasing the CFRP bar diameter by about 13% led to 22% increase in the failure load characterised by the same failure mode observed at maximum load (i.e. failure at bar-epoxy interface) [77], while 50% increase in the GFRP bar diameter produced about 75% increase in the failure load. However, Soliman et al. [50] found that using CFRP rods with 12.7 mm diameter instead of 9.5 mm reduced the pull-out load and the average bond stress by 53% and 160%, respectively, and changed the failure mode from concrete tension failure and splitting of epoxy to bar slippage. With regard to the FRP geometry, Merdas et al. [52] found that using CFRP plates instead of CFRP rods yielded a 29% improvement in the maximum pull-out load despite both of them had a similar cross-sectional area of 50 mm^2. This might be due to that the plates provided a greater contact surface area so that a greater pull-out force was achieved. However, about 30% drop in bond stress was noticed.

5) Groove size and geometry

Several research studies [40, 44, 68, 77, 96] found that the bond strength, the ultimate load and the fracture energy of the NSM joints increase with larger groove size, which also provides a higher resistance to splitting of the epoxy cover, because that decreases the state of stress in the concrete adjacent to the groove sides, which ultimately delays its cracking phenomena.

For instance, De Lorenzis and Nanni [40] found that the ultimate load of the GFRP-bonded specimens increased by 8% and 24%, respectively with increasing the groove size from 16 mm to 19 mm and to 25 mm, while those values were 15% and 8% for CFRP-bonded joints. This increase can be justified considering that as the groove size increases, the thickness of the epoxy cover increases, which offers a higher resistance to splitting and eventually shifts the failure from epoxy to the surrounding concrete. In similar manner, increasing the groove size from 13 mm to 19 mm and to 25 mm was found to respectively increase the ultimate load by 15% and 8%, which was due the same reason reported in [40]. Increasing the groove width by one-third (i.e. from 12 mm to 16 mm) increased the bond strength of CFRP-bonded joints by 39%, and cracks are no longer observed in the concrete surrounding the grooves at failure [44]. Similar observations were reported by De Lorenzis et al. [57], where increasing groove depth form $1.25d_b$ to $1.5d_b$ enhanced the ultimate load and the average bond strength by approximately 25% and 12%, respectively, however, the trend of the average bond strength dependent on the failure mode, especially when failure is at the epoxy-concrete interface.

It was found by Sharaky et al. [77] that increasing the width of the square grooves by one-third resulted in about 9% and 12% increase in the failure loads, respectively for specimens bonded with CFRP bars and GFRP bars, while increasing the size of the square grooves from $1.5d_b$ to $2d_b$ was found in [96] to increase the failure load by about 15%, which also delayed the failure at bar-epoxy interface. Novidis et al. [48] found that, when failure is controlled by pull-out at the bar-epoxy interface, increasing the groove size (i.e. groove depth) from 20 mm to 25 mm led to higher average bond strength by about 11%, 40% and 11% for the bonded length $3d_b$, $5d_b$, $10d_b$, respectively. However, when the failure occurs at epoxy-concrete interface increasing the groove depth either decreases the average bond strength of epoxy-concrete interface as in case of bonded lengths $3d_b$ (13%) and $10d_b$ (12%) or has a slight effect (12% increase) as in the case of bonded length $5d_b$.

However, it was found by Soliman et al. [50] that increasing the groove size from $1.5d_b$ to $2.0d_b$ did not have a notable effect on the failure load of the specimens bonded using epoxy adhesive, and it decreased the failure load for specimens with cement adhesive by about 27%. Nevertheless, it was observed that increasing the groove width enhances the resistance to splitting of epoxy. On the other hand, it was reported by Gómez et al. [51] that ultimate load of the bonded joints increased by about 7-10% with decreasing the groove thickness from 10 mm to 7.5 mm, which also changed the failure modes from FRP-adhesive interface to failure in concrete-adhesive interface. It's noteworthy that increasing the groove dimensions was found in [47] to have no effect on the maximum pull-out force installed in the FRP if the failure mode is cohesive in concrete or at the FRP/adhesive interface.

Concerning the groove geometry, it was noticed by Al-Mahmoud et al. [49] that the maximum pull-out loads were 44% lower in the case of rectangular grooves (i.e. 20x50mm) than in the case of square grooves (i.e. 20x20m and 30x30mm). It was also found that a groove width to nominal rod diameter ratio between 1.7 and 2.5 appears to be optimal. Also, for 12 mm diameter CFRP rods, a groove section of 25 × 25 mm could be adequate.

6) Concrete strength

The concrete compressive strength was found to have a slight influence on the maximum loads, bond strength and failure modes of the NSM joints [17, 47, 49, 52, 55, 56, 69, 77, 96]. For instance, it was reported in [52] that increasing the concrete strength from 30 MPa to 50 MPa led to 33% increase in maximum pull-out load and bond stress. This influence was more pronounced for smaller bond lengths (i.e. 40 mm). Barros and Sena-Cruz [55, 56] reported that,

for the specimens bonded by 40 mm-long CFRP strips, increasing the concrete strength from 35 MPa to 45 MPa and to 70 MPa led to 3% and 5% increase in the maximum pull-out load, respectively, and about 4% and 5% corresponding increase in the bond strength was observed. In addition, doubling the concrete strength resulted in about 10% enhancement in the maximum deflection. However, increasing the concrete strength by about 30% decreased the maximum deflection by about 8%. Using concrete with 65.7 MPa compressive strength rather 34.0 MPa was found in [49] to increase the ultimate load by only 4%.

However, by comparing the specimens considered by Sharaky et al. [77], which were made of concrete with an average compressive strength ranging between 22 MPa and 25 MPa with those tested by Sharaky et al. [96] which produced from concrete with an average compressive strength ranging between 35.2 MPa and 42.2 MPa, it was found that concrete strength had a slight influence on the load-carrying capacity of the specimens failed by epoxy splitting or at bar-epoxy interface, knowing that the same epoxy resin was used to bond both specimens.

Finally, Coelho et al. [47] reported that the ultimate pull-out force detected in the FRP increases with the concrete compressive strength as long as the failure mode is cohesive within concrete, while for another failure mode changing the compressive strength has no effect on the maximum pull-out force. Besides, it was reported by Bilotta et al. [69] that using low-strength concrete led to most NSM-FRP specimens to fail at the concrete-adhesive interface at low ultimate pull-out load.

Modes of failure associated with bond tests of NSM-FRP bonded joints

As reported in the literature [2, 36], several modes of failure, including bond failure, rupture and pull-out of FRP and splitting of adhesive cover, have been observed in regard with the bond behaviour between NSM-FRP reinforcement, concrete, and adhesive, as follows:

The bond failure at the FRP-concrete interface may happen either by pure interfacial failure (BE-I), or by cohesive shear failure in the groove filler (BE-C) [36], as shown in Fig. 2.13. The BE-I mode was observed in NSM-FRP bars with a smooth or lightly sand-blasted surface, while the BE-C failure mode was noticed in NSM-FRP strips with a roughened surface. This mode happens when the shear strength of the epoxy is exceeded, which leads the crack to propagate in the concrete next to the NSM-FRP reinforcement, causing debonding failure. This failure type was also observed in specimens with low-strength concrete or with high tensile strength adhesive [2], as shown in Fig. 2.14 (a).

While the failure at the adhesive-concrete interface may take place as pure interfacial failure (EC-I), or as cohesive shear failure in the concrete (EC-C) [36], as shown in Fig. 2.13. The EC-C failure mode has never been observed in bond tests, but it has been observed in bending tests on beams within the strengthened region or at the bar cut-off point. Rupture of FRP materials occurs because of effective confinement, which was noticed in specimens with adequate bonded lengths [2], as shown in Fig. 2.14 (b).

Pull-out of FRP was recorded in specimens with low tensile strength adhesive or inadequate bonded lengths, and it happens on account of the weak bond between the adhesive and the concrete at the adhesive/concrete interface, or between the FRP and the adhesive at the FRP/adhesive interface [2], as shown in Fig. 2.14 (c).

Splitting of adhesive cover was found to be the critical failure mode for deformed (i.e. ribbed and spirally wound) round bars. It is caused by longitudinal cracking of the adhesive and/or fracture of the surrounding concrete along inclined planes. There are different patterns of this failure type. For example, when the ratio k (k = groove width / FRP bar diameter) is very low, failure is limited to the epoxy cover and involves little damage in the surrounding concrete (SP-E). For higher values of k, failure involves a combination of longitudinal cracking in the epoxy cover and fracture of the surrounding concrete along inclined planes (SP-C1). For large groove depths and/or when the tensile strength ratio between concrete and epoxy is small, fracture of concrete may happen before the epoxy crack has reached the external surface (SP-C2). The bond failure modes mentioned above are for an NSM-FRP bar located centrally in a wide member, where edge effects are not significant. If an NSM-FRP bar is placed close to the concrete edge, failure involves the splitting of the concrete edge (SP-ED) [36], as shown in Fig. 2.14. This type of failure may also take place because of the small depth of groove, which leads to the local splitting of the adhesive cover without cracking in the concrete substrate [2], as shown in Fig. 2.14 (d).

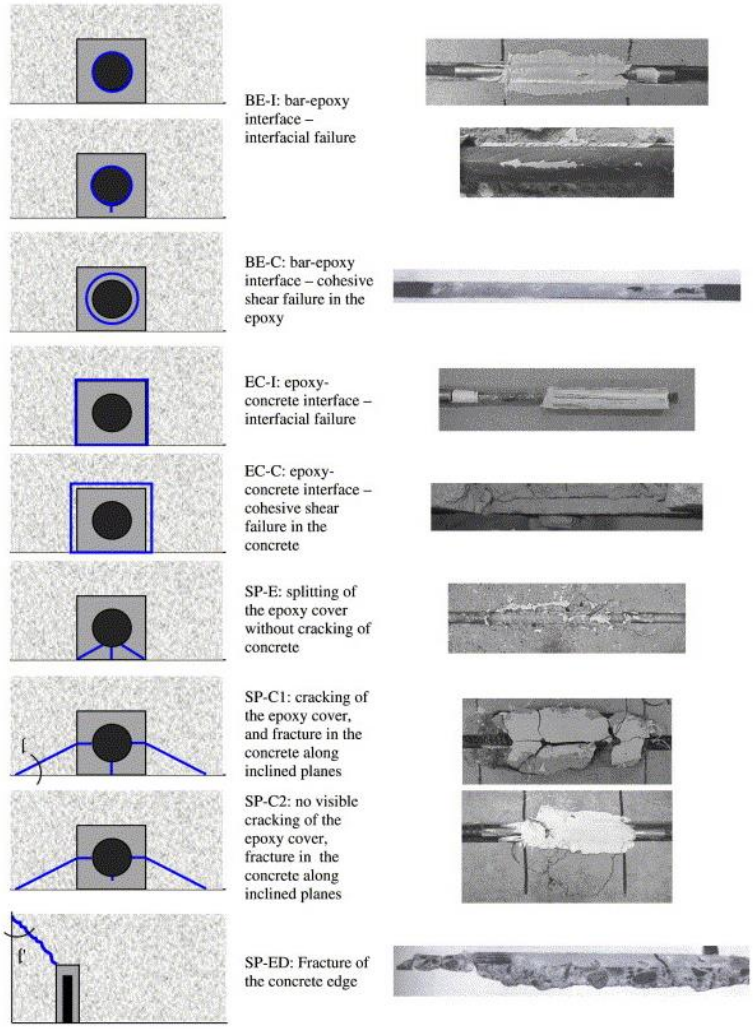

Fig. 2.13 Failure modes of NSM system observed in bond tests [36].

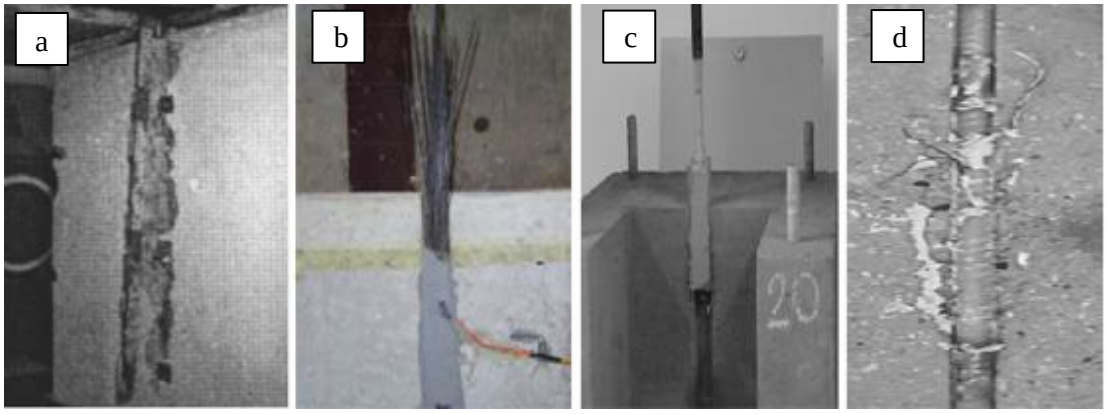

Fig. 2.14 Failure modes of NSM-FRP pull-out specimens; (a) Bond failure, (b) Rupture of FRP, (c) Pull-out of FRP, (d) Splitting of adhesive [2].

2.2 Effect of bonding agents on the efficiency of concrete retrofitting

The type of the bonding agent used in concrete retrofitting with FRP composites plays a key role in such processes since their success is highly dependent on the bond characteristic of the FRP-adhesive-concrete interfaces. It is because of the fact that the adhesive layer works as a medium to transfer and distribute stresses between concrete and FRP reinforcement. Therefore, the properties of adhesives are crucial in determining the FRP-adhesive-concrete interfacial bond strength, thus, attentions must be paid to selecting suitable bonding agents for a specific retrofitting process [100]. And as reported earlier, the performance of the NSM-FRP flexural- and shear-retrofitted concrete members and the NSM bonded joints was found to be considerably affected by the type of bonding agent used in retrofitting or bonding process.

2.2.1 Neat epoxy adhesives for concrete retrofitting

Thermosetting polymers are the most preferred polymer matrices for research and industrial purposes, such as adhesives, coatings, semiconductor encapsulation, hardware components, electronic circuit board materials, aerospace, and composite matrix, because of their high performance, such as high tensile strength and stiffness, superior electrical performance, and excellent chemical resistance compared to thermoplastics. The characteristics of epoxy, such as low residual stress due to its low shrinkage during curing and low pressure required for fabrication, make it a unique resin among other thermosetting resins. As epoxy resin, when cured, is an amorphous and highly cross-linked polymer, it is the most used polymer matrix to bond FRP materials to the substrate of deteriorated concrete members to restore their strength, stiffness, and integrity [100, 103, 132]. The formation of such microstructure systems gives rise to many useful properties for structural purpose, such as a high modulus and failure strength, low creep, good performance at elevated temperatures, and excellent thermal stability. The process-ability, compatibility of epoxy resin with most fibres, wear resistance and cost-effectiveness, and good affinity to heterogeneous materials, chemical erosion resistance and on-the-spot processing capability have made the epoxy bonding systems preferable and widely used to join FRP materials onto structural components in retrofitting structures [100, 108, 132-134]. Therefore, the epoxy layer plays a key role in the retrofitting processes, and if it offers a strong bond with both FRP and concrete, creating an improved interface region, this will lead to a successful retrofitting process.

Despite the excellent properties offered by the epoxy matrix, there are some major drawbacks, for instance, the structure of some thermosetting polymers leads to a highly undesirable property in that they are relatively brittle, which is detrimental to the inter-laminar properties,

having a poor resistance to crack initiation and growth. The highly cross-linked structure of epoxies also results in inherently low fracture toughness and hence poor resistance to fracture [102, 108, 133, 134]. The retrofitting of concrete members using FRP composites has some drawbacks regarding the performance of the epoxy layer, which acts as a transition layer to transfer stresses between concrete and FRP materials. These disadvantages may include the debonding of FRP materials from concrete substrates, which may be caused by the non-uniform stress distribution between concrete/adhesive and FRP/adhesive interfaces, and eventually leads to the debonding of FRP-retrofitted concrete members. Debonding is considered as the main issue of retrofitting process. Consequently, these weaknesses make the debonding of FRP materials strengthened concrete elements predominant (failure mode), therefore, the total utilisation of the tensile strength of the FRP materials becomes impossible [97].

The typical failure modes of EBR-FRP-retrofitted concrete elements are summarised in Fig. 2.15. It's noteworthy that Fig 2.15 (b) is similar to Fig. 2.13 included previously, but it was added once again for the convenience of the reader. The failure modes shown in Fig. 2.15 indicates that the main reason of failure in concrete retrofitting process by FRP composites is either due to the failure in epoxy layer itself or debonding at FRP/epoxy or epoxy/concrete interfaces. Therefore, the performance of epoxy adhesives needs to be enhanced so they can be effectively used in the EBR-FRP and NSM-FRP applications. The addition of nanoparticles to epoxy was found to be an ideal solution, as they showed significant improvements in the mechanical, thermal, and bond properties of epoxy adhesives, as detailed in the subsequent section.

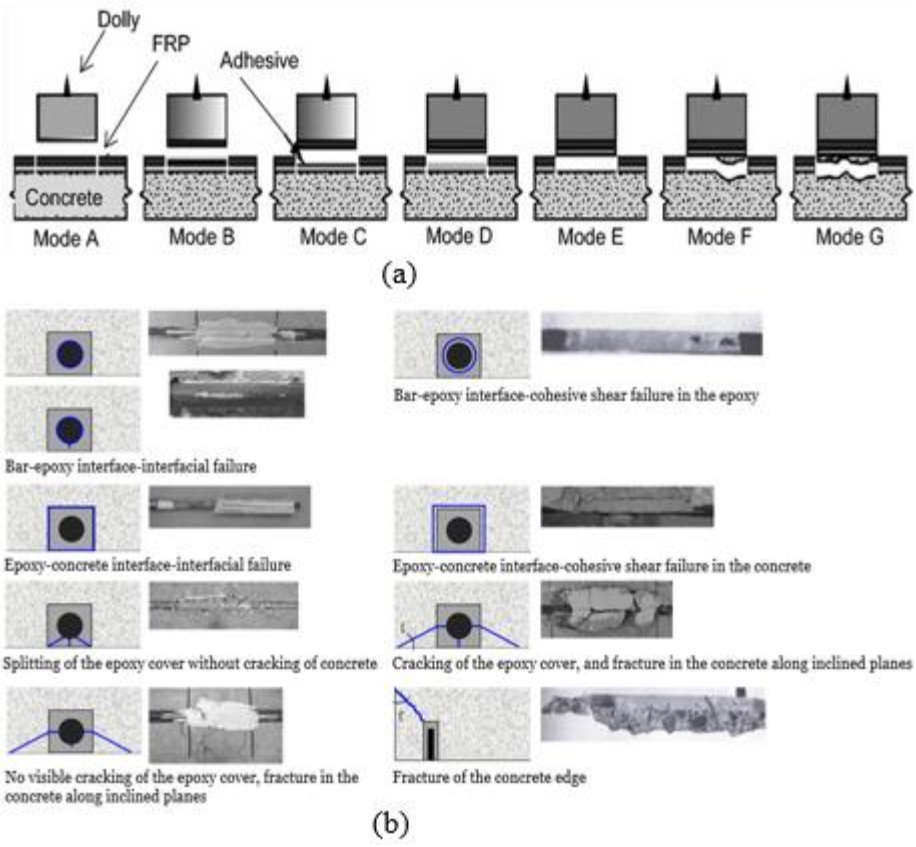

Fig. 2.15 Failure modes of FRP-retrofitted concrete elements using EBR retrofitting [132] and (b) NSM retrofitting [36]. Notes for (a): A=Bonding epoxy failure at dolly (loading fixture), B= Cohesive failure in FRP laminate, C= Epoxy failure at FRP/epoxy interface, D= Cohesive failure in epoxy, E= Epoxy failure at FRP/concrete interface, F=Mixed cohesive failure in concrete and epoxy at the epoxy/concrete interface and G= Cohesive failure in the concrete substrate.

2.2.2 Nanomaterial-modified epoxy adhesives for concrete retrofitting

2.2.2.1 Preface

As aforementioned, the highly cross-linked epoxy resins are rigid and brittle and have relatively poor resistance to crack initiation and growth, which limit their use in structural retrofitting. Many attempts have been made to improve their properties using various toughening or strengthening agents. Directly blending the epoxy resins and nano-fillers, such as carbon, silica, and clay, provides a convenient route to form epoxy resin inorganic hybrid composites. These nanoparticles are widely used in the preparation of epoxy adhesives to enhance their mechanical and thermal properties, owing to their extraordinary thermo-mechanical and flame-retardant properties, which also allows to obtain light weight, high strength epoxy composites, and to improve the thermal stability, glass transition temperature (T_g) and dimensional stability. However, among these nano-fillers used for preparing high performance epoxy

nanocomposites, carbon nanomaterials have been more attractive to be used as an epoxy modifier in concrete retrofitting applications, as shown in the following section, due to their unique physical, mechanical, and thermal properties [102-107]. Further details about effect of adding nanomaterials on mechanical and thermal properties of epoxy adhesives can be found in our comprehensive review article [95].

2.2.2.2 The effect of using nanomaterial-modified epoxy adhesives on the behaviour of FRP-strengthened/repaired concrete elements

It is evident that a good understanding of the behaviour of carbon fibre (CF)/epoxy with nanomaterials has been established. However, investigations on the influence of Nano-modified adhesives on the efficiency of repairing and strengthening processes of concrete elements are scarce. It is noteworthy that a small number of studies investigated the effect of Nano-modified epoxy resins on the behaviour of FRP/concrete jointed elements 97-101, 109-112].

For example, the effect of strengthening reinforced concrete (RC) beams with CF using neat and carbon Nanotubes (CNTs)-modified epoxy adhesives on their ultimate loads, initial stiffness (slope of the initial linear part of the load-deflection curve), and toughness (area under the curve), was investigated by Irshidat et al. [97]. The test results showed that using CNTs-modified epoxy slightly improved the beams ultimate load by 5%, but significantly enhanced their stiffness and toughness by 35% and 28%, respectively, compared to the neat epoxy specimens. These improvements were attributed to the ability of CNTs in effectively suppressing the formation and propagation of micro-cracks at the interphase between CF and epoxy matrix, enhancing the CF/epoxy resin and concrete/epoxy resin adhesion, leading to proper load transfer between the matrix and the concrete. The ability of CNTs to restrict the micro-cracks of the matrix which increases the energy absorption of the whole system before debonding or sheet rupturing, resulting in toughness improvement. Furthermore, it was reported that the beams retrofitted with CF sheet embedded in CNTs-modified epoxy failed by sudden debonding of CF sheet with concrete splitting as shown in Fig. 2.16. Whereas the presence of CNTs delayed the propagation and debonding of the CF sheets, which was ascribed to the improvement in concrete/epoxy adhesion.

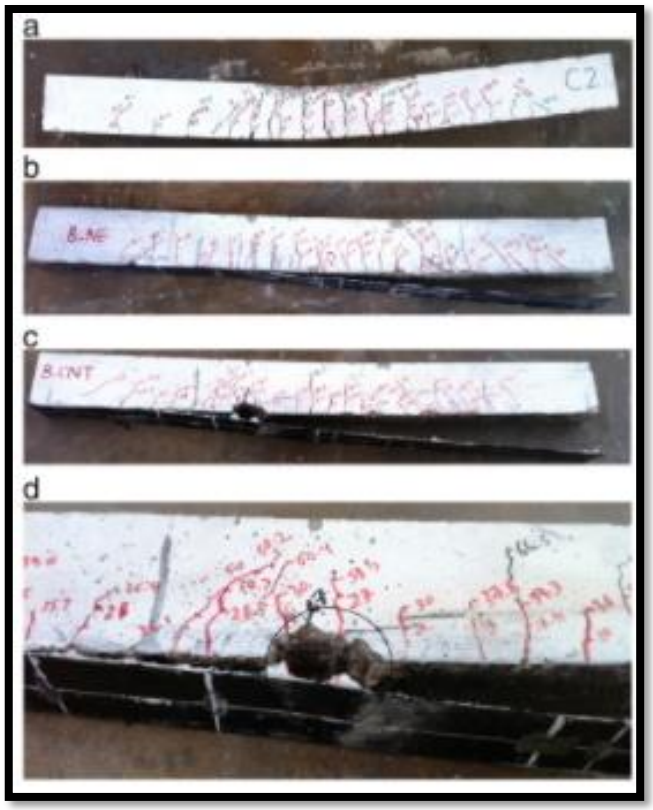

Fig. 2.16 Failure modes of (a) Control specimen, (b) Neat epoxy specimen, and (c) CNTs-modified epoxy specimen, (d) concrete splitting region of CNTs-modified epoxy specimen [97].

The flexural strength recovery of heat-damaged (at 500 °C and 600 °C) RC beams repaired with CFRP sheets incorporated in the composite systems by either using neat or CNT-modified epoxy resins was investigated by Irshidat et al. [98]. The results showed that CNTs-modified epoxy slightly enhanced the ultimate load and stiffness for specimen heated at 500 °C by 11% and 5%, respectively, compared to the neat epoxy specimen, while these properties were significantly improved by 24% and 22% for specimens heated at 600 °C compared to the neat epoxy specimens. Fig. 2.17 shows the failure modes of tested beams heated at 500 °C, while Fig. 2.18 shows the SEM images of epoxy adhesive debris attached to the CFRP sheet. It is obvious that using epoxy or sizing agent with CNTs increased the amount of matrix debris when. This result indicated that the improvement in the FRP/matrix adhesion could be achieved by either using CNTs-modified epoxy or sized fibre.

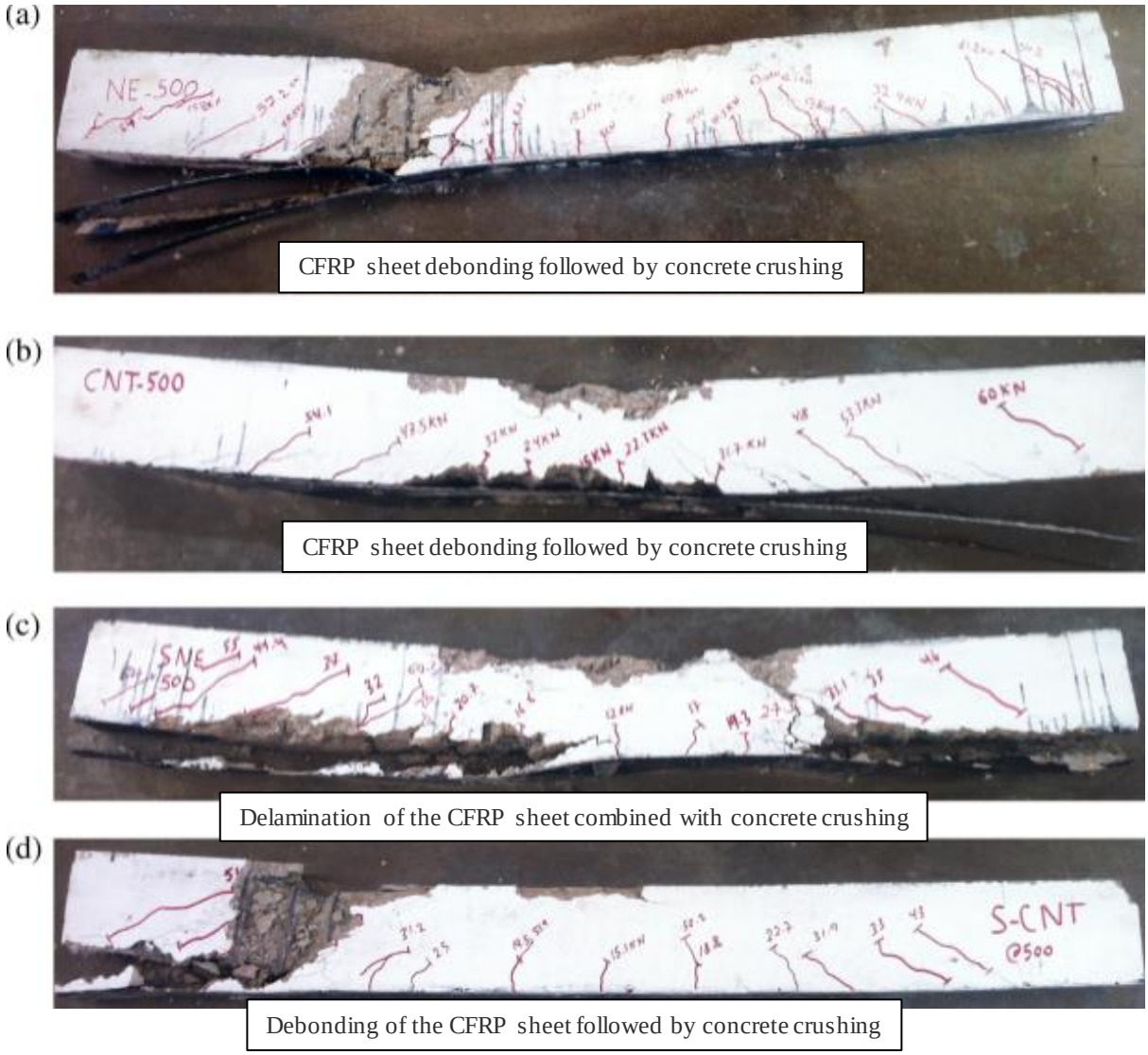

Fig. 2.17 Failure modes of 500 °C beams repaired using (a) neat epoxy; (b) CNT-modified epoxy; (c) neat epoxy with sizing agent; and (d) CNT-modified epoxy with sizing agent [98].

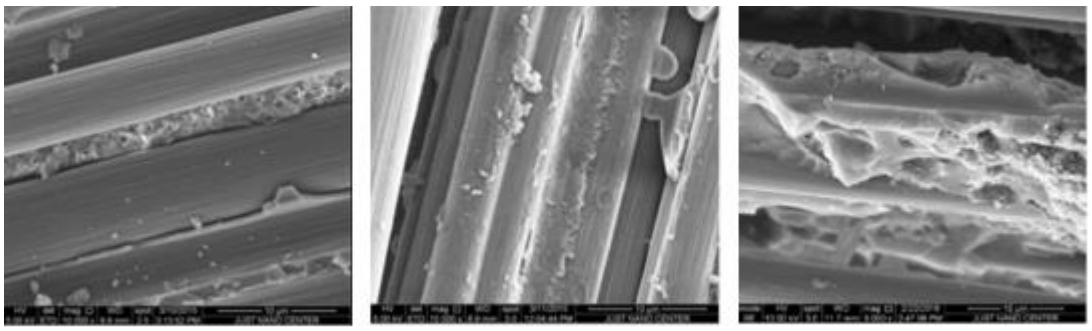

Fig. 2.18 SEM images epoxy matrix debris attached to CFRP sheet in the case of (a) neat epoxy specimen; (b) CNT-modified epoxy; and (c) CNT-modified epoxy with sizing agent specimen [98].

Irshidat et al. [99] investigated the effectiveness of using CNTs to improve the strengthening efficacy of CF/epoxy composites confined rectangular RC columns. The results indicated that using CNTs modified epoxy resin increased the axial load-carrying capacity and toughness of wrapped columns by 12% and 19%, respectively, as compared to the neat epoxy specimens. However, both CNT's specimens (CNTE) and neat epoxy specimens (NE) showed a ductile failure mode. Furthermore, SEM images showed that more cement debris was attached to the CF in the case of using CNTs-modified epoxy compared to the neat epoxy specimens, which led to improve the adhesion at the concrete/epoxy and fibre/epoxy interfaces resulting in improvement the load transfer and load-carrying capacity of wrapped columns. It was also found that using sized CF embedded in either neat epoxy (SNE) specimen or CNTs-modified (SCNTE) specimen enhanced the columns axial carrying capacity by 10% and 15%, respectively, compared to the neat epoxy specimens, and reduced the buckling of tested columns and changed their mode of failure from ductile failure to sheet rupture. Fig. 2.19 shows the failure modes of some tested specimens. Fig. 2.20a shows that some matrix debris attached to the fibre in the case of NE specimens while a significant amount of debris attached to the fibre in the case of CNTE specimens, as shown in Fig. 2.20b. This observation may explain the enhancement in the carrying capacity of the CNTE specimen compared to the NE specimen. In the case of using sized fibre (SNE and SCNTE specimens), more matrix debris were found to stick on the fibre surface as shown in Fig. 11c and d. This could be ascribed to the high concentration of CNTs on the CFRP sheet/epoxy interface which enhanced the interfacial shear capacity. The stronger interfacial bonding between the sized CF and epoxy matrix might result in enhancement the load-carrying capacity of SNE and SCNTE specimens compared to NE specimens.

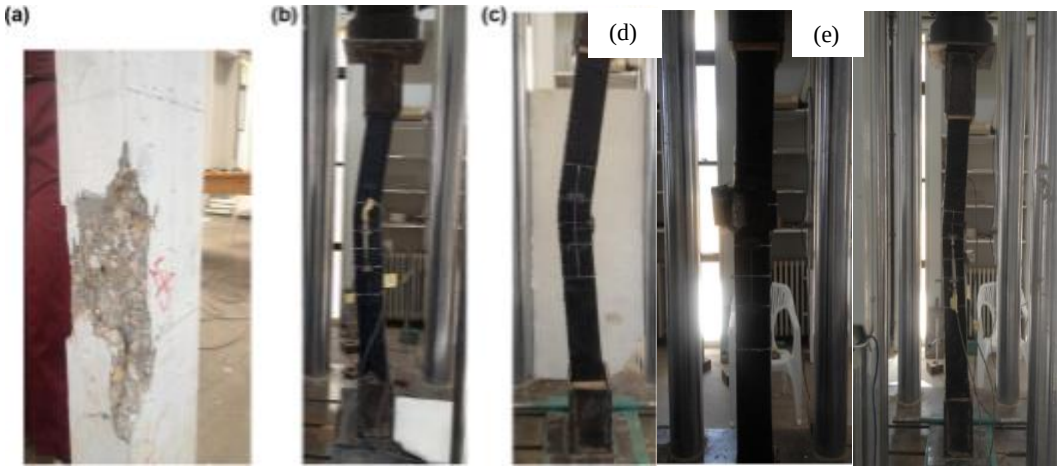

Fig. 2.19 Failure modes of (a) control specimen; (b) neat epoxy specimen (NE); and (c) CNT-modified epoxy specimen (CNTE); (d) neat epoxy with sizing agent specimen (SNE); and (e) CNT-modified epoxy with sizing agent specimen (SCNTE) [99].

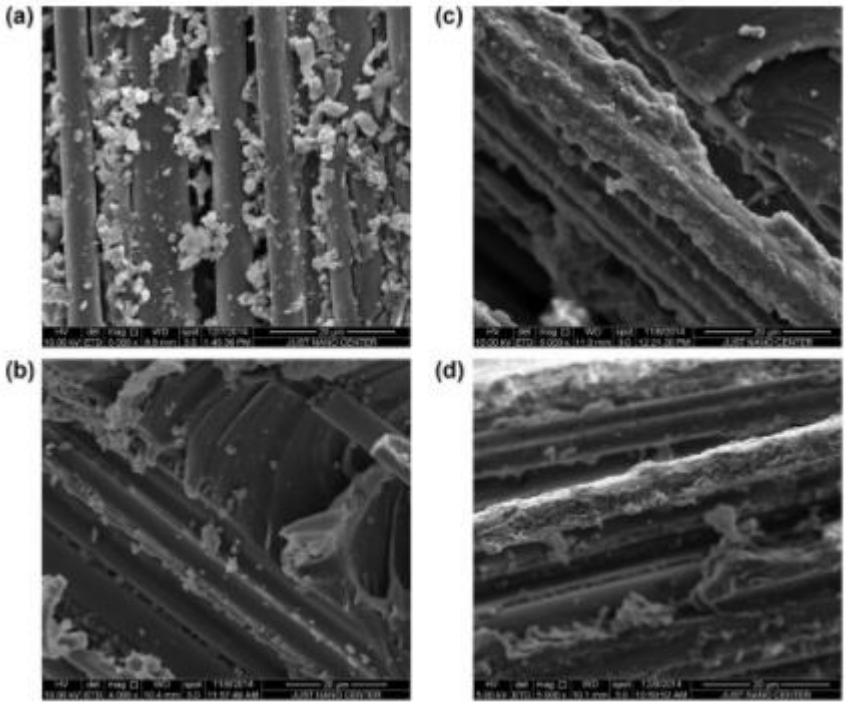

Fig. 2.20 SEM images show epoxy matrix debris attached to CFRP in the case of (a) NE specimen, (b) CNTE specimen, (c) SNE specimen, and (d) SCNTE specimen [99].

The influence of CNTs-modified epoxy on the bond-slip behaviour between concrete surfaces and carbon and glass FRP sheets was investigated by Irshidat and Al-Saleh [100]. A series of concrete prisms were cast, reinforced with FRP sheets, and tested under double-shear test. Experimental results showed that using CNTs-modified epoxy resin enhanced the bond strength and slip at failure of the tested specimens by 35% and 52% in the case of CF and by

26% and 83% in the case of glass fibre, respectively. The main failure mode for specimens based on neat epoxy was de-bonding at the interface between fibre sheet and concrete surface, as shown in Fig. 2.21 (a-c), while using the CNTs-modified epoxy led to cohesive failure, as shown in Fig. 2.21 (d-f).

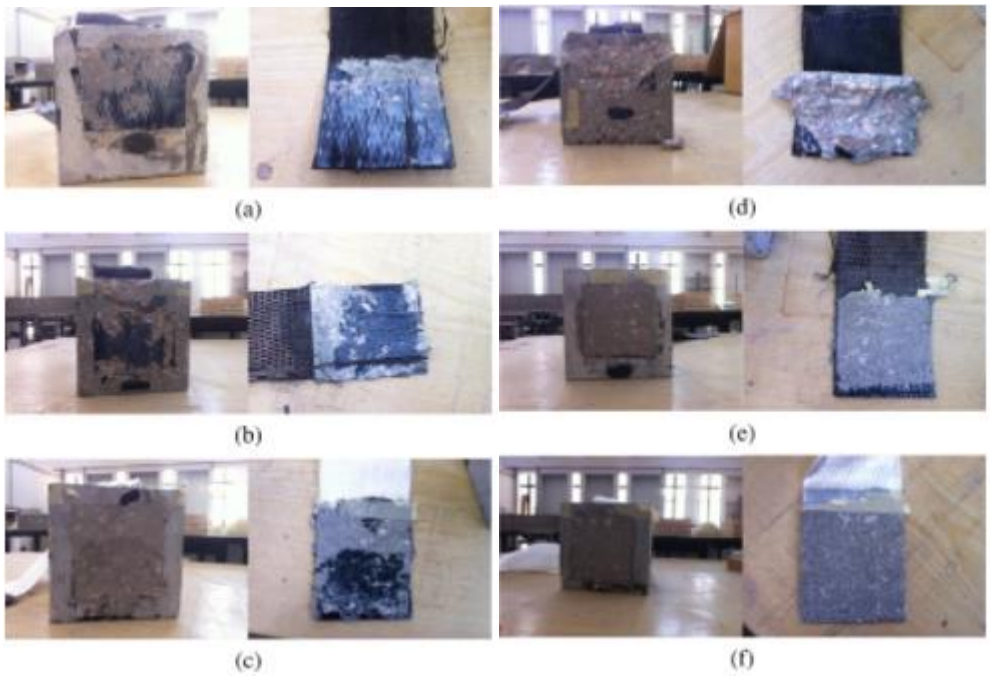

Fig. 2.21 Modes of failure of tested specimens [100].

The use of Multi-Walled CNTs (MWCNTs) in repair and strengthening epoxy resin systems for FRP-confined concrete cylinders was investigated by Rousakis et al. [109]. The results confirmed the potential of the MWCNTs-reinforced epoxy resins for use in advanced crack repair of high-performance concrete. Irshidat et al. [110] investigated the influence of using CFRP sheets embedded in CNTs-modified epoxy composites on the strengthening RC columns. The test results revealed that wrapping RC columns with CFRP sheets embedded in CNTs-modified epoxy resin increased their axial load resistance, maximum displacement, and toughness by 11%, 6%, and 19%, respectively, compared with the neat epoxy specimens. Irshidat and Al-Saleh [101] reported that incorporation of CNT-modified resin and/or CNT-enriched sizing agent in the CFRP composite enhanced the axial load capacity and the toughness of the repaired columns. Morshed et al. [111] evaluated the role of Core-shell Rubber (CSR)-modified epoxy adhesive and surface functionalisation by silane agents in improving the bond durability of adhesive joints between EB-CFRP and concrete under hydrothermal exposure. The results of bond tests indicated that CSR toughening and silane coupling agent led the CFRP/concrete/adhesive bond strength retention following accelerated conditioning to

15% improvement, as compared to that of neat epoxy samples. Further study [140] investigated the effect of epoxy adhesive modified with Nano silica, CSR nanoparticles, and MWCNTs on the bond strength of CFRP-concrete adhesively bonded joints. Results indicated that the nanoparticle-modified epoxy adhesives did not significantly affect FRP-concrete bond strength when compared to the neat epoxy. Increased viscosity of nano-modified adhesives may have led to non-uniform wetting of concrete surface, and the consequent introduction of air bubbles along the interface.

2.3 Nano-modification of polymer matrices

2.3.1 Introduction

Owing to its high thermal and mechanical stabilities and superior chemical resistance and electrical isolating properties, in combination to its light weight, epoxy is considered one of the most important thermosetting polymers with a wide range of applications in the fields of adhesives, coatings, paints, innovative materials for the electronics and aerospace industries, electrical/ electronic insulation and composite applications, to name a few [123, 135-140]. However, the highly cross-linked nature of epoxy resins results in inherently low fracture toughness and consequently poor resistance to fracture, which seriously restrict their applications. This leads to the need to improve the performance of epoxy resins [95].

Recently, introducing Nano fillers into epoxy resins has received strong attention, due to their extraordinary thermo-mechanical and flame-retardant properties, which lead to obtain high strength, thermally stable and light weigh epoxy composites [95]. Among several Nano fillers that can be used for preparing high performance epoxy nanocomposites, carbon nanomaterials, owing to their exceptional mechanical, thermal and physical properties, have become essential for the preparation of composites with multiple enhanced properties [95, 141]. Those nanomaterials include CNTs, Graphene Oxide (GO), Graphene Nano Platelets (GNP) and Nano Sheets (GNS), graphite, Carbon Nanofibres (CNFs) and Cellulose nanocrystals (CNCs).

Although CNTs are considered as one of the most effective Nano fillers in the field of polymer composites and they could significantly improve both mechanical and thermal properties of epoxy adhesives, the high aspect ratio and flexibilities of CNTs along with the van der Waals forces between them cause CNTs to be severely entangled in close packing upon synthesis. Moreover, the chemically inert nature of CNTs leads to poor dispersibility and weak interfacial interactions with epoxy matrices. These issues would hinder the full utilisation of these particles in enhancing properties of epoxy adhesives [95]. Compared to CNTs, graphite platelets are about 500 times less expensive, and easily unfolded, whereas the CNT-based

composites need an advanced processing technique in order to obtain uniform dispersion, waviness, and alignment of nanotubes [137]. CNFs, on the other hand, have a better chance in large-volume industrial applications than CNTs, due to their lower manufacturing cost (up to 500 times) and mass production scalability, and can be manufactured at high yields, which means that a lot of the reactant chemicals that were used successfully reacted to make the products, in addition to their good dispersion into epoxy resins. All those advantages have led to further in-depth investigation of their impact on epoxy nanocomposites [135, 141, 142].

2.3.2 Effect of the Nano-modification on the polymers' properties

It has been confirmed that incorporating carbon-based nanomaterials, such as CNTs [115, 143-149], CNFs [150-154], graphene and graphite [106, 127, 143, 155-162] and CNCs [116, 117, 126, 138-140, 163] into epoxy resins improved their mechanical and thermal properties and were also found to provide outstanding reinforcing potential and demonstrates efficient stress transfer behaviour. Those improvements are attributed to the fact that incorporating the nanoparticles into epoxy provides strong interfacial interactions with the epoxy system through a chemical reaction, furthermore the uniform dispersion of the nanoparticles into epoxy enhances the bond between unreacted epoxy functional groups and nanoparticles, which eventually leads to arresting and suppressing the crack propagation, resulting ultimately in improved properties/performance [95].

In addition, silicon-based nanomaterials, such as silica [107, 108, 112, 165, 166] and clay [115, 167, 200] nanoparticles, have also showed their efficiency in improving both mechanical and thermal performance of epoxy polymers. For instance, Chisholm et al. [165] found that adding silicon carbide (SiC) to epoxy matrix led to enhanced mechanical properties. This improvement was credited to the uniform dispersion of the nanoparticles over the entire body of the matrix. Furthermore, the overall porosity of the composites was found to be reduced. It was also found that the thermal stability was improved by the addition of the nanoparticles, which was attributed to the additional cross-linking in the polymer owing to the catalytic effects produced by the presence of SiC nanoparticles. The effect of dispersing Montmorillonite (MMT) Nano clays into epoxy resin was studied by Hsour et al. [115], as it was found that adding MMT yielded an improvement in mechanical properties. That was due to the uniform dispersion of nanoparticles, which ensured more viable sites for polymer and nanoparticles interaction, which also enhanced the thermal properties. Moreover, higher crosslinking between the nanoparticles and the epoxy molecules was observed, which eventually led to interlocking

resin-nanoparticles structure in the matrix and might facilitate stress transfer process when the nanocomposite is loaded.

Introducing nanoparticles to polymer matrices has also been found to highly influence the chemical structure of the matrices. Hence, identifying the chemical reactions taking place and the changes happening in the chemical composition of the matrix as a result of introducing the nanoparticles is of high importance. Some effective tools have been adopted for those purposes, such as FTIR and Raman spectroscopies, which are used to better understand the molecular structure of materials through identifying the functional groups that appear and those that disappear because of the addition of the nanomaterials to the polymer, which eventually helps to know the characteristic changes that happen to the polymer.

2.3.3 Characterisation of the nanomaterial-modified polymers

Among the many studies [113, 114, 116-118, 120, 121, 123, 135, 136, 139, 149, 163, 164, 167-181] that have performed FTIR analysis on both pure epoxy matrices and the modified ones, only very few of them [167, 170, 176, 181] have investigated the effect of adding nanoparticles on the chemical composition (i.e. changes in functional groups) of epoxy. For instance, a research study [167] concluded that the presence of the clay nanoparticles in the epoxy matrix did not show any new peaks, even though, the location of some of the characteristic IR peaks were shifted. Further investigation [170] found that when 0.5 wt.% ultra-sonicated ozonolytic (USO) treated CNTs (OZ-CNTs) were dispersed in DGEBA epoxy resin, the formation of an esters peak corresponding to 1754 cm^{-1} was observed, which indicated that OZ-CNTs have reacted with the epoxy matrix. In another study [176], the FTIR analysis of epoxy specimens modified with CNT, GNP, and fullerene-C60 was investigated. It was found that the characteristic peaks for all specimens were identical, indicating that there was no new chemical bonding between the polymer and Nano fillers. However, disappearance of the peak at a wavenumber of 913 cm^{-1} for all specimens indicated the ring-opening polymerisation during crosslinking, which reflected the curing process. Another investigation [181] observed no additional bands introduced when 2 wt.% MWNT-OH was mixed with DGEBA epoxy.

Raman spectroscopy has also been considered in many studies [109, 114, 119, 123, 124, 135, 136, 142, 159, 169, 170, 180, 182] to investigate the chemistry of epoxy polymers and its nanocomposites. It's noteworthy that one of the most important characteristics of Raman analysis of carbon-based materials is the ratio of intensity of D/G bands (I_D/I_G), as it is a measure of the defects present on carbon nanomaterials structure. The G band is a result of in-

plane vibrations of sp^2 bonded carbon atoms whereas the D band is due to out of plane vibrations attributed to the presence of structural defects. For example, it was observed in [123] that the Poly phosphamide (PPA)/epoxy and PPA-GNS/epoxy specimens exhibited the D band at 1358 cm^{-1} and the G band at 1593 cm^{-1}. The typical Raman spectra of GNS-based epoxy resin in [124] exhibited the spectral ranges of D band at 1250~1450 and of G band at 1500~1700 cm^{-1}, which were ascribed to the location of the D and G peaks of the pure carbon-related materials (i.e. graphene), indicating the dispersion of the GNS in the epoxy matrix. Further research study [136] indicated that almost no changes happened in the peak intensity ratios of disordered (D) band to G band of single-walled CNTs (SWCNTs) before ($I_D/I_G = 0.09$) and after adsorption of epoxy (i.e. EpPy-16) ($I_D/I_G = 0.11$).

The degree of crystallinity of the polymer nanocomposite, which is a measure of the extent to which the material is crystalline, is also essential to be known and understood in order to predict the properties of the polymers and determine their potential fields of application. XRD has widely been utilised for crystallinity determination [113, 114, 121, 139, 159, 163, 177, 179, 183, 200].

Several studies investigated the effect of adding nanoparticles on the crystallinity of polymers [122, 125-129, 184-188]. For example, it was found that the nanoparticles in a polymer matrix can act as nucleating agents, which increase the crystallinity of the composite, or act as an impurity that hinders the formation of the ordered structure [122]. Mahmood et al. [125] found that the addition of amine functionalised CNTs to Polyamide 6 (PA6) increased the crystallinity of the nanocomposites. Morimune et al. [184] studied GO-PVA (Poly Vinyl Alcohol) nanocomposites, and it was found that the addition of GO led to increase the crystallinity of the nanocomposites from 28% for the neat PVA to 30%, 33%, 35% and 39% for 0.1%, 0.5%, 1%, and 5% GO loading, respectively. However, Bhattacharyya et al. [127] studied the graphene-reinforced ultrahigh molecular weight polyethylene (UHMWPE), and a reduction in crystallinity of the nanocomposites was observed. A study on PVA-cellulose nanocomposites was carried out by Kumar et al. [126], where a reduction in the crystallinity of the nanocomposite was observed. This was ascribed to the strong interaction of the CNCs with the -OH groups of PVA and twisting together into a confused mass between them, which eventually caused steric effect and destroyed the highly-ordered arrangement of PVA.

Similar observations were reported by van Zyl et al. [128], where adding silica nanoparticles to PA6 was found to reduce its crystallinity and the crystallinity continued to decrease further

with increase the silica concentration. Further study [129] found that the crystallinity of the Ethylene Vinyl Acetate (EVA)-silica nanocomposites dropped when compared to that of pure EVA. Similar results were reported by Chen et al. [185] in silica-PVA nanocomposites. On the other hand, another investigation on PVA-silica nanocomposites was carried out by Peng et al. [186]. It was found that there was an increase in the crystallinity of the PVA at a relatively low silica loading (i.e. 0.5 wt.%), which was ascribed to the fact that the silica nanoparticles might be acting as a heterogeneous nucleating agent during crystallisation.

Besides the techniques mentioned previously, SEM analysis is also employed to examine the microstructure of the epoxy nanocomposites and to investigate the dispersibility of the nanoparticles through the matrix [109, 113, 114, 123, 124, 135, 136, 140, 142, 159, 167, 170-173, 176, 181, 182, 194-202]. The porosity analysis of polymers has been scarcely addressed [208], where that research work mainly aimed at quantitatively evaluating the mechanical strength of polymer specimens (Sikadur®-30 and Sikadur®-30 LP (Long Pot)) subjected to different curing procedures and aging durations, in addition to assessing the porosity of tested specimens. The authors recommended to investigate the effects of an increased porosity of the structural adhesives used in the retrofitting works on the durability of retrofitted structures.

2.3.4 Using the nanomaterial-modified polymers in the adhesive-bonded joints

The effect of incorporating nanoparticles to epoxy adhesives on the LSS of metal-adhesive joints was investigated in the literature [143, 170, 189-193]. For instance, it was found by Jojibabu et al. [143] that the LSS of the aluminium joints increased by 53%, 49% and 46% with adding 1 wt.% CNT, 0.5 wt.% GNP and 0.5 wt.% single-walled Carbon Nano Horns (CNH), respectively. It was also confirmed by Panta et al. [170] that the LSS of adhesive-aluminium joints was improved by 26% (23.6 MPa) with using CNTs-modified epoxy compared to that of pure epoxy, while results of another study [189] showed that adding an Epoxy-functionalised CNTs (EpCNT) at 1 wt.% increased the LSS of the joints by 36% over the unfilled epoxy. However, Moriche et al. [190] found that incorporating of GNPs into the epoxy had no effect on the LSS results of adhesive-copper and adhesive-aluminium joints, which was due to a weak interface reinforcement-matrix. In contrast, Jongvivatsakul et al. [193] found that adding 0.5 wt.% of SWCNTs to low density epoxy increased the bond strength (9%), ultimate slip (21%), and interfacial fracture energy (70%) between CFRP plates and concrete. In addition, the previous values were increased by up to 6%, 0.3%, and 13%, respectively by adding 1.0 wt.% MWCNTs.

2.4 Concluding remarks

An inclusive state-of-the-art review in regard with the context of the present work in this thesis has been presented in this chapter. First, the developments of both the materials and techniques used for concrete retrofitting since the forties of the last century has been covered. The advances in the bonding agents used for retrofitting purposes have also been included, in addition to their essential roles in the success of the retrofitting processes. Finally, the effect of incorporating various nanomaterials into polymer matrices on their chemical, physical and microstructural properties along with its influence on the bond characteristics of the adhesive-bonded joints has been encompassed.

From the literature review provided in this chapter, the following observations could be drawn:

- Retrofitting/strengthening of existing concrete structures is of high significance in order to guarantee the structural integrity, strength and stiffness in addition to ensure the compatibility of all structural concrete elements together. All of the previous factors are important to guarantee the safety, durability and serviceability of the structures.

- Several materials, such as concrete and steel, were effectively applied through different mechanisms, e.g. jacketing, for strengthening deteriorated structures. However, FRP composites have showed much better performance than that of the conventional materials.

- The FRP composites alongside NE adhesives were firstly used by means of EBR system, but some drawbacks in the system (i.e. premature FRP debonding) have led to consider the NSM technique instead.

- Despite the NSM-FRP technique has provided an unprecedented performance in retrofitting concrete structures, the debonding issues, that that are associated with using pure/neat adhesives, have not been completely solved.

- Since the bond behaviour is the key for the success of any retrofitting/strengthening process, modified adhesives obtained from mixing nanomaterials with epoxy adhesives were used to enhance the bond behaviour of the EBR-FRP-retrofitted concrete elements.

- The addition of nanomaterials to epoxy adhesives has efficiently overcome the drawbacks associated with using these adhesives in retrofitting concrete members with FRP materials by improving their mechanical and thermal properties, interfacial bond and ultimate

slippage between FRP reinforcement and concrete, and interfacial adhesion between epoxy matrix and FRP composites.

- The Nano-modified epoxy adhesives are still limited to use in the EBR-FRP strengthening applications focusing only on the CNTs as adhesive Nano-fillers.

- In regard with the chemical and physical characterisation of the epoxy nanocomposites, even though spectroscopic observations of the Nano-modified epoxy in terms of FTIR and Raman analyses were conducted in some of the literature, the chemical interaction and the physical state of epoxy matrix with the nanoparticles is not fully presented.

- Most of the investigations that have studied the crystallinity of the polymer nanocomposites addressed the thermoplastic polymers, while only few of them were interested in the thermosetting polymers (i.e. epoxy matrix), which mainly examined the effect of the carbon-based of the nanoparticles that have an influence on the composites' crystallinity, with very few studies that addressed the silicon-based nanocomposites.

- The porosity characteristics of the epoxy nanocomposites have been rarely studied, and its effect on the mechanical behaviour in the retrofitted members has not been investigated yet, similarly regarding the chemical, physical and microstructural properties of the nanocomposites.

- Concerning the effect of the Nano-modification of epoxy adhesives on the LSS of the adhesive joints, the research work has only been dedicated to the metal-adhesive joints, while no work, to the best of my knowledge, has studied the CP-adhesive joints, which will be considered in concrete-related works (i.e. concrete retrofitting) later on. Furthermore, the previous studies were limited to utilise the carbon-based Nano-fillers, where the silicon-based ones have not been addressed.

Chapter 3: Materials and methodology

3.1 Introduction

This chapter is dedicated to a comprehensive presentation of the materials integral to this research endeavour, accompanied by a thorough examination of their properties and the underlying rationale governing their selection. Additionally, it elucidates the methodologies deployed for materials characterisation and testing alongside the reasons behind adopting them. It's noteworthy to highlight that the research methods employed in this study were systematically categorised into three distinct domains; (I) those used for the chemical and physical characterisation in addition to microstructural analysis of the NE and the NMEAs, (II) those employed for the mechanical testing (i.e. LSS) of the CP-adhesive-bonded joints and finally (III) those considered for the three-point bending test of the NSM-FRP-retrofitted concrete specimens.

3.2 Materials

All materials that were used in this research are included in this section.

3.2.1 Epoxy adhesive

Sikadur®-30, a thixotropic, structural 2-component adhesive, based on a combination of epoxy resins and special hardener (A & B) was used. The composition and properties of the adhesive are shown in Tables 3.1 and 3.2, respectively. The two epoxy components are shown in Fig. 3.1. The epoxy adhesive was provided by Sika Limited, UK, and it cost about £75.

Sikadur®-30 is an adhesive for bonding structural reinforcement, particularly in the NSM/EBR structural strengthening/retrofitting works, and it offers numerous advantages, for instance, it is easy to mix and apply, eliminating the need for a primer. It also boasts high creep resistance even under permeant loads, and humidity doesn't compromise its hardening. With exceptional adhesive strength, it hardens without shrinkage, aided by distinguishable color-coded components. It demonstrates remarkable initial and ultimate mechanical resistance, along with impressive abrasion and shock resistance. Moreover, it forms an impermeable barrier against liquids and water vapour, providing comprehensive protection.

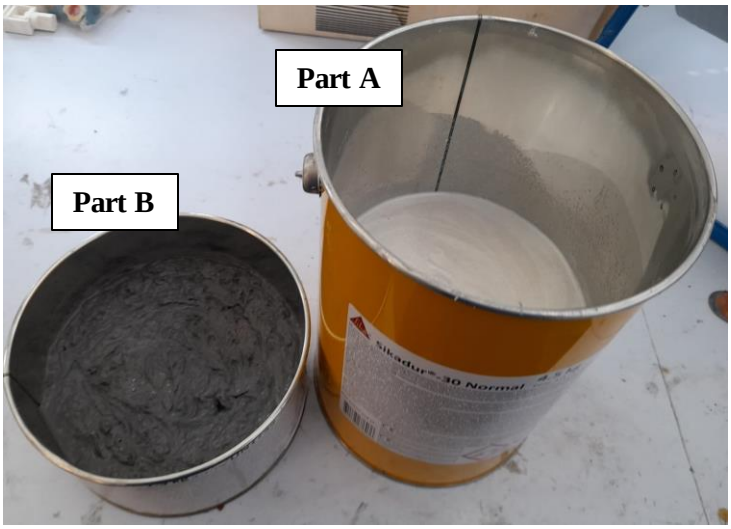

Fig. 3.1 The two-component epoxy adhesive used in this study.

Table 3.1 Composition/ingredients of epoxy adhesive (As per supplier).

Part A		**Part B**	
Chemical name	Concentration (%)	Chemical name	Concentration (%)
Reaction product: bisphenol-A-(epichlorohydrin) (C15-H16-O2.C3-H5-Cl-O) x-) and epoxy resin (number average molecular weight ≤ 700)	≥ 10 - < 20	Quartz (SiO_2)	≥ 50 - ≤ 100
1,4-bis(2,3-epoxypropoxy) butane (C_{10}-H_{18}-O_4)	≥ 3 - < 5	2,2,4 (or 2,4,4)-trimethylhexane-1,6-diamine ($C_9H_{22}N_2$)	≥ 10 - < 20
Hydrocarbons, C10-C13, aromatics, <1% naphthalene	≥ 1 - < 2.5	Quartz, (SiO_2) <5µm	≥ 0 - < 1

Table 3.2 Mechanical and thermal properties of epoxy adhesive (As per supplier).

	Property		**Code(s)**
Mechanical properties (curing time)	Tensile strength (7 days)	~ 26 MPa	DIN EN ISO 527-3
	Tensile adhesion strength (with dry concrete substrate) (7 days)	> 4 MPa	(EN ISO 4624, EN 1542, EN 12188)
	Tensile modulus of elasticity	~11.2 GPa	ISO 527
	Compressive strength (7 days)	~ 75 MPa	EN 196
	Modulus of elasticity in compression	~ 9.6 MPa	ASTM D 695
	Shear strength (7 days)	~18 MPa	FIP 5.15
Thermal properties (curing time)	Coefficient of thermal expansion (Temperature range: −20 °C to +40 °C)	2.5 x 10^{-5} / °C	EN 1770
	Glass Transition Temperature (T_g) (30 days)	+52 °C	EN 12614

3.2.2 Nanoparticles

Five different nanoparticles (Fig. 3.2), which are: CNF, silica Nano powder, CNCs, MMT Nano clay and graphite Nano powder, were used for the purpose of this study. Their composition and properties are listed in Table 3.3. The nanomaterials were provided by Nanografi, Turkey.

It's worthy to note that the nanomaterials used belong to two different families, e.g. carbon-based nanomaterials; e.g. CNF, CNCs and graphite Nano powder, and the silicon-based nanomaterials including the silica Nano powder and the MMT Nano clay.

1) Carbon-based nanomaterials

Carbon-based materials, including CNF, CNCs and graphite are utilised to reinforce epoxy polymers due to their unique compositions and properties that contribute to enhanced mechanical and thermal characteristics. These materials offer different reinforcement mechanisms based on their distinctive features.

CNF:

CNFs are cylindrical structures with a high aspect ratio, composed of carbon atoms arranged in a graphitic structure. Their exceptional mechanical properties, including high strength and stiffness, make them effective reinforcements for epoxy polymers. When incorporated into epoxy, CNFs create a network-like structure that reinforces the epoxy matrix. The strong interfacial interactions between CNFs and epoxy enhance load transfer and resist crack propagation, leading to improved mechanical performance. Its cost was about €4 per gram.

CNCs:

CNCs are derived from cellulose, a natural polymer found in plant cell walls. CNCs have a rod-like shape with high aspect ratios. Their incorporation into epoxy enhances mechanical properties due to their reinforcing effect. CNCs can form strong interactions with epoxy through hydrogen bonding and electrostatic forces, improving load transfer and preventing crack propagation. Its cost was about €4 per gram.

Graphite Nano powder:

Graphite is a naturally occurring form of carbon arranged in layers of hexagonal structures. When exfoliated into thin layers, it becomes graphene, which is an exceptional two-dimensional nanomaterial. In epoxy composites, graphite or graphene serves as a filler,

enhancing mechanical properties by increasing stiffness and strength. The large surface area of graphene allows for better stress distribution, improving load-bearing capabilities. Its cost was about €5 per gram.

Differences in reinforcement mechanisms:

CNFs reinforce epoxy by creating a strong three-dimensional network, distributing stress throughout the composite. Their high aspect ratio and mechanical strength contribute to load-bearing capacity and crack resistance.

CNCs reinforce epoxy through their rod-like shape and intermolecular interactions. Their hydrogen bonding with epoxy enhances stress transfer and prevents crack propagation.

Graphite and graphene act as Nano-fillers that increase stiffness and strength. Graphene's 2D structure provides excellent mechanical reinforcement and enhances interfacial bonding.

In summary, carbon-based materials like CNFs, graphite and CNCs are chosen to reinforce epoxy polymers due to their distinctive mechanical properties. CNFs offer a three-dimensional network, while graphite and graphene provide stiffness and strength, and CNCs enhance mechanical properties through their rod-like shape and interactions.

2) Silicon-based nanomaterials

Silicon-based nanomaterials, e.g. silica nanoparticles (Nano powder) and MMT Nano clay, are employed to enhance epoxy polymers' mechanical and thermal properties owing to their unique characteristics.

Silica nanoparticles (Nano powder):

Silica nanoparticles are ultrafine particles composed of silicon and oxygen atoms. When integrated into epoxy, they create a reinforcing effect by forming a strong network within the epoxy matrix. Silica nanoparticles significantly increase the epoxy's mechanical strength and stiffness due to their small size, high surface area and excellent dispersion. This enhanced network structure improves load transfer and crack resistance, leading to improved overall mechanical performance. Its cost was about €4 per gram.

MMT Nano clay:

MMT Nano clay consists of layered silicate minerals. These Nano clays have a layered structure with nanometre-scale thickness. When dispersed in epoxy, MMT Nano clays provide

reinforcement through a combination of factors. The intercalation of Nano clays between epoxy layers enhances mechanical properties, such as stiffness and strength. Additionally, the strong interfacial interactions between the Nano clays and epoxy hinder crack propagation, further enhancing the composite's durability. Its cost was about €1.50 per gram.

Differences in reinforcement mechanisms:

Silica nanoparticles reinforce epoxy by forming a dense network within the matrix. Their small size and high surface area allow for efficient stress distribution, improving overall strength and stiffness. Silica nanoparticles enhance load transfer and resist crack propagation.

MMT Nano clays reinforce epoxy through intercalation within the epoxy layers. This arrangement increases stiffness and strength while also providing strong interfacial interactions that prevent crack propagation and improve the composite's mechanical properties.

In conclusion, silicon-based nanomaterials enhance epoxy polymers by contributing distinct mechanical properties. Silica nanoparticles form a network, whereas MMT Nano clays intercalate between layers, both resulting in improved mechanical performance. The choice of nanomaterial depends on the desired reinforcement effects and specific application demands.

Moreover, as reported earlier (in section 2.3.2), the incorporation of carbon-based nanomaterials (CNF, CNCs and graphite) into epoxy resins was confirmed for its ability to enhance the epoxy's mechanical properties. These nanomaterials also exhibit strong reinforcing potential and effective stress transfer behaviour. These positive changes are a result of the robust interfacial interactions between the nanoparticles and the epoxy, established through chemical bonding. Additionally, the nanoparticles' uniform distribution within the epoxy reinforces the linkage between unreacted epoxy groups and the nanoparticles. This, in turn, hinders and suppresses the propagation of cracks, ultimately leading to a significant improvement in overall properties and performance. Silicon-based nanomaterials like silica and clay nanoparticles have also proven their effectiveness in elevating the mechanical and thermal attributes of epoxy polymers.

The selection of appropriate reinforcing nanomaterials hinges on the specific properties sought and the particular needs of the application at hand. In alignment with this principle, the aforementioned materials have been deliberately chosen for the primary objective of the current research. This objective pertains to the augmentation of mechanical attributes, coupled with the enhancement of bond characteristics, within retrofitted concrete specimens. Through this

strategic selection, the overarching goal is to propel the advancement of concrete retrofitting systems towards a paradigm that is not only more effective but also ecologically sustainable in the long run.

Table 3.3 Description, composition and physical properties of nanomaterials (As per supplier).

Nanoparticle (Purity)	**Particle size**	**Elemental analysis (%)**		**Density (g/cm^3)**	**Specific Surface Area (SSA) (m^2/g)**
		Element	**Value (wt.%)**		
CNF (> 96%)	Outside Diameter: 190-590 nm, Length: 5.0-55.0 µm	C	> 96 %	2.2	20
		Co	≤ 6000 ppm		
		Mg	≤ 5000 ppm		
		Al	≤ 5000 ppm		
		Mo	≤ 2000 ppm		
		Ca	≤ 1000 ppm		
		Na	≤ 500 ppm		
		Fe	≤ 100 ppm		
		Ni	≤ 100 ppm		
		Zn	≤ 100 ppm		
		Mn	≤ 50 ppm		
		Cr	≤ 50 ppm		
		Cu	≤ 50 ppm		
Silicon Dioxide (SiO_2) Nano powder/Nanoparticles, coated with 2 wt.% Silane (97.3%+)	16 nm (average)	SiO_2	97.3	2.2	150-550
		Silane	2.0		
		Ca	0.022		
		S	0.0126		
		Mg	0.0056		

		Fe	0.005		
Cellulose nanocrystals (Nanocrystalline Cellulose, CNCs) (92 %)	Width: 10-20 nm, Length: 300-900 nm	N/A		1.49	~ 14
MMT Nano clay (99.9 %)	800 nm	LOI	45.6	2.35 (Avg.)	Up to 450
		SiO_2	44.3		
		Al_2O_3	6.67		
		MgO	1.41		
		Na_2O	0.70		
		CaO	0.47		
		Fe_2O_3	0.41		
		K_2O	0.30		
		TiO_2	0.04		
Graphite (C) Nano powder/Nanoparticles (99.9 %)	< 50 nm	C	99.90	2.26	>100
		O	< 0.06		
		Ni	0.009		
		C (Free)	0.004		
		Ag	0.003		
		W	0.002		
		Fe	0.002		
		N	0.001		
		Cu	0.001		
		Zn	0.001		

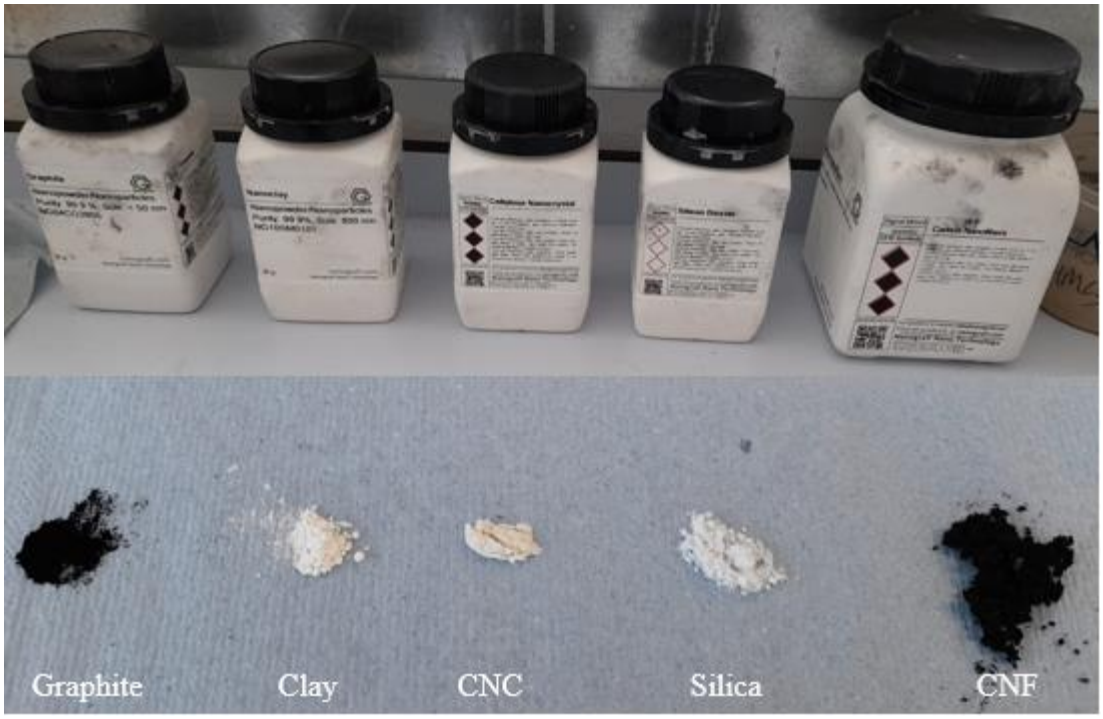

Fig. 3.2 Nanoparticles used in this study.

3.2.3 FRP bars

CFRP, GFRP and BFRP round bars with 6mm diameter were used for the purpose of this study. The FRP bars are shown in Fig. 3.3 and their mechanical properties are provided in Table 3.4. The carbon bars were provided by Sika Limited, UK, while Engineered Composites Ltd, UK provided the glass and the basalt bars.

Strategically harnessing the strength of CFRP, the corrosion resistance of the GFRP and the durability of BFRP for the NSM retrofitting of concrete members form a dynamic and adaptable approach. The versatility of CFRP, the resilience of GFRP and the eco-friendly nature of BFRP make them compelling choices for enhancing structural integrity. Capitalising on the NSM technique's strong bond with these distinct FRP materials presents a robust solution for reinforcing concrete elements. By integrating CFRP's exceptional strength-to-weight ratio, GFRP's corrosion resistance and BFRP's inherent durability, this retrofitting strategy promises to effectively enhance load-bearing capacity, deter crack propagation, and extend the lifecycle of the structure. This integrated approach marries the unique attributes of CFRP, GFRP and BFRP with the efficacy of NSM retrofitting, resulting in a comprehensive and sustainable solution for enhancing the performance and longevity of concrete members.

Table 3.4 Mechanical properties of the FRP bars (As per supplier).

Property / **Fibre** (description)	**Tensile strength (MPa)**	**E-modulus (GPa)**	**Elongation at break (%)**	**Code**
Carbon (Sika® CarboDur® BC 6)	3100	148	1.6	EN 2561
Glass (GRP bar)	1280	> 40	N/A	ASTM D7205
Basalt (Basalt bar)	1000	≥ 45	N/A	N/A

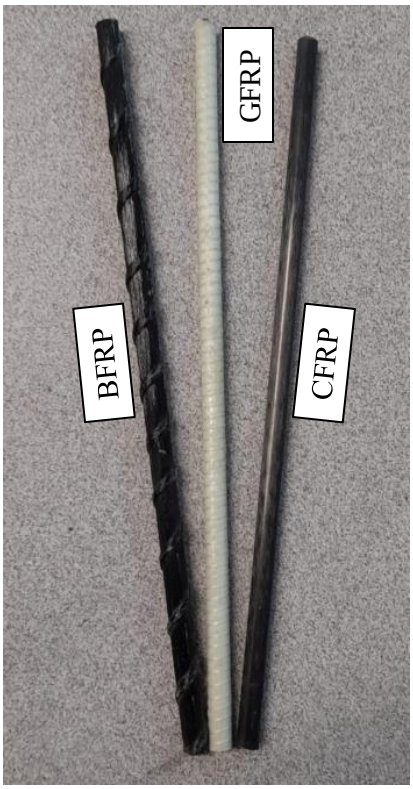

Fig. 3.3 FRP bars used in this study.

3.2.4 Concrete

Concrete used in the current study was prepared by considering the ingredients and the mix design provided in Table 3.5. Three standard concrete cylinders (i.e. 100 mm diameter x 200 mm height), as shown in Fig. 3.4, were cast and then cured in water for 28 days to gain strength. The cylinders were then tested according to the ASTM C39 [203] to determine the average concrete compressive strength, which was found to be 29.6 MPa. It's noteworthy that the concrete cylinders were sulphur capped before testing them in order to ensure a more uniform distribution of the applied load and to minimise the potential for localised stress concentrations that could lead to premature failure during testing. The sulphur capping process involves placing thin layers of sulphur on the ends of the concrete cylinder specimens, creating smooth and flat surfaces.

Selecting a concrete class with a 28-day compressive strength of 29.6 MPa for NSM-FRP retrofitting of concrete members is a compelling choice. Falling within the spectrum of Normal Strength Concrete (NSC), this level of strength aligns effectively with the retrofitting requirements. The familiarity of NSC, with its compressive strength ranging from 20 to 40 MPa, attests to its widespread usage in various structural applications, rendering it particularly suitable for retrofitting endeavours. By leveraging this well-established strength range, coupled with the NSM technique, the proposed retrofitting approach holds promise for enhancing structural integrity. This aligns with the NSC's reputation for offering a balanced combination of cost-effectiveness, strength and workability. Through the synergy of NSC's attributes and the NSM-FRP strategy, a robust and practical solution is envisaged, bolstered by the potential to achieve substantial strengthening outcomes. This strategy merits consideration as an integral component of an effective and sustainable retrofitting solution for concrete members.

Table 3.5 Concrete ingredients and mix design.

Ingredient	**Description**	**Bulk density (Kg/m³)**	**Quantity (Kg/m³)** (w/c = 0.50)
Cement	Type I Ordinary Portland cement (OPC)	1360	340
Coarse sand	Crushed stones with angular edges (1mm < size < 5mm)	1560	780
Fine sand	Sharp silica sand with uniform grain size (250µm < size < 1mm)	1590	397.5
Water	Tap water	1000	170

Fig. 3.4 Concrete cylinders tested for compression.

3.3 Methodology

The methodology adopted for the purpose of this research study was in the form of an extensive experimental programme, which includes multistage lab work including, first, the Nano-modification of epoxy adhesives, which was done through preparing both NE and NMEAs samples and characterise them by means of FTIR and Raman spectroscopies in addition to XRD and SEM analyses. The second stage included the LSS test of the CP-adhesive joints. The NSM-FRP retrofitting of concrete specimens with FRP bars alongside NE and NMEAs, and then testing them under three-point bending was the last stage of the experimental work.

3.3.1 Preparation and characterisation of NE and NMEAs samples

3.3.1.1 The rationale behind selecting the nanomaterials dosages into epoxy adhesive

First of all, it's worthy to note that the meticulous selection of nanoparticle concentrations in the epoxy adhesive was guided by a scientific framework aimed at capturing the diverse range of potential effects that nanoparticles can impart on adhesive performance. The chosen concentrations of 0.5%, 1.0% and 1.5% by weight of epoxy, that were considered for the preparation of the NMEAs, were influenced by established research in nanocomposite material science and adhesive mechanics.

At the lower end, the concentration of 0.5 wt.% was purposefully introduced to examine the initial stages of nanoparticle interaction with the epoxy matrix. At this level, the nanoparticles' presence might lay the foundation for interfacial improvements, such as enhanced adhesion and modulus, while avoiding any potential detrimental effects arising from excessive agglomeration or interference with the epoxy's curing process. This concentration choice aligns with previous studies that have highlighted the potential for nanoparticles to act as adhesion promoters at low loadings.

The mid-range concentration of 1.0 wt.% was strategically positioned as a pivotal point for investigation. In this regime, it was anticipated that a balanced interplay between the nanoparticles' reinforcing effects and their potential to alter adhesive properties would manifest. This concentration finds support in literature where researchers have reported optimal performance improvements in polymers at similar levels of nanoparticle incorporation. By focusing on this concentration, the study aimed to discern the maximum benefit that could be derived from nanoparticle reinforcement without reaching a point of diminishing returns.

The higher concentration of 1.5 wt.% ventured into a territory where the potential drawbacks associated with nanoparticle agglomeration and hindered polymerisation become more likely.

While previous research has indicated that increasing nanoparticle loadings beyond a certain threshold can lead to reduced mechanical properties due to aggregation, this concentration choice was meant to serve as an exploration of the concentration-effect relationship. By deliberately approaching this upper limit, the study sought to unveil any potential trade-offs between enhanced strength and compromised matrix integrity.

Incorporating these concentrations into the epoxy adhesive aligns with the principles of materials science and optimisation, leveraging established trends in nanoparticle dispersion and interfacial effects. By systematically varying the concentrations within this scientifically motivated range, the study aimed to capture a holistic picture of how different levels of nanoparticle inclusion would influence the mechanical properties, adhesion and overall performance of the epoxy adhesive in the context of the specific testing scenarios.

3.3.1.2 Preparation of NE and NMEAs samples

NE samples were prepared by mixing the two components, part A (resin) and part B (hardener) (A: B = 3:1 by weight as recommended by the manufacturer) manually for 4 minutes.

For the preparation of NAMEs, a few drops of acetone were first added to the nanoparticles (1:10 concentration), to enhance their dispersibility and reduce agglomeration, and manually mixed for 3 minutes. Afterwards, the pre-weighted nanoparticles were dispersed in part A, which is less reactive to ultrasound irradiation than part B [209], and were then manually mixed together in a suitable beaker for 2 minutes. The mix was then carried out through a high intensity ultrasonic irradiation for 5 min using Fisher Scientific FB 15051 with ultrasonic frequency of 37 kHz (Fig. 3.5). Once the irradiation completed, part B was then added to the modified part A and manually mixed for 2 min. After that, the whole mix of each sample was cast in a 1cm-cubic rubber silicon mould and left to harden, as shown in Fig. 3.6. those samples were then tested FTIR, Raman, XRD and SEM analyses. A schematic that shows the synthesis of the NMEAs is illustrated in Fig. 3.7. The samples were then left for 7 days at room temperature to cure. It is noteworthy that the NMEAs were prepared by incorporating different concentrations of the nanoparticles into the NE, which are, as mentioned earlier, 0.5%, 1.0% and 1.5% by the total weight of epoxy (A+B).

Reasons for considering some synthesis procedures

First, the adoption of a straightforward, simple and cost-effective mixing method in the preparation of the nanocomposites was a deliberate choice made with the aim of optimising

efficiency without compromising quality. While more complex and resource-intensive techniques exist, this approach has demonstrated its effectiveness in achieving homogeneity and ensuring relatively uniform distribution of nanoparticles within the epoxy matrix (as shown in the results). Furthermore, its simplicity allows for easy scalability and reproducibility, making it a practical choice for research and industrial applications. By demonstrating that effective results can be obtained through a simplified approach, this study not only contributes to cost savings but also underscores the versatility and accessibility of the method for a wide range of applications, offering a viable alternative to more intricate processes.

Second, in the current study, I deviated from the manufacturer's recommended mixing procedure for NE samples due to the specific constraints of working with very small amounts of epoxy. While the manufacturer suggests using a mixing spindle attached to a slow-speed electric drill for a minimum of 3 minutes, followed by additional stirring to minimise air entrapment, this approach was not feasible given the limited quantities of epoxy involved. Instead, I manually mixed the resin and hardener components for 4 minutes, striving for thorough homogenisation despite the smaller scale. This modification was a practical adaptation necessary to ensure consistent results within the constraints of my research, and it reflects the need for flexibility when working with varying quantities of materials in laboratory settings.

Furthermore, the epoxy adhesive was cured for 7 days before use for characterisation (also for retrofitting purposes) purposes to ensure maximum strength and durability. This extended curing period allows the epoxy to reach its full chemical and mechanical properties (as per supplier), providing reliable and consistent performance in various applications. It ensures that the adhesive is fully bonded and hardened, enhancing its load-bearing capacity, chemical resistance and long-term stability, making it a dependable choice for demanding projects.

Moreover, for the preparation of the NMEAs, acetone is frequently employed to improve the distribution and mitigate the clustering of nanoparticles owing to its several advantages, for instance, its polar aprotic nature facilitates effective interaction with nanoparticles of varying surface characteristics, promoting their dispersion. Its low surface tension also aids in breaking nanoparticle agglomeration forces, ensuring even dispersion. Furthermore, its rapid evaporation leaves a dry, evenly distributed nanoparticle coating, minimising agglomeration risks. Acetone also exhibits broad material compatibility, encompassing many carbon-based and silicon-based nanoparticles.

It’s also noteworthy that the decision not to cure the nanoparticles and epoxy mix in a vacuum chamber, despite the common practice of doing so to eliminate air bubbles, was a deliberate choice driven by the specific research goals. By intentionally avoiding the vacuum curing process, I aimed to assess the inherent porosity of both the unmodified epoxy and the modified nanocomposites under realistic conditions. This approach provides valuable insights into the actual porosity levels that may be encountered in practical applications, enhancing the relevance and applicability of the study's findings.

Finally, considering the nanoparticles' concentration by the total weight of epoxy, which includes both the part A and part B, is a valid and technically sound approach. This method accounts for the entire epoxy system and reflects the real-world conditions in which the nanocomposites will be utilised.

It's essential to consider the entire epoxy system because both the resin and hardener contribute to the final properties of the cured epoxy, including mechanical, thermal and chemical characteristics. By measuring the nanoparticles' concentration relative to the total epoxy weight, one effectively assesses their impact on the entire composite material, ensuring that the results obtained are relevant and applicable to practical scenarios.

Adopting this approach allows for a more comprehensive evaluation of the nanocomposite's performance and properties, aligning with real-world applications where the entire epoxy formulation, including both resin and hardener, is used.

The designation of the NMEAs samples was the nanoparticles’ name followed by the nanoparticles’ concentration. For instance, the sample CNF-0.5 is the NMEA sample which is composed of epoxy adhesive loaded with 0.5 wt.% of CNF.

Fig. 3.5 The Fisher Scientific FB 15051 ultrasonic bath.

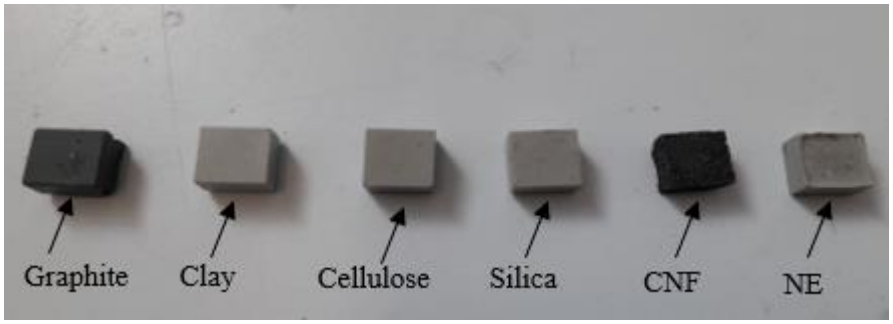

Fig. 3.6 The NE and some of the NMEAs samples.

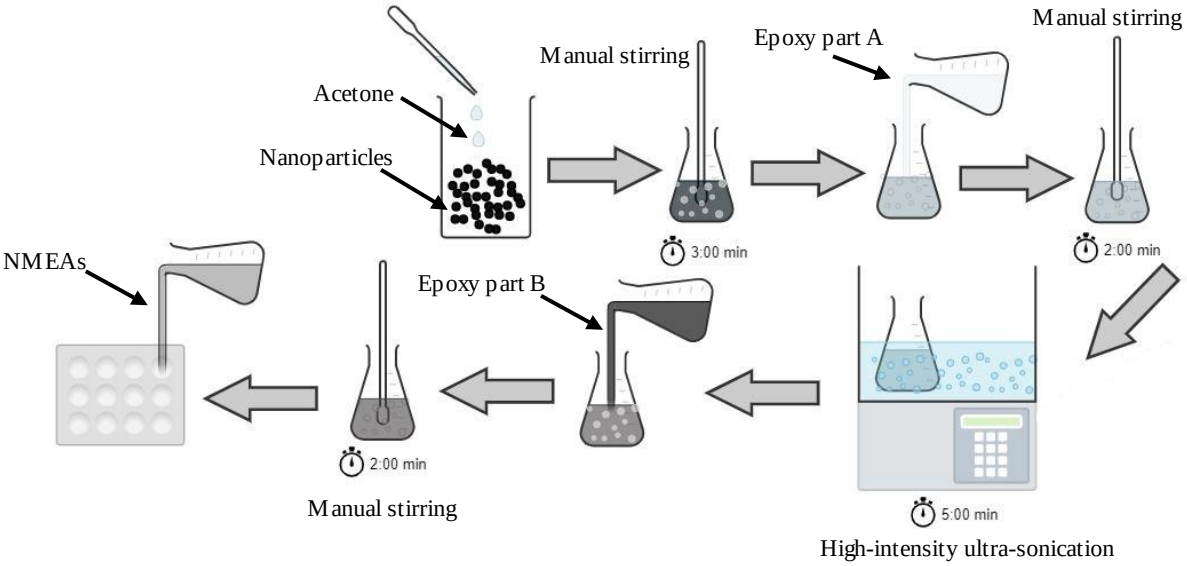

Fig. 3.7 Synthesis of the NMEAs.

3.3.1.3 Characterisation of NE and NMEAs samples

3.3.1.3.1 ATR-FTIR Spectroscopy

The changes in the chemical bonds, in terms of appearance and disappearance of their functional groups, in the NE due to adding the nanoparticles was investigated through ATR-FTIR spectroscopy using PerkinElmer Spectrum One device. Both the NE and the NMEAs samples (Fig. 3.6) were placed on ATR stage (Fig. 3.8) that has a diamond detector, where the Infrared beam goes inside the sample and the resultant transmitted energy is measured. Afterwards, the Perkin Elmer device produces a spectrum with a wavenumber range of 600-4000 cm^{-1} at a resolution of 4 cm^{-1}, over 14 scans for each sample. This technique is well known for its high sensitivity, accuracy and reliability in quantifying and analysing materials.

In order to obtain comprehensive investigation, further FTIR spectroscopy of the nanoparticles was carried out with Potassium Bromide (KBr) pellets technique. The KBr pellets (Fig. 3.9a) were prepared by, first, mixing the nanoparticles with KBr powder at 1:100 weight ratio and then press the mix through a hydraulic press at the pressure of 10 tonnes. The KBr pellets were then placed in the same device used before but with different sample holder, as shown in Fig 3.9b.

3.3.1.3.2 Raman Spectroscopy

Further chemical investigation was done by means of Raman spectroscopy to examine the chemical structure of the nanoparticles, NE and the NMEAs samples. The test was conducted using RENISHAW inVia Raman Microscope, considering the Raman shift range from 0 to 3200 cm^{-1} to test the NE and the NMEAs samples, and from 1000 to 3200 cm^{-1} to test the nanoparticles. The spectra were collected by accumulating 5 scans. To test the nanoparticles, a little amount of the particles was mixed with Isopropanol (IPA) using the ultrasonic bath. Some drops of the solution were then taken and put on a silica wafer (Fig. 3.10) and waited until the IPA volatilised and then tested, as shown in Fig. 3.11a. The test setup of the NE and the NMEAs samples is shown in Fig. 3.11b.

3.3.1.3.3 XRD Analysis

Physical characterisation of the NE and the NMEAs was done through the XRD analysis to investigate the crystallinity of the samples and to evaluate the effect of adding the nanoparticles on the crystallinity of NE. The test was carried out using a Bruker D8 Advance diffractometer equipped with copper tube and Lynxeye position sensitive detector. The diffractogram were recorded with 2Theta ranging from 5° to 100°, with a scan step size of 1.0°, and then the

crystallinity of each sample was directly obtained from Eva software based on its diffractogram. The test setup and how the crystallinity was obtained from the software are shown in Fig. 3.12a and Fig. 3.12b, respectively.

3.3.1.3.4 SEM Analysis

The microstructural analysis of the NE and the NMEAs samples and the dispersibility check of the nanomaterials through epoxy were done through SEM analysis. It's noteworthy that all tested samples were sputter-coated with a thin film of gold before analysing them under the SEM because of their non-conductive characteristics. The coating process was run for 90 seconds for each sample by using a Polaron-SC7640 coating device (Fig. 3.13).

The SEM analysis was conducted using Zeiss LEO and Zeiss Supra 35VP microscopes with a high filed emission was employed to serve this purpose by producing micro images of the tested samples. It is worthy to note that the LEO microscope was used to analyse the NE and the clay nanocomposites, while the analysis of the rest of the samples were done using the Supra microscope, since the latter provides higher magnification images than the former. It was therefore used for the nanocomposites prepared with smaller nanoparticles to obtain better images. The SEM instruments used for the microstructural investigation are shown in Fig. 3.14.

Moreover, the SEM images of samples' surfaces were also analysed through ImageJ software for the porosity study, as shown in Fig. 3.15. It's noteworthy that ImageJ serves as a powerful tool in the process of quantifying porosity within samples. How it works is that after obtaining digital images of the samples, thresholding techniques are applied to differentiate pores from the background based on pixel intensity. This leads to the creation of a binary image, where pores are depicted as red regions against a black backdrop. By calculating the ratio of red pixels (those indicated by the white arrows) to the total number of pixels, the porosity percentage is derived.

Fig. 3.8 ATR-FTIR test setup of NE and NMEAs samples.

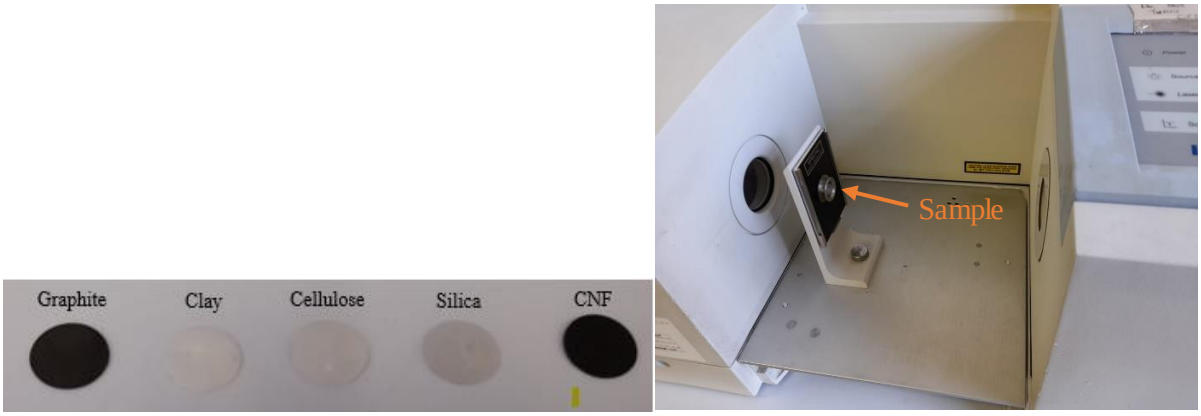

(a) (b)

Fig. 3.9 (a) KBr pellets containing the nanoparticles and (b) FTIR test of the pellets.

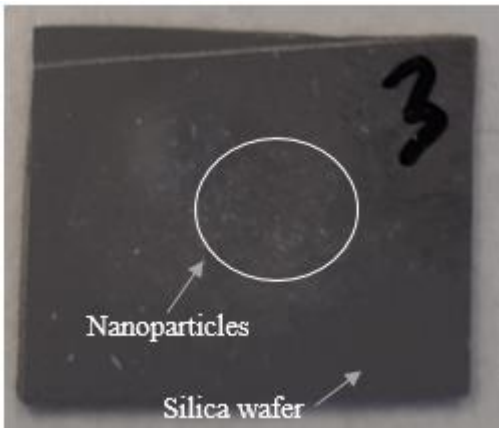

Fig. 3.10 The silica wafer used for Raman testing of the nanoparticles.

(a) (b)

Fig. 3.11 Raman test setup of (a) nanomaterials and (b) NE and NMEAs samples.

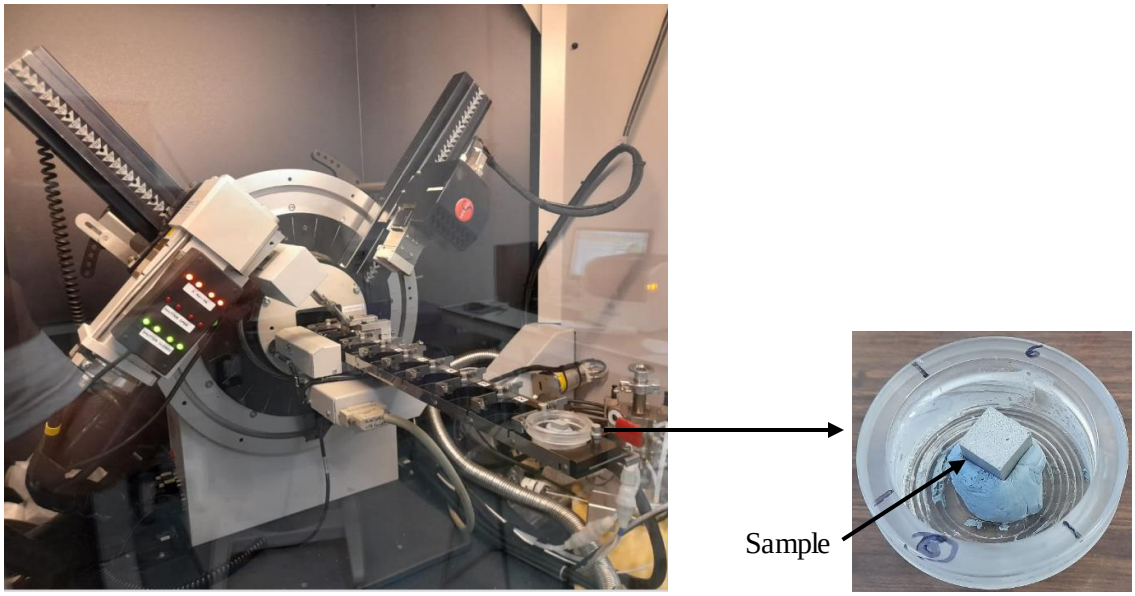

(a)

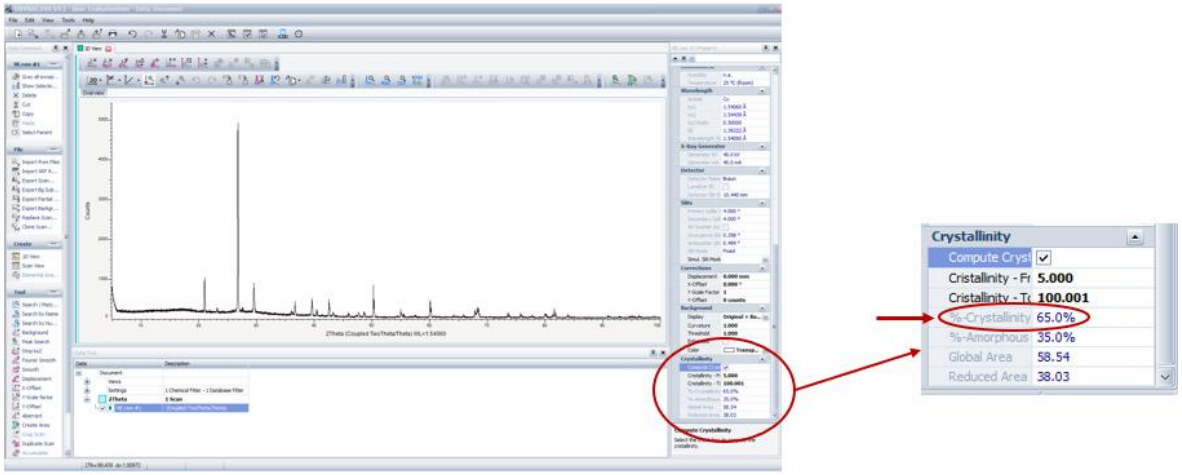

(b)

Fig. 3.12 (a) XRD test setup of NE and NMEAs samples and (b) obtaining the crystallinity from Eva software.

Fig. 3.13 The Polaron-SC7640 coating device.

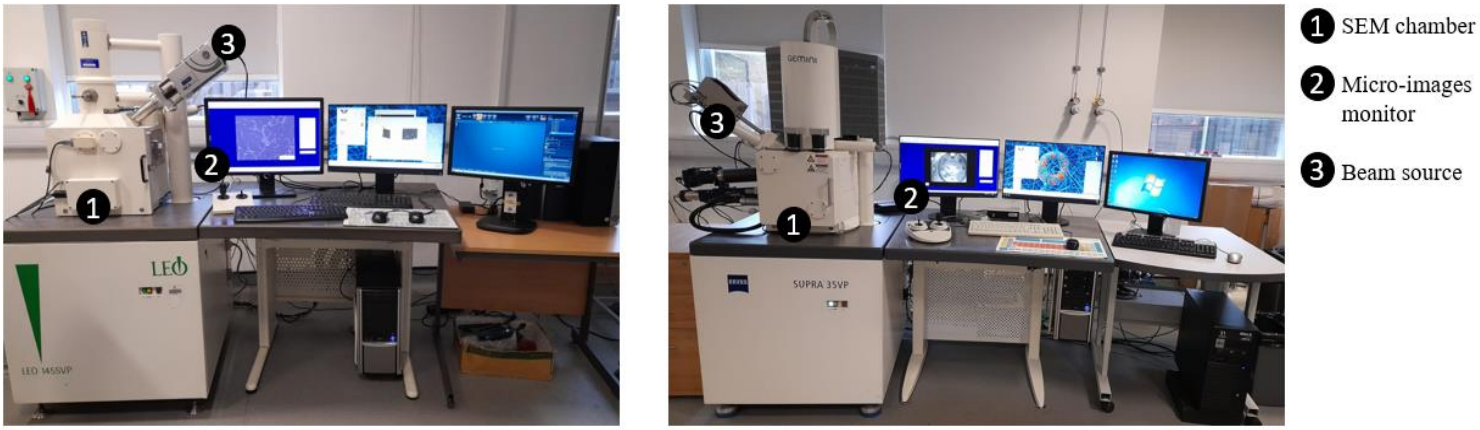

(a) (b)

Fig. 3.14 The SEM instrument used for the microstructural investigation: (a) LEO and (b) Supra 35VP.

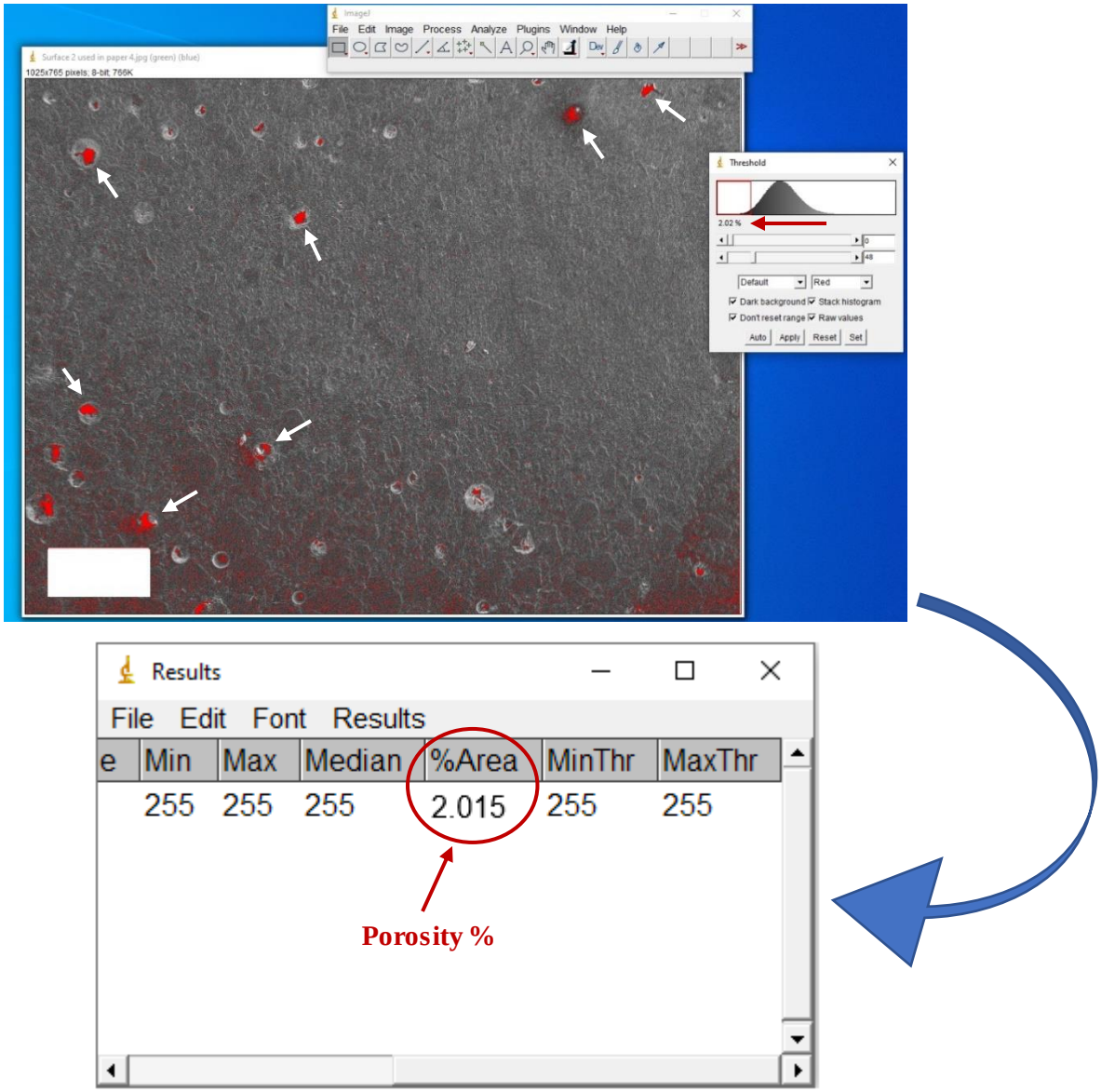

Fig. 3.15 The process of obtaining the porosity % from ImageJ software.

3.3.2 Preparation and testing of the CP-adhesive-bonded joints

3.3.2.1 Reasons behind adopting the test procedures

Central to the overarching goal of enhancing bond strength and optimising the interfacial characteristics within concrete-adhesive-FRP interfaces, the strategic utilisation of CP-adhesive-bonded joints as a testing platform under lap-shear conditions stands as a linchpin of this study's methodology. By subjecting CP joints to meticulous lap-shear testing, this approach offers a controlled environment to dissect adhesive behaviour and performance on a micro scale, simulating the intricate interactions occurring at the concrete-adhesive-FRP interfaces. The utilisation of three distinct nanoparticle concentrations within the CP joints facilitates a granular understanding of how varying adhesive formulations influence bond strength.

As a cornerstone of the research framework, these lap-shear experiments not only yield insights into adhesive strength trends but concurrently pave the way for refining subsequent stages of investigation. This systematic approach, where CP-adhesive joints serve as a microcosm of the broader interface, empowers the study to holistically address the complex mechanics of adhesive interaction. Moreover, these results, offering a glimpse into the subtleties of nanoparticle concentration effects, shape the strategic decisions taken for subsequent concrete testing.

Additionally, while ASTM D3163 is specifically designed for 'Determining Strength of Adhesively Bonded Rigid Plastic Lap-Shear Joints in Shear by Tension Loading,' it was selected for the testing purposes of the CP-adhesive joints due to the alignment of key testing objectives. Despite the slight disparity in material characteristics, the fundamental mechanics of shear loading in lap-shear joints remain consistent. The choice of this test procedure was made after careful consideration of available standards, and it was deemed the closest match to our research requirements. Moreover, this approach facilitates comparability and allows us to leverage established testing methodologies and data interpretation techniques. While acknowledging the subtle variation in materials, I believe that the ASTM D3163 test provides valuable insights into the performance of our CP-adhesive joints, enabling meaningful analysis and conclusions to be drawn for our specific application.

3.3.2.2 Preparation of the CP-adhesive-bonded joints

The bond performance of the CP specimens bonded with NE and NMEAs was evaluated through testing the CP-adhesive joints by means of the lap-shear test.

The CP specimens were obtained by manually (due to the small amount) Type I ordinary OPC and tap water at a water-cement ratio (w/c) of 0.50 (to simulate the w/c used in the concrete mix design). The mix was then cast in a silicon mould containing a set of 2.5cm cubes (Fig. 3.16). The specimens were then cured in water for 28 days to gain strength. Afterwards, two cubes (one cube is shown in Fig. 3.17) were glued to each other using either NE or NMEAs (same nanomaterials and wt.% mentioned in Section 3.3.1) and then cured for 7 days at room temperature to ensure sufficient bond at the interface. The CP-adhesive-bonded joints are shown in Fig 3.18.

Fig. 3.16 Fresh CP samples.

Fig. 3.17 CP sample used in preparing the CP-adhesive joints.

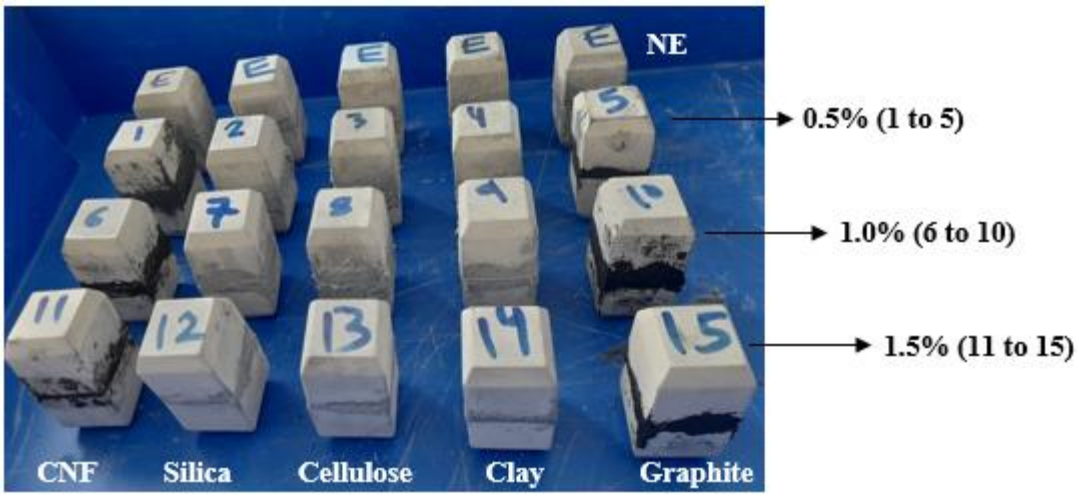

Fig. 3.18 The CP-adhesive-bonded joints.

3.3.2.3 Testing of the CP-adhesive-bonded joints

A compression lap-shear test, as shown in Fig. 3.19, was conducted on the adhesive joints using INSTRON 5969 with a load rate of 1.30 mm/min, according to the ASTM D3163 [204]. The ultimate LSS values were recorded using a data acquisition system, and the modes of failure were also monitored. It's noteworthy that five CP specimens bonded with NE were made, two

of them served as trial specimens to check the test setup, while the remaining three were considered in the test results for comparison purposes.

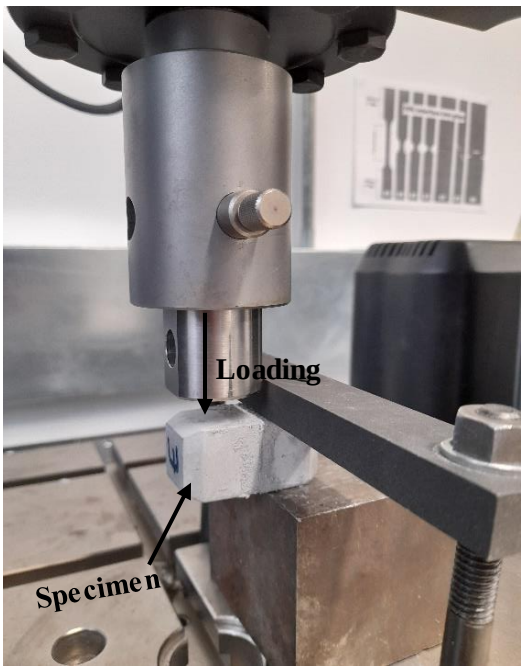

Fig. 3.19 Test setup of the compression lap-shear test.

3.3.3 Preparation and testing of the NSM-FRP-retrofitted concrete specimens

3.3.3.1 Factors shaping the adoption of testing approach: test specimens and parameters

3.3.3.1.1 The selection of testing approach

First of all, in the context of our chosen methodology for testing the NSM-FRP-retrofitted specimens and in alignment with the overarching objective of improving the interfacial bond strength and characteristics within these retrofitted structures, a valid and important question naturally arises: Why did I opt for the three-point bending test instead of the Direct Pull-out test (DPT), the test method that is more directly associated with assessing bond-related behaviour? After all, the DPT is specifically tailored for evaluating adhesive bonds, while the three-point bending test may not seem inherently designed for this purpose. To address this query comprehensively, I present my rationale below.

In the pursuit of comprehensively understanding the structural behaviour and performance of NSM-FRP-retrofitted concrete members, the choice of testing methodology plays a pivotal role. This selection is not only pivotal in achieving the study's core objective but also in unravelling a wealth of insights that span beyond its initial scope, as follows:

Holistic Understanding of Behaviour: The three-point bending test offers a holistic understanding of the behaviour of NSM-FRP-retrofitted concrete members. While its primary objective is to investigate the mechanical behaviour of tested specimens, it also presents a unique opportunity to glean valuable insights into the bond strength and characteristics at the concrete-adhesive-FRP interfaces. This dual nature of the test aligns seamlessly with the core objective of my study and ensures a comprehensive evaluation that captures both mechanical and bond-related behaviours within a single experimental framework.

Mechanical Properties: Unlike the DPT, the three-point bending test allows me to evaluate mechanical properties such as load-carrying capacity, flexural strength and ductility. These properties are crucial to assess the overall structural performance of retrofitted members, considering real-life scenarios where multiple modes of loading and interaction occur.

Failure Modes Analysis: The three-point bending test enables in-depth analysis of failure modes. By observing where and how the specimen fails, one gains insights into the interplay between adhesive, concrete and FRP, shedding light on the effectiveness of the bond and the mechanisms that contribute to failure.

Real-World Application: The goal of retrofitting is to enhance the performance of structures under various loading conditions. The three-point bending test better simulates actual structural behaviour by subjecting the specimen to a combination of bending and shear forces, which accurately represents the complexities of real-world scenarios.

Comprehensive Data: By combining mechanical behaviour and bond-related insights, the three-point bending test provides a comprehensive dataset. This approach allows me to make informed decisions about the effectiveness of the retrofitting technique not only in terms of bond strength but also its implications on the overall structural response.

In summary, the three-point bending test offers a multi-dimensional approach that aligns with the holistic objective of the study. It considers both bond-related behaviour and broader mechanical properties, providing a more accurate representation of real-world scenarios, which reflects a balanced consideration of different aspects, ultimately enhancing the credibility and applicability of research findings to practical engineering scenarios.

3.3.3.1.2 The selection of test specimens

Amidst the prevailing landscape of steel-reinforced concrete structures, the deliberate inclusion of unreinforced concrete prisms as a cornerstone of this research strategy emerges as a

masterstroke that emboldens the quest for innovation and real-world applicability. While the majority of global constructions feature steel reinforcement, the strategic introduction of unreinforced specimens serves as a powerful tool to unravel latent insights that transcend the boundaries of convention. The rationale behind investigating the efficacy of modified adhesives using unreinforced concrete prisms is underpinned by a meticulous blend of ingenuity and realism. The very absence of steel reinforcement hones the focus onto the inherent capabilities of the novel adhesives, isolating their impact on strengthening the material matrix. Unencumbered by the interaction of steel elements, the behaviour of the adhesive-concrete interface takes centre stage, providing a clear lens to scrutinise the adhesive's transformative potential. This approach sets the stage for comprehensive lap-shear testing to discern the interplay between adhesive behaviour and interface strength.

3.3.3.1.3 The adoption of some critical test parameters

1) Wt.% concentration of the nanoparticles

Motivated by the lap-shear results (discussed in Chapter Five), where increasing concentrations led to reduced adhesive strength (due to increased % porosity and decreased % crystallinity, shown in Chapter Four), the decision to adopt a 0.1% nanoparticle concentration for concrete testing emerges as an outcome of thoughtful analysis. This selection not only conserves valuable resources but is also guided by the intent to explore whether this lower concentration might offer a favourable balance between adhesive performance and material consumption. The synergy between the lap-shear outcomes and the concrete testing strategy accentuates the role of the former as a predictive benchmark for the latter.

In essence, the lap-shear tests serve as a discerning precursor, delineating the influence of nanoparticle concentration on adhesive bond strength. This critical information, when extrapolated to concrete testing, adds layers of comprehension to the broader picture. The adoption of 0.1% nanoparticle concentration in concrete specimens, stemming from lap-shear-derived insights, not only aligns with economic considerations but bridges the gap between these distinct test types. Together, they synergistically paint a comprehensive portrait of adhesive behaviour across diverse scenarios.

In order to delve deeper into the concentration-effect relationship and establish a proof of concept, a subset of experiments involved the use of 0.2% and 0.3% nanoparticle concentrations, specifically within the context of graphite nanocomposites. This strategic choice was based on the recognition that different nanoparticles can exhibit varying response

patterns to concentration changes, and graphite nanocomposites warranted exploration in this regard. By focusing on these concentrations exclusively for graphite nanocomposites, the study aimed to understand whether distinct nanoparticles could present unique concentration-dependent behaviours, further enriching the understanding of nanoparticle interactions within the adhesive matrix. This targeted exploration enhances the comprehensiveness of the research findings and unveils nuances that might be masked by a broader set of concentrations.

2) Groove dimensions/size

While the groove sizes of 8x8 mm, 10x10 mm and 12x12 mm were thoughtfully chosen for the purpose of this study to represent 1.33, 1.67 and 2.00 times the groove width or depth to FRP bar diameter (b/d_b), respectively, it's important to delve into the underlying considerations that prompted the decision to not rigidly adhere to the minimum groove dimensions of $1.5d_b$ as proposed by the ACI 440.2R-08 [26].

The ACI guideline's recommendation of a minimum groove size is an invaluable starting point for structural integrity, aligning with general safety standards. However, it's essential to recognise that real-world scenarios can be inherently complex and multifaceted. The selection of an optimal groove size cannot be governed by a one-size-fits-all approach, as the performance of the FRP-adhesive interface involves intricate interplays of factors such as material properties, loading conditions and interface mechanics.

Innovative research pursuits necessitate a balanced blend of adherence to industry guidelines and tailored experimentation to unravel uncharted nuances. The decision to explore groove sizes beyond the minimum recommendation stems from the quest to achieve holistic insights. A groove size that exceeds the ACI guideline's minimum might, in certain contexts, offer advantages such as enhanced bond surface area, optimised stress distribution and improved load transfer mechanisms. The variances in structural behaviour that emerge from different groove sizes underscore the importance of acknowledging the dynamic nature of adhesive-FRP interactions.

While the ACI guideline forms a bedrock of structural safety, the forefront of research seeks to transcend established norms and sculpt new realms of knowledge. The deviation from a singularly prescribed groove size is a testament to the research's ambition to unearth novel possibilities and redefine the boundaries of retrofitting efficacy. By embracing controlled variations in groove dimensions, the study endeavours to provide a more nuanced understanding of the intricate adhesive-FRP interplay and its interwoven complexities.

In the quest for advancement, adherence to guidelines is balanced by a calculated exploration of uncharted dimensions. The research respects the ACI suggestion as a foundational guidepost, but also acknowledges that there's a realm of unexplored potential beyond its confines. The endeavour to transcend boundaries and push the envelope of understanding underscores the spirit of innovative research, where the pursuit of knowledge takes precedence over the confines of convention.

3.3.3.1.4 Strategic choice of specific FRP materials for specific parameters

The thoughtful choice to employ distinct types of FRP reinforcement bars for various retrofitting parameters relevant to FRP reinforcement in the study was grounded in both practical and research-driven considerations. For instance, the selection of CFRP bars for one parameter, e.g. the number of FRP bars and GFRP bars for another (i.e. the position of FRP bars), to name a few, was predicated on the distinct mechanical properties and behaviours exhibited by these materials. This strategic variation facilitated an in-depth exploration of how different FRP types influence the structural response of the specimens, thereby enriching the overall analysis.

The more frequent use of CFRP bars in this study can be attributed to their superior mechanical properties, including higher tensile strength and stiffness, which make them well-suited for load-bearing applications. Additionally, it's noteworthy that CFRP is the most commonly employed FRP type in retrofitting purposes within the construction and engineering industries, further justifying its prominent role in the study. This choice not only aligns with the research's focus but also reflects real-life situations, ensuring that the study mirrors practical applications of FRP materials in structural retrofitting, thus enhancing the study's relevance and significance.

Furthermore, the limited use of BFRP bars was a purposeful decision. Although BFRP possesses unique characteristics, its extensive inclusion might not have significantly contributed to the specific research objectives under investigation. By judiciously limiting the use of BFRP, the study was streamlined, ensuring that the research focus remained sharply aligned with key variables, enhancing research clarity and optimising resource efficiency. This strategic approach, thus, facilitated a more targeted and in-depth examination of the chosen FRP materials, including CFRP and GFRP, and their impact on the structural behaviour of the concrete specimens, ultimately enhancing the overall quality and depth of the research.

3.3.3.1.5 Specimen replication strategy: Effects of groove size and presence of FRP reinforcement bars

The choice to produce three replicates of the NE-8 specimens while creating only one replicate each for the NE-10 and NE-12 specimens was carefully considered to align with the specific research objectives and enhance the comprehensiveness of our study. The NE-8 specimens played a pivotal role in our research as they were primarily designed for the critical investigation of the effect of the presence of FRP reinforcement bars on the efficiency of the retrofitting process. This particular aspect was of paramount importance, given that the use of FRP reinforcement alongside NE in retrofitting is not a common practice, making it necessary to have multiple replicates for a thorough examination.

In contrast, the NE-10 and NE-12 specimens were exclusively created to study the influence of varying groove sizes in the absence of FRP reinforcement. Moreover, it is not common to use NE-only retrofitting, which further justifies the need to have a single replicate for each. While these specimens were originally considered for exclusion due to their single replicate nature, it was ultimately decided to retain them in the study to provide an even more comprehensive understanding of the retrofitting process, encompassing various groove sizes. As those specimens were the only ones to have only one replicate, while all the rest had three.

In summary, the strategic allocation of specimen replication was tailored to the specific research goals, with NE-8 serving as the reference group to investigate the synergy between NE and FRP, while NE-10 and NE-12 focused on the singular variable of groove size. This approach optimises resource allocation and ensures a comprehensive assessment of the retrofitting process.

3.3.3.2 NSM-FRP retrofitting of the concrete specimens

The ingredients shown in Table 3.5 were first mixed and then cast in 50 mm wide, 50 mm deep and 200 mm long wooden moulds containing either 8x8, 10x10 or 12x12 mm wooden strip lying along in the mid-bottom face of the mould, as shown in Fig 3.20. Some specimens were done with two or three grooves as well (Fig. 3.21). The specimens were then cured in water for 28 days to gain strength. The specimens were then taken out of water and left a bit to dry.

The NSM-FRP retrofitting process was then implemented on the concrete specimens starting with the roughening of the groove sides using sandpaper. The grooves were subsequently cleaned using an air compressor to eliminate any generated dust. Following this, the grooves were partially filled with adhesive (either NE or NMEAs), employing a trowel. Afterwards, the

FRP reinforcement bars were positioned within the grooves and gently pressed, enabling the paste to flow around the strip and to fully fill the space between the bars and the groove sides. Finally, the grooves were filled with additional adhesive, and the surface was levelled. The retrofitting procedure is also shown in Fig. 3.22.

The retrofitted specimens were then air-cured at room temperature for 7 days to guarantee a proper curing of the adhesive and to ensure sufficient bond between concrete, adhesive and FRP reinforcement, and to simulate the curing time and conditions of the NE and the NMEAs samples. Retrofitted specimens are shown in Fig. 3.23.

It's of note that three replicates (i.e. A, B and C) of each retrofitting design were prepared and the average capacities (i.e. ultimate loads, max flexural strength and the maximum displacement (i.e. ductility)) were calculated. The average values were calculated and considered in the performance analysis to provide a representative measure that accounts for variability and ensures a more reliable and accurate assessment of the structural behaviour and response of the tested specimens. It is important to note that while the displacement at maximum load serves as an indirect measure of ductility, it provides valuable insights into the material's ability to undergo deformation before reaching its ultimate capacity. In this study, the displacement at maximum load is utilised as a practical indicator of the material's behaviour under loading conditions. While traditional measures of ductility, such as elongation or strain at failure, offer direct assessments, the displacement parameter offers a more practical approach to evaluating the structural behaviour of the retrofitted members. Therefore, while interpreting the results, it is crucial to consider the displacement at maximum load as an implicit indicator of ductility, which complements the overall understanding of the structural performance of the retrofitted concrete members.

Furthermore, the test matrix (i.e. parameters) of the NSM-FRP retrofitting process is divided into three categories/groups, as shown in the schematic diagram shown in Fig. 3.24. Moreover, the retrofitting design of the specimens and the comparisons made between them according to the considered parameters are also provided in Tables 3.6 and 3.7, respectively.

The specimens bonded with NE alongside FRP bars (i.e. specimens numbered 1-3 and 18-24) were designated in the form of J-NE-L, where "J" represents the FRP type (C for CFRP, G for GFRP and B for BFRP) and "L" indicates the groove size (8, 10 or 12). For example, the specimen C-NE-8 is that specimen retrofitted with CFRP bar inserted in an 8x8 mm groove.

It's noteworthy that the word "Edge" was added after L for the specimens retrofitted with FRP installed on the groove edge, while using the letters "D" or "T" after L indicates the specimens retrofitted with two or three FRP bars (doubled or tripled number of bars), respectively. For those bonded with NE only (specimens numbered 15-17), they were designated as "NE-groove size".

While the designation of those bonded with the NMEAs (i.e. specimens 4-14) followed the form of W-X-Y-Z as follows: "W" indicates the FRP type (same as before), while "X" indicates the type of the bonding agent (i.e. S for silica, Cel for cellulose, Cl for clay and Gr for graphite NMEAs). "Y" is the wt.% of nanomaterials (i.e. 0.1, 0.2 or 0.3) and "Z" specifies the groove size (same as before). For example, the specimen C-Gr-0.1-8 is that retrofitted with CFRP bar inserted in an 8x8 mm groove and bonded using graphite NMEAs at 0.1 wt.%.

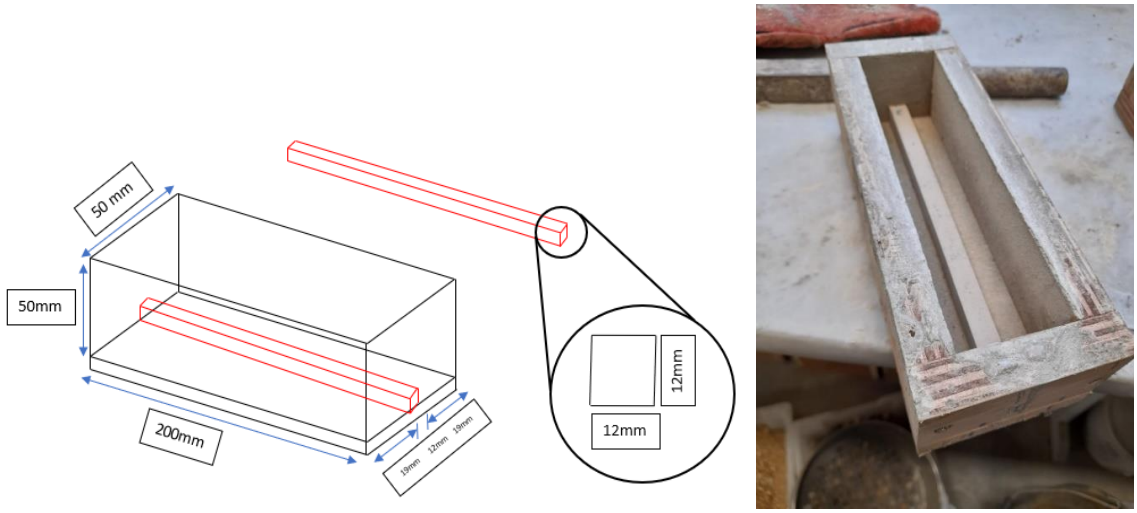

(a) (b)

Fig. 3.20 (a) Sketch of the moulds with 12x12 mm groove and (b) the actual mould.

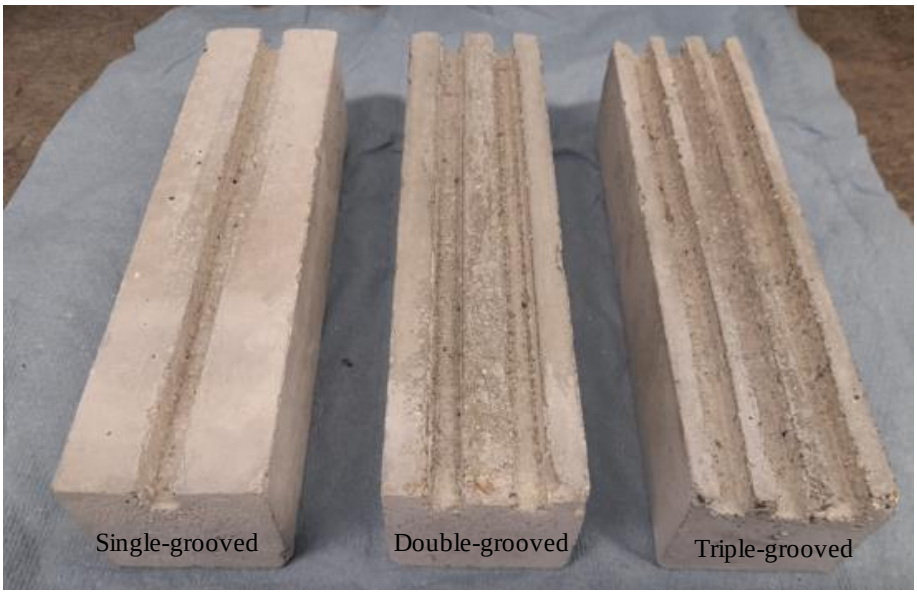

Fig. 3.21 Concrete specimens grooved with one, two or three grooves.

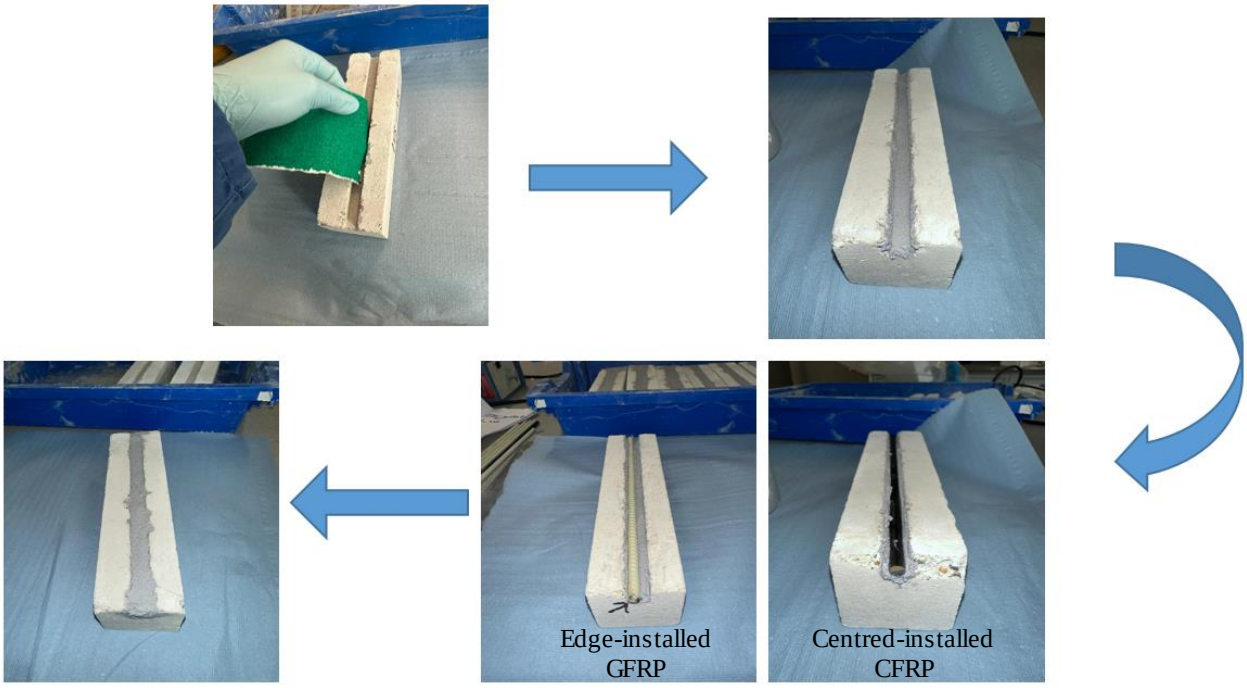

Fig. 3.22 NSM-FRP retrofitting of concrete specimens.

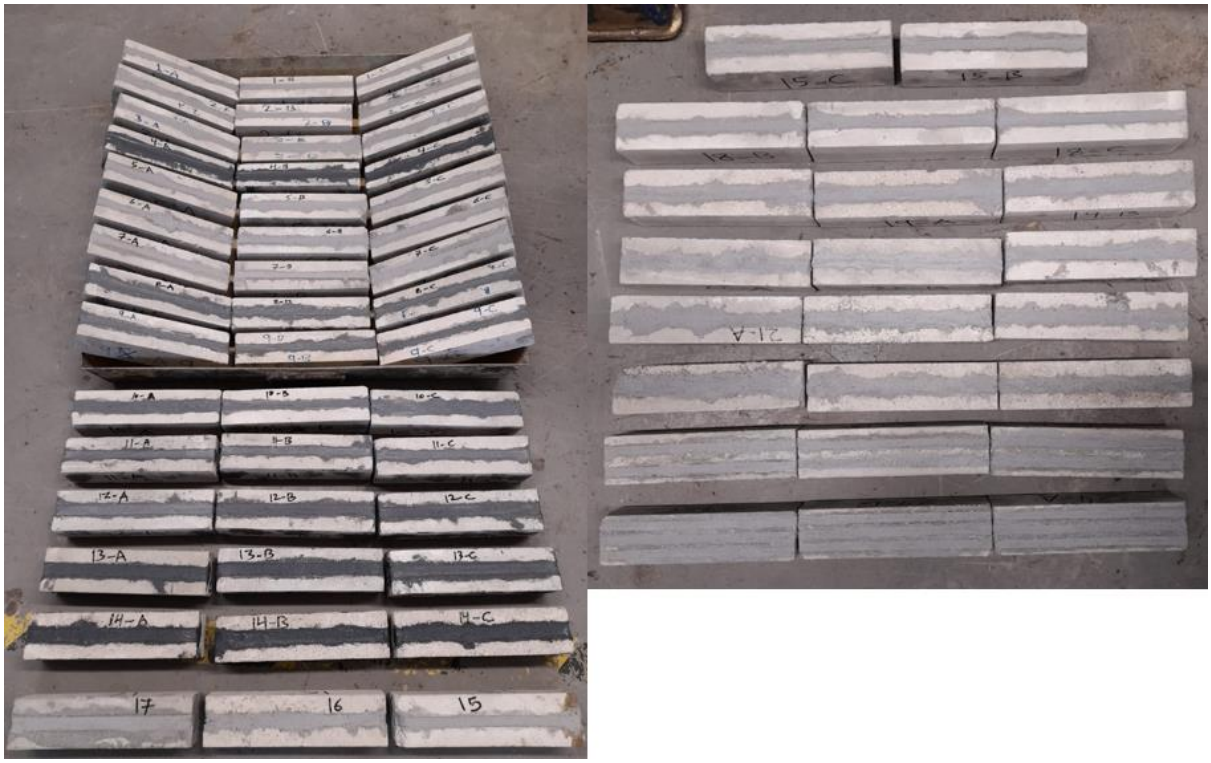

Fig. 3.23 The NSM-FRP-retrofitted concrete specimens.

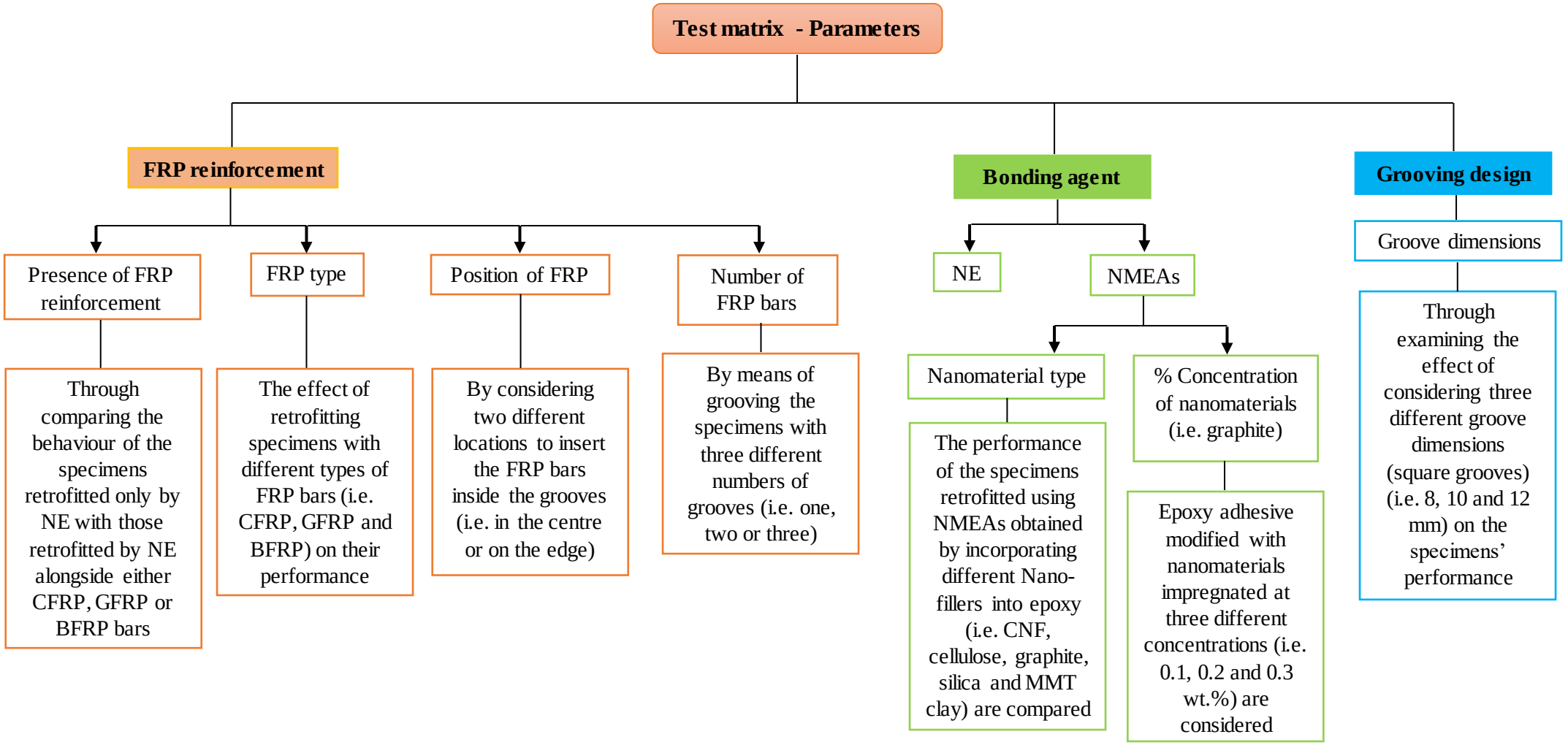

Fig. 3.24 Test matrix of NSM-FRP retrofitting of concrete specimens.

Table 3.6 The NSM-FRP retrofitting design of concrete specimens.

Specimen No.	Specimen code	FRP type	Groove dimensions (W x D) (mm)	Nano-filler (NF)	NF concentration by wt. of epoxy
1	C-NE-8	CFRP	8 x 8	-	-
2	G-NE-8	GFRP	8 x 8	-	-
3	B-NE-8	BFRP	8 x 8	-	-
4	C-CNF-0.1-8	CFRP	8 x 8	CNF	0.1 %
5	C-S-0.1-8			Silica	
6	C-Cel-0.1-8			Cellulose	
7	C-Cl-0.1-8			Clay	
8	C-Gr-0.1-8	CFRP	8 x 8	Graphite	0.1 %
9	G-Gr-0.1-8	GFRP			
10	B-Gr-0.1-8	BFRP			
11	C-Gr-0.1-10	CFRP	10 x 10	Graphite	0.1 %
12	C-Gr-0.1-12	CFRP	12 x 12	Graphite	0.1 %
13	C-Gr-0.2-12				0.2 %
14	C-Gr-0.3-12				0.3 %
15	NE-8	-	8 x 8	-	-
16	NE-10		10 x 10		
17	NE-12		12 x 12		
18	C-NE-10	CFRP	10 x 10	-	-
19	C-NE-12	CFRP	12 x 12	-	-
20	G-NE-10-Edge	GFRP	10 x 10	-	-
21	G-NE-10	GFRP	10 x 10	-	-
22	G-NE-12-Edge	GFRP	12 x 12	-	-
23	C-NE-8-D	CFRP	8 x 8 - Double-grooved	-	-
24	C-NE-8-T	CFRP	8 x 8 - Triple-grooved	-	-

Table 3.7 Demonstration of the test parameters.

Group	Parameter	Specimens to be considered for comparison purposes
FRP reinforcement	Presence of FRP reinforcement bars	Specimens 1, 2 and 3 with specimen 15
	Type of FRP reinforcement bars	Specimens 1, 2 and 3 with each other Specimens 8, 9 and 10 with each other Specimen 18 with 21
	Position of FRP reinforcement bars	Specimen 20 with 21
	Number of FRP bars	Specimen 1, 23 and 24 with each other
Bonding agent	Nanomaterial-modified adhesives	Specimen 1 with 4, 5, 6, 7 and 8 Specimen 2 with 9 Specimen 3 with 10 Specimens 11 with 18 Specimens 12 with 19
	Nanomaterial type	Specimens 4, 5, 6, 7 and 8 with each other
	Concentration of nanomaterials (i.e. graphite)	Specimens 12, 13 and 14 with each other
Grooving design	Groove size	Specimens 1, 18 and 19 with each other Specimens 8, 11 and 12 with each other Specimens 15, 16 and 17 with each other Specimen 2 with 21 Specimen 20 with 22

3.3.3.3 Testing of the NSM-FRP-retrofitted concrete specimens

The retrofitted concrete specimens were tested under three-point bending test, which was conducted by an INSTRON 5969 Universal testing machine under a 150 kN load cell with a crosshead speed of 1.04 MPa/min (avg.) according to the ASTM C 78-02 [205]. The ultimate loads, flexural strength and displacements at maximum loads (described as maximum displacements) were then recorded using a data acquisition system, and the modes of failure were also monitored. The test setup is depicted in Fig. 3.25.

Additionally, the microstructure, in terms of the dispersion of the nanoparticles across the matrix and the % porosity of the nanocomposites, and the crystallinity analyses of the NE and the NMEAs samples were investigated by means of SEM and XRD analyses, respectively to further deepen the understanding of the performance of the NMEAs for their application as bonding agents in NSM-FRP retrofitting applications. It's noteworthy that the terms NMEAs and nanocomposites are used interchangeably through the thesis.

The seemingly simple test setup for the NSM-FRP-retrofitted specimens, which excludes the Linear Variable Differential Transformer (LVDT) for measuring the displacements and utilises relatively small specimens, may raise initial concerns about the comprehensiveness of the experimental approach. However, it's crucial to emphasise that the choice of this setup was deliberate and justified by several key factors.

Firstly, consistency is paramount in any scientific study. All specimens were subjected to the same testing conditions and parameters, ensuring that any observed differences or trends were not influenced by varying experimental setups. This consistency strengthens the reliability of the comparative analysis.

Secondly, the decision to exclude the LVDT for deflection measurements could have been influenced by practical considerations, such as budget constraints or the specific objectives of the study. While LVDTs offer precise deflection measurements, their use can be resource-intensive, and in certain cases, their exclusion may be justifiable, provided other means of data collection and analysis are employed effectively.

Moreover, the decision to exclude load-deflection relations for the tested specimens was driven by the considerable volume of data generated during the experimental phase. Each specimen, subjected to three repetitions, yielded an extensive dataset, numbering tens of thousands of data points for both load and deflection parameters. Managing this dataset proved challenging, as consolidating this data into meaningful load-deflection relations, even with the aid of tools like Excel, was a complex task.

Attempting to derive load-deflection relations from this extensive dataset could have resulted in suboptimal or non-representative outcomes.

Therefore, the exclusion of load-deflection relations did not substantially compromise the quality or comprehensiveness of the analysis. Instead, the study's approach concentrated on the overall capacities and structural failure modes of the tested specimens, providing a robust understanding of their behaviour under various retrofitting parameters. This strategy facilitated a comprehensive insight into the structural response of the specimens.

Lastly, the use of relatively small specimens should not undermine the validity of the study, as long as these specimens were representative of the real-world scenarios or conditions under investigation. Small-scale testing can provide valuable insights, especially when large-scale testing is impractical or cost-prohibitive. The focus should be on the relevance of the results to the intended application and whether the chosen test setup effectively addresses the research questions or hypotheses.

In conclusion, the apparent simplicity of the test setup should not be perceived as a limitation but rather as a conscious choice made to ensure consistency, feasibility and relevance to the study's objectives. The key lies in demonstrating that the chosen approach was appropriate and that the results obtained are meaningful within the context of the research.

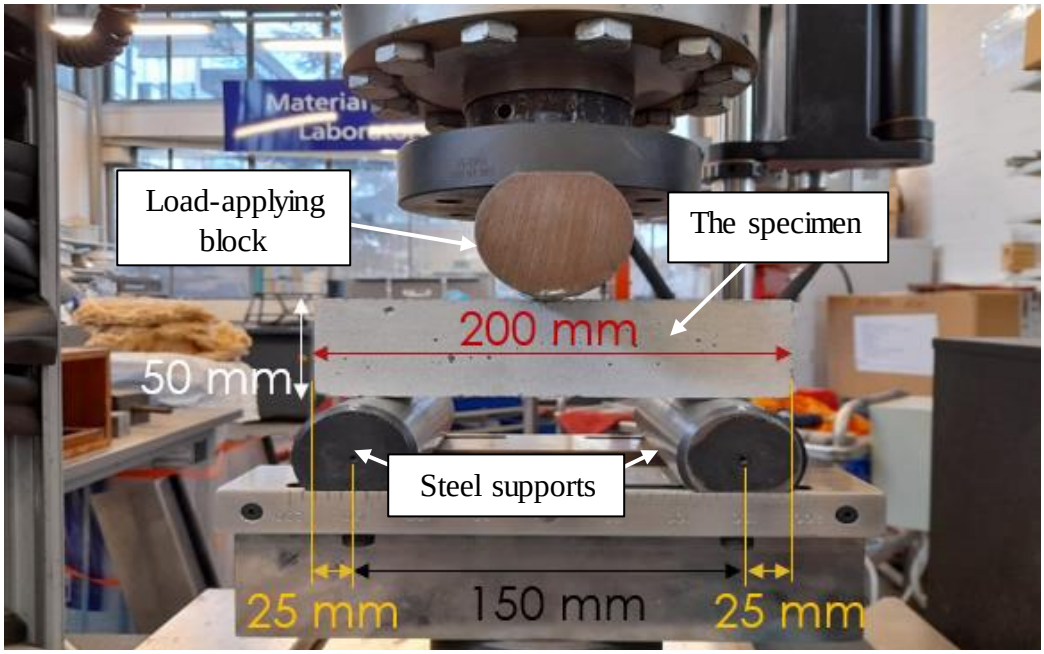

Fig. 3.25 The three-point bending test setup.

3.3.3.4 COV in the experimental results: Significance and exclusion

The coefficient of variation (COV) is a valuable statistical measure that quantifies the relative variability of a dataset, expressed as a percentage of the mean. Originally introduced as a tool for quality control and assessing the precision of measurements, the COV has found its way into research tables for multiple reasons.

Firstly, the COV provides readers with a quick and concise assessment of the data's dispersion. A high COV indicates greater variability in the dataset, which can be crucial for understanding the reliability and consistency of experimental results. This information is particularly vital in fields where data consistency is paramount, such as quality control, manufacturing or scientific research. The COV serves as an effective at-a-glance indicator of data quality, enabling researchers and decision-makers to assess the robustness of the findings.

Secondly, the COV offers a standardised measure of variability, making it easier to compare results across different studies or between different experimental conditions. In many cases, presenting the COV in tables is part of the effort to enhance the transparency and replicability of research. By providing this measure, researchers signal their commitment to methodological rigor and the objective reporting of results.

Despite the inclusion of the COV in tables displaying experimental results is a common practice in scientific research for several important reasons, but its significance may not always be explicitly discussed in the written analysis. This omission can be attributed to several factors. One possibility is that the COV's significance is assumed to be self-evident or well-established in the field, especially when it's a common practice. Additionally, it could be better prioritising other aspects of data analysis, choosing to discuss the implications of variability and reliability in the context of the broader research findings rather than delving into specific statistical measures.

In conclusion, the inclusion of the COV in tables displaying experimental results serves to enhance the transparency, comparability and reliability of research findings. While its importance is well-recognised, it may not always be explicitly addressed in the written analysis due to various factors, including assumed familiarity or the prioritisation of other critical findings.

3.4 Summary

This chapter has served as an extensive exposition, offering an in-depth account of the materials carefully chosen for this research study, as well as the meticulously designed experimental procedures and techniques adopted. The selection of these materials and the rationale behind their choice, alongside the methodology and testing approach employed, have thoroughly been elucidated in this chapter. The underlying reasons for opting for specific materials and the thought process behind the chosen testing methodologies have also been articulated, shedding light on the deliberate decisions made to ensure the validity and robustness of the research. Furthermore, it is important to note that the testing methods introduced herein were not only employed for data acquisition but were also instrumental in facilitating data analysis, a pivotal step in achieving the previously outlined objectives. By providing a detailed account of the materials, methods and motivations behind them, this chapter aims to offer a comprehensive foundation for the ensuing research findings and discussions.

Chapter 4: Effect of incorporating carbon- and silicon-based nanomaterials on the physico-chemical properties of a structural epoxy adhesive

4.1 Introduction

This chapter is concerned with presenting the results and discussion of the chemical, physical and microstructural characterisation of the NE and the NMEAs. The chapter starts with showing and discussing the results of the SEM analysis in terms of the microstructural, morphology and the state of dispersion of the Nano-fillers into the epoxy matrix. Moreover, the porosity analysis of the characterised samples is also addressed. Afterwards, the changes happened in the physical structure of the NE as a result of adding the nanoparticles has been characterised in terms of changes in the % crystallinity, which was examined by means of the XRD analysis. Finally, the chemical characterisation and analysis of the targeted samples are considered, where the changes in the chemical composition (i.e. bonding) of the NE with incorporating the nanomaterials have been also investigated by means of the ATR-FTIR and Raman spectroscopies. It's worthy to note that the results of the different analyses performed on the tested specimens were correlated to each other in order to be assessed in an efficient and comprehensive way. It's worthy to mention that the NMEA samples were labelled based on the name of the nanoparticles followed by their concentration. For example, the sample CNF-0.5 denotes an NMEA sample consisting of epoxy adhesive infused with 0.5 wt.% of CNF.

4.2 Results and discussion

4.2.1 SEM and porosity analyses

The NMEAs samples were analysed by means of the SEM to investigate their microstructure and morphology in terms of the degree of dispersibility of the nanoparticles through epoxy matrix, that is, whether they are agglomerating or uniformly dispersed through the matrix. Moreover, the % porosity of the NE and the nanocomposites in terms of the amount of the air voids appearing on their surfaces was also considered. The NE sample was also analysed in order to assess the distribution of the quartz grains prior the addition of the nanoparticles to benchmark the nano-modified materials against it. High-magnification SEM images of the NE and the NMEAs are shown in Fig. 4.1. The SEM images of the samples' surfaces are shown in Fig. 4.2, and the % porosity of samples is provided in Table 4.1.

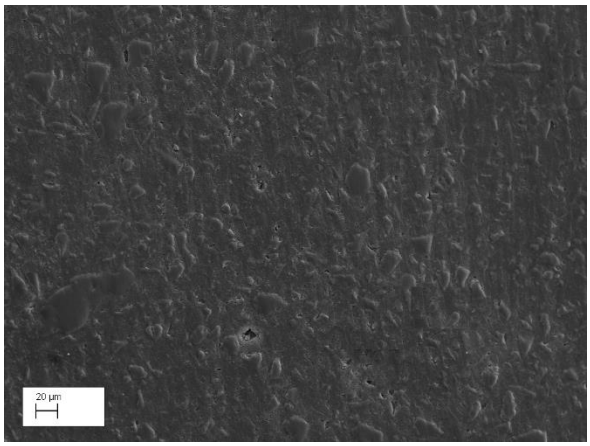
20 µm

(a)

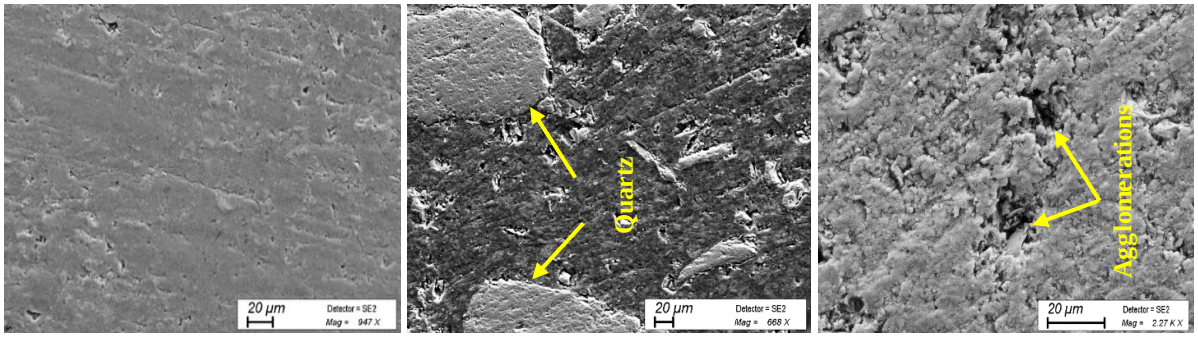
Quartz
Agglomerations
20 µm
Detector = SE2
Mag = 947 X
20 µm
Detector = SE2
Mag = 668 X
20 µm
Detector = SE2
Mag = 2.27 K X

(b)

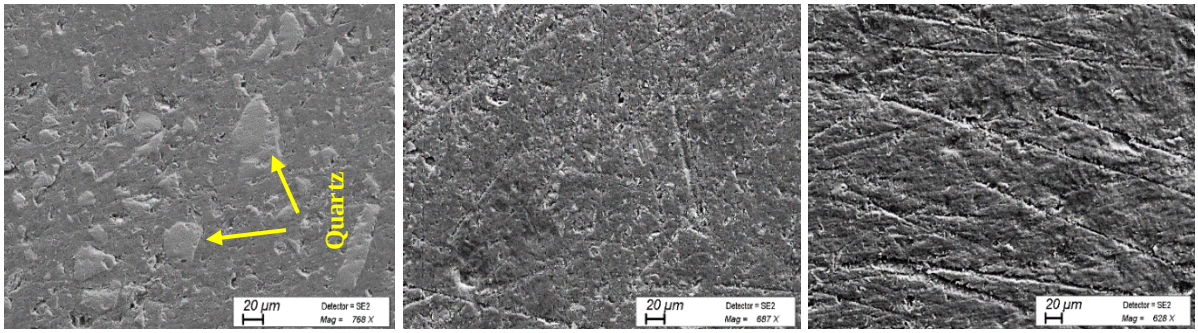
Quartz
20 µm
Detector = SE2
Mag = 768 X
20 µm
Detector = SE2
Mag = 687 X
20 µm
Detector = SE2
Mag = 628 X

(c)

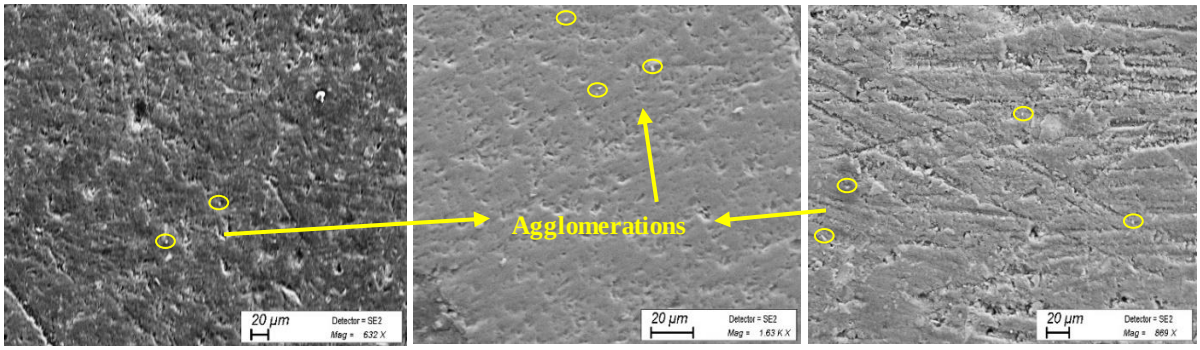
Agglomerations
20 µm
Detector = SE2
Mag = 632 X
20 µm
Detector = SE2
Mag = 1.63 K X
20 µm
Detector = SE2
Mag = 869 X

(d)

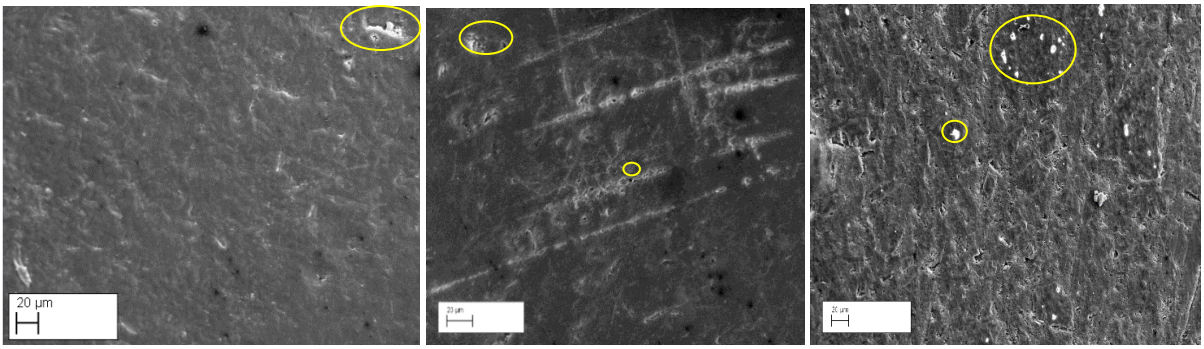

(e)

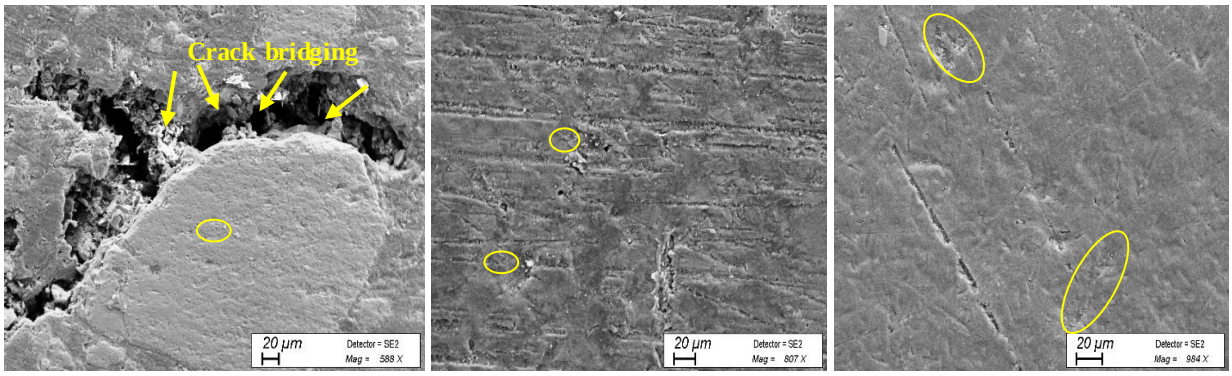

(f)

Fig. 4.1 SEM images of (a) NE, (b) CNF-0.5. CNF-1.0 and CNF-1.5 (from left to right), (c) Silica-0.5, Silica-1.0 and Silica-1.5, (d) Cellulose-0.5, Cellulose-1.0 and Cellulose-1.5, (e) Clay-0.5, Clay-1.0 and Clay-1.5 and (f) Graphite-0.5, Graphite-1.0 and Graphite-1.5.

4.2.1.1 SEM analysis

As shown in Fig. 4.1, as the nanoparticles' wt.% within the matrix increases, a noteworthy phenomenon comes to light; the progressive agglomeration of nanoparticles across the matrix. This agglomeration, the clumping together of nanoparticles, becomes more pronounced at higher concentrations due to the enhanced likelihood of nanoparticle collisions and interactions. As nanoparticles draw closer in proximity, attractive forces, such as van der Waals interactions (more in the carbon-based materials), can lead to their aggregation, forming larger clusters. Moreover, as the concentration increases, there's a higher likelihood of nanoparticle agglomeration due to the increased number of nanoparticles trying to occupy the same space.

This agglomeration has far-reaching consequences on the materials' (i.e. nanocomposites) structural integrity and porosity, as discussed in detail in the next section. The clustered nanoparticles introduce localised regions of increased particle density, altering the distribution of void spaces. These regions of heightened nanoparticle concentration can disrupt the uniformity of polymer chain interlocking during curing, rendering certain areas more susceptible to void formation. Consequently, the increase

in nanoparticle agglomeration with rising concentrations serves as a crucial factor in shaping the observed linear relationship between concentration and % porosity. The intricate interplay between aggregation dynamics, curing kinetics and polymer mobility underscores the multifaceted nature of nanoparticle-polymer interactions and their intricate impact on material porosity profiles.

4.2.1.2 Porosity analysis

First, it's worthy to note that porosity refers to the presence of empty spaces (i.e. air voids) within a material. In this study, % porosity in terms of the samples' surface area were considered, which typically refers to the percentage of the air voids present on the external surface of a sample relative to its total surface area. It's noteworthy that the previous definition of the porosity may appear unconventional, however, it has been chosen to emphasise the examination of voids specifically on the external surface, aligning with our research focus on surface properties and adhesion.

In this section, a detailed assessment of porosity within the nanocomposite systems has been conducted, examining the % porosity increases in comparison to the NE for both carbon-based and silicon-based nanocomposites. Additionally, comprehensive performance comparisons are provided between the two nanocomposite families and within each family is provided and the influence of nanoparticle modifications on porosity was quantified, as presented in Table 4.1, while offering further insights to enhance understanding of porosity changes within these materials.

4.2.1.2.1 Comparison between NE and NMEAs

It was observed that the NE had lower porosity than those of the NMEAs. The shorter mixing time of the NE could be amongst the reasons behind "catching" less amount of air voids (i.e. less % porosity) than in the case of the NMEAs.

For the NMEAs, as shown in Fig. 3 and Table 4, air bubbles showed up on the surface of all samples, but unevenly, where more air bubbles showed in some samples than others. This difference was attributed to differences in the curing conditions, specifically, curing time, where the % porosity is inversely proportional to curing time. Longer curing times allow more air bubbles to escape, resulting in less porosity. In other words, if a polymer is not fully cured within a specified time, it might retain some degree of mobility among its polymer chains. This mobility could allow trapped air or volatiles to escape during the curing process, leading to reduced porosity. As the curing time increases, the polymer chains become more cross-linked, reducing the potential for trapped voids, and vice versa.

Furthermore, the integration of diverse nanomaterials into epoxy polymer matrices introduces a sophisticated interplay of factors that intricately shape material porosity. Each nanomaterial type, distinguished by its SSA, density and wt.% concentration, contributes distinctly to the observed variations in porosity, underlining the intricacies of nanoparticle-polymer interactions.

Nanomaterials characterised by higher SSA, such as graphite and silica Nano powders, offer an abundance of reactive sites, engendering nucleation sites for void generation during curing. This characteristic inclination is palpably reflected in the observed increase in porosity with ascending concentration levels. Conversely, nanomaterials with a relatively lower SSA, such as CNCs and CNF, exhibit a nuanced interplay of effects encompassing aggregation and concentration. While limited nucleation sites are intrinsic due to their lower SSA, the emergence of concentration-driven aggregation and the consequential modifications in curing kinetics potentially account for the observed fluctuations in porosity.

The distinctive SSA of Nano clay begets an intricate correlation between porosity and concentration, marked by an intriguing increase in porosity with elevated concentrations. While its higher SSA initially suggests an ample platform for nucleation, the observed rise in porosity at higher concentrations reveals a complex interplay of factors that override the straightforward association between SSA and porosity. This phenomenon of increased porosity challenges the conventional expectation of porosity reduction with higher SSA and demonstrates the dominance of concentration-dependent influences. These may encompass aggregation dynamics, intricate mechanistic nuances and interactions with the polymer matrix. Similarly, graphite Nano powder, exhibiting a relatively moderate SSA, showcases nuanced behaviour with fluctuations in porosity at varying concentrations. These thought-provoking observations collectively underscore the multifaceted nature of nanoparticle-polymer interactions, where factors beyond SSA, including concentration-dependent effects, wield substantial influence over the material's porosity profile.

The intriguing relationship between nanoparticle concentration and porosity manifests as a complex interplay of diverse mechanisms. As the concentration of nanoparticles within the epoxy polymer matrix increases, several contributing factors converge to promote heightened % porosity. Firstly, an elevated nanoparticle concentration fosters a denser nanoparticle packing, thereby leading to increased obstacles for polymer chain mobility during curing. This phenomenon impedes the creation of an ideal, tightly knit network structure and paves the way for the formation of voids. These voids result from the inability of the polymer chains to uniformly interlock due to the presence of closely spaced nanoparticles. Consequently, the aggregation of nanoparticles amplifies the likelihood of forming regions of low-density material, culminating in the observed higher porosity.

Furthermore, the augmented concentration of nanoparticles engenders a greater concentration of potential nucleation sites for void formation. These nucleation sites originate from the nanoparticles' surfaces, which offer reactive sites for the initiation of voids during the curing process. As the nanoparticle concentration increases, the density of these initiation points surges, facilitating the

generation of voids upon curing. This interaction is accentuated by nanoparticles with higher SSA's, such as graphite and silica Nano powder, which provide a surplus of active sites for nucleation. Consequently, the combined influence of hindered polymer chain mobility and a heightened density of nucleation sites synergistically fosters an environment conducive to greater porosity.

Moreover, it was observed, as shown in Table 4.1, that the increase in the NMEAs porosity is more pronounced when moving from 0.5 to 1.0 wt.% concentrations (i.e. 100% concentration increase) than in the case of 50% further increase in the concentration (i.e. from 1.0 to 1.5 wt.%). This was attributed to that, since the particles agglomerations and clustering increase with the concentration, when nanoparticles cluster together, forming groups or agglomerations, they tend to occupy certain areas within the material more densely compared to other regions. These dense regions with a higher concentration of nanoparticles are what we refer to as "regions of concentrated nanoparticles". Now, these agglomerations of nanoparticles don't fit perfectly within the material's structure, and they can create irregularities or gaps between them and the surrounding matrix.

Therefore, these two effects — the concentration of nanoparticles in certain areas and the formation of voids due to agglomeration — work together to influence the overall structure of the material. When there are areas with concentrated nanoparticles and voids, the material's overall arrangement becomes less uniform. This lack of uniformity disrupts the optimal arrangement of polymer chains and nanoparticles that is necessary for minimising porosity.

In summary, the specific attributes of each nanoparticle type, including the SSA and density, synergistically interact with their concentration to exert a profound influence on the observed % porosity in NMEA samples. The linear correlation between concentration and porosity highlights the essential role of considering a comprehensive array of factors that extend beyond concentration alone. Among these pivotal factors are nanoparticle behaviour, intricate interactions and the intricacies of curing kinetics. The harmonious interplay of these elements serves to precisely delineate the distinctive contribution of each nanoparticle type and its concentration to the overall porosity observed within the NMEA samples.

4.2.1.2.2 Comparison between the different NMEAs

First, in the context of the carbon-based nanocomposites — CNF, cellulose and graphite — a non-consistent trend in porosity changes, with the wt.%, compared to the NE was observed. As the nanoparticle concentration increased from 0.5 to 1.0 wt.%, the order of porosity increases consistently followed "CNF < cellulose < graphite". However, when the concentration was further elevated from 1.0 to 1.5 wt.%, the order shifted to "CNF < graphite < cellulose", as shown in Table 4.1.

The observed variations in porosity increases among the nanocomposites stem from a multifaceted interplay of critical factors. These include the distinctive attributes of nanoparticle size, shape, SSA, agglomeration behaviour and concentration effects, which collectively influence their performance within the epoxy matrix.

Nanoparticle size plays a pivotal role in determining their efficacy in reducing porosity. CNF, despite exhibiting a wide size range, possesses a notable length advantage, which allows it to effectively bridge and fill voids within the epoxy matrix. On the other hand, cellulose, with its smaller width and shorter length, offers a lower SSA (~ 14 m^2/g) but may compensate through increased opportunities for interaction with the epoxy, potentially leading to superior dispersion and porosity reduction. Meanwhile, graphite nanoparticles, with their diminutive size, may face challenges related to agglomeration, impeding their ability to uniformly fill voids and reducing their overall effectiveness in porosity reduction.

Interestingly, the changing order of porosity increase from 0.5 to 1.0 wt.% and 1.0 to 1.5 wt.% concentrations suggests a nuanced relationship between nanoparticle concentration and porosity reduction. At lower concentrations (0.5 to 1.0 wt.%), CNF, with its remarkable aspect ratio and length, might dominate in porosity reduction. However, as the concentration increases further (1.0 to 1.5 wt.%), the smaller graphite particles may become more effective, potentially overcoming their initial limitations. This phenomenon underscores the importance of considering concentration-dependent saturation effects in nanocomposite design.

Furthermore, the unique characteristics inherent to each nanoparticle type significantly impact their performance within the epoxy matrix. Variability in factors such as dispersion, distribution and chemical interactions introduces sample-to-sample differences, which can influence the observed results.

Second, in the realm of silicon-based nanocomposites, encompassing silica and clay nanoparticles, a persistent order of % porosity increase (clay >> silica) when compared to the NE comes to the forefront. This order remains consistent across varying wt.% concentrations, notably from 0.5 to 1.0 wt.% and from 1.0 to 1.5 wt.%.

These observations can be explained by examining the distinct material properties of clay and silica and considering several key factors. For instance, the SSA of the silicon-based nanoparticles emerging as a pivotal element. Silica nanoparticles, boasting an SSA ranging from 150 to 550 m^2/g, and clay particles, with a maximum SSA of 450 m^2/g, showcase differences in their potential for interaction with the epoxy matrix. The higher SSA of silica grants it an augmented number of interaction sites with the epoxy, enabling superior dispersion and enhanced porosity reduction. In

contrast, although clay nanoparticles exhibit a respectable SSA, their larger size may limit their effectiveness in uniformly filling voids and reducing porosity.

Nanoparticle size remains a critical determinant in shaping their performance within the epoxy matrix. Silica, characterised by an average size of 16 nm, significantly outpaces clay, which has a larger average size of 800 nm. This substantial size difference underscores silica's adeptness at penetrating and effectively filling gaps within the epoxy matrix, resulting in a pronounced reduction in porosity.

Agglomeration tendencies further influence porosity reduction. Smaller silica nanoparticles exhibit a lower propensity for agglomeration, ensuring a more uniform dispersion within the epoxy matrix. Conversely, clay nanoparticles, due to their larger size, may encounter more pronounced agglomeration, compromising their ability to uniformly fill voids and thus reducing their overall effectiveness in porosity reduction.

The unwavering order of porosity increase across different concentration ranges signifies the robustness of this phenomenon. This consistency underscores the need to consider concentration-independent factors, such as particle size, SSA and agglomeration behaviour, as the primary drivers behind the observed trend.

Finally, in comparing the carbon-based and silicon-based nanocomposites, a notable difference emerges in their porosity changes relative to the NE. The carbon-based nanocomposites exhibited a varying order of % porosity increase with changing concentrations. In contrast, the silicon-based nanocomposites consistently maintained the order of % porosity increase across different concentration increases. This distinction underscores the complexity and variability inherent in carbon-based nanocomposite systems, while the silicon-based counterparts demonstrated a more consistent and predictable behaviour in porosity increase.

Therefore, to gain a more comprehensive understanding of these intricate interactions and further optimise nanocomposite materials, additional experimental studies and computational modelling efforts are warranted. These endeavours will enable a deeper exploration of the dynamic relationships between nanoparticle properties, concentration and their effects on porosity reduction, ultimately contributing to the refinement of nanocomposite design and engineering.

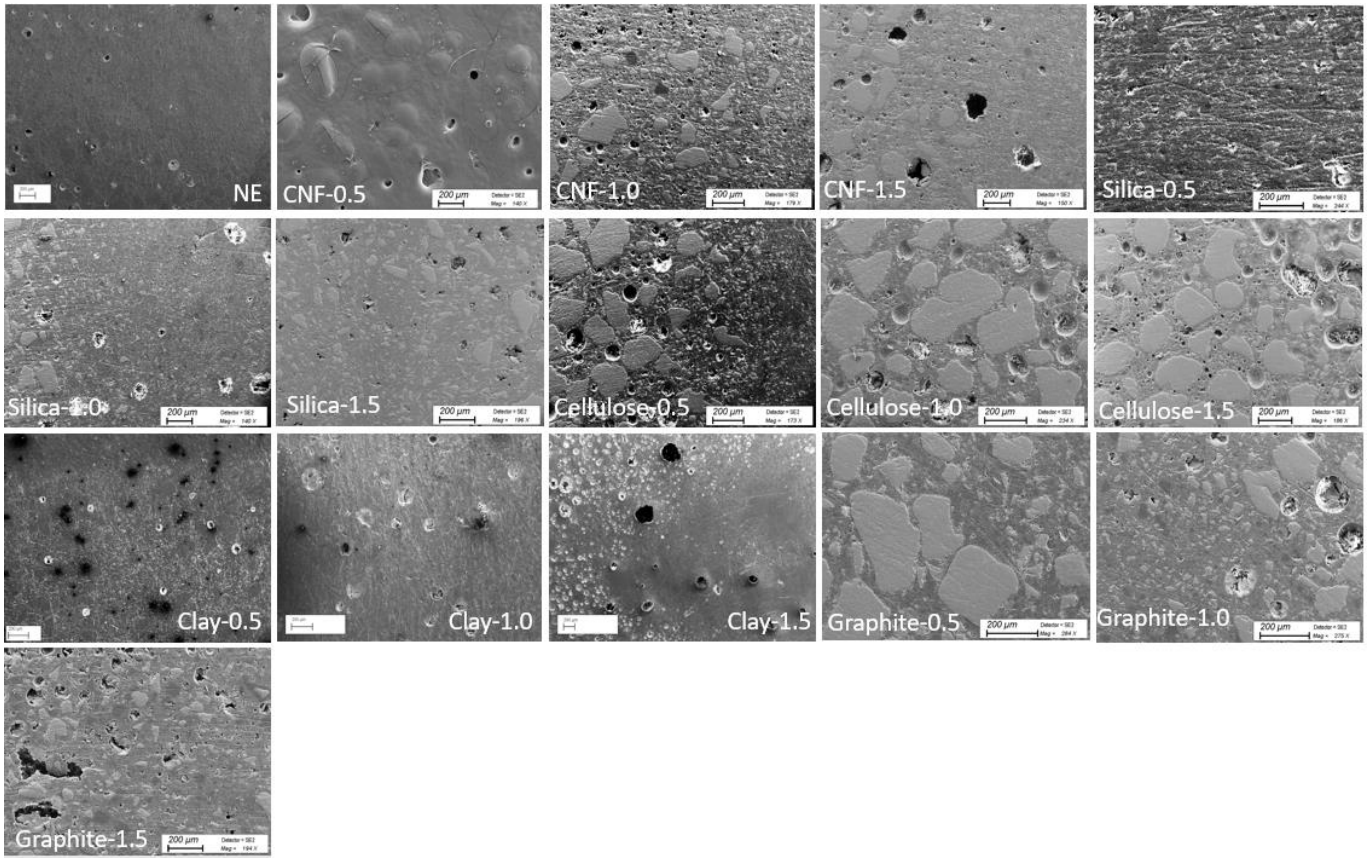

Fig. 4.2 SEM images of surfaces of the NE and the NMEAs samples.

Table 4.1 % Porosity of the NE and the NMEAs.

Nanocomposite	Sample	% Porosity	% Porosity increase of the NMEAs compared to the NE	% Porosity increase of the NMEAs with the wt.% increase	
				From 0.5 to 1.0 wt.%	From 1.0 to 1.5 wt.%
	NE	2.015	-	-	
CNF	CNF-0.5	2.501	24.1	7.0	4.6
	CNF-1.0	2.676	32.8		
	CNF-1.5	2.800	39.0		
Silica	Silica-0.5	2.630	30.5	2.9	2.7
	Silica-1.0	2.734	35.7		
	Silica-1.5	2.807	39.3		
Cellulose	Cellulose-0.5	2.945	46.2	11.8	8.5
	Cellulose-1.0	3.292	63.4		
	Cellulose-1.5	3.571	77.2		
Clay	Clay-0.5	2.225	10.4	21.2	15.0
	Clay-1.0	2.697	33.8		
	Clay-1.5	3.101	53.9		
Graphite	Graphite-0.5	2.395	18.9	12.4	6.1
	Graphite-1.0	2.693	33.6		
	Graphite-1.5	2.856	41.7		

4.2.2 Crystallinity analysis

The % crystallinity of the NE and the NMEAs samples is provided in Table 4.2. It was observed that all NMEAs, regardless of the nanomaterial type or their wt.%, had lower % crystallinity than that of the NE.

For the CNF nanocomposites, the crystallinity reduction, which disagrees with what was found by Mahmood et al. [125], can be attributed to the influence of CNF on the behaviour of the epoxy matrix. Specifically, the presence of CNF can create a physical barrier that hampers the movement of epoxy chains, thereby diminishing their capacity to organise themselves into well-structured arrangements. Consequently, the polymer chains encounter limitations in their ability to achieve the necessary regular alignment for the development of crystalline domains. Furthermore, the process of crystallisation hinges on the availability of specific sites where crystals can initiate and grow. The incorporation of CNF can, in some instances, disrupt the formation of these critical nucleation sites or even impede their development, ultimately leading to a reduction in the overall crystallinity of the

material. Whereas for the cellulose nanocomposites, the crystallinity reduction was ascribed to the strong interaction of the cellulose with the OH groups of the epoxy forming a twisted mass, causing steric effect, which resulted in the destruction of the epoxy-ordered structure, as confirmed by Kumar et al. [126]. Whereas in the case of incorporating the graphite nanoparticles, the crystallinity reduction is ascribed to that, as reported by Bhattacharyya et al. [127], the exfoliated state of graphite, which restricted the free movement of polymer chains to arrange themselves in an orderly fashion, hindering the crystallisation, thus reducing its crystallinity.

For the silicon-based nanocomposites, the crystallinity decrease below that of the NE could be, as observed in [128, 129], due to the fact that adding silica nanoparticles to the polymer decreased the chain orders which in turn disturbed the crystallisation process, which can be an indication of the reduction in crystalline areas of epoxy. Similar interpretation could be drawn in the case of adding clay nanoparticles.

It was also found that the % crystallinity of the NMEAs decreased with the wt.%. This can be due to both nanoparticle agglomerations and increased porosity with the wt.%, which would introduce structural complexities that hinder the establishment of ordered molecular arrangements. These factors contribute to reduced crystallinity by preventing the formation of well-defined and organised crystalline regions within the material.

More specifically, when nanoparticles agglomerate, they create zones of constrained molecular movement, impeding the polymer chains' ability to achieve the necessary alignment for crystalline structures. Furthermore, these agglomerations disrupt the formation of nucleation sites, which are pivotal for initiating the growth of well-defined crystalline regions. The irregularities introduced by these agglomerations hinder the material's capacity to achieve the desired ordered arrangement, resulting in reduced crystallinity. Furthermore, agglomerations or uneven distribution of nanoparticles can create areas of differing polymer density, leading to variations in crystallinity. The interface between the nanoparticles and the epoxy matrix can introduce irregularities in the molecular arrangement. These irregularities can propagate throughout the material, affecting the overall crystalline structure. The stress and strain at the interface can also influence crystallisation behaviour.

The influence of increased porosity on reduced crystallinity in materials is rooted in the intricate interplay between molecular arrangement, density and nucleation sites. Porosity refers to the presence of voids or open spaces within a material's structure, which can arise from incomplete packing of molecules or the inclusion of gas or other substances. This porosity introduces a level of complexity that significantly impacts the material's ability to form and maintain well-defined crystalline regions.

One of the primary mechanisms by which increased porosity contributes to reduced crystallinity is through the disruption of molecular packing. In a crystalline material, polymer chains ideally arrange themselves in an organised and tightly packed manner. However, the presence of voids and gaps hinders the optimal arrangement of these chains, preventing them from achieving the required alignment for crystalline growth. As a result, the material experiences decreased crystallinity because the irregular void-filled regions prevent the propagation of ordered structures.

Furthermore, the presence of porosity limits the availability of suitable nucleation sites. Nucleation sites are specific locations within a material where the initiation of crystalline growth occurs. In porous materials, the irregular surfaces of voids and pores do not possess the necessary characteristics for effective nucleation. This deficiency in proper nucleation sites disrupts the crystallisation process, as the growth of crystals necessitates organised starting points. Without adequate nucleation sites, the material's ability to develop well-structured crystalline regions becomes compromised.

In essence, increased porosity acts as a barrier to both molecular alignment and nucleation site availability, culminating in a reduction of crystallinity. The irregularities introduced by the presence of voids and gaps prevent the formation of the orderly arrangements essential for crystalline growth. As a result, materials with heightened porosity exhibit diminished crystallinity due to the challenges posed to the establishment of well-defined, organised molecular structures.

It's noteworthy that, consistent with what was revealed in the case of porosity change with the concentration, the crystallinity of the nanocomposites showed higher decrease when doubling the concentration (i.e. from 0.5 to 1.0 wt.%) compared to when the concentration was further increased by an additional 50%. This was due to, as discussed previously, the relationship between porosity and crystallinity.

Table 4.2 % Crystallinity of the NE and the NMEAs.

Sample	% Crystallinity	% Crystallinity decrease of the NMEAs compared to the NE
NE	65	-
CNF-0.5	43.8	32.6
CNF-1.0	42.5	34.6
CNF-1.5	41.5	36.2
Silica-0.5	50.4	22.5
Silica-1.0	48.0	26.2
Silica-1.5	47.0	27.7
Cellulose-0.5	52.1	19.8
Cellulose-1.0	48.9	24.8
Cellulose-1.5	46.7	28.2
Clay-0.5	54.9	15.5
Clay-1.0	51.2	21.2
Clay-1.5	48.9	24.8
Graphite-0.5	54.7	15.8
Graphite-1.0	49.3	24.2
Graphite-1.5	45.7	29.7

4.2.3 ATR-FTIR spectroscopy

FTIR analysis was performed to assess the intensities of functional groups in both the NE and the carbon-based NMEAs. The study examines the intensity orders of various functional groups and their corresponding wavenumbers. The comparison helps assess the chemical changes brought about by the incorporation of nanoparticles to the epoxy resin. The order of intensities is used to evaluate changes in the composition. The analysis is presented for the carbon-based NMEAs. New peaks and disappearing peaks in the NMEAs compared to the nanoparticles and epoxy are also discussed. Changes in functional groups and their appearance or disappearance indicate interactions between the nanoparticles and the epoxy matrix. This section provides detailed information on intensity changes, wavenumbers and specific functional groups affected in each nanocomposite.

The intensity order of the functional groups and their corresponding wavenumbers that showed in NE and the carbon-based NMEAs samples is listed in Table 4.3 and it is used as a base to assess the chemical changes. Also, Fig. 4.3 shows the FTIR spectrum of those samples. It's noteworthy that the numbers 0.5, 1.0 and 1.5 in Table 4.3 indicate the carbon-based NMEAs samples with 0.5, 1.0 and 1.5 wt.% concentration of nanoparticles, respectively. Moreover, the intensity order, for instance,

NE<0.5<1.0<1.5 indicates that the intensity of a bond is the minimum in the NE sample, higher in the samples prepared with 0.5 wt.% followed by that made with 1.0 wt.% sample and the highest in the 1.5 wt.% one.

Table 4.3 The intensity order of the functional groups that showed in the NE and the carbon-based NMEAs.

NMEAs	**Wavenumber (cm^{-1})**	**Functional group(s)**	**Order of intensity (lower to higher)**
CNF			
	3318	N–H bending vibration / N-H stretching	NE<0.5<1.0<1.5
	2921.8	CH stretching	NE<0.5<1.0<1.5
	2851	CH stretching	NE<0.5<1.0<1.5
	1605.7	C=C stretching	NE<0.5<1.0<1.5
	1581	C-C stretching	NE<0.5<1.0<1.5
	1413.1	CH_3 sym. bending vim/ asym CH_3 def. vib	NE<1.0<0.5<1.5
	1295.8	asym -CH_2 deformation	NE<0.5<1.0<1.5
	1237.6	asym aromatic C-O stretch	NE<0.5<1.0<1.5
	1028.6	= C-O-C (sym. C-O str.)	NE<1.5<0.5<1.0
Cellulose			
	3318	N–H bending vibration / N-H stretching	NE<0.5<1.0<1.5
	2921.8	CH stretching	1.0<NE<0.5<1.5
	2851.8	CH stretching	1.0<NE<0.5<1.5
	2502	-OH str./ O-H str.	1.0<1.5<0.5<NE
	1605.7	C=C stretching	NE<0.5<1.0<1.5
	1582	C-C stretching	NE<0.5<1.5<1.0
	1413.1	CH_3 sym. bending vib/ asym. CH_3 def. vib	1.0<1.5<0.5<NE
	1295.6	asym -CH_2 deformation	1.5<1.0<0.5<NE
	1237	asym aromatic C-O stretch	1.0<0.5<NE<1.5
	1180.3	acyclic diaryl ethers, =C-O-C=	NE<0.5<1.0<1.5
	1077.2	C-O-C str./ C-H bonds	NE<0.5<1.0<1.5
	1032.2	= C-O-C (sym. C-O str.)	NE<0.5<1.0<1.5
Graphite			
	3305.7	O–H str	NE<0.5<1.0<1.5
	2921.8	Asym. C-H stretching	NE<0.5<1.5<1.0

	2851.8	Sym. C-H stretching	NE<0.5<1.5<1.0
	1605.7	C=C stretching	NE<0.5<1.5<1.0
	1581	C-C stretching	NE<0.5<1.0<1.5
	1429.5	CH_2 del' vib/ sym. CO_2 – str./ asym. CH_3 def. vib	1.5<NE<0.5<1.0
	1298.4	asym -CH_2 deformation	1.5<NE<0.5<1.0
	1241	C–OH str	1.5<0.5<NE<1.0
	1179.8	acyclic diaryl ethers, =C-O-C=	1.0<NE<0.5<1.5
	1081.3	C-O-C str.	1.0<NE<0.5<1.5
	1035.8	= C-O-C (sym. C-O str.)	NE<0.5<1.0<1.5

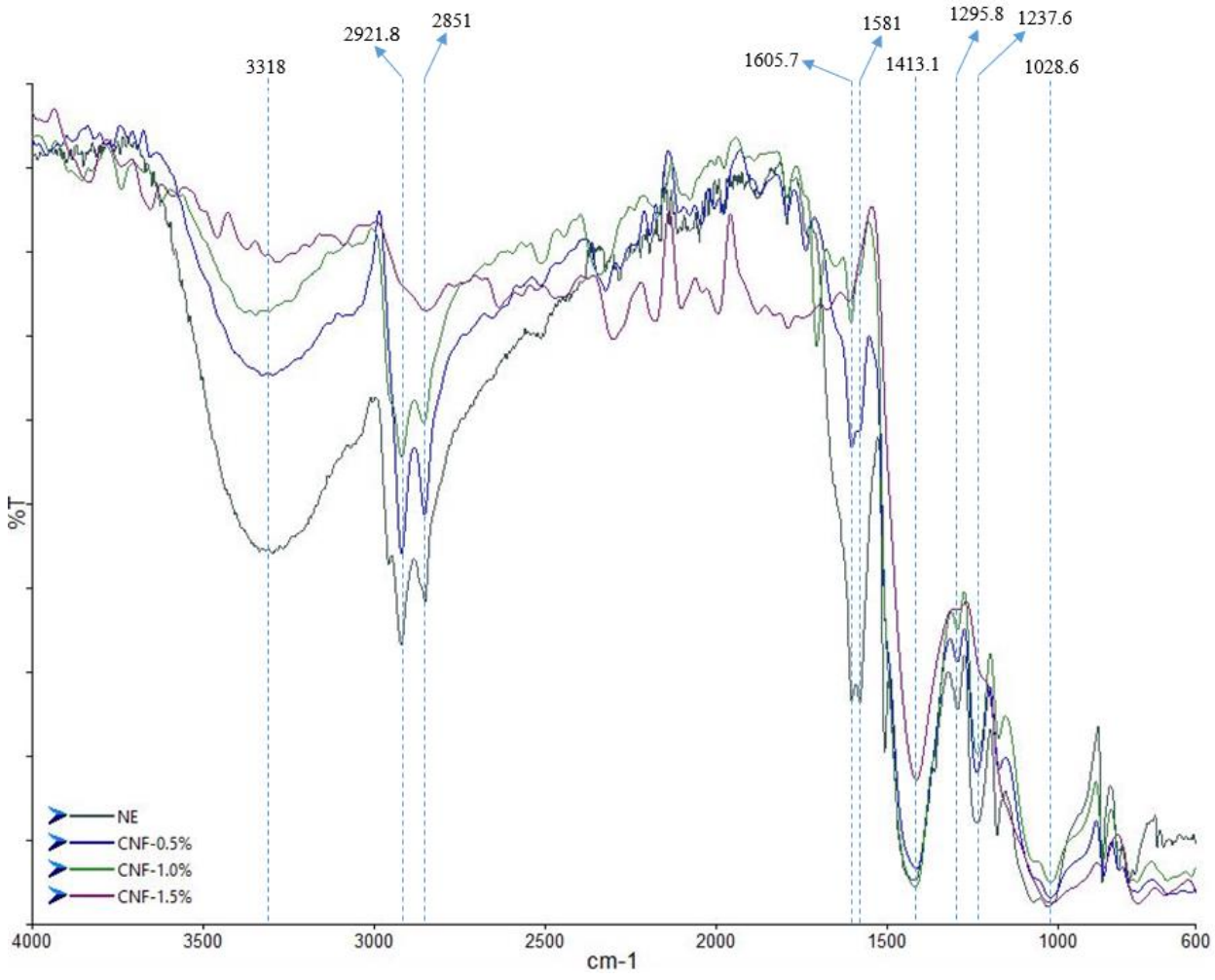

(a)

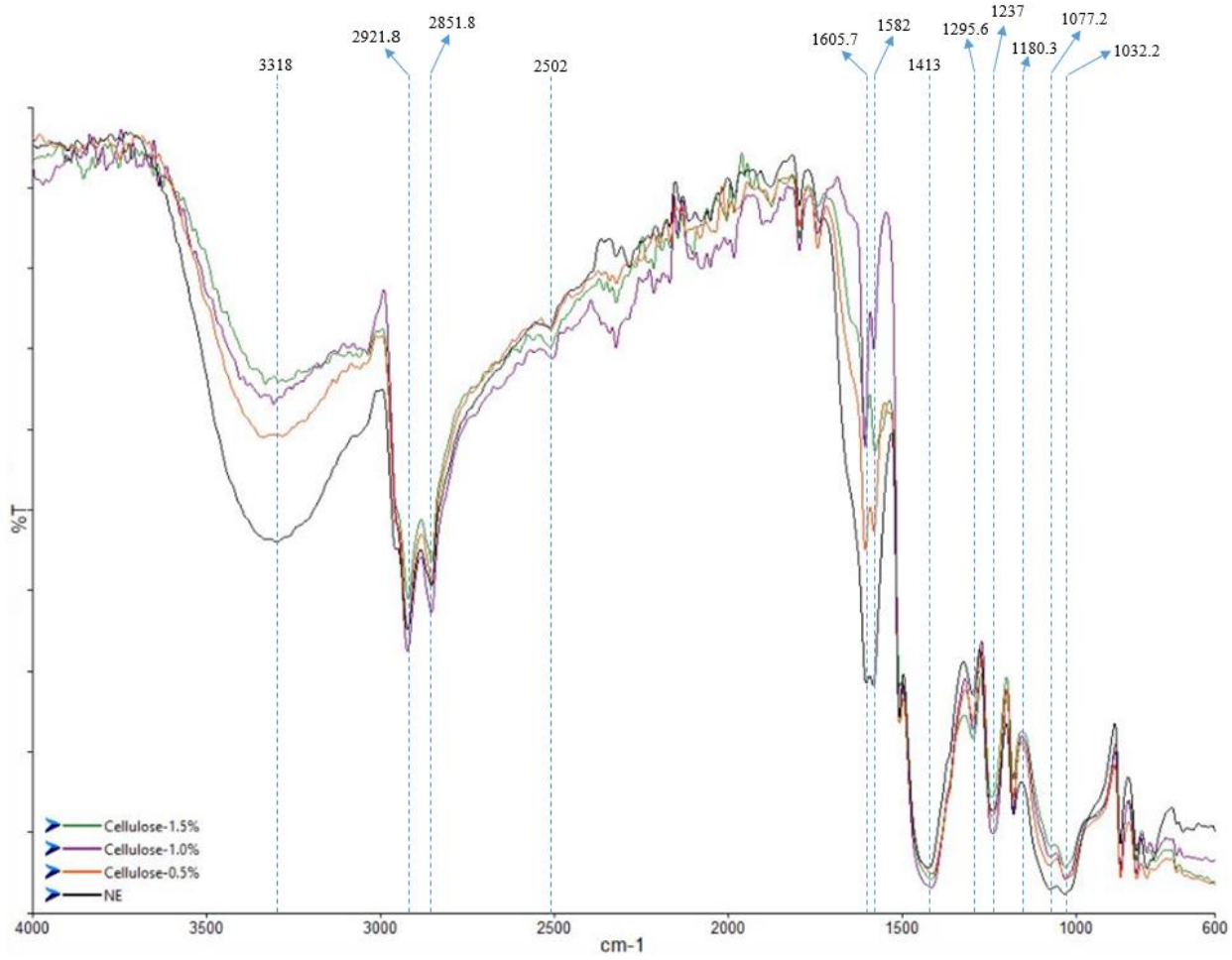
3318
2921.8
2851.8
2502
1605.7
1582
1413
1295.6
1237
1180.3
1077.2
1032.2
%T
Cellulose-1.5%
Cellulose-1.0%
Cellulose-0.5%
NE
4000
3500
3000
2500
2000
1500
1000
600
cm-1

(b)

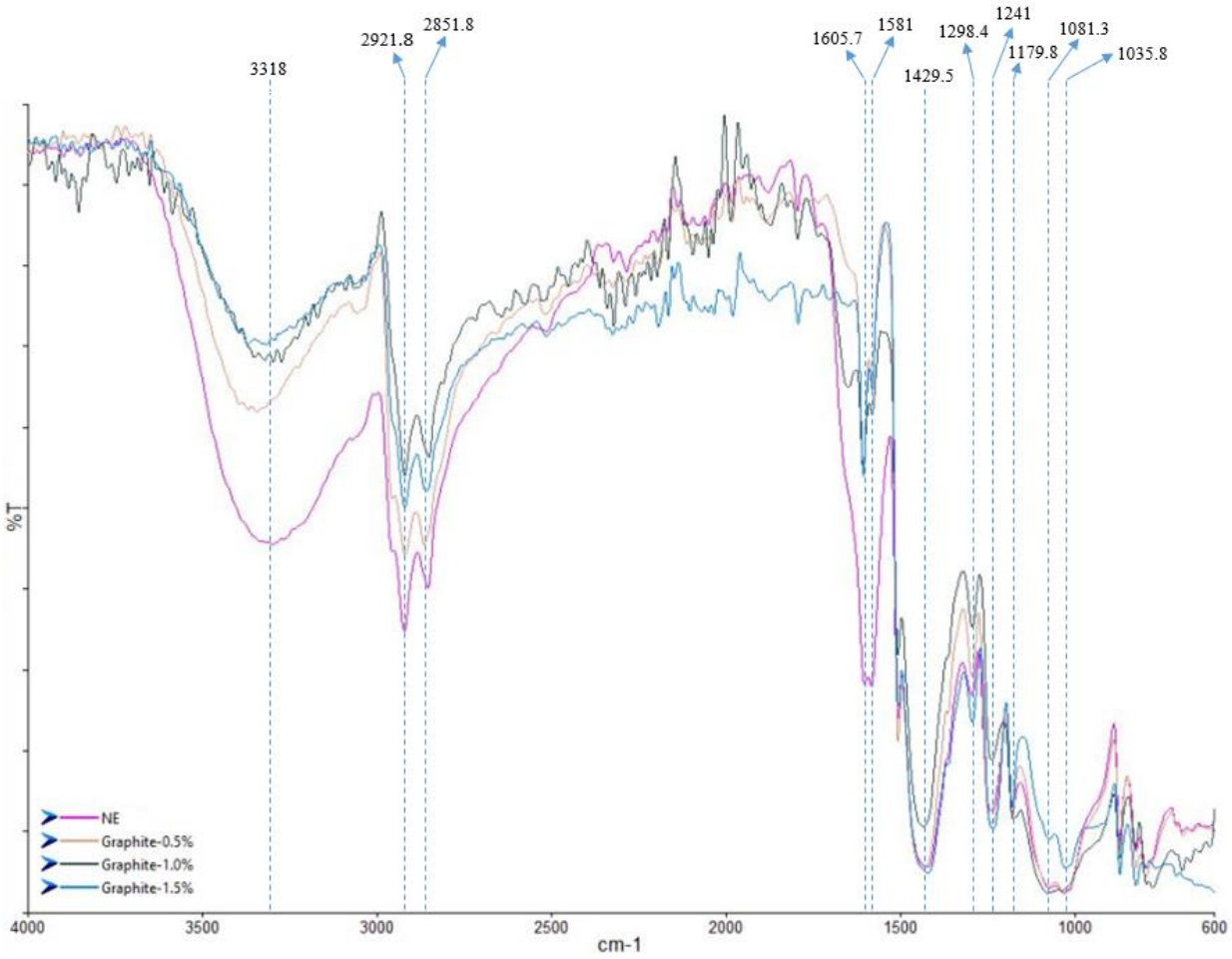

(c)

Fig. 4.3 FTIR spectrum showing the differences in the intensity orders of the functional groups of (a) NE and CNF nanocomposites, (b) NE and cellulose nanocomposites and (c) NE and graphite nanocomposites

As shown in Table 4.3 and Fig. 4.3, the intensity of the N-H bending vibration in all nanocomposite was higher than in the NE sample. Moreover, it was observed that it increased with the wt.% of the nanoparticles. Similarly, C-C stretching was also found to have the same behaviour in the CNF and cellulose samples at 1605.7 cm^{-1}, and in graphite sample at 1581 cm^{-1}. The -CH_2- (acyclic)/ CH stretching, which corresponds to 2921.8 and 2851 cm^{-1} and the asym. -CH_2 deformation at 1295.8 cm^{-1} also show the same trend in the CNF samples. Moreover, the same observation was found for the C-C stretching at 1581 cm^{-1} and the asym. aromatic C-O stretch at 1237.6 cm^{-1}, but the former (i.e. C-C stretching at 1581 cm^{-1}) disappeared in the samples CNF-1.0 and CNF-1.5, which also did not have the latter functional group. The same order was also noticed in the cellulose samples for the functional groups acyclic diaryl ethers, =C-O-C= at 1180.3 cm^{-1}, C-O-C str./C-H bonds at 1077.2 cm^{-1} and =C-O-C (sym. C-O str.) at 1032.2 cm^{-1}, which also followed the same order in the graphite sample, but at 1035.8 cm^{-1}.

On the other hand, it was observed that the intensity orders in some of the nanocomposites are not proportional to the wt.% concentration of the nanomaterials. For example, in the cellulose samples the intensity order (i.e. NE<0.5<1.5<1.0) showed for the C-C stretching at 1582 cm^{-1}, and in the graphite samples for the -CH_2- (acyclic)/ CH stretching at 2921.8 and 2851.8 cm^{-1} and the C-C stretching at 1605.7 cm^{-1}.

Other intensity orders were observed to show in only one nanocomposite. For example, the order NE<1.0<0.5<1.5 and the order NE<1.5<0.5<1.0 appeared in the functional groups CH_3 sym. bending vib/ asym. CH_3 def. vib at 1413.1 cm^{-1} and in the =C-O-C (sym. C-O str.) at 1028.6 cm^{-1}, respectively.

In cellulose samples, the intensity order 1.0<1.5<0.5<NE was found to be followed for the functional groups -OH str./ O-H str. at 2502 cm^{-1} and for the CH_3 sym. bending vib/ asym. CH_3 def. vib at 1413.1 cm^{-1}. While the functional group -CH_2- (acyclic)/ CH stretching at 2921.8 and 2851.8 cm^{-1} was found to follow the order 1.0<NE<0.5<1.5. and finally, the groups asym. -Ch_2 deformation at 1295.6 cm^{-1} and asym. aromatic C-O stretch at 1237 cm^{-1} were found in the order 1.5<1.0<0.5<NE and 1.0<0.5<NE<1.5, respectively.

The order 1.5<NE<0.5<1.0 showed, in the graphite samples, was followed by the CH_2 del' vib/ sym. CO_2 – str./ asym. CH_3 def. vib at 1429.5 cm^{-1} and the asym. -CH_2 deformation at 1298.4 cm^{-1}. In the same samples, the functional groups acyclic diaryl ethers, =C-O-C= at 1179.8 cm^{-1} and C-O-C str./ C-H bonds at 1081.3 cm^{-1} followed the intensity order 1.0<NE<0.5<1.5.

In addition to the changes shown in the intensity of some chemical bonds, further changes in the chemical composition of the raw materials, e.g. epoxy matrix and the pristine nanomaterials, were observed. Where new functional groups appeared in the NMEAs, that were not there in the raw materials, and others disappeared from the raw materials as a result of the interaction between the nanoparticles and the epoxy matrix.

It was observed that all the carbon-based NMEAs showed disappearance of the C=C bond, which appeared at about 1632 cm^{-1}, 1639 cm^{-1} and 1632 cm^{-1}, in the spectrum of the nanoparticles, respectively, which was also observed in [113, 114] for GO nanoparticles at 1631 cm^{-1}, and its presence was also confirmed in cellulose nanofibres at 1640 cm^{-1} [139]. Furthermore, it was observed that CNF-1.5 showed disappearance of the NH_2 group /aromatic C=C str. at 1508 cm^{-1}, which was confirmed that they are there in epoxy at that wavenumber [115, 116].

For cellulose nanocomposites, the O-H stretching vibration of the OH groups at about 3417 cm^{-1} and C-H stretching vibration at about 2901 cm^{-1}, which where there in the nanoparticles, which were also noticed in [116] between 3500 and 3000 cm^{-1} and 2901 cm^{-1}, respectively, disappeared in all the

cellulose NMEAs samples. Moreover, in agreement with [116, 117], bands at 1112, 1059 and 898 cm^{-1}, assigned to C-O stretching and the glycosidic linkages were observed in the cellulose nanoparticles, which are characteristic of the cellulose structure, also disappeared in the NMEAs samples.

However, no new peaks were observed as a result of incorporating the carbon-based materials with epoxy except in the case of the sample CNF-1.0, as the presence of the carboxyl groups on CNF was confirmed by the appearance of the stretching vibration of C=O at 1710 cm^{-1}, which suggested the formation of amides as a result of the reaction between C=O in CNF with amine in the epoxy hardener. It's noteworthy that FTIR studies showed no indication of chemical interaction between CNF and epoxy matrix, concluding that the immobilisation of epoxy monomer on CNF is purely by physical interaction, as confirmed in [116].

For the silicon-based NMEAs samples (i.e. silica and clay samples), no any change (i.e. appearance and/or disappearance) of the chemical bonds took place in silica samples. While in the case of the clay samples, some functional groups disappeared from both epoxy and nanoparticle. For example, in agreement with [118, 119, 120-122], some of the peaks showed in the clay nanoparticles such as –OH stretching at 3627 cm^{-1}, -OH stretching, hydration at 3445 cm^{-1}, OH bending, hydration at 1636 cm^{-1}, can be attributed to adsorbed water molecules, and Al-Al-OH bending at 914 cm^{-1} or it is related to Si-O bond and Al-Fe-OH bending at 848 cm^{-1}. All those peaks disappeared in the clay NMEAs. In addition, the peak that was observed at 3305 cm^{-1} for N–H bending vibration/ N-H stretching in the neat epoxy disappeared in the clay NMEAs samples.

4.2.4 Raman spectroscopy

One of the main indicators of the defects present on the structures of the carbon-based materials and those of their nanocomposites is the characteristics of the D- and G-bands and the corresponding I_D/I_G values.

The section introduces Raman spectroscopy as a technique to study defects in carbon-based materials and nanocomposites. It highlights the significance of the D- and G-bands and the I_D/I_G values in assessing structural defects. Raman spectra of the pristine carbon-based nanomaterials (CNF and graphite) and their respective nanocomposites (CNF NMEAs and graphite NMEAs) are presented and discussed. The location of D and G bands, their intensities and the I_D/I_G values are provided for each sample. These parameters offer insights into the quality and defects of the carbon-based nanomaterials and the resulting nanocomposites.

The results of Raman analysis of the NE, CNF and graphite NMEAs are included in this section. Raman spectra of tested samples are shown in Fig. 4.4 and the locations of both D and G-bands, their corresponding intensities in addition to the I_D/I_G values of the pristine CNF and graphite and their NMEAs are listed in Table 4.4.

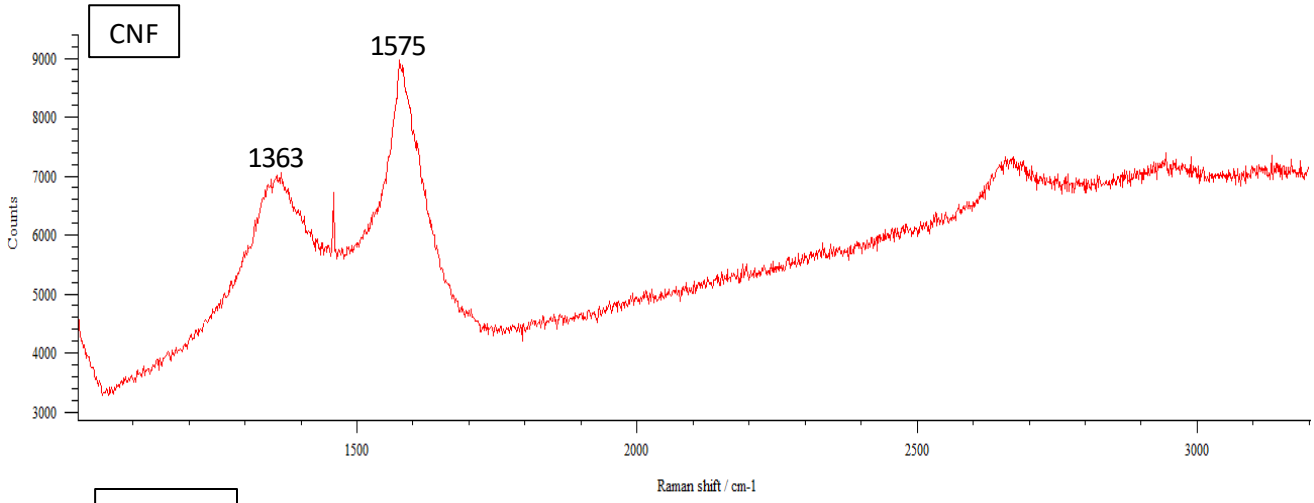
CNF
1575
1363
Counts
Raman shift / cm-1

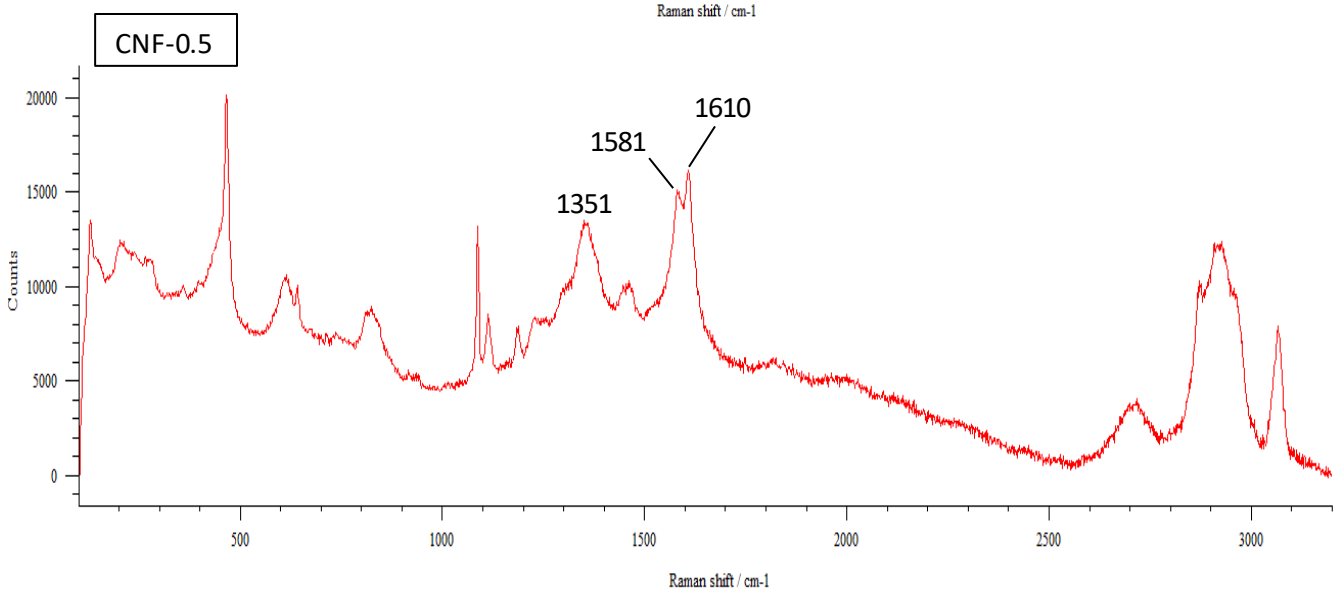
CNF-0.5
1610
1581
1351
Counts
Raman shift / cm-1

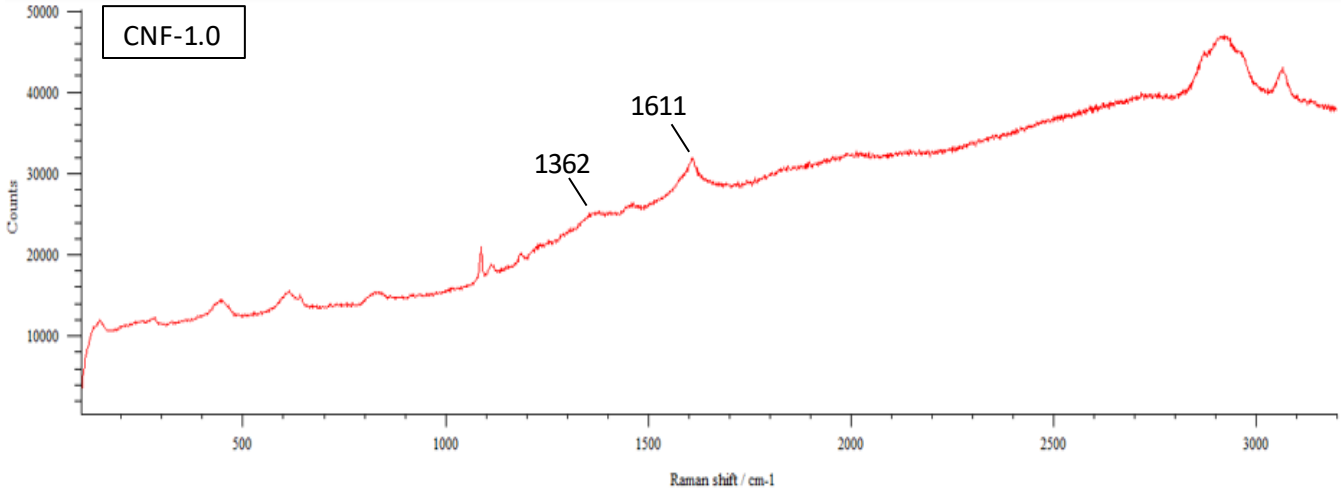
CNF-1.0
1611
1362
Counts
Raman shift / cm-1

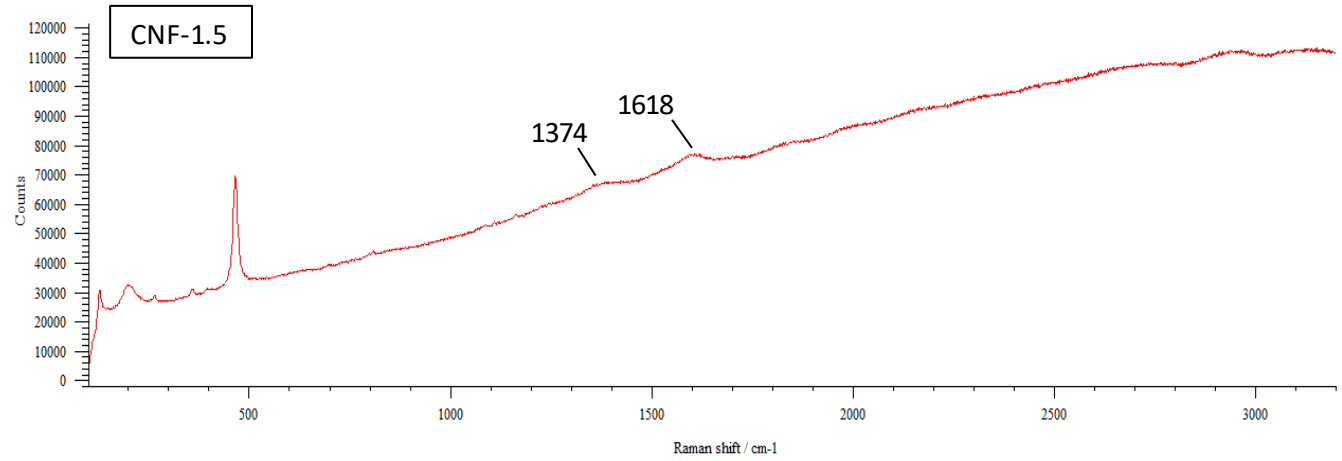
CNF-1.5
1374
1618
Counts
Raman shift / cm-1

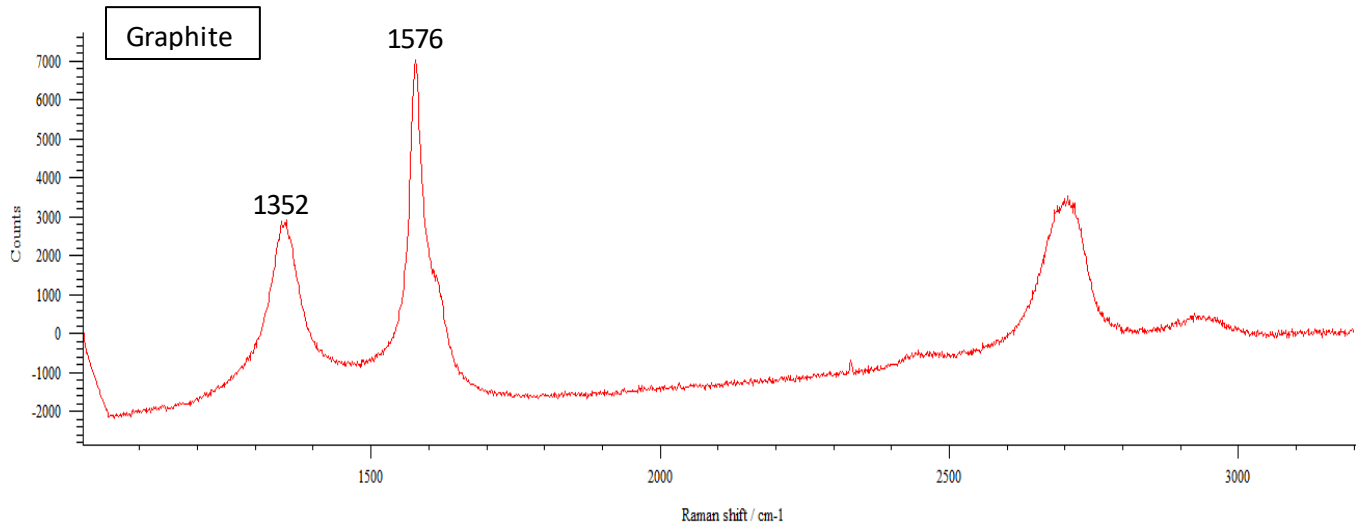
Graphite
1576
1352
Counts
Raman shift / cm-1

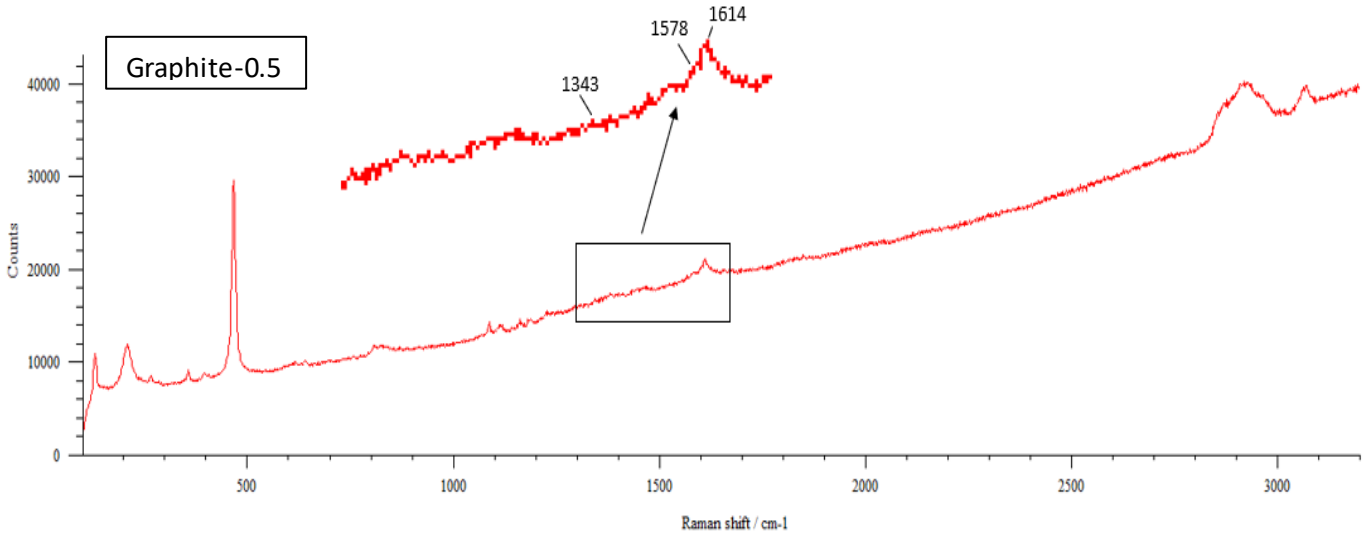
Graphite-0.5
1614
1578
1343
Counts
Raman shift / cm-1

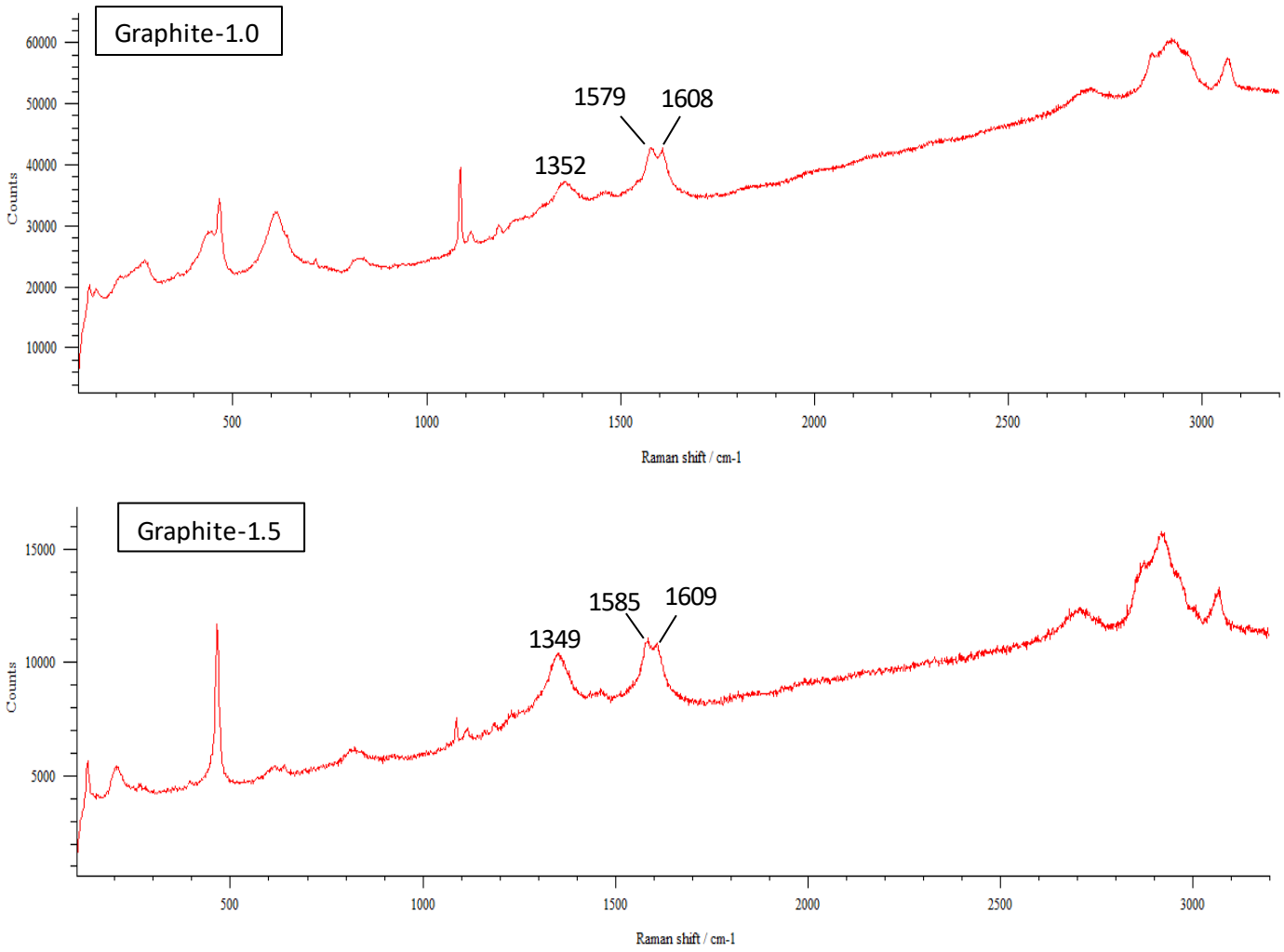

Fig. 4.4 Raman spectra of the pristine carbon-based nanomaterials and their NMEAs.

Table 4.4 Locations and intensities of the D- and G-bands and the corresponding I_D/I_G values of the pristine CNF and graphite and their NMEAs.

Sample	**D-band (location (cm^{-1}) - intensity)**	**G- band (location (cm^{-1}) - intensity)**	**I_D/I_G**
CNF (pristine material)	1363- 7066.96	1575- 8978.22	0.7871
CNF-0.5	1374-13538.5	1579-15136.2	0.8944
CNF-1.0	1362-25111.5	1611-31733.1	0.7913
CNF-1.5	1351-67322.5	1618-77236.1	0.8716
Graphite (pristine material)	1352-2924.27	1576- 7051.46	0.4147
Graphite-0.5	1343 - 16811.4	1578 - 19550.3	0.8599
Graphite-1.0	1352-37270.4	1579-42802.2	0.8708
Graphite1.5	1349-10447.7	1585-11072.9	0.9435

As shown in Table 4.4, the D-band values of the CNF NMEAs samples followed the order 0.5>1.0>1.5, which agrees with that of the crystallinity values of those samples. This was attributed to that the D peak associated with nano-crystalline carbon. The same observation was found in the graphene NMEAs samples. Moreover, the higher D peak means that the sp^2 bonds are broken which in turn means that there are more sp^3 bonds and more transition from sp^2 to sp^3 material, as the nanoparticles concentration increases. In addition, since G-band arises from the stretching of the C-C bond in graphitic materials, it was noticed that the order (i.e. 0.5<1.0<1.5) of the G-band of the CNF and graphite NMEAs samples agreed with what was found in the FTIR analysis in regard with the intensity order of C-C stretching at 1581 cm^{-1} and 1605.7 (only in CNF). Moreover, it was also observed that the G-peak, as shown in Fig. 7, did split into two peaks in some of the NMEAs, e.g. G-peak (1575-1585 cm^{-1}) and D'-peak (~1610-1620 cm^{-1}), which was ascribed to the presence of some randomly distributed impurities or surface charges in the samples.

The I_D/I_G of the carbon-based nanocomposites were higher than those of the pristine materials, which means that incorporating the nanoparticle into epoxy adhesive led the structure of the nanomaterial to defect which results in decreasing in ordering of sp^2 bonded graphitic domains. Moreover, the order of the I_D/I_G of the graphite nanocomposites, which was in agreement with that of the intensity of C-O-C str. at 1035.8 cm^{-1}, confirmed that the oxidation of carbon material leads to that sp^2 bonds to break which in turn means that there are more sp^3 bonds and more transition from sp^2 to sp^3 material, which would eventually lead to higher I_D/I_G, as it is

directly related to sp^3/sp^2 carbon ratio. These observations are in contradict with what was found by Zhao et al. [136], as it was observed that incorporating epoxy had no effect on the I_D/I_G in the spectra of the pristine material (i.e. SWCNTs).

It's noteworthy that the presence of the D and G bands in the NMEAs in those ranges, as shown in Table 7, that belong to carbon-based materials indicated a good dispersion of the nanoparticles in epoxy, as confirmed in the literature [123, 124].

4.3 Summary

This chapter has presented a comprehensive investigation into the effect of incorporating both carbon-based - including CNF, CNCs and graphite Nano powder - and silicon-based - including silica Nano powder and MMT Nano clay - nanomaterials into epoxy adhesive at three distinct weight concentrations; 0.5%, 1.0% and 1.5%. This study focuses on multiple facets, including investigating the dispersibility of nanoparticles within the epoxy matrix, changes in porosity, alterations in physical state and changes in chemical composition. Various analytical techniques, such as SEM analysis for microstructural and porosity investigations, XRD measurements for crystallinity assessment, as well as ATR-FTIR and Raman spectroscopies for chemical characterisation, were employed to investigate these aspects comprehensively. It's worthy to note that, as mentioned earlier, the outcomes derived from those various analyses were individually evaluated and also interlinked to provide a holistic assessment, leading to the following conclusions:

- Using such simple and cost-effective synthesis method (i.e. a combination of manual mixing and ultra-sonication) resulted in producing nanocomposites with relatively good dispersion (but not agglomeration-free) of the nanoparticles within the epoxy matrix.
- As the concentration of nanoparticles increased, their tendency to agglomerate also increased. These agglomerations tend to occupy certain areas within the material denser compared to other regions.
- Irregularities introduced by the agglomerations, with both densely packed areas, collectively result in a higher level of porosity in the produced nanocomposites, which had higher % porosity as the nanoparticles' concentration increased. Furthermore, more % porosity increase was observed when going from 0.5 to 1.0 wt.% concentrations compared to going from 1.0 to 1.5 wt.%.

- Porosity performance within the carbon-based nanocomposites exhibits concentration-dependent variations, with "CNF < cellulose < graphite" at concentrations ranging from 0.5 to 1.0 wt.%, but shifting to "CNF < graphite < cellulose" at concentrations from 1.0 to 1.5 wt.%. In contrast, silicon-based nanocomposites consistently maintain the order of porosity increase (clay >> silica) across all concentration ranges. This distinction underscores the complexity of carbon-based systems, while silicon-based counterparts demonstrate a more consistent behaviour in porosity reduction.

- Both nanoparticle agglomerations and increased % porosity contributed to the overall reduction in crystallinity in all nanocomposites compared to that of the NE. in addition, the nanocomposites became less crystalline much more when the concentration was doubled (from 0.5 to 1.0 wt.%) than when it was just increased by half more (from 1.0 to 1.5 wt.%).

- According to the results obtained from FTIR spectroscopy, the intensities of chemical bonds in both NE and carbon-based nanocomposites were found to change based on the type of the nanomaterial and its concentration in the epoxy matrix.

- No new chemical bonds were formed when carbon-based materials were incorporated, except for CNF-1.0, which showed the formation of a specific bond (C=O stretching at 1710 cm^{-1}). However, some functional groups disappeared in the nanocomposites. On the other hand, the silicon-based materials did not introduce any changes (neither appearance of disappearance) in the chemical bonds that already exist in the NE.

- The Raman spectroscopy results revealed that both CNF and graphite NMEAs exhibited higher I_D/I_G values compared to their pristine materials. Furthermore, for CNF NMEAs, the D-band values followed the order of 0.5>1.0>1.5, whereas the G-band values showed the opposite order of 0.5<1.0<1.5. A similar G-bands trend was observed in graphite NMEAs, with a D-band order of 0.5<1.5<1.0.

Chapter 5: Bond characteristics of the CP-adhesives-bonded joints

5.1 Introduction

This chapter delves into the results and discussion of the lap-shear test conducted on the CP-adhesive-bonded joints. Within this analysis, the influence of employing various adhesives, namely NE and NMEAs, which were prepared with various Nano-fillers incorporated into NE at different wt.%, in the bonding process (i.e. strength) of the CP-adhesive joints was investigated. The primary focus revolves around assessing the interfacial bonding strength, primarily characterised by the ultimate LSS, of the specimens subjected to testing. Moreover, the observed failure modes of these joints were also monitored and analysed.

5.2 Results and discussion

5.2.1 Ultimate shear strength

The results of the lap-shear test of the CP-adhesive joints are shown and analysed in this section, where the ultimate LSS of the joints in addition to the % increase in the shear strength of specimens bonded with NMEAs compared to those bonded with NE. The test results are summarised in Table 5.1. It's noteworthy that, for instance, the specimens designated as "NE" are those bonded using NE, while, for example, CNF-0.5 is the one bonded with NMEAs made with 0.5 wt.% CNF, and so forth. Furthermore, it's worth mentioning that five CP specimens were bonded with NE, two of them served as trial specimens to check the test setup, while the remaining three were considered in the test results for comparison purposes, as the average LSS was utilised for that purpose.

Table 5.1 Results of the lap-shear test of the CP-adhesive-bonded joints.

Specimen	Ultimate shear strength (MPa)	% increase in the LSS compared to the NE
NE (Average)	4.25	-
CNF-0.5	7.51	76.71
CNF-1.0	1.83	-
CNF-1.5	0.22	-
Silica-0.5	11.63	173.65
Silica-1.0	7.86	84.94
Silica-1.5	5.28	24.24
Cellulose-0.5	11.27	165.18
Cellulose-1.0	8.72	105.18
Cellulose-1.5	3.19	-
Clay-0.5	8.33	96.00
Clay-1.0	7.53	77.18
Clay-1.5	5.60	31.76
Graphite-0.5	8.03	88.94
Graphite-1.0	7.67	80.47
Graphite-1.5	2.19	-

First, for the specimens bonded with carbon-based Nano-fillers, it was observed, for those bonded with CNF-modified epoxy, that at lower CNF concentration (i.e. 0.5 wt.%), CNF particles were dispersed quite uniformly within the matrix (Fig. 4.1), which led to a strong interfacial bonding between the matrix and the fillers which enabled effective load transfer between them leading to a stronger bond with the CP substrate, which eventually resulted in about 77% higher shear strength than those bonded with NE.

However, at higher concentrations (i.e. 1.0 and 1.5 wt.%), the strengthening effect started to significantly reduce, even lower than that of the NE-bonded joints. This was due to the formation of agglomerates, which are expected to have a weak interface with epoxy due to stress concentration at the areas of agglomerations, as found in [143], which would ultimately weaken the bonding with the CP surface. Moreover, due to the high volume-to-weight ratio of the CNF, using higher concentrations lead to thicker adhesive layer, which yielded a decrease in the adhesive properties, as confirmed in [130], causing a detrimental effect on the bond behaviour of the bonded joints.

Similar observations were reported in the case of the cellulose-epoxy- and graphite-epoxy-bonded specimens, but unlike the CNF, the powder nature of the CNCs and the graphite nanoparticles, which had an insignificant effect on the thickness of the adhesive layer and also showed better dispersion quality within the adhesive, could enhance the shear strength of the joints with incorporating the Nano-filler up to 1.0 wt.%, as an increase of about 165% and 105%, respectively was found due to using epoxy with 0.5 and 1.0 wt.% CNCs, while these values were about 89% and 80% when using graphite-modified epoxy. Similar to what was found in the case of the CNF-bonded joints, the strength % increase was decreased with nanoparticles wt.%, where about 23% and 4.5% strength reduction, respectively was observed with doubling the cellulose and graphite wt.%. That was attributed to the increasing agglomerations with the wt.%, which led to not only no further strength increase with incorporating 1.5 wt.%, but also reduced the strength of the joints even below that of the NE joints.

Second, for the specimens bonded with silicon-based Nano-fillers, all of them showed higher strength than that in the case of using the pure adhesive. Where bonding the joints with silica-modified epoxy at 0.5, 1.0 and 1.5 wt.% considerably improved their shear strength by about 174%, 85% and 24%, respectively. However, doubling and tripling the wt.% of the silica Nano-filler, respectively resulted in about 32% and 55% strength decrease, while about 33% reduction in the joint strength was caused with 50% (i.e. from 1.0 to 1.5 wt.%) increase in the filler concentration into epoxy. Incorporating epoxy with 0.5, 1.0 and 1.5 wt.% clay Nano-fillers also exhibited a significant LSS enhancement of about 96%, 77% and 32%, respectively in the joints' strength. Though, as noticed in all specimens, increasing the wt.% of the fillers had a reverse effect on the shear strength, as reinforcing epoxy with further 50%, 100% and 200% of the Nano clay led to about 26%, 10% and 33% receptive drop in the joints' strength. This could be due to the same reasons that were mentioned in the case of using the carbon-based fillers.

From the results obtained, using epoxy loaded with silicon-based Nano-fillers was found to be able to enhance the joints' strength even with high wt.% concentrations (i.e. 1.5 wt.%) of the Nano-fillers. While bonding the joints with carbon-based-modified epoxies could improve the joints' strength but that was limited by the wt.% of the fillers. This could be due to that the higher wt.% of the materials would increase the possibility of particles' agglomeration and producing clusters, which form because of the van der Waals interactions, which are much

stronger in the carbon-based materials, especially in the CNF. These interactions would lead the particles to aggregate into entangled bundles that prevent the formation of uniform and optimal materials [131]. This would eventually lead to that the Nano-fillers would not be able to provide the epoxy with their ultimate enhancement capacity, which ultimately cannot be fully utilized.

It is also worthy to note that the increased % porosity within the nanocomposites, coupled with a concurrent decrease in the % crystallinity with the concentration of the nanoparticles, as shown in Tables 4.1 and 4.2, collectively play a key role in diminishing the interfacial adhesion between these nanocomposites and the CP substrate. This adverse effect, in turn, results in a notable reduction in the LSS of the CP-adhesive joints. Several key mechanisms can explain this phenomenon:

1) Reduced contact area: The increased % porosity in the nanocomposites creates voids or gaps within the structure, reducing the actual contact area available for bonding with the CP substrate. As a consequence, there is a limited surface for effective adhesion to occur.

2) Weakened mechanical integrity: The presence of porosity introduces structural weaknesses within the nanocomposite, rendering it less robust. This decreased mechanical integrity compromises the ability of the nanocomposite to withstand the stresses and forces acting at the interface with the CP substrate.

3) Interfacial gaps: Porosity can create interfacial gaps or microscale defects at the boundary between the nanocomposite and the CP substrate. These gaps act as stress concentration points and can lead to premature failure under load.

4) Reduced load transfer: A lower % crystallinity may impair the nanocomposite's ability to effectively transfer mechanical loads across the interface, further compromising the joint's overall strength.

5) Lower surface energy: Crystallinity typically enhances the surface energy of a material, which is beneficial for promoting adhesion. However, decreased % crystallinity in the nanocomposite can result in a lower surface energy, making it less prone to forming strong bonds with the CP substrate.

5.2.2 Modes of failure

The modes of failure of the bonded joints are depicted in Fig. 5.1. It's noteworthy that the failure mode of only one NE specimen is shown since all specimens failed in the same manner.

First of all, it's worth mentioning that the adhesive failure mode is interfacial bond failure between the adhesive and the CP substrate, while the cohesive failure occurs when a fracture allows a layer of adhesive to remain on both surfaces. When the adhered fails before the adhesive, it is known as a cohesive failure of the substrate indicating excellent adhesion.

From the failure mores obtained from the test, it was observed that the NE-bonded joints failed in mixed cohesive and adhesive modes. While for the carbon-based NMEAs-bonded joints, the failure modes were also found to be in a combined (i.e. cohesive and adhesive) mode. Furthermore, it was noticed that as the wt.% of Nano-filler increased, the cohesively-failed regions were observed to be larger. This was ascribed to that the agglomeration of the nanoparticles increases with their concentration into epoxy, and the resulting clusters are expected to have poor adhesion with the CP substrate and consequently act as nucleation sites for the growth of interface cracks leading to delamination [143].

For the joints bonded with silicon-modified epoxy, it was observed that reinforcing epoxy with 0.5 wt.% of silica was enough to keep interface intact, as the failure occurred in the CP itself away from the interface, as the specimen failed due to CP breaking. At higher concentrations (i.e. 1.0 and 1.5 wt.%), the modes of failure were back to the mixed type observed in the carbon-based joints, which was attributed to the same reasons reported earlier. Similarly, the joints bonded with the clay-modified epoxies at 0.5 and 1.5 wt.% failed in a combination of adhesive and cohesive modes, as the adhesively-failed regions decrease as the wt.% increases. For the joint bonded with 1.0 wt.%, the adhesive failure mode was the dominant with insignificant regions of the cohesive failure were seen.

Fig. 5.1 Failure modes of the CP-adhesive joints.

5.3 Summary

This chapter has provided a comprehensive examination of lap-shear test results for CP-adhesive-bonded joints. The investigation encompassed an exploration of the impact of different adhesives, e.g. NE and NMEAs, considering different Nano-fillers introduced into NE at varying weight concentrations, on the LSS of these joints. The central objective was to appraise the interfacial bonding strength, represented by the ultimate LSS exhibited by the tested specimens. Additionally, the chapter diligently scrutinised and analysed the failure modes manifested by these joints. Through this analysis, valuable insights have been gained into the performance and behaviour of CP-adhesive joints under various adhesion conditions, leading to the subsequent findings:

- The LSS of the CP-adhesive joints could be improved by using epoxy adhesive loaded with small amounts of carbon-based or silicon-based Nano-fillers, which may enhance the intrinsic properties of the adhesive.
- A significant increase (up to 165%) in the joints' strength bonded by epoxy filled with carbon-based Nano-fillers over that bonded with NE was obtained. However, this strength enhancement was limited by the wt.% of the fillers, since further increase in the fillers' concentration, e.g. 1.0 wt.% CNF and 1.5 wt.% of all Nano-fillers, resulted in a detrimental effect (i.e. strength decrease) because of settling of particle clusters.
- Dissimilar to what was observed in the case of using carbon-based-modified epoxies, using epoxy reinforced with either 0.5, 1.0 or 1.5 wt.% of the silicon-based Nano-fillers showed a considerable enhanced strength of the joints if compared to that bonded with NE. But a reduction in the joints' strength was reported as the wt.% increased, which was attribute to increasing the particles' agglomerations.
- The increased % porosity and reduced % crystallinity in nanocomposites have collectively hindered the establishment of a robust interfacial bond with the CP substrate. This diminished adhesion ultimately results in a decreased LSS in CP-adhesive joints due to reduced contact area, weakened structural integrity, lower surface energy, interfacial gaps and impaired load transfer capabilities.
- Almost all joints failed due to a combination of cohesive and adhesive failure mode. Nevertheless, the adhesively-failed regions were observed to expand with increasing the concentration of the Nano-fillers, which was mainly due to clustering of particles.

Chapter 6: Effect of FRP reinforcement on the behaviour of the retrofitted concrete specimens

6.1 Introduction

In this chapter, the behaviours of NSM-FRP-retrofitted specimens have been examined, focusing on key performance indicators. The assessment includes an evaluation of the load-carrying capacities, represented by the maximum load they can sustain, as well as an analysis of the maximum displacement at this load, alongside a thorough investigation of the specific modes of structural failure. This assessment takes into consideration the influence of the presence, type, position and quantity (i.e. number) of FRP reinforcement bars. Through a detailed analysis and discussion, a comprehensive understanding of the interactions and impacts of these factors on the structural performance of the retrofitted specimens is provided. The test results are listed in Table 6.1.

As mentioned previously (in Section 3.3.3.2), the specimens followed a designation format denoted as J-NE-L, where "J" represents the FRP type (C for CFRP, G for GFRP, and B for BFRP), and "L" indicates the groove size (8 or 10). For instance, specimen C-NE-8 denotes the retrofitting with a CFRP bar inserted into an 8x8 mm groove.

It's also important to note that the term "Edge" was appended after "L" for specimens retrofitted with FRP installed on the groove edge. Additionally, the letters "D" or "T" following "L" signify specimens retrofitted with two or three FRP bars, respectively, indicating a doubled or tripled number of bars. For specimens bonded with NE only, they were designated as "NE-groove size".

Table 6.1 Test results of specimens considered for the effect of FRP reinforcement.

Specimen No.	Specimen code	Max load (kN)			Avg. (kN) (COV)	Max flexural stress (MPa)			Avg. (MPa)	Max displacement (mm)			Avg. (mm) (COV)
		A	B	C		A	B	C		A	B	C	
-	Control	3.30	3.50	3.84	**3.55 (0.08)**	5.94	6.30	6.92	**6.39**	0.64	0.47	0.64	**0.58 (0.17)**
1	C-NE-8	14.71	15.34	14.20	**14.75 (0.04)**	26.48	27.61	25.56	**26.55**	1.35	1.14	1.31	**1.27 (0.09)**
2	G-NE-8	14.26	16.08	14.24	**14.86 (0.07)**	25.67	28.95	25.63	**26.75**	2.01	1.91	1.60	**1.84 (0.12)**
3	B-NE-8	11.60	16.33	16.62	**14.85 (0.19)**	20.88	29.38	29.92	**26.73**	1.96	2.13	1.98	**2.02 (0.05)**
8	C-Gr-0.1-8	16.68	15.71	18.36	**16.92 (0.08)**	30.02	28.28	33.04	**30.45**	1.29	0.97	1.11	**1.12 (0.14)**
9	G-Gr-0.1-8	16.11	13.25	16.82	**15.39 (0.12)**	28.99	23.84	30.27	**27.70**	1.81	1.72	2.03	**1.85 (0.09)**
10	B-Gr-0.1-8	14.49	18.07	13.05	**15.20 (0.17)**	26.09	32.52	23.48	**27.36**	1.73	1.84	2.40	**1.99 (0.18)**
15	NE-8	5.24	4.66	4.79	**4.90 (0.06)**	9.43	8.39	8.62	**8.81**	0.59	0.40	0.77	**0.59 (0.32)**
18	C-NE-10	17.54	23.70	23.75	**21.67 (0.16)**	31.57	42.66	42.74	**38.99**	1.53	1.81	1.49	**1.61 (0.11)**
20	G-NE-10-Edge	16.06	16.49	11.13	**14.56 (0.20)**	28.90	29.69	20.03	**26.21**	2.60	1.80	1.61	**2.00 (0.26)**
21	G-NE-10	17.48	12.94	12.67	**14.36 (0.19)**	31.47	23.28	22.80	**25.85**	2.52	2.07	3.31	**2.63 (0.24)**
23	C-NE-8-D	17.34	19.61	16.46	**17.80 (0.09)**	31.21	35.30	29.62	**32.04**	5.92	1.42	1.85	**3.06 (0.81)**
24	C-NE-8-T	23.84	24.32	26.72	**24.96 (0.06)**	42.96	43.78	48.09	**44.94**	2.41	2.30	1.66	**2.12 (0.19)**

6.2 Results and discussion

6.2.1 The effect of presence of FRP reinforcement

In this section, the investigation was conducted to assess the impact of incorporating FRP bars in the retrofitting process of the concrete specimens. An evaluation was undertaken to compare the performance of concrete prisms that underwent retrofitting only with NE with those that were retrofitted with the inclusion of FRP bars, namely CFRP, GFRP and BFRP. This assessment aimed to reveal the influence of integrating FRP reinforcement bars into the retrofitting process. One FRP bar fixed in an 8x8 mm groove was used in retrofitting the latter specimens.

6.2.1.1 Overall flexural capacities and ductility response

It was observed that retrofitting concrete by epoxy only (i.e. NE-8) resulted in about 38% and 2% increase in the ultimate load and ductility, respectively over the un-retrofitted specimen. The capacity increase may be due to the high tensile strength of epoxy compared to that of concrete, which enhanced the flexural capacity of concrete specimens. On the other hand, using such brittle adhesive had a trivial effect on the ductility. While using CFRP, GFRP or BFRP bars alongside NE resulted in about 315%, 319% and 318% increase in the ultimate loads, respectively with accompanying 119%, 217% and 248% ductility increase over the control specimen.

In comparison with specimen NE-8, it was found that using CFPR bars combined with NE (i.e. specimen C-8) for retrofitting showed about 201% increase in the load-carrying capacity of the specimens and about 115% in ductility. Retrofitting specimens with GFRP bars resulted in about 203% and 212% ultimate load and ductility increase, respectively, while the BFRP-retrofitted specimens showed about 203% and 242% increase, respectively in the ultimate load and ductility. It is apparent that using the FRP reinforcement alongside epoxy would resist the crack progression in addition to enhance the bond at the interfaces, which would eventually delay the failure. It was also noticed that using different types of FRP bars had a similar contribution (i.e. increase) in the load-bearing capacities, but different ductility response was observed. This could be due to the difference in the mechanical properties of FRPs (Table 3), which affected the bond behaviour of the interfaces, and ultimately the specimens' ductility. The test results are shown in Fig. 6.1.

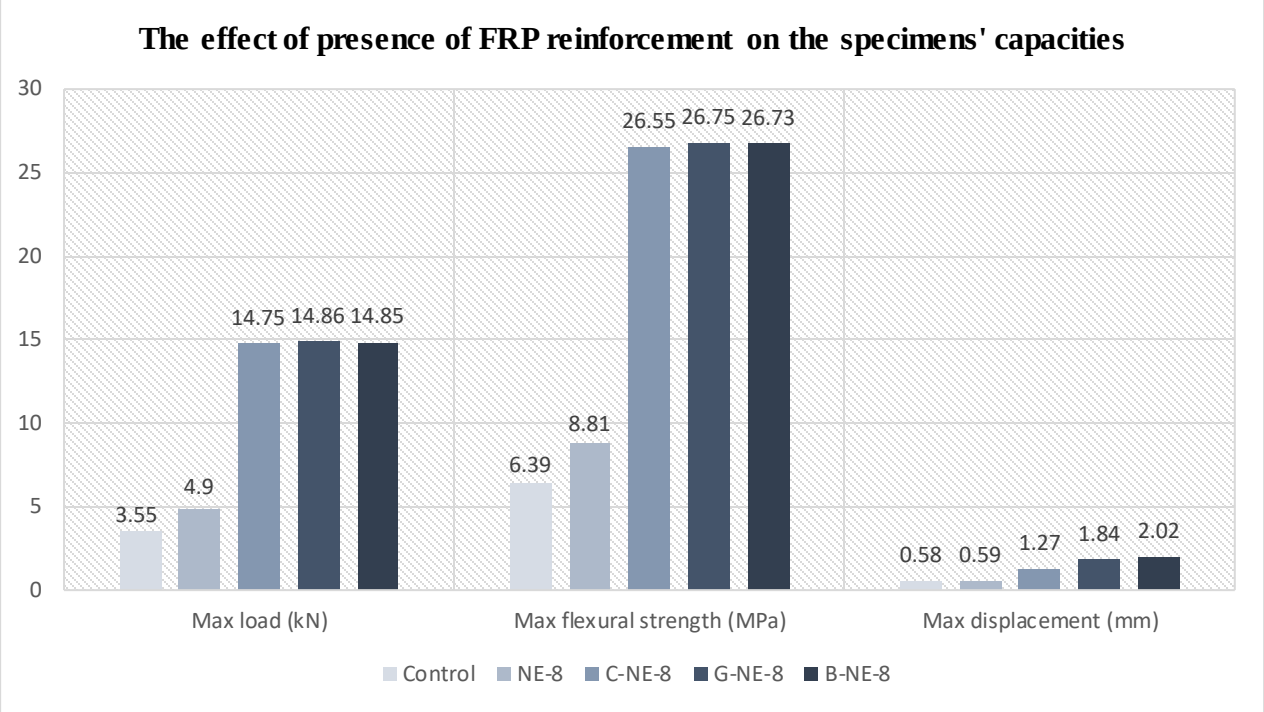

Fig. 6.1 Effect of presence of FRP reinforcement on the specimens' capacities.

6.2.1.2 Failure modes

As shown in Fig. 6.2, using NE alone for retrofitting resulted in a brittle failure mode, as it resulted in an insignificant improvement in the ductility of the retrofitted concrete, as discussed in the previous section. Thus, the flexural crack can be seen to easily propagate through the epoxy line passing to the other side of concrete substrate, breaking the specimens into two parts. While in the case of considering FRP reinforcement bars in the retrofitting process, the modes of failure seemed to be more ductile and they changed to shear failure mode combined with bar slippage in the CFRP-retrofitted specimens, while the specimens retrofitted with GFRP bars mainly failed in flexure, which resulted in peeling-off of the adhesive layer at the bar-epoxy interface followed by a partial detachment of concrete substrate. A mixed shear and flexural failure modes were shown by the BFRP-retrofitted specimens, leading to minor concrete crushing.

It's worth mentioning that, owing to the comparatively lower mechanical properties of the BFRB bars (Table 3.4), the BFRP-retrofitted specimens exhibited a higher degree of ductility. This enhanced ductility was manifested through the presence of a greater number of minor cracks around the concrete-adhesive interface prior to failure, which contrasted with the behaviour observed in the GFRP-retrofitted specimens. The latter, on the other hand, demonstrated a higher incidence of hairline cracks (i.e. higher ductility) before reaching the failure point compared to specimens retrofitted with CFRP bars, known for their superior mechanical properties.

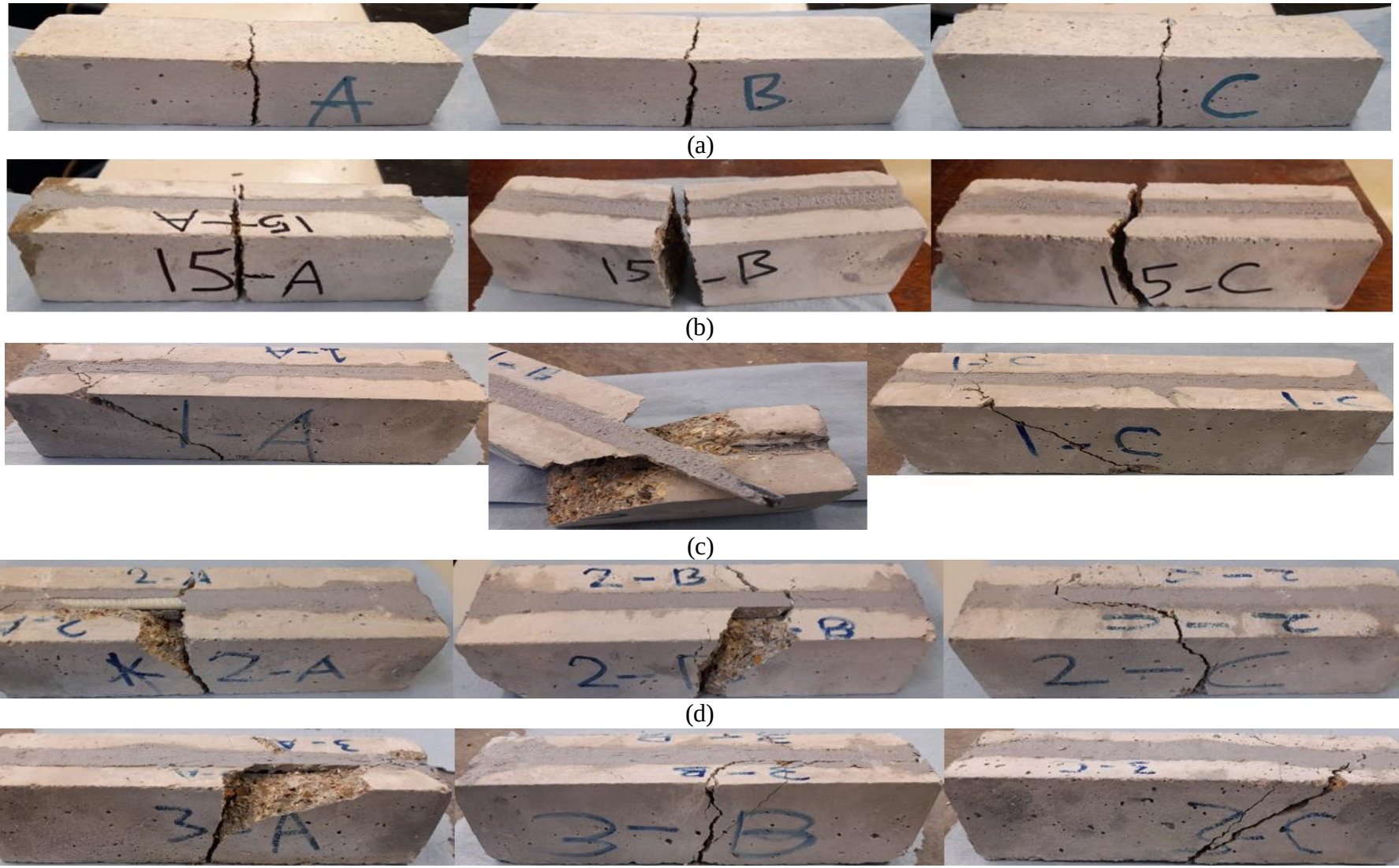

Fig. 6.2 Failure modes of specimens (a) control, (b) NE-8, (c) C-NE-8, (d) G-NE-8 and (e) B-NE-8.

6.2.2 The effect of type of FRP reinforcement bars

In order to comprehensively investigate the effect of the FRP reinforcement type on specimens' structural behaviour, three groups of specimens, as provided in Table 3.7, were considered for the comparison purposes, as shown and discussed in this section. The first group includes the NE-bonded specimens (i.e. C-NE-8, G-NE-8 and B-NE-8), while the NMEAs-bonded specimens (i.e. C-Gr-0.1-8, G-Gr-0.1-8 and B-Gr-0.1-8) are considered in the second group. It's worthy to mention that all specimens in the first two groups had the same retrofitting scheme of one FRP bar inserted in an 8x8 mm groove. 10 mm-grooved specimens retrofitted with CFRP or GFRP bars (i.e. C-NE-10 and G-NE-10) were considered in the third group.

6.2.2.1 Overall flexural capacities and ductility response

For the specimens bonded with NE, the capacities in terms of maximum load or flexural strength, of the GFRP- and the BFRP-retrofitted specimens were very close, which were only 1% higher than those retrofitted using CFRP bars. This observation agrees with what was found by Soliman et al. [93]. The ductility was found to be the highest in the case of the BFRP-retrofitted specimens, which showed about 59% and 10% higher maximum displacement than those retrofitted by CFRP and GFRP rods, respectively. While using GFRP reinforcement bars, exhibited about 45% increase in the ductility than those retrofitted with CFRP bars. This could be, as confirmed in the literature [86, 93], due to that the mechanical properties (i.e. tensile strength and elastic modulus), as shown in Table 3.4, of the CFRP bars are much higher than those of the GFRP bars, which in turn has higher mechanical properties than those of the BFRP bars.

On the other hand, changing the type of the FRP reinforcement in the specimens bonded with the graphite-modified epoxies was found to have more influence on the bending behaviour in terms of load-carrying capacity and ductility. For instance, using CFRP bars showed about 10% and 12% flexural capacity increase, respectively compared to utilising GFRP and BFRP bars, which could be due to the high mechanical properties of the CFRP rods compared to those of the other FRP's. While a slight increase in the capacity was reported when using the GFRP bars rather than the BFRP ones. Regarding the ductility, about 44% and 8% higher maximum displacement were reported in the case of utilising BFRP bars, respectively, than when CFRP and GFRP rods were used, which could be due to the same reason mentioned above, which would justify the 65% higher ductility that was exhibited in the GFRP-retrofitted specimens over those retrofitted by CFRP bars.

Consequently, the performance in terms of the load-carrying capacity was pretty much similar in the case of bonding specimens with NE, so it was difficult to determine the most efficient FRP bars to be used, while using the modified adhesive revealed the best FRP choice clearly. Furthermore, similar observations to those found in the NE-bonded specimens in regard with the maximum displacement were reported using the modified adhesive. However, the % increase were a bit different. Where compared to using the NE adhesive, using modified adhesive lowered the % increase in the ductility from 59% to 44% and from 10% to 8% when moving from BFRP reinforcement to GFRP and to CFRP, respectively. In contrast to that, a higher % increase (i.e. from 45% to 65%) was observed when moving from GFRP to CFRP.

Differing from what was observed in the 8 mm-grooved specimens (in the first group), it was noted that, in the 10 mm-grooved specimens, a substantial increase in the load-carrying capacity of about 51% was achieved by the CFRP-retrofitted specimens in comparison to those retrofitted with GFRP bars. This increase is attributed to the greater strength and stiffness of CFRP bars than those of the GFRP counterparts.

Nonetheless, those higher mechanical properties of CFRP bars had a detrimental effect on the ductility of the specimens, resulting in a reduction of about 39% compared to the GFRP-retrofitted specimens. Therefore, it can be concluded that altering the type of FRP reinforcement proved to be a more efficient strategy for enhancing ductility in the case of the 10 mm-grooved specimens. This nuanced interplay between material properties and structural response underscores the need for tailored retrofitting strategies according to groove dimensions and performance requirements. A graphical representation of the test results is depicted in Fig. 6.3.

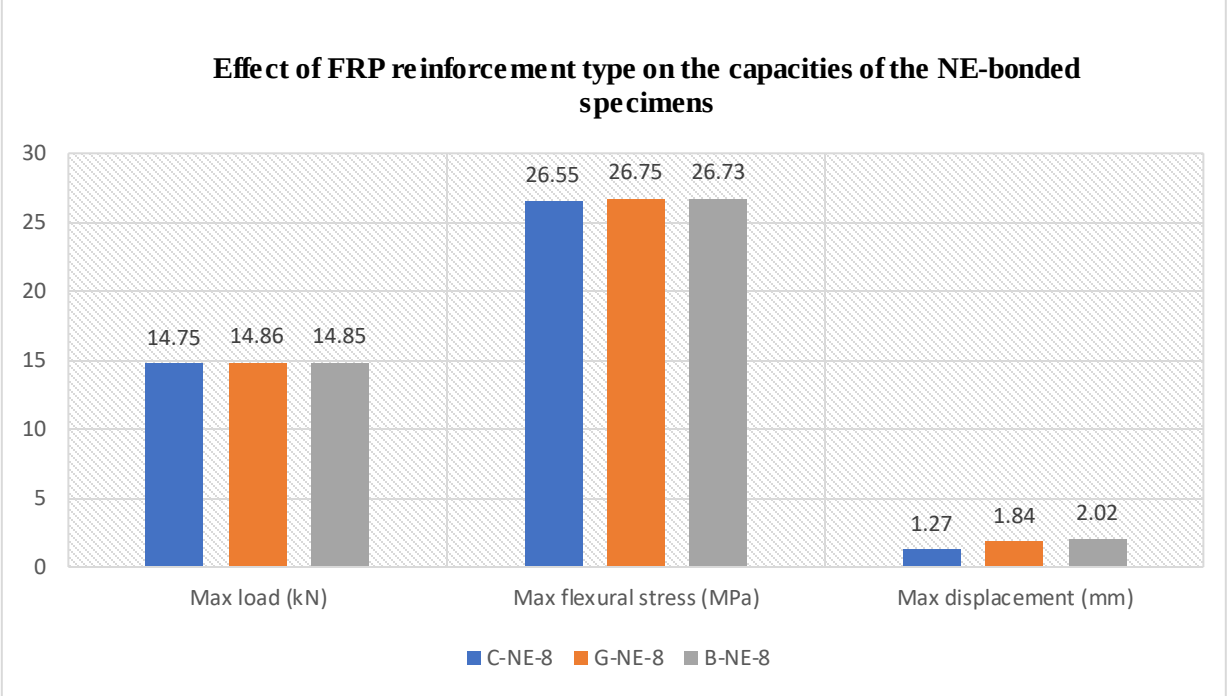
Effect of FRP reinforcement type on the capacities of the NE-bonded specimens
30
25
20
15
10
5
0
14.75
14.86
14.85
26.55
26.75
26.73
1.27
1.84
2.02
Max load (kN)
Max flexural stress (MPa)
Max displacement (mm)
C-NE-8
G-NE-8
B-NE-8

(a)

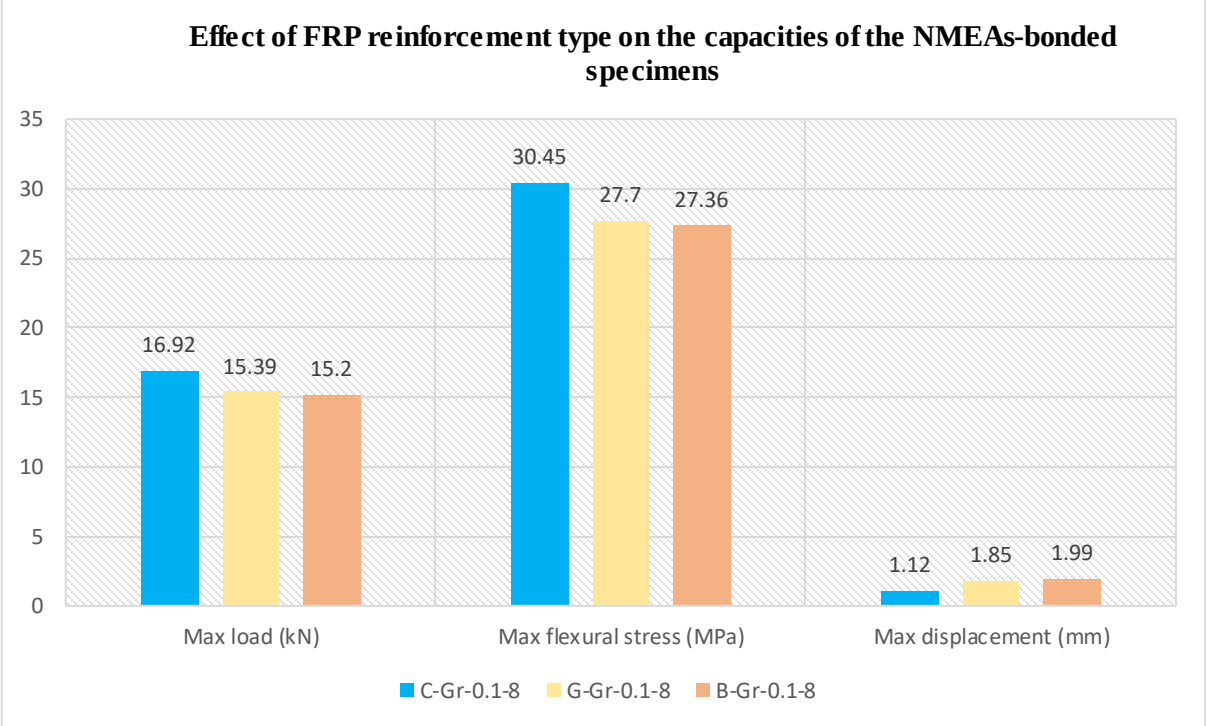
Effect of FRP reinforcement type on the capacities of the NMEAs-bonded specimens
35
30
25
20
15
10
5
0
16.92
15.39
15.2
30.45
27.7
27.36
1.12
1.85
1.99
Max load (kN)
Max flexural stress (MPa)
Max displacement (mm)
C-Gr-0.1-8
G-Gr-0.1-8
B-Gr-0.1-8

(b)

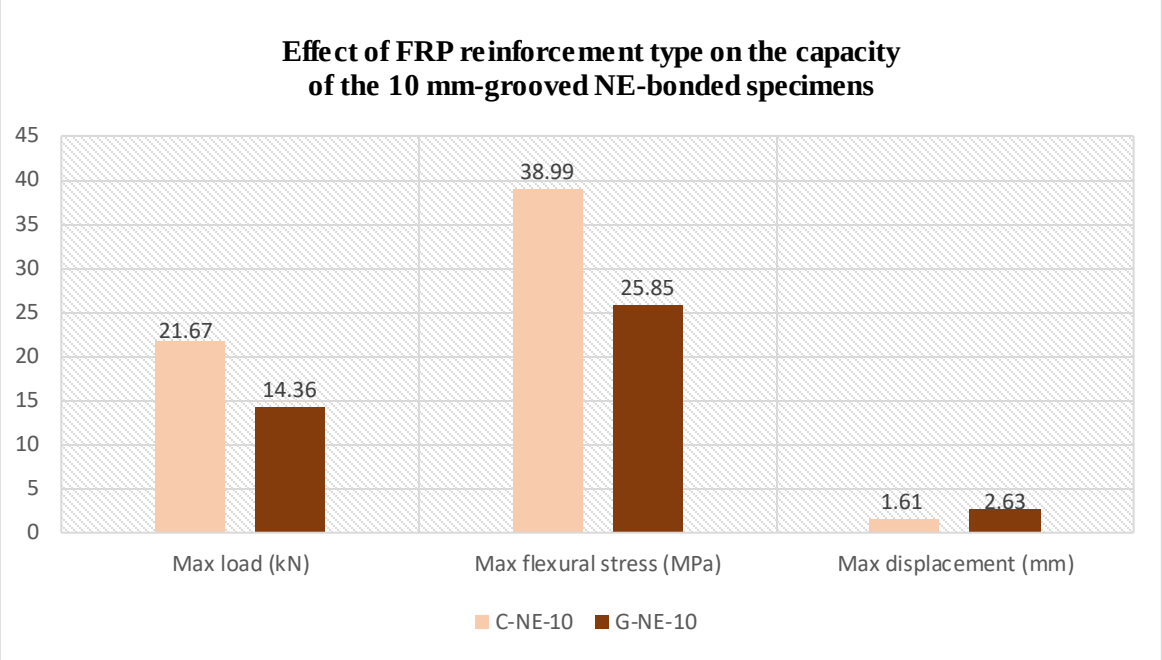

Fig. 6.3 Effect of FRP type on the capacities of (a) the 8 mm-grooved NE-bonded specimens, (b) the 8 mm-grooved NMEAs-bonded specimens and (c) the 10 mm-grooved NE-bonded specimens.

6.2.2.2 Failure modes

The failure modes of the specimens retrofitted with different FRP reinforcement types are shown in Fig. 6.4. In the first group, which includes the NE-bonded specimens, specimens C-NE-8 (i.e. A, B and C), which were retrofitted by CFRP bars, mainly failed in shear. Where in specimen A, as shown in Fig. 6a (on the left), the shear crack generated in concrete and continued to pass through the epoxy layer but with less width than in the concrete, since epoxy is stronger, which was able to stop its progress. Similar mode of failure was noticed in specimen C (on the right), but the crack continued to progress through concrete after it passed the epoxy layer, which was able to curb the crack to pass through it in specimen B (in the middle), but that led to debonding (i.e. CFRP bar slippage) at the FRP-epoxy interface. This could arise because of the smooth surface of the CFRP rods (Fig. 3.3), which did not provide enough bond strength with epoxy.

Unlike what was observed in C-NE-8, flexural failure was the dominant in G-NE-8 (Fig. 6.2d), which were retrofitted with GFRP bars. In specimen A, a wide flexural crack generated into concrete and broke through the epoxy layer to the other side, and also kept progressing align to the GFRP-epoxy interface resulting in a partial peeling-off of the epoxy layer at the bar-epoxy interface and causing a part of concrete to detach. Specimen B failed by approximately the same manner, but the epoxy layer did not peel off. Similar observations were reported in specimen C,

but the major crack that led the specimen to fail was narrower than those appeared in the previous specimens.

A combined shear and flexural failure mode were shown in the specimens retrofitted with BFRP bars (i.e. B-NE-8) (Fig. 6.2e), where main flexural crack alongside minor shear crack, appeared in specimen A, which aligned with the adhesive line at the concrete-epoxy interface leading parts of concrete to peel off with thin layers of epoxy stuck on them. Similar observations were reported in regard with specimen B, with a bit more cracks appeared on concrete surface at failure, however no peeling off took place. Different failure mode was noticed in specimen C, which mainly failed due to number of shear cracks appeared at failure, that did not align with the epoxy line, but alternatively crossed it only in one place, in addition to that the epoxy line was able to limit the crack from progressing to the other side of the specimen. Contrary to what was observed in C-NE-8 and G-NE-8, fewer visible cracks were able to penetrate the epoxy layer, which indicates a stronger bond at the concrete-epoxy-BFRP interfaces.

In the specimens bonded with NMEAs (i.e. group 2), on the other hand, changing the type of the FRP reinforcement led specimens to fail in different ways. For example, CFRP bars that was used in C-Gr-0.1-8 caused a shear failure in specimen A, which was represented by a major shear crack, which began as flexural, appeared in the concrete body with a short tail continued to align with the adhesive line, which was approximately the same that happened in specimen C. Specimen B exhibited a similar failure mode, but the shear crack was less broad, which gave the opportunity to the flexural crack to generate, which had longer tail lying on the edge of the adhesive line, but without breaking through it. Contrary to that, the cracks that produced in specimens retrofitted with GFRP bars (i.e. G-Gr-0.1-8), which were flexural cracks in specimen A and combined flexural and shear in B and C, broke through the adhesive line and crossed to the other side of the specimens and continued their progression into through concrete substrate, which did not happen in the BFRP-retrofitted specimens (i.e. B-Gr-0.1-8). Where the flexural cracks that formed in specimens A and B and the shear crack in C extended to progress next to the adhesive line at the concrete-adhesive interface border but without penetrating the adhesive line. Concrete detachment took place in B-Gr-0.1-8 -B, which did not neither in C-Gr-0.1-8 nor in G-Gr-0.1-8.

For specimens in both groups, it's noteworthy that, due to the lower mechanical properties of the BFRB bars, the BFRP-retrofitted specimens showed, generally, the most ductile behaviour, which was represented by having more minor cracks around the concrete-adhesive interface

before failure, than the GFRP-retrofitted ones, which in turn failed with higher number of hairline cracks than those shown when using CFRP bars, which have the highest mechanical properties.

Consequently, replacing CFRP bars with GFRP and BFRP bars in the NE-bonded specimens was found to induce a shift in failure modes, transitioning from shear to a combination of shear and flexural. This alteration proved effective in preventing the occurrence of debonding failure. Conversely, the transition from CFRP to GFRP in the NMEAs-bonded specimens yielded no discernible impact on the failure mode. However, the shift to GFRP reinforcement resulted in a distinct flexural failure mode, followed by concrete crushing. Evidently, the utilisation of distinct reinforcement types manifested varying failure behaviours and responses to applied stresses.

For the 10 mm-grooved specimens, it was noticed that the shear failure was the governing in the CFRP-retrofitted specimen. Where almost the same failure modes took place in specimens A and B, as a main shear crack produced in the middle of the specimens from the bottom and kept progressing to break through the epoxy layer with a short tail along the edge of the epoxy line until, eventually, broke through it to the other side. Similar details were observed in specimen C, but one more shear crack generated with longer tail, but it kept beside the epoxy line without passing through it. A combined shear and flexural mode of failure was noticed in specimen 21, which retrofitted by GFRP bars. Where specimens A and B mainly failed in flexure, as a wide flexural crack produced in the middle of the specimens breaking through the epoxy line to the other side. A minor shear crack appeared to the right of the main crack, but it did not contribute to the failure mode. Specimen C failed due to a major shear crack, that led a part of concrete to detach, in addition to that it caused a debonding failure at the GFRP bar-epoxy interface. No minor cracks produced.

(a)

(b)

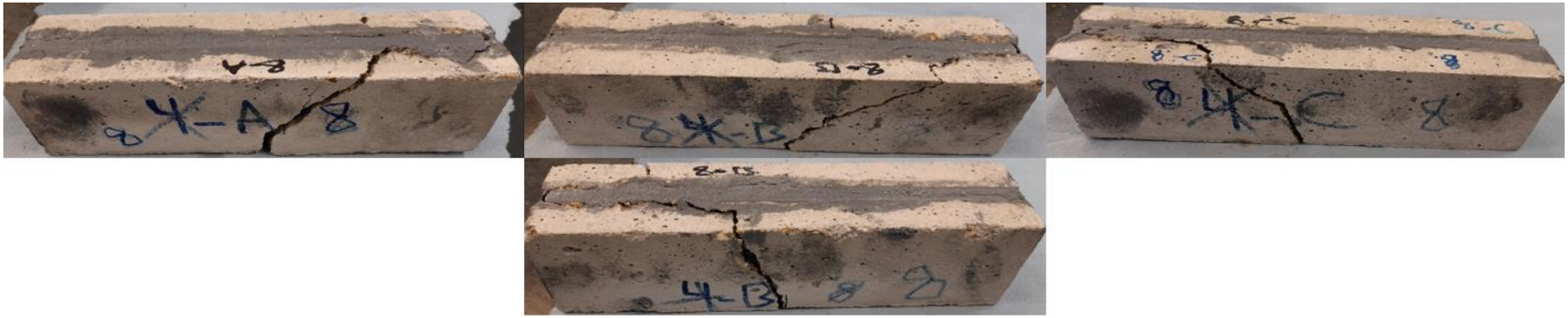

(c)

(d)

(e)

(f)

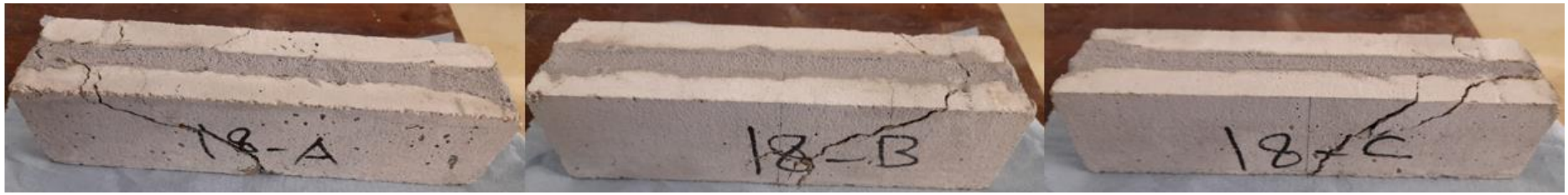

(g)

(h)

Fig. 6.4 Failure modes of specimens (a) C-NE-8, (b) G-NE-8, (c) B-NE-8, (d) C-Gr-0.1-8, (e) G-Gr-0.1-8, (f) B-Gr-0.1-8, (g) C-NE-10 and (h) G-NE-10.

6.2.3 The effect of position of FRP reinforcement bars

As depicted in Fig. 3.22, the FRP reinforcement bars were strategically placed within grooves in two distinct locations: one at the midpoint and the other at the edge of the groove. This deliberate placement variation allows for an in-depth exploration of the influence of GFPR bars positioning on both the load-carrying capacities of the specimens and the specific modes of failure they exhibit. Consequently, within this section, a comprehensive investigation into the effect of these different bar positions on the specimens' structural behaviour and failure characteristics is undertaken. It's noteworthy that one GFRP bar installed in a 10x10 mm groove was adopted in retrofitting the specimens.

6.2.3.1 Overall flexural capacities and ductility response

Test results exhibited that changing the position of the GFRP bars inside the grooves had trivial effect on the load-carrying capacities of the specimens, where only about 1% capacity increase was observed with considering the edge-installed reinforcement over the centred-installed one. However, a considerable increase of about 32% in the ductility was observed by the latter configuration over the former one. This could be because of in the case of the edge-installed FRP bar the thickness of the epoxy layer between the bar and the concrete substrate at that edge was less compared to that in the case of the middle-installed bar, and as the epoxy layer acts as a medium to transfer stress from concrete to FRP, thinner epoxy layer might not be able to work properly (i.e. transfer stress) amongst the interfaces as it did in the other specimen, which eventually increased the stress concentration on the edge leading the specimen to behave in more brittle mode. Fig. 6.5 shows the results graphically.

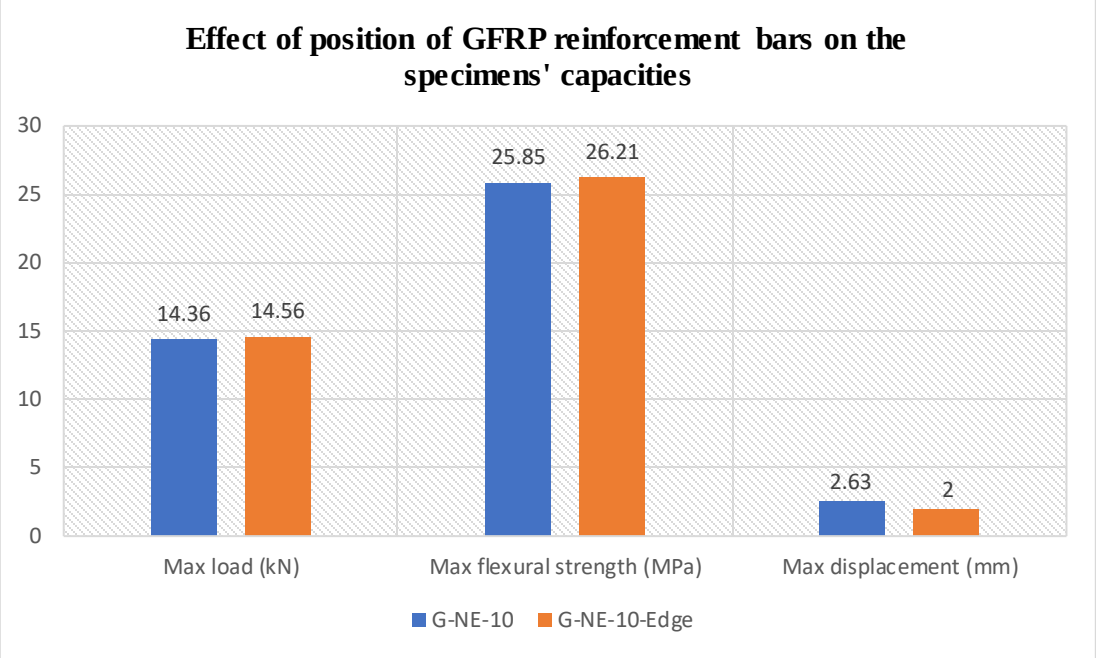

Fig. 6.5 Effect of position of GFRP reinforcement bars on the specimens' capacities.

6.2.3.2 Failure modes

A combined shear and flexural mode of failure was noticed in specimen G-NE-10. Where specimens A and B mainly failed in flexure, as a wide flexural crack produced in the middle of the specimens breaking through the epoxy line to the other side, however, no debonding was observed. A minor shear crack appeared to the right of the main crack, but it did not contribute to the failure mode. Specimen C failed due to a major shear crack, leading to peeling-off of a small part of concrete and epoxy layer at the epoxy-FRP interface (i.e. debonding), however no minor cracks were noticed.

Similar observations were reported in specimen G--NE10-Edge, in which specimens A and B failed in pure flexure with one main crack produced and progressed through concrete and directly moved to pass through the entire epoxy layer to the other side without generating a crack tail along the epoxy line, which also occurred in specimen G-NE-10. Specimen G-NE-10-Edge-C failed in similar manner to that noticed in specimen G-NE-10-C, but no debonding or concrete detachment took place in the former specimen. This was attributed to that, as previously discussed, putting the FRP bar on the groove edge decreased the specimens' ductility, which could lead to premature failure before any type of peeling-off happens. In addition, being the bar closer to the concrete edge, this might protect it, to some extent, from debonding, as stresses might not be able to progress into the concrete body. The failure modes of specimens G-NE-10 and G-NE-10-Edge are shown in Fig. 6.6.

(a)

(b)

Fig. 6.6 Failure modes of specimens (a) G-NE-10-Edge and (b) G-NE-10.

6.2.4 The effect of number of FRP reinforcement bars

To examine the structural behaviour, mirroring the previous methodology, concrete prisms were subjected to retrofitting with varying quantities of CFRP reinforcement bars. Specifically, three specimens were retrofitted with one, two or three CFRP bars, strategically placed at the centre of 8x8 mm grooves. The ensuing section presents a detailed analysis of their structural performance, including observations and discussions.

6.2.4.1 Overall flexural capacities and ductility response

Test results showed that increasing the amount of the CFRP reinforcement resulted in an enhancement in the load-carrying capacities in addition to the ductility response. Where doubling the number of the CFRP bars yielded about 21% and about 141% increase in the ultimate loads and ductility, respectively, about 69% capacity increase and about 67% ductility enhancement were obtained with tripling the number of bars. Moving from two to three bars was found to increase the capacity by about 40%, however, about 44% reduction in the ductility was remarked.

It could be axiomatic to obtain a capacity increase with increasing the number of bars, which would enhance the resistance to failure cracking and eventually delay the failure. However, the ductility improvement could be referred to that using more reinforcement would make the crack progression more difficult, as the crack in the single FRP-retrofitted specimens, for instance, would need to break though only one adhesive layer to cause the failure at the interface and eventually in the specimen, but in the case of the presence of two or three adhesive layers, the task would be harder and would take longer to be achieved. This would end up with higher-strength specimens and result in a more ductile behaviour, since the specimen would keep displaced for longer time. Nevertheless, increasing the number of FRP bars by 50% (i.e. from two bars to three) negatively affected the average ductility of the retrofitted concrete, as found in some previous studies [86, 90]. The results are shown in Fig. 6.7.

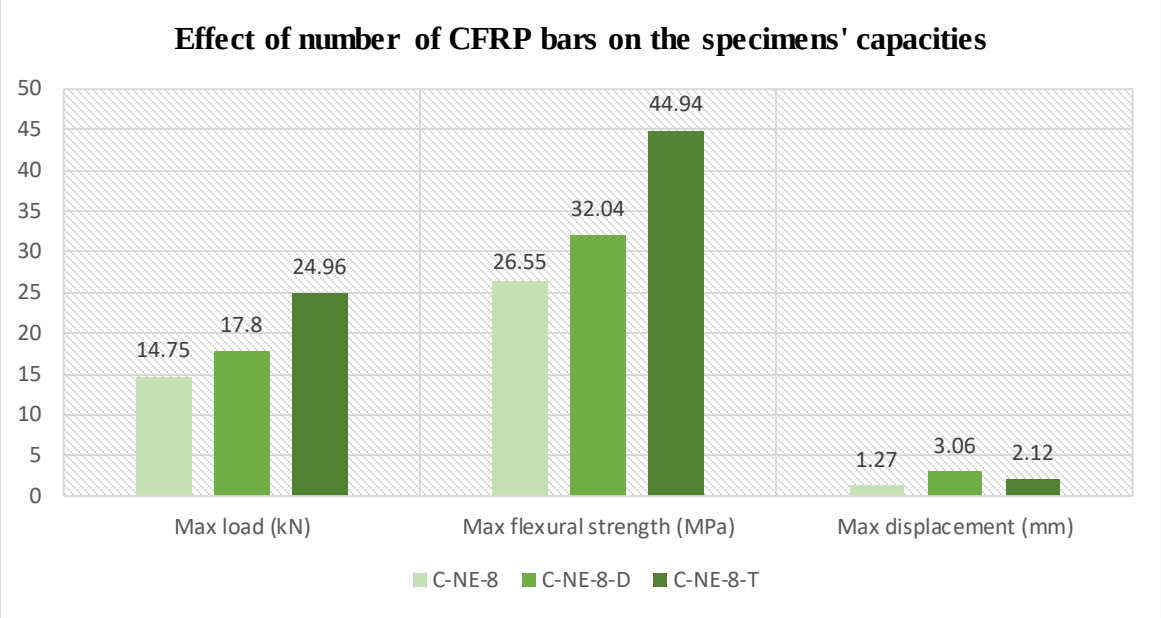

Fig. 6.7 Effect of the number of the CFRP bars on the specimens' capacities.

6.2.4.2 Failure modes

It is evident that the specimens C-NE-8 (i.e. A, B and C) mainly failed in shear. Where in specimen A, the shear crack produced in the concrete body and continued to pass through the epoxy layer but with less width than in the concrete, since epoxy is stronger, which was able to stop its progress. Similar mode of failure was noticed in specimen C, but the crack continued to progress through concrete after it passed the epoxy layer, which was able to curb the crack to pass through it in specimen B, but that led to debonding (i.e. CFRP bar slippage) at the FRP-epoxy interface. A shear failure followed by debonding at the bar-epoxy interface was noticed in specimen C-8-D-A, in addition to CFRP rupture. While debonding at both the concrete-epoxy and epoxy-bar interfaces was noticed in specimens B and C, with partial concrete detachment in C, no minor cracks were remarked in C-8 and C-NE-8-D. For specimen C-NE-8-T, it was noticed that A, B and C failed in the same manner, which was due to shear cracks that eventually led to debonding at both interfaces. Some minor cracks showed up near the surface. The failure modes of specimens C-NE-8-D and C-NE-8-T are shown in Fig. 6.8.

Therefore, the increase in the number of CFRP bars resulted in the retention of the shear failure mode within the concrete structures. However, an increase in debonding at the interfaces was observed, potentially attributable to inadequate clear groove spacing and clear edge distance. The insufficiency in clear groove spacing and edge distance can lead to a reduced bonding area between the CFRP bars and the concrete substrate, consequently promoting the debonding mechanism and impacting the overall effectiveness of the retrofitting process.

(a)

(b)

Fig. 6.8 Failure modes of specimens (a) C-NE-8-D and (b) C-NE-8-T.

6.3 Summary

In this chapter, a thorough investigation of the structural behaviour of NSM-FRP-retrofitted concrete prisms has been conducted, considering the presence of FRP reinforcement bars, as well as the variations in their types, positions and percentages. These parameters have been subjected to investigation to assess their influence on the performance of the specimens, encompassing load-bearing capacities/ maximum flexural stress, ductility responses and failure modes. The ensuing analysis has yielded a wealth of valuable insights into the diverse aspects of structural performance and behaviour exhibited by the retrofitted concrete prisms across a spectrum of retrofitting design parameters in terms of the impact generated by the FRP reinforcement. From the results obtained, the following conclusion could be drawn:

- Retrofitting specimens with NE only increased the capacity and ductility by about 38% and 2%, respectively over the un-retrofitted specimens. No change on the mode of failure (i.e. flexural) was noticed.

- Using CFRP, GFRP and BFRP reinforcement bars with NE achieved about 201%, 203% and 203% increase in the load-carrying capacity, respectively with accompanying 115%, 212% and 242% ductility increase over those retrofitted with NE only.

- Using FRP reinforcement bars alongside NE rather than NE only resulted in more ductile failure mode, in addition to significantly improving the resistance to the crack progression unlike what happened in the specimens retrofitted only with NE.

- Insignificant changes in the capacities were observed in the GFRP- and BFRP-retrofitted specimens bonded with NE, which had only 1% higher capacities than those retrofitted with CFRP bars. However, the specimens' ductility was found to be the highest in the case of the BFRP-retrofitted specimens, which showed about 59% and 10% more deflection at failure than those retrofitted by CFRP and GFRP rods, respectively.

- The CFRP-retrofitted concrete bonded with the graphite-modified epoxies showed capacity increase of about 10% and 12%, respectively compared to the ones retrofitted with the GFRP and the BFRP bars. Furthermore, about 44% and 8% higher ductility were observed in the BFRP-retrofitted than the CFRP and GFRP-retrofitted concretes respectively.

- Moving from CFRP to GFRP and BFRP for NE-bonded retrofit resulted in change of failure mode from shear to flexural and to shear and flexural, and could avoid the debonding failure,

while moving from CFRP to GFRP in the NMEAs-bonded specimens had no effect on the failure mode and moving to BFRP showed a flexural failure followed by concrete crushing.

- Installing the GFRP reinforcement on the edge of the groove rather than in the centre had a trivial effect on the load-carrying capacity, but decreased the ductility by about 24%, which could be due to the increase in the stress concentration at the interfaces.

- The debonding at the bar-epoxy interface and the concrete detachment could be avoided through installing the GFRP reinforcement on the groove edge instead of in its centre, as the bar was closer to the concrete substrate and was protected by it.

- Doubling and tripling the number of the CFRP bars led, respectively to about 21% and 69% increase in the load-carrying capacities, with accompanying ductility increase of about 141% and 67%. While about 40% capacity increase was obtained when moving from two to three bars, however, about 44% ductility drop was observed.

- Increasing the number of the CFRP bars kept the shear failure mode, but increased the debonding at the interfaces, which could be due to the insufficient clear groove spacing and the clear edge distance.

Chapter 7: Performance of the NSM-FRP-retrofitted specimens bonded using nanomaterial-modified epoxy adhesives

7.1 Introduction

The performance, in terms of capacities and failure modes, of the specimens bonded using different bonding agents is discussed in this chapter. To comprehensively investigate the effect of that parameter, three distinct groups of sub-parameters (as shown in Table 3.7) were considering for comparison and analysis purposes.

The effect of bonding specimens with either NE or NMEAs is shown and discussed the first group, which has five different sub-groups tailored for that purpose. Group one (i.e. the first sub-group) includes the 8mm-grooved CFRP-retrofitted specimens bonded using NE or 0.1 wt.% NMEAs (i.e. CNF, silica, cellulose, clay and graphite). The second and third groups consider the 8mm-grooved GFRP- and BFRP-retrofitted specimens, respectively bonded with NE or 0.1 wt.% graphite nanocomposites, while the specimens 10mm- and the 12mm-grooved CFRP specimens bonded with NE or 0.1 wt.% graphite nanocomposites are encompassed in groups four and five, respectively. Considering several groups of specimens was to examine the effect of using different bonding agents in specimens bonded with different types of FRP reinforcement bars inserted into different-sized grooves.

The second group includes the second sub-parameter, which was the type of the NMEAs themselves. Where two "families" of nanoparticles were incorporated into epoxy at 0.1 wt.%, which are (1) carbon-based nanomaterials including CNF, CNCs and graphite nanoparticles, and (2) silicon-based nanomaterials comprehending silica nanoparticles and MMT Nano clay. Therefore, the effect of using those different types of the NMEAs (both comparing the two families together and the Nano-fillers in each of them) were evaluated in that group. The impact of considering three different wt.% concentrations (i.e. 0.1, 0.2 and 0.3 wt.%) of the NMEAs (i.e. graphite) on the specimens' behaviour were assessed in the third group. It's worthy to mention that, in order to enhance the comprehensiveness and criticality of the performance analysis, the investigation done in this chapter was supported with the SEM (i.e. dispersion quality), porosity and the crystallinity analyses of the NE and the NMEAs. It's noteworthy that the chemical characterisation of the 0.1, 0.2 and 0.3 wt.% NMEAs was not conducted because of the insignificant chemical changes induced by incorporating the nanoparticles into the NE at 0.5, 1.0 and 1.5 wt.% concentrations. As no chemical changes were evident in the higher

weight percentages, it is highly likely that such changes would not occur in the lower wt.% concentrations. This conclusion is supported by the consistent trend of chemical stability observed in the higher weight percentages, indicating that the impact of nanoparticle inclusion on the chemical composition of the epoxy matrix is minimal and likely consistent across different concentrations. This, in turn, reinforces the rationale behind excluding chemical characterisation for the lower weight percentages, allowing a more streamlined focus on the physical and microstructural properties that have demonstrated significant relevance in the structural performance analysis, as shown and discussed in this chapter.

As indicated previously (in Section 3.3.3.2) the designation of specimens considered in this chapter followed the form of W-X-Y-Z as follows: "W" indicates the FRP type (C for CFRP, G for GFRP, and B for BFRP), while "X" indicates the type of the bonding agent (i.e. S for silica, Cel for cellulose, Cl for clay and Gr for graphite NMEAs). "Y" is the wt.% of nanomaterials (i.e. 0.1, 0.2 or 0.3) and "Z" specifies the groove size (8, 10 or 12) For example, the specimen C-Gr-0.1-8 is that retrofitted with CFRP bar inserted in an 8x8 mm groove and bonded using graphite NMEAs at 0.1 wt.%.

7.2 Results and discussion

7.2.1 Characterisation of the NE and the NMEAs

7.2.1.1 SEM and porosity analyses

The NMEAs samples were analysed through SEM (Fig. 7.1a) to investigate their microstructure, morphology, in addition to the degree of dispersibility of the nanoparticles through epoxy matrix, and the % porosity analysis was conducted on the images of the samples' surfaces (Fig. 7.1b) and the results are provided in Table 7.1.

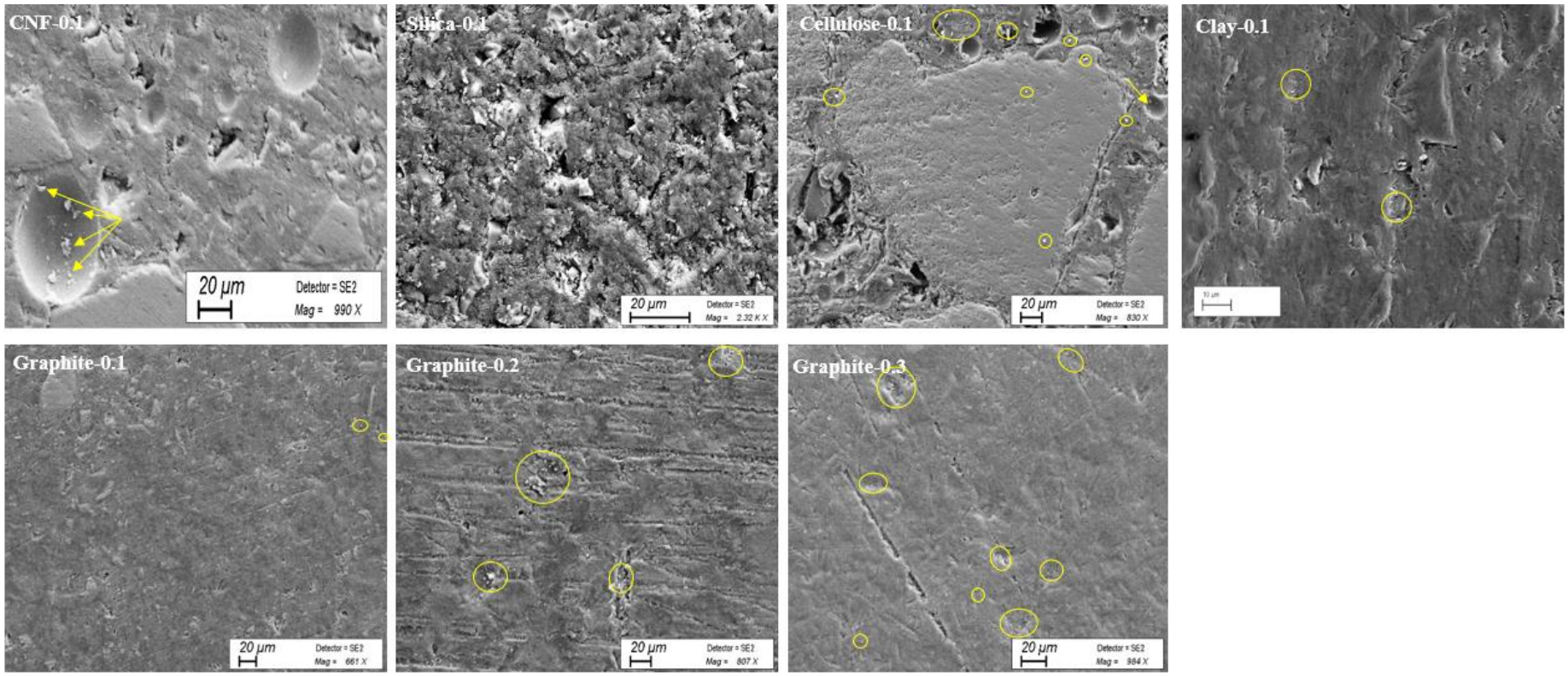
CNF-0.1
20 µm
Detector = SE2
Mag = 990 X
Silica-0.1
20 µm
Detector = SE2
Mag = 2.32 K X
Cellulose-0.1
20 µm
Detector = SE2
Mag = 830 X
Clay-0.1
Graphite-0.1
20 µm
Detector = SE2
Mag = 661 X
Graphite-0.2
20 µm
Detector = SE2
Mag = 807 X
Graphite-0.3
20 µm
Detector = SE2
Mag = 984 X

(a)

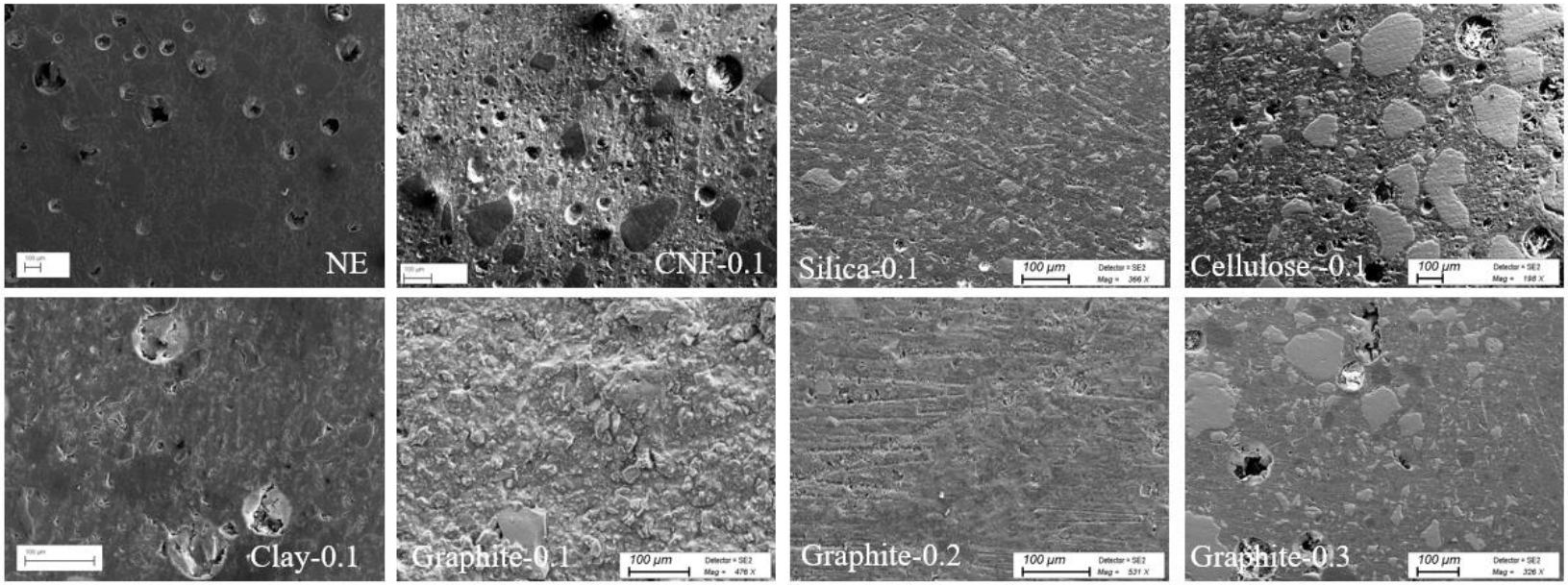

(b)

Fig. 7.1 SEM images of (a) the NE and the NMEAs and (b) their surfaces.

As shown in Fig. 7.1a, the CNF nanocomposite had particles agglomerating within the matrix, while it could be seen that the silica nanoparticles are uniformly-dispersed through the adhesive. Whereas many particles aggregating are shown in the cellulose sample. An insignificant amount of clay particles clustering through the matrix. The graphite-0.1 sample was noticed to have very few agglomerations, which seem to increase with the wt.%.

Table 7.1 % Porosity of the NE and the NMEAs.

Sample	**% Porosity**	**% Porosity increase (+) or decrease (-) compared to the NE**
NE	2.015	-
CNF-0.1	2.407	19.5
Silica-0.1	1.727	-14.3
Cellulose-0.1	2.704	34.2
Clay-0.1	1.814	-10.0
Graphite-0.1	1.386	-31.2
Graphite-0.2	1.492	-26.0
Graphite-0.3	2.228	10.6

For the % porosity, the NE sample has significant amount of air voids showing up on its surface. For the NEMAs, it was observed that the nanoparticles that dispersed well within the matrix could fill the gaps between polymer chains, leading to a more compact structure with fewer voids. In addition to that, those uniformly-dispersed nanoparticles act as nucleation sites for polymer crystallisation (discussed in detail in section 7.2.2), promoting the formation of ordered structures and reducing the occurrence of voids during the curing process.

The presence of the well-dispersed nanoparticles can also enhance the packing efficiency of the epoxy matrix, due to their small size and high surface area, nanoparticles can fit more closely together, reducing the interstitial spaces and minimising porosity. Moreover, some nanoparticles have barrier properties that can hinder the diffusion of gases (i.e. air bubbles) through the matrix. This property can prevent the incorporation of air voids or pockets, contributing to a lower overall porosity. Furthermore, the nanoparticles that have exceptional mechanical properties can reinforce the epoxy matrix and hinder the propagation of micro cracks, consequently reducing porosity associated with crack formation.

On the other hand, it was also observed that the modified nanocomposites could have an increased porosity over than that of the NE, this could be due to that the agglomeration of nanoparticles within the matrix, which would lead to the formation of nanoparticle clusters. These clusters can create localised regions of high viscosity, making it difficult for the epoxy

to flow and fill all the void spaces effectively during curing. As a result, trapped air may be incorporated into the composite, leading to increased porosity. Moreover, uneven dispersion can hinder the nanoparticles from effectively filling the interstitial spaces, creating voids and ultimately increasing porosity. Additionally, the incorporation of nanoparticles can alter the curing kinetics of the epoxy matrix, as they may affect the curing process, leading to incomplete curing and the presence of unreacted or partially reacted epoxy, resulting in increased porosity. Also, the porosity increases as the curing time decreases, which is because of that there would be no enough time for the air bubbles to come out of the samples. So, the faster the curing the higher the porosity.

7.2.1.2 Crystallinity analysis

The % crystallinity of the NE and the NMEAs samples are provided in Table 7.2. The analysis results showed that adding 0.1 wt.% CNF and cellulose to epoxy decreased its crystallinity by about 5 % and 14%, respectively. For the CNF nanocomposites, the crystallinity reduction could be due to that the presence of CNF would create a physical barrier hindering the mobility of epoxy chains and reduce their ability to form ordered structures. As a result, the polymer chains are less able to freely move and align themselves in a regular pattern, which is necessary for the formation of crystalline regions. Moreover, since crystallisation requires the presence of nucleation sites where crystal growth can initiate, the introduction of CNF, in some cases, can disrupt these sites or prevent their formation, leading to a reduced crystallinity. For the cellulose-epoxy nanocomposites, the reduction of crystallinity was ascribed to the strong interaction of the cellulose with the OH groups of the epoxy forming a twisted mass, causing steric effect, which resulted in the destruction of the epoxy-ordered structure, as confirmed in by Kumar et al. [126]. It was also observed that incorporating 0.3 wt.% graphite nanoparticles led to approximately 6% reduction in the crystallinity of the NE, which was ascribed to that, as found by Bhattacharyya et al. [127], the exfoliated state of graphite, which restricted the free movement of polymer chains to arrange themselves in an orderly fashion, hindering the crystallisation and therefore reducing its crystallinity. Moreover, in the case of adding a high concentration of the graphite nanoparticles to the epoxy, the particles act as fillers and could dilute the concentration of the polymer chains. This dilution effect reduces the ability of the epoxy chains to organise and crystallise, leading to a decrease in overall crystallinity of the producing composite.

On the other hand, the epoxy samples filled with 0.1 wt.% silica, clay and graphite (and 0.2 wt.%) nanoparticles yielded about 19%, 6%, 18% and 7% crystallinity increase, respectively.

For the silica nanocomposites, the presence of the silica nanoparticles can enhance the mobility of the epoxy chains during curing and solidification. The improved chain mobility would allow the polymer chains to rearrange more effectively and form well-organised crystalline structures. Moreover, the strong interfacial interactions between the silica nanoparticles and the epoxy matrix can lead to better alignment and arrangement of the chains, contributing to increased crystallinity. The clay nanoparticles can act as templates for the organisation of epoxy chains. In addition, the layered structure of clay provides a favourable environment for the alignment and arrangement of polymer chains, leading to the formation of crystalline regions, and eventually increasing the crystallinity. Graphite nanoparticles can hinder the mobility of epoxy chains during curing and solidification. The hindered chain mobility can restrict the movement of the chains, facilitating the formation of crystalline regions. Furthermore, the enhanced interfacial interactions between graphite nanoparticles and the epoxy matrix have the potential to facilitate improved chain alignment, thereby promoting the process of crystallisation, since the interaction between the nanoparticles and the matrix could influence the conformation and packing of polymer chains.

It's worthy to note that the crystallinity of epoxy can have a significant impact on its mechanical properties and the interfacial bonding characteristic with the matrix material [210]. For instance, since the crystalline regions act as reinforcing elements within the epoxy matrix, the increased crystallinity would provide additional resistance to deformation and enhance the overall strength and stiffness of the material. On the other hand, the less crystalline epoxies are generally more ductile and less prone to brittle fracture compared to the crystalline ones, which may be more rigid and susceptible to brittle failure. These are reflected in the retrofitted results which are discussed in next sections.

Table 7.2 % Crystallinity of the NE and the NMEAs.

Sample	**% Crystallinity**	**% Crystallinity increase or decrease compared to the NE**
NE	65	-
CNF-0.1	61.5	-5.4
Silica-0.1	77.6	19.4
Cellulose-0.1	56.2	-13.5
Clay-0.1	68.7	5.7
Graphite-0.1	76.5	17.7
Graphite-0.2	69.4	6.8
Graphite-0.3	61.2	-5.8

7.2.2 Structural behaviour of retrofitted specimens

As mentioned previously in 7.1, the behaviour of the specimens bonded using various bonding agents was analysed to investigate the effect of different groups of parameters on the structural performance of the retrofitted concrete prisms. The test results are listed in Table 7.3.

Table 7.3 Test results of specimens considered for the effect of FRP reinforcement.

Specimen No.	Specimen code	Max load (kN)			Avg. (kN) (COV)	Max flexural stress (MPa)			Avg. (MPa)	Max displacement (mm)			Avg. (mm) (COV)
		A	B	C		A	B	C		A	B	C	
1	C-NE-8	14.71	15.34	14.20	**14.75 (0.04)**	26.48	27.61	25.56	**26.55**	1.35	1.14	1.31	**1.27 (0.09)**
2	G-NE-8	14.26	16.08	14.24	**14.86 (0.07)**	25.67	28.95	25.63	**26.75**	2.01	1.91	1.60	**1.84 (0.12)**
3	B-NE-8	11.60	16.33	16.62	**14.85 (0.19)**	20.88	29.38	29.92	**26.73**	1.96	2.13	1.98	**2.02 (0.05)**
4	C-CNF-0.1-8	10.27	9.71	8.01	**9.33 (0.13)**	18.48	17.48	14.42	**16.79**	1.85	2.32	1.50	**1.89 (0.22)**
5	C-S-0.1-8	15.41	18.04	18.20	**17.22 (0.09)**	27.74	32.46	32.76	**30.99**	1.45	1.56	1.69	**1.57 (0.08)**
6	C-Cel-0.1-8	11.98	15.73	12.37	**13.36 (0.15)**	21.56	28.32	22.27	**24.05**	1.74	1.64	1.80	**1.73 (0.05)**
7	C-Cl-0.1-8	14.56	15.00	16.79	**15.45 (0.08)**	26.20	27.01	30.22	**27.81**	1.93	1.09	1.50	**1.51 (0.28)**
8	C-Gr-0.1-8	16.68	15.71	18.36	**16.92 (0.08)**	30.02	28.28	33.04	**30.45**	1.29	0.97	1.11	**1.12 (0.14)**
9	G-Gr-0.1-8	16.11	13.25	16.82	**15.39 (0.12)**	28.99	23.84	30.27	**27.70**	1.81	1.72	2.03	**1.85 (0.09)**
10	B-Gr-0.1-8	14.49	18.07	13.05	**15.20 (0.17)**	26.09	32.52	23.48	**27.36**	1.73	1.84	2.40	**1.99 (0.18)**
11	C-Gr-0.1-10	13.28	17.74	17.12	**16.05 (0.15)**	23.90	31.94	30.82	**28.89**	2.23	1.74	1.50	**1.82 (0.20)**
12	C-Gr-0.1-12	21.62	20.22	15.35	**19.06 (0.17)**	38.91	36.39	27.63	**34.31**	1.38	1.67	0.89	**1.31 (0.30)**
13	C-Gr-0.2-12	15.91	19.20	20.19	**18.43 (0.12)**	28.63	34.56	36.35	**33.18**	1.55	1.28	1.60	**1.48 (0.12)**
14	C-Gr-0.3-12	10.54	12.77	13.27	**12.19 (0.12)**	18.97	22.99	23.89	**21.95**	1.95	1.71	1.12	**1.59 (0.27)**
18	C-NE-10	17.54	23.70	23.75	**21.67 (0.16)**	31.57	42.66	42.74	**38.99**	1.53	1.81	1.49	**1.61 (0.11)**
19	C-NE-12	11.29	14.57	13.09	**12.98 (0.13)**	20.33	26.22	23.56	**23.37**	1.78	2.08	1.67	**1.84 (0.12)**

7.2.2.1 The effect of bonding agent type

7.2.2.1.1 Overall flexural capacities and ductility response

The comparison begins with the C-NE-8 with those bonded with the NMEAs. Using the CNF-modified epoxies led to a significant drop of about 37% in the specimens' capacities. This could be due to potentially poor dispersion of the CNF into epoxy, which caused the formation of agglomerates within the epoxy body, as shown in Fig. 6a. Only 0.1 wt.% was high enough to allow the particle-to-particle interaction instead of the intended particle-to-polymer interaction. Once it reaches this state, the particles begin to agglomerate forming clusters, which ultimately affect the Van der Waals interaction between the polymer chains, reduce the cross-linking and increase (about 20%) the void content of the matrix (i.e. porosity) (Table 7.1) in the nanocomposite. The resulting mechanical properties are therefore degraded. Furthermore, the agglomerations and the high void ratio are also expected to lead to a weak interface between nanoparticles and epoxy due to stress concentration at the areas of agglomerations, resulting in poor interfacial stress transfer. This eventually impaired the bonding between adhesive and concrete substrate. Moreover, due to the cotton-like nature of the CNF and its high volume-to-weight ratio, using such materials leads to thicker adhesive layer, which yielded a decrease in the adhesion properties, as confirmed by Tomblin et al. [130], which eventually led to a premature failure. Moreover, the low SSA (as shown in Table 3.3) of the CNF could limit the interaction between the nanoparticle with the matrix, which in turn contributed to a weaker interfacial bonding and resulted in poor stress transfer, which ultimately deteriorated the overall capacity of the specimen.

About 9% capacity drop was observed for specimens bonded with cellulose-epoxy nanocomposites. This was attributed to the particles' agglomeration alongside the huge increase (about 34%) in the % porosity compared to the NE, that would negatively impact the interfacial adhesion and therefore the stress transfer, as they act as "contraindications" for particle-matrix bonding, and they are also considered as stress concentration generators. All these reasons would influence the interfacial adhesion, and ultimately the overall performance of the retrofitting system.

On the other hand, a capacity increase of about 15% was observed in the specimens retrofitted using graphite-modified epoxies. These improvements were apparently due to the uniform dispersion of the nanoparticle into matrix preventing the formation of agglomeration, which in turn enhanced the interfacial adhesion between epoxy and the nanoparticle, leading to a higher effective interfacial area in the composite. This good bonding leads to an improvement in mechanical properties the nanocomposites, as found by Kumar et al. [158], which reflected on

the interfacial bonding with FRP reinforcement and concrete, leading to the improved performance.

Furthermore, the high SSA of the graphite nanoparticles, due to their high aspect ratio, provided a huge surface area to interact with the matrix, leading to a higher effective interfacial area in the composite, resulting in efficient stress transfer from matrix to particles ant to matrix, enhancing the interfacial adhesion between the matrix and the particle and hindering in polymer chain mobility [158], and eventually improving the mechanical properties of the matrix. Moreover, the uniform dispersion of graphite nanoparticles within the epoxy matrix as shown in Fig. 4a of the graphite-epoxy nanocomposites indicates the good compatibility between the nanoparticles and the epoxy matrix in addition to the rough surface of the nanocomposite, which made the crack propagation difficult and less prone to breakage. Moreover, the significant decrease in the void content by about 31% also expected to reduce the stress concentration and provides more uniform stress transfer. All the previous reasons would contribute to the good performance of the nanocomposites under mechanical loading, which reflected on the overall performance of the retrofitting process.

About 17% and 5% capacity increase, respectively was observed in the specimens retrofitted using silica- and clay-modified epoxies. The capacity enhancement in the silica specimens was attributed to the uniformly dispersed nanoparticles over the entire body of the matrix, as shown in Fig 4a, which in turn provided strength for the Nano-phased composites and eventually translated into improved mechanical properties, as observed in [165]. The reduction in void content of the matrix by about 14% in addition to the increased crystallinity gave rise to a more compact Nano-phased composites, leading, ultimately, to the enhanced mechanical performance (flexural capacity in this context). Inherent toughening properties of the Nano-silica may also contribute to increasing the strength of the epoxy adhesive [211]. Moreover, the high SSA of the silica nanoparticles could also contribute to the improved performance, due to similar reasons mentioned earlier (i.e. in the graphite specimens).

The enhancement in the mechanical properties of the epoxy by the addition of the clay nanoparticles was reflected on the overall capacities of the retrofitted specimens. It was found that filling the matrix with clay nanoparticles would ensure more viable sites for polymer and nanoparticles interaction [115]. Nano clays are dispersed in epoxy, ring-opening reactions took place followed by higher crosslinking between epoxy molecules, which resulted in interlocking resin-nanoparticles structure in the matrix and might improve the interfacial bonding strength, facilitating stress transfer when loaded, enhancing the mechanical properties (i.e. strain at failure)

of the matrix. Further explanation was provided by Huttunen-Saarivirta et al. [167] that the homogeneous dispersion of the clay nanoparticles within epoxy, which led to the interfacial bond strength between the nanoparticles and the matrix, showed an improved tensile strength and elongation at break, which (the latter) best reflected the uniformity of stress distribution. Moreover, Shi et al. [212] reported that the addition of the clay nanoparticles to epoxy matrix led to more integrated micro- and Nano-structures, through occupying the free volume, such as voids and defects that yields enhanced cross-linking density and crystallinity, improving in the mechanical properties of the matrix. In addition to that, the very high SSA of the clay nanoparticles alongside the 10% porosity reduction could also contribute to the enhanced performance, as explained earlier in the case of the silica specimens. On the other hand, although the particles aggregations showing in the clay nanocomposites (Fig. 7.1a) did not contribute to decrease the capacity, but they hindered achieving higher ductility enhancement. This was because of similar justifications to that reported previously.

Filling epoxy with CNF and cellulose yielded about 49% and 36% ductility increases compared to NE, which could likely be driven by plasticisation of epoxy cross-link network domains, in addition to the decreased crystallinity, which would provide the polymer chains with more freely movement. In contrast to that, about 12% reduction was observed in the graphite specimens, which could be due to the stiffening effect of graphite nanoparticles on the epoxy, which would limit the deformation capacity [211], which could also be due to its increased crystallinity.

Unlike what was noticed in the carbon-based specimens, both strength and ductility of silica and clay modified epoxy bonded retrofitted concrete increased compared to the NE-bonded ones, with about 19% and 24% increase in ductility. This may be ascribed to the same mechanism took place for the enhanced strength, as discussed previously. Additionally, the silicon-based nanoparticles can help redistribute stresses during mechanical loading. Hence, these nanoparticles may act as stress transfer mediators, redistributing stress from the polymer matrix to the nanoparticles, thereby preventing localised failure and enhancing overall ductility.

In contrast with that was observed in specimen C-Gr-0.1-8 compared to its control version (i.e. C-NE-8), specimen C-Gr-0.1-10 showed about 35% capacity decrease with accompanying ductility increase of approximately 13% compared to C-NE-10. The reason for this is still unclear. On the other hand, it was observed that, compared to the control specimen (C-NE-12), C-Gr-0.1-12 showed about 47% capacity increase with, conversely, about 29% ductility drop. Both capacity increase and ductility decrease could be due to the same reasons mentioned previously (i.e. in C-Gr-0.1-8).

For the GFRP-retrofitted specimens, which were bonded with NE or graphite-modified epoxy at 0.1 wt.%, it was found that using the modified adhesive yielded a slight increase in the ultimate load and displacement of about 4% and 1%, respectively over that bonded using NE, while for those retrofitted with BFRP bars, only about 2% enhancement in the load-capacity was observed, however, the ductility decreased by about 2%. Fig. 7.1 represents the test results of the CFRP- (a, b and c), GRRP- (d) and the BFRP- (e) retrofitted specimens, respectively.

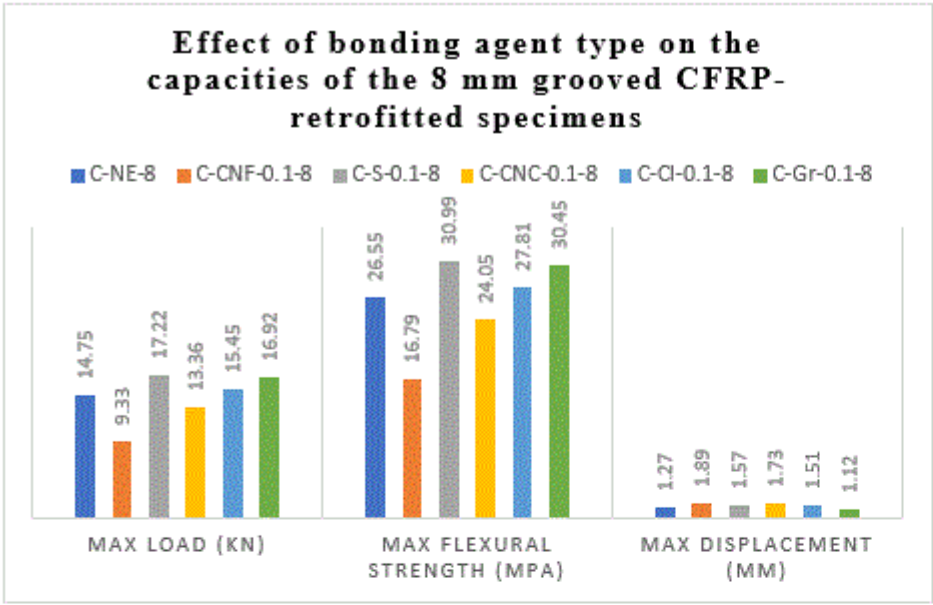
Effect of bonding agent type on the capacities of the 8 mm grooved CFRP-retrofitted specimens
C-NE-8
C-CNF-0.1-8
C-S-0.1-8
C-CNC-0.1-8
C-CI-0.1-8
C-Gr-0.1-8
14.75
9.33
17.22
13.36
15.45
16.92
26.55
16.79
30.99
24.05
27.81
30.45
1.27
1.89
1.57
1.73
1.51
1.12
MAX LOAD (KN)
MAX FLEXURAL STRENGTH (MPA)
MAX DISPLACEMENT (MM)

(a)

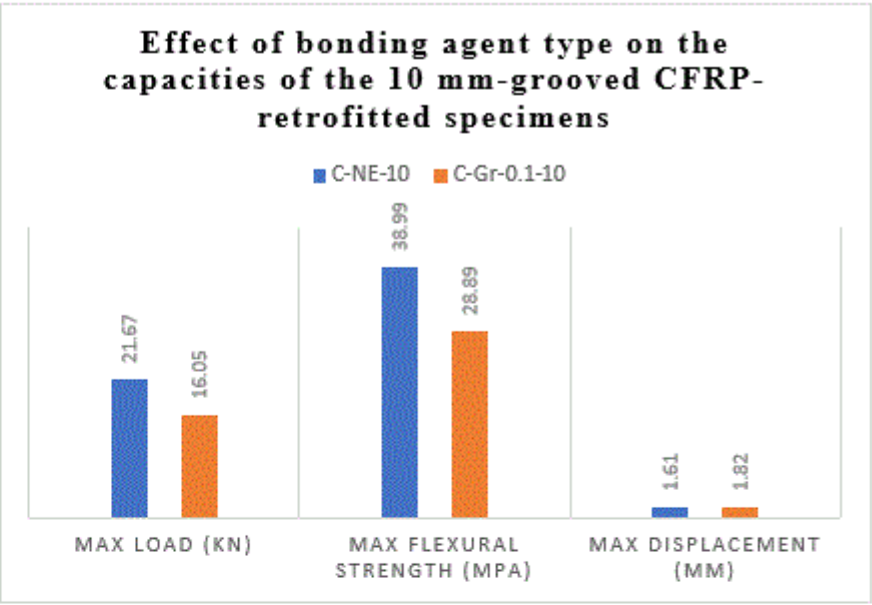
Effect of bonding agent type on the capacities of the 10 mm-grooved CFRP-retrofitted specimens
C-NE-10
C-Gr-0.1-10
21.67
16.05
38.99
28.89
1.61
1.82
MAX LOAD (KN)
MAX FLEXURAL STRENGTH (MPA)
MAX DISPLACEMENT (MM)

(b)

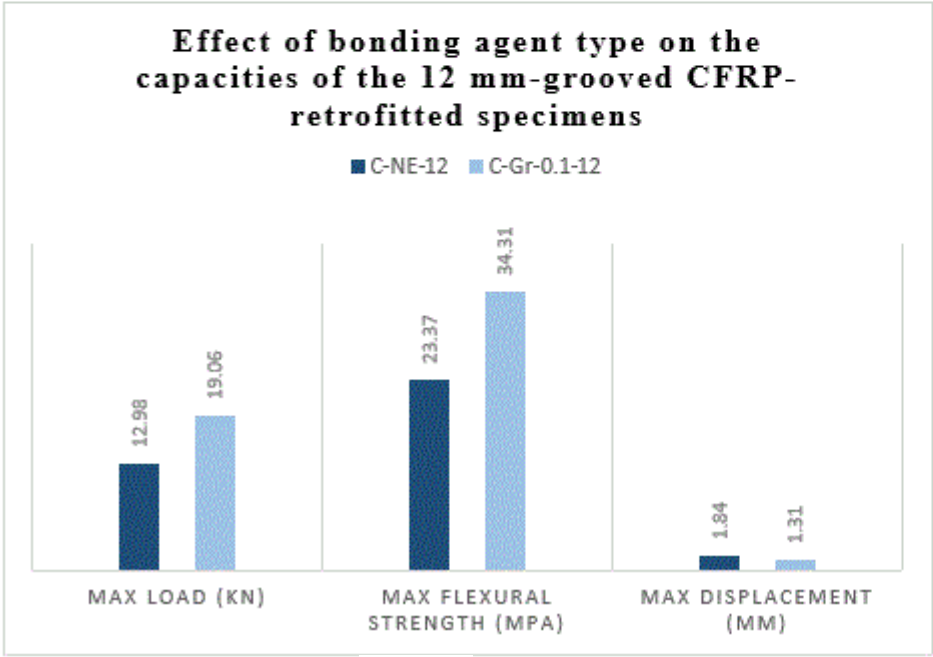
Effect of bonding agent type on the capacities of the 12 mm-grooved CFRP-retrofitted specimens
C-NE-12
C-Gr-0.1-12
12.98
19.06
23.37
34.31
1.84
1.31
MAX LOAD (KN)
MAX FLEXURAL STRENGTH (MPA)
MAX DISPLACEMENT (MM)

(c)

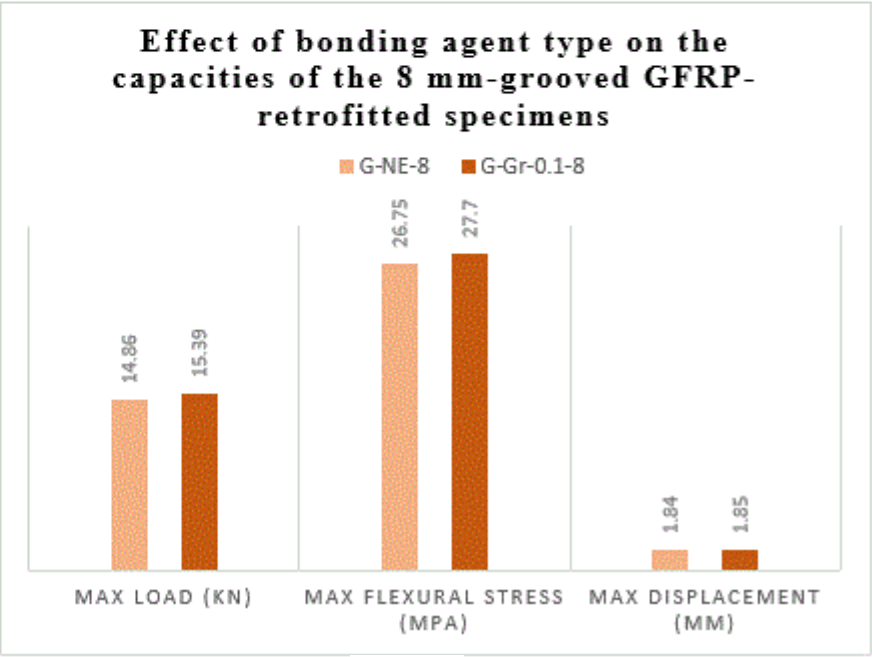
Effect of bonding agent type on the capacities of the 8 mm-grooved GFRP-retrofitted specimens
G-NE-8
G-Gr-0.1-8
14.86
15.39
26.75
27.7
1.84
1.85
MAX LOAD (KN)
MAX FLEXURAL STRESS (MPA)
MAX DISPLACEMENT (MM)

(d)

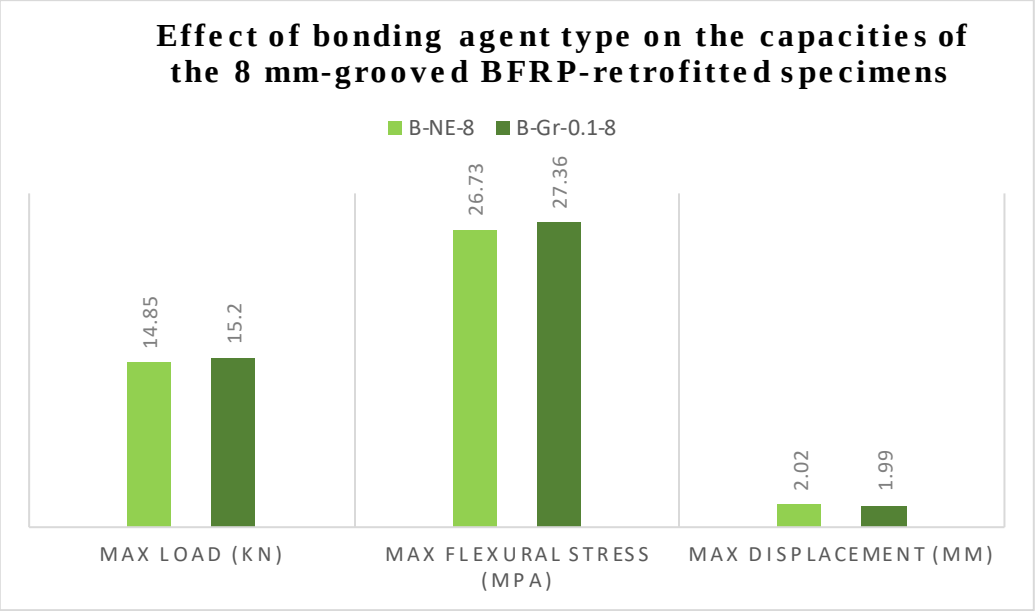

(e)

Fig. 7.2 Effect of the type of the bonding agent on the capacities of the (a) 8 mm-grooved, (b) 10 mm-grooved, (c) 12 mm-grooved CFRP- retrofitted specimens, (d) 8 mm-grooved GFRP- and (e) BFRP-retrofitted specimens.

7.2.2.1.2 Failure modes

It can be seen in Fig. 7.3 that C-NE-8 mainly failed due to shear cracks that arose into concrete and epoxy layer, in addition to CFRP bar slippage that occurred in specimen B. C-CNF-0.1-8, which was retrofitted with CNF-modified epoxy, failed in flexure (i.e. A and B), as the adhesive layer was not strong enough to stop the crack from crossing it, which also passed to the other side. A mixed shear and flexural failure were noticed in specimen C, where the shear cracks led to partial concrete crushing accompanied by cohesive failure in the adhesive layer, which was due to, as reported earlier, the particles' agglomeration that negatively influenced the bond at the interface. So, the adhesive remained fully attached to the concrete substrate and to the CFRP bar, and no debonding took place. Bonding CFRP by epoxy-CNCs nanocomposites led specimen C-Cel-0.1-8 to fail in shear, with more minor cracks showing up on the concrete surface. The shear cracks caused small parts of concrete to peel off, but no debonding was detected. For specimen C-Gr-0.1-8, that was bonded with graphite nanocomposite, a shear failure in specimens A and C, represented by a major shear crack, appeared in the concrete body with a short tail continued to align with the adhesive line. Specimen B exhibited a similar failure mode, but with smaller (i.e. less wide) shear crack, which gave the opportunity to the flexural crack to generate, which had longer tail lying on the edge of the adhesive line, but without breaking through it.

The C-S-0.1-8 that was retrofitted with CFRP alongside silica-modified epoxy mainly failed in shear, where the shear crack that passed through concrete and aligned with the concrete-adhesive

interface could be curbed by the adhesive layer. More importantly, the shear cracks in specimen A had long tails aligning with the adhesive line, causing minor debonding failure at the bar-epoxy interface accompanied with cohesive failure. However, a stronger bond at the interfaces can be seen in specimens B and C, as no debonding was observed. Some minor cracks, especially in specimen C, appeared on the concrete surface. For specimen C-Cl-0.1-8 that was retrofitted using epoxy-clay nanocomposites, all specimens generally failed due to shear cracks, which had long extensions in specimens A and B aligning with the adhesive line from both sides of the specimens yielding a cohesive failure escorted with partial concrete crushing. The shear crack in specimen C, which failed at the highest ultimate load, was not able to affect the interfaces and its tail could not extend long beside the adhesive line.

For the 10 mm-grooved specimens, it was noticed that the shear failure was the governing failure mode in specimen C-NE-10, where almost the same failure modes took place in specimens A and B, as a main shear crack produced in the middle of the specimens from the bottom and kept progressing to break through the epoxy layer with a short tail along the edge of the epoxy line until, eventually, broke through it to the other side. Similar details were observed in specimen C, but one more shear crack generated with longer tail, but it kept beside the epoxy line without passing through it. No debonding was remarked in any of the specimens. Specimen C-Gr-0.1-10 failed in shear, similarly to what was observed in the C-NE-10, but more minor cracks appeared on the concrete surface at failure, which is linked to the failure with higher ductility. Furthermore, the main crack was observed to break through the adhesive line, leading to minor concrete crushing in A and B.

The specimen C-NE-12 (A, B and C) failed in shear, where a major shear crack began created and progressed through concrete without breaking through the adhesive layer, it leading, eventually, to minor concrete crushing. Some additional cracks also generated in specimens A and C. Bonding the CFRP reinforcement with epoxy modified with 0.1 wt.% graphite (i.e. specimen C-Gr-0.1-12) resulted in a pure shear failure mode. One main shear crack was produced in specimens A and C, while multiple cracks were found to generate in specimen B. The adhesive line was not able to curb the cracks from progressing, where they could penetrate the adhesive line and cross it (in specimens B and C) to the other side of the specimens, which yielded concrete in specimen B to peel off and also resulted in minor debonding failure at the concrete-adhesive interface.

The second group to be considered, as mentioned earlier, includes the specimens retrofitted with GFRP bars alongside NE (i.e. G-NE-8) and graphite-modified epoxy (i.e. G-Gr-0.1-8). The

failure modes of both specimens were previously discussed. Specimens G-NE-8-A, B and C failed due to flexural crack that broke through the epoxy layer leading it to peel off at the bar-epoxy interface in specimen A. Crushing of a part of concrete was also observed in specimens A and B. For G-Gr-0.1-8, flexural failure was noticed in A, while a combined flexural and shear failure mode occurred in B and C. The cracks were observed to penetrate the adhesive line to the other side of the specimens and continued their way into through concrete, but with no debonding at the interfaces or concrete detachment. Therefore, in the GFRP-retrofitted specimens, using graphite-modified epoxy adhesive instead of NE could enhance the bond at the interfaces, as no debonding mode of failure or concrete detachment took place.

The BFRP-retrofitted specimens alongside NE (i.e. B-NE-8) and graphite-modified epoxy (i.e. B-Gr-0.1-8) are comprised in the third group. Modes of failure of both specimens are included in a previous section. In specimens B-NE-8-A and B, a mixed shear and flexural failure mode was observed, where main flexural crack alongside minor shear crack extended to align with the adhesive line at the concrete-epoxy interface. In specimen A, the crack was noticed to further progress leading parts of concrete to peel off with thin layers of epoxy stuck on them. Specimen C mainly failed in shear, but the shear cracks did not align with the epoxy line, but alternatively crossed it only in one place. Moreover, the epoxy line could limit the crack to progress to the other end of the specimen. For specimens B-Gr-0.1-8, the flexural cracks that formed in specimens A and B and the shear crack in C extended to progress next to concrete-adhesive interface border but without penetrating the adhesive line. So, it can be concluded that using the graphite-modified adhesive rather that NE, in the BFRP-retrofitted specimens, contributed to a stronger bond at the concrete-adhesive interface, as no cracks could break through the adhesive line at the interface.

(a)

(b)

(c)

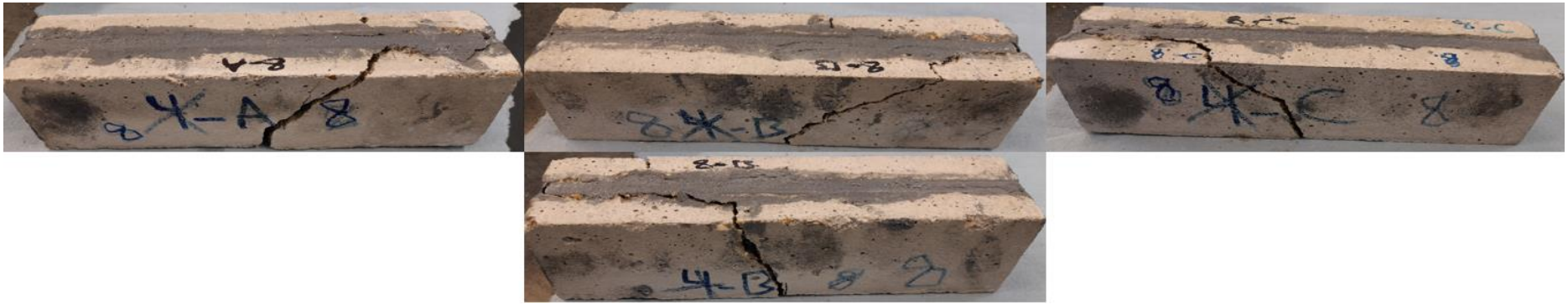

(d)

(e)

(f)

(g)

(h)

(i)

(j)

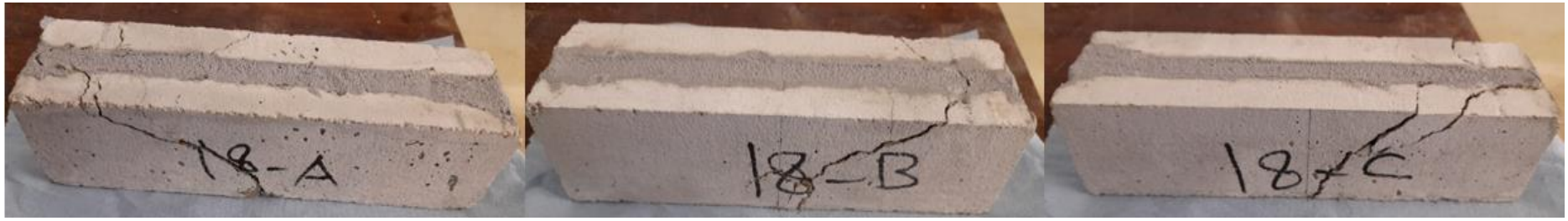

(k)

(l)

(m)

(n)

Fig. 7.3 Failure modes of specimens (a) C-NE-8, (b) G-NE-8, (c) B-NE-8, (d) C-Gr-0.1-8, (e) G-Gr-0.1-8, (f) B-Gr-0.1-8, (g) C-CNF-0.1-8, (h) C-S-0.1-8, (i) C-Cel-0.1-8, (j) C-Cl-0.1-8, (k) C-NE-10, (l) C-Gr-0.1-10, (m) C-NE-12 and (n) C-Gr-0.1-12.

7.2.2.2 The effect of the nanoparticles used in the NMEAs

7.2.2.2.1 Overall flexural capacities and ductility response

First, for the specimens bonded with epoxy adhesive loaded with carbon-based nanoparticles, e.g. CNF, cellulose and graphite, the specimens retrofitted using epoxy modified with graphite gave the best performance compared to the ones loaded with CNF and cellulose nanocomposites, resulting in about 81% and 27% higher ultimate loads, respectively compared to those retrofitted with CNF- and cellulose-modified epoxies. This could be due to (I) the highest % crystallinity accompanied with the lowest % porosity and (II) the agglomeration-free appearance seen in the graphite nanocomposites alongside the rough surface of the composite. The non-formation of the agglomerations could be due to the higher SSA of the graphite nanoparticles compared to those of the other nanoparticles, which could contribute to the uniform dispersion of the particles within the adhesive body, resulting in the better performance. Moreover, the highest density of the graphite particles among the carbon-based particles could lead to "densify" the nanocomposites, minimising the pores in the adhesive body, that act as stress concentration areas and facilitate the crack propagation, providing more favourable stress transfer and better mechanical performance.

The specimens retrofitted with cellulose nanocomposites failed at about 43% higher ultimate load than that retrofitted by CNF nanocomposites. This was because of the CNF particles, as shown in Fig. 6a, were agglomerating in larger clusters within the adhesive body compared to the small agglomerating cellulose particles that were scattered throughout the adhesive body. Therefore, the gathering of agglomerates in the form of large bundles, as shown in the CNF, could eventually lead to higher stress concentration and less efficient stress transfer process, deteriorating the interfacial bond strength, that directly affected the capacities of the specimens. Furthermore, the better performance provided by the cellulose nanocomposites could also be due to the powder nature of the cellulose nanoparticles rather than the cotton-like nature of the CNF nanoparticles, which had a negligible effect on the thickness of the adhesive layer and eventually on the adhesion strength.

It is noteworthy that although the cellulose nanoparticles have lower SSA and density than the CNF, which were expected to better enhance the performance of the specimens bonded with the CNF-epoxy than those bonded with cellulose nanocomposites, the reasons mentioned above seem to have "stronger" impact in lowering the specimens' capacities. However, the effect of the better physical properties alongside the higher % crystallinity of the CNF nanocomposites compared to those of the cellulose might reflect on the ductility response, as

the specimens bonded with CNF nanocomposites were more ductile showing about 9% higher ductility at failure than those bonded with cellulose-modified epoxies. It was also observed that the latter were about 35% more ductile than those bonded with graphite nanocomposites, which showed about 41% more brittle behaviour than those bonded with the CNF nanocomposites, which could be ascribed to the high % crystallinity, which is known to increase the brittleness of the composite, as discussed earlier.

Second, in regard with using epoxy filled with silicon-based nanoparticles (i.e. silica and clay), even though the SSA of the Nano clay is much higher than that of the silica particles, which have also less density, lower capacities and ductility were obtained with the specimens bonded with the clay nanocomposites. The specimens bonded using silica-modified epoxy exhibited about 11% and 4% increase in the capacity and ductility, respectively over those bonded with clay NMEAs. This could be due to that the size of the silica nanoparticles, as shown in Table 5, is about 50 times smaller than that of the clay ones, which led the silicon particles to disperse more uniformly within the epoxy preventing the formation of agglomeration unlike what was observed in the clay nanocomposites, leading to enhanced interfacial bonding and resulting in more efficient interfacial stress transfer, which ultimately yielded better overall performance. The higher crystallinity and lower % porosity of the silica nanocomposites also contributed to the better behaviour.

Higher increase of capacity resulted from the silicon-based nanocomposites could be due to the lower % porosity and the higher % crystallinity. This behaviour could be also due to the fact that the van der Waals interactions between molecules are much stronger in the carbon-based materials, especially in the CNF, causing them to aggregate into entangled bundles that prevent the formation of uniform and optimal materials [131]. This would eventually lead to that the nanoparticles would not be able to provide the epoxy with their ultimate enhancement capacity, which ultimately cannot be fully utilised. However, using carbon-based nanoparticles could improve the specimens' ductility slightly more than that in the case of using the silicon-based ones, which could be owing to their lower % crystallinity.

Consequently, it was found that the specimens bonded with epoxy modified with silicon-based nanoparticles showed, on average, about 24% higher capacities than those bonded using epoxy loaded with carbon-based nanoparticles, which, on the other hand, showed about 3% more ductile behaviour.

A comparison between using the carbon-based and the silicon-based nanocomposites, as bonding agents, in terms of specimens' capacities and the ductility is shown in Fig. 7.4.

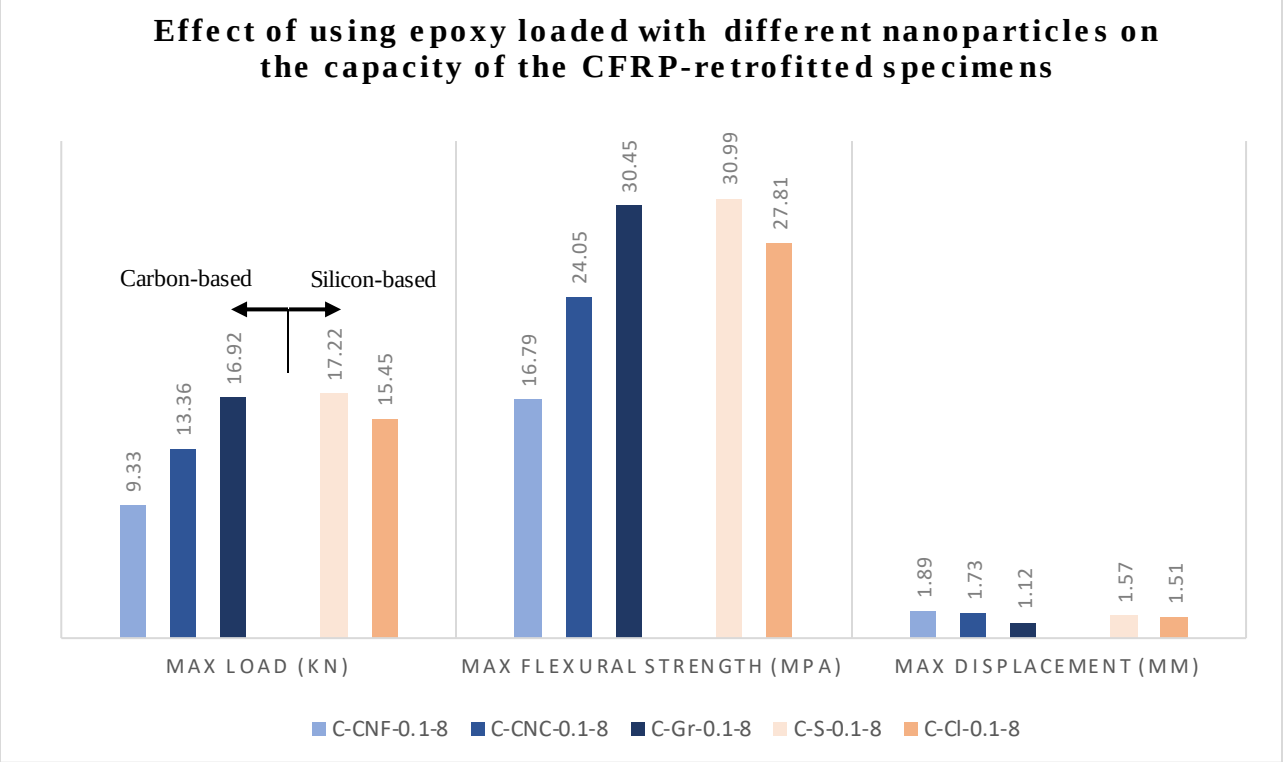

Fig. 7.4 Effect of using different nanoparticles in the NMEAs on the capacities of the CFRP-retrofitted specimens.

7.2.2.2.2 Failure modes

The failure modes were previously discussed in detail in section 7.2.1.2. It was found that the specimens retrofitted using silicon-epoxy nanocomposites mainly failed in shear, while a mixed shear and flexural failure mode was observed in those retrofitted using carbon-epoxy nanocomposites. Moreover, the debonding at bar-adhesive interface (i.e. bar slippage) could be avoided by using epoxy reinforced with carbon-based nanoparticles, while using epoxy loaded with silicon-based nanoparticles was not able to prevent the debonding failure, which happened at the bar-epoxy interface with using silica-epoxy nanocomposites.

7.2.2.3 The effect of the wt.% concentration of the nanoparticles (i.e. graphite)

7.2.2.3.1 Overall flexural capacities and ductility response

Graphite nanoparticles, as a representative, were employed to further study the effect of concentration (wt.%), that is, the epoxies filled with 0.2 and 0.3 wt.% graphite nanoparticles were used to bond the concrete specimens prepared for that purpose. It can be seen that capacities decreased with increasing the wt.% concentration of the nanoparticle used to prepare the nanocomposites. Where about 3% and 36% capacity reduction were observed, respectively

with doubling (i.e. 0.2 wt.%) and tripling (i.e. 0.3 wt.%) the graphite wt.% incorporated into epoxy. In addition, increasing the graphite wt.% from 0.2 to 0.3 wt.% decreased the capacity by about 34%. The capacity drop took place with the wt.% was ascribed to multiple reasons; (I) the increasing agglomerations with the concentration, as shown in Fig. 7, that, as discussed previously in more detail, could deteriorate the adhesion properties of epoxy, which weakened the interfacial bond yielding premature failure of the specimen, (II) the increase in the % porosity by about 8% and 61%, respectively with doubling and tripling the wt.%, which also negatively affected the performance, as discussed in section 7.2.1.1, and (III) the increased crystallinity which has its effect explained previously, which in turn led the specimens' ductility response to improve, where doubling and tripling the wt.% resulted in about 11% and 21% ductility increase, respectively, while moving from 0.2% to 0.3% enhanced the ductility by about 7%. Fig. 7.5 represents the effect of the wt.% of the nanoparticles (i.e. graphite) on the capacities of the CFRP-retrofitted specimens.

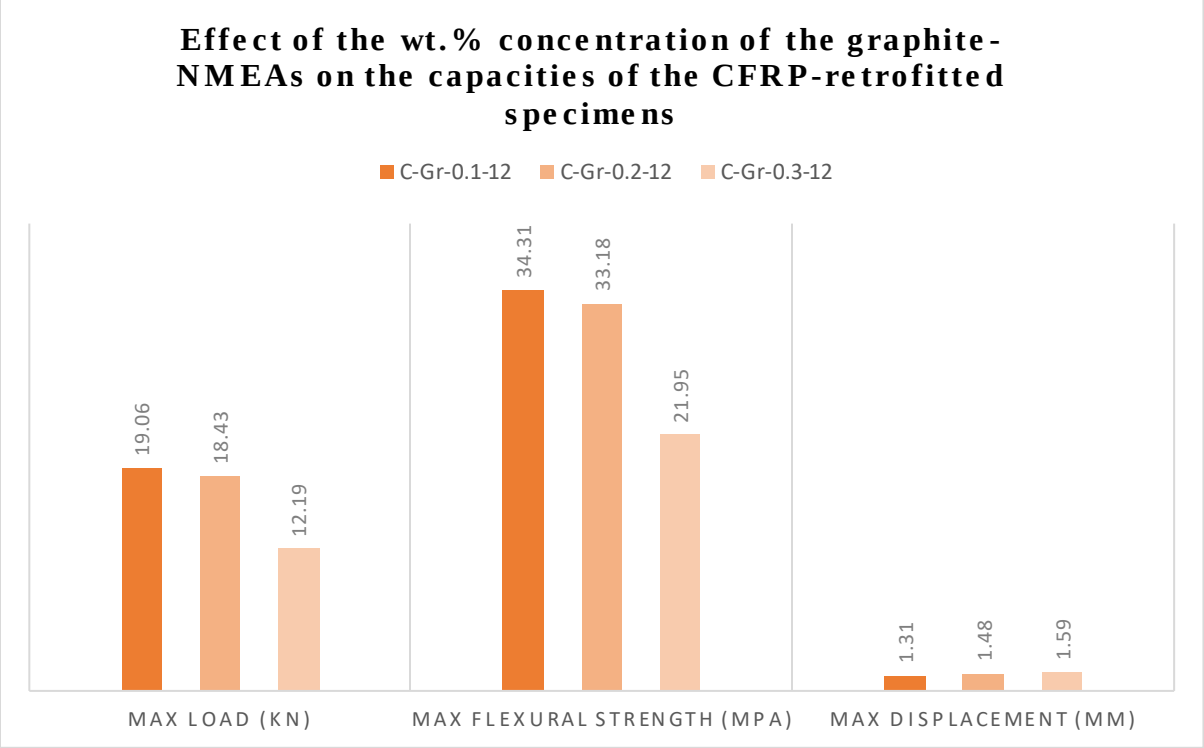

Fig. 7.5 Effect of graphite NMEAs wt.% concentration on the capacities of the CFRP-retrofitted specimens.

7.2.2.3.2 Failure modes

Specimen C-Gr-0.1-12, as discussed in section 7.2.1.2, failed due to pure shear failure mode. Using epoxy loaded with 0.2 wt.% of graphite led specimen C-Gr-0.2-12 to fail in a similar mode to that of C-Gr-0.1-12, but in a more ductile way, as more minor cracks showed up at failure. Moreover, no debonding failure or concrete detachment took place. Finally, specimens

C-Gr-0.3-12-A, B and C failed due to shear cracks, which led to partial concrete crushing. However, the adhesive line was strong enough to prevent the cracks from penetrating it, since these specimens (i.e. C-Gr-0.3-12 B and C) showed the most ductile behaviour compared to the previous ones (i.e. C-Gr-0.1-12 and C-Gr-0.2-12). Compared to using NE (C-NE-12), bonding the 12 mm-grooved specimens with the NMEAs could minimise the concrete crushing failure, even though it reduced the ductility. The failure modes of specimens C-Gr-0.2-12 and C-Gr-0.3-12 are illustrated in Fig. 7.6.

(a)

(b)

Fig 7.6 Failure modes off specimens (a) C-Gr-0.2-12 and (b) C-Gr-0.3-12.

7.3 Summary

In this chapter, the effect of using different bonding agents (i.e. NE and NMEAs) on the efficiency of the NSM-FRP flexural retrofitting of concrete was examined and achieved through a comprehensive experimental programme, including mechanical testing (i.e. three-point bending tests), microstructural (i.e. SEM analysis) and physical (i.e. XRD measurements) characterisations. A thorough investigation of the performance analysis, in terms of the maximum capacities and failure patterns, was conducted considering the effect of using the NMEAs rather than the NE, investigating the most efficient NMEAs and their wt.% concentration (belong to graphite NMEAs) to be used for the optimum retrofitting process of concrete members, in terms of their mechanical strength and interfacial bond behaviour. The main conclusions can be inferred from the results acquired, as follows:

- A consistent correlation was observed between the SEM and the XRD results, where the NMEAs specimens with high agglomeration and high % porosity had low values of % crystallinity and vice versa. These characteristics had a direct effect on the mechanical behaviour of the nanocomposites in the retrofitting system.

- Compared to specimens bonded with NE, using CNF and cellulose NMEAs reduced the capacities by about 37% and 9%, respectively, which was due to the weak interfacial bonding caused by particles' agglomeration and the high % porosity of the produced nanocomposites. Nevertheless, significant increases in ductility of about 49% and 36% were achieved.

- Bonding specimens with silica-, clay- and graphite-modified epoxies resulted in capacity increases of approximately 17%, 5% and 15%, respectively, over those bonded with NE. However, the higher crystallinity of the graphite nanocomposites led to about 12% ductility reduction in the graphite-epoxy-bonded specimens, while using silica and clay nanocomposites resulted in about 19% and 24% ductility enhancement, respectively.

- Overall, the specimens retrofitted with silicon-based-modified epoxies resulted in higher ultimate loads compared to those retrofitted with carbon-based-loaded ones, which, on the other hand, exhibited better ductility response.

- About 35% capacity decrease with accompanying ductility increase of approximately 13% were achieved by the 10 mm-grooved specimens (i.e. C-Gr-0.1-10) compared to C-NE-10.

- Bonding the 12 mm-grooved specimens with 0.1 wt.% graphite nanocomposites (i.e. C-Gr-0.1-12) increased the capacity by about 47%, but led to about 29% ductility reduction.

- Using epoxy filled with carbon-based nanoparticles rather than NE was able to prevent the interfacial debonding and switched the failure mode, as occurred in C-CNF-0.1-8, from shear to flexural. While slight debonding at the bar-adhesive interface was observed in the specimens retrofitted using silicon-based NMEAs (i.e. silica nanocomposites) accompanied with cohesive failure in the adhesive layer alongside minor concrete crushing. However, the concrete-adhesive interfacial bonding could be kept intact and the shear failure mode was maintained.

- The specimens retrofitted with silicon-epoxy NMEAs predominantly failed in shear, whereas a mixed shear and flexural failure modes were exhibited by those retrofitted with carbon-epoxy NMEAs.

- Using the graphite NMEAs rather than NE to bond the 10 and the 12 mm-grooved specimens did not affect the failure modes, in which the former failed in shear while the latter failed due to shear and concrete crushing.

- The capacities of NMEAs-bonded retrofitted concretes decreased as the wt.% concentration of the nanoparticles (i.e. graphite) increased because of nanoparticles' agglomeration within the epoxy body beside the increase in the void content and the crystallinity decrease. However, a ductility enhancement with the concentration was observed.

- Bonding specimens with epoxy filled with nanoparticles at different wt.% had trivial effect on the failure modes, where all specimens mainly failed in shear, with minor concrete crushing noticed in C-Gr-0.3-12.

Chapter 8: Influence of groove size on the NSM-FRP retrofitting efficiency

8.1 Introduction

The influence of using different groove sizes on the specimens' behaviour, in terms of their capacities and modes of failure, are shown and discussed in this chapter. Three square grooves dimensions, that is, 8x8-, 10x10- and 12x12 mm with b/d_b of 1.33, 1.67 and 2.00, respectively were considered for this purpose, represented through five different groups of specimens, as shown in Table 3.7. The first two groups include the specimens that were retrofitted with CFRP bars alongside NE and with 0.1 wt.% graphite-filled epoxy, respectively. The third and fourth groups, respectively include the specimens retrofitted with GFRP bars fixed, with NE, either in the middle and on the edge of the grooves. The specimens retrofitted with NE only were considered in the last group. The test results are provided in Table 8.1.

Table 8.1 Test results of specimens considered for the effect of groove size.

Specimen No.	Specimen code	Max load (kN)			Avg. (kN) (COV)	Max flexural stress (MPa)			Avg. (MPa)	Max displacement (mm)			Avg. (mm) (COV)
		A	B	C		A	B	C		A	B	C	
1	C-NE-8	14.71	15.34	14.20	**14.75 (0.04)**	26.48	27.61	25.56	**26.55**	1.35	1.14	1.31	**1.27 (0.09)**
2	G-NE-8	14.26	16.08	14.24	**14.86 (0.07)**	25.67	28.95	25.63	**26.75**	2.01	1.91	1.60	**1.84 (0.12)**
8	C-Gr-0.1-8	16.68	15.71	18.36	**16.92 (0.08)**	30.02	28.28	33.04	**30.45**	1.29	0.97	1.11	**1.12 (0.14)**
11	C-Gr-0.1-10	13.28	17.74	17.12	**16.05 (0.15)**	23.90	31.94	30.82	**28.89**	2.23	1.74	1.50	**1.82 (0.20)**
12	C-Gr-0.1-12	21.62	20.22	15.35	**19.06 (0.17)**	38.91	36.39	27.63	**34.31**	1.38	1.67	0.89	**1.31 (0.30)**
15	NE-8	5.24	4.66	4.79	**4.90 (0.06)**	9.43	8.39	8.62	**8.81**	0.59	0.40	0.77	**0.59 (0.32)**
16	NE-10	**4.86**				**8.74**				**0.85**			
17	NE-12	**5.89**				**10.61**				**0.55**			
18	C-NE-10	17.54	23.70	23.75	**21.67 (0.16)**	31.57	42.66	42.74	**38.99**	1.53	1.81	1.49	**1.61 (0.11)**
19	C-NE-12	11.29	14.57	13.09	**12.98 (0.13)**	20.33	26.22	23.56	**23.37**	1.78	2.08	1.67	**1.84 (0.12)**
20	G-NE-10-Edge	16.06	16.49	11.13	**14.56 (0.20)**	28.90	29.69	20.03	**26.21**	2.60	1.80	1.61	**2.00 (0.26)**
21	G-NE-10	17.48	12.94	12.67	**14.36 (0.19)**	31.47	23.28	22.80	**25.85**	2.52	2.07	3.31	**2.63 (0.24)**
22	G-NE-12-Edge	10.59	12.96	15.75	**13.10 (0.20)**	19.06	23.34	28.35	**23.58**	1.85	3.11	2.50	**2.49 (0.25)**

8.2 Results and discussion

8.2.1 The NE-bonded specimens retrofitted with CFRP bars

The effect of grooving the specimens with the three different sizes (mentioned previously) on the behaviour of concrete prisms retrofitted with one CFRP reinforcement bars bonded with NE (i.e. group 1, specimens C-NE-8, 10 and 12) or with 0.1 wt.% graphite NMEAs (i.e. group 2, specimens C-Gr-0.1-8, 10 and 12) are discussed in this section. The performance analysis will include, as done in the case of the other parameters, the overall flexural capacities and ductility response of the tested specimens, in addition to their structural failure modes.

8.2.1.1 Overall flexural capacities and ductility response

It was found, in the first group, that considering the groove size 10x10 rather than 8x8 yielded a significant increase in the load-carrying capacity of the specimens and their ductility of about 47% and 27%, respectively, which disagrees with what was reported in the literature [90, 94]. Further increase in the groove dimensions (i.e. using 12x12 mm grooves) led to a capacity drop by about 14% and 67% compared to using 8x8 and 10x10 mm grooves, respectively. Nevertheless, a corresponding increase in the specimens' ductility of about 45% and 14% was remarked.

It's noteworthy that increasing the groove size with keeping the same FRP bar dimensions means that more adhesive was utilised. Thus, installing the FRP reinforcement further to the groove edge; in a bigger groove, would delay the stresses generated in the specimen from affecting the FRP-adhesive interface, which would eventually delay the failure, ending up with a higher-capacity specimen. Furthermore, it was reported by Hassan and Rizkalla [21] that increasing the thickness of the adhesive (i.e. by increasing the groove size) reduces the stress deformation within the adhesive layer, which eventually reduces the interfacial stresses. However, further increasing in the groove size resulted in a reverse effect, as a sharp drop in the capacity was reported. This might be due to that using too much adhesive generated more interfacial stresses, which negatively affected the interfacial adhesion, leading to a premature failure.

It was also detected that the ductility increased with the groove size. This could be due to that increasing the groove dimensions means increasing the distance between the grooves' sides. That the FRP bar is surrounded with more adhesive might delay the crack progression, which would take longer to cross from one side to another and cause the failure, leading ultimately to more ductile behaviour.

For the specimens in the second group, it was observed that increasing the groove size (in mm^3) by about 56% (i.e. from 8x8x200 to 10x10x200) decreased the load-carrying capacity of the specimens by about 5%. However, the ductility significantly increased by about 63%. While about 13% and 17% increase in the capacity and ductility, respectively was observed with about 125% increase in the groove size (i.e. from 8x8 mm to 12x12 mm). The greatest increase in the capacity of about 19% was found when moving from 10x10 to 12x12 mm groove dimensions, with a corresponding increase in the groove size of about 44%. Nevertheless, about 28% reduction in the specimens' ductility was noticed.

Therefore, it could be observed that a non-monotonic trend in the load-carrying capacity took place with changing the groove dimensions from 8x8 to 10x10 and to 12x12 mm. However, it could be seen that the increasing the groove dimensions resulted in a clearer trend in the specimens' ductility, as it increased with moving from 8x8 to 10x10 and to 12x12 mm. This could be due to the same reasons observed in the first group. Nevertheless, ductility decrease was reported with moving from 10x10 to 12x12 mm. It could be concluded, as previously observed, that there is an inverse relationship between the change in the load capacity and the ductility with moving from 8x8 to 10x10 and to 12x12 mm groove dimensions, as shown in Fig. 8.1.

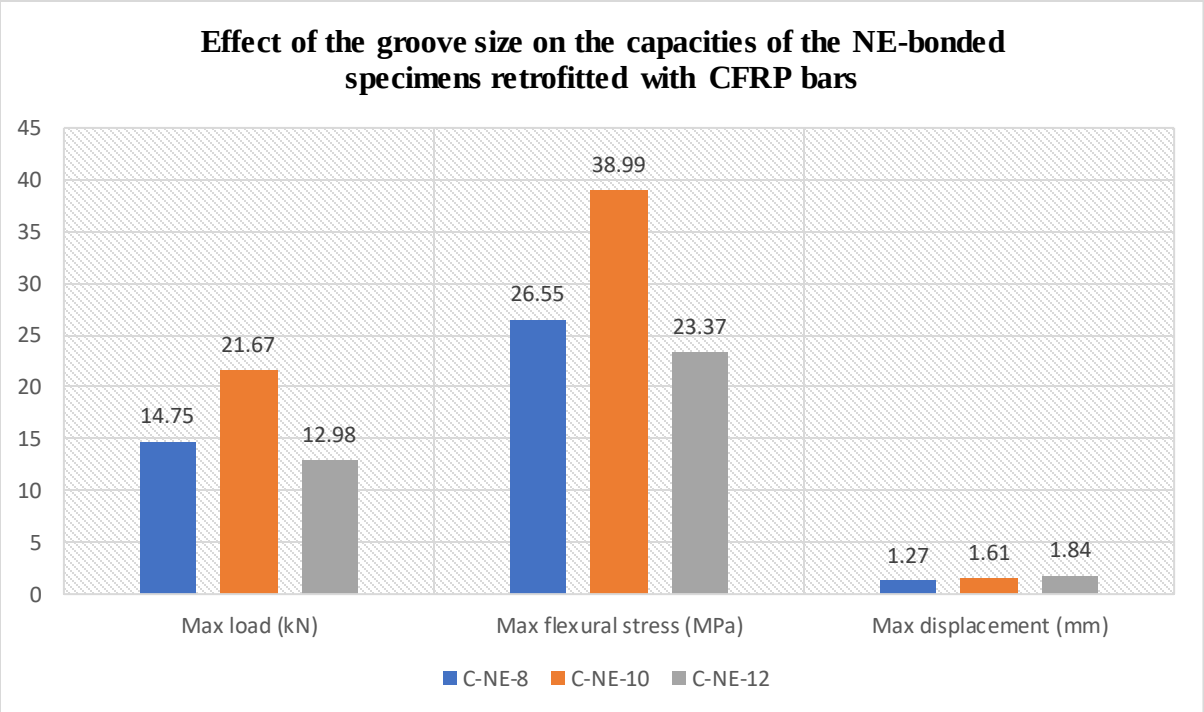

(a)

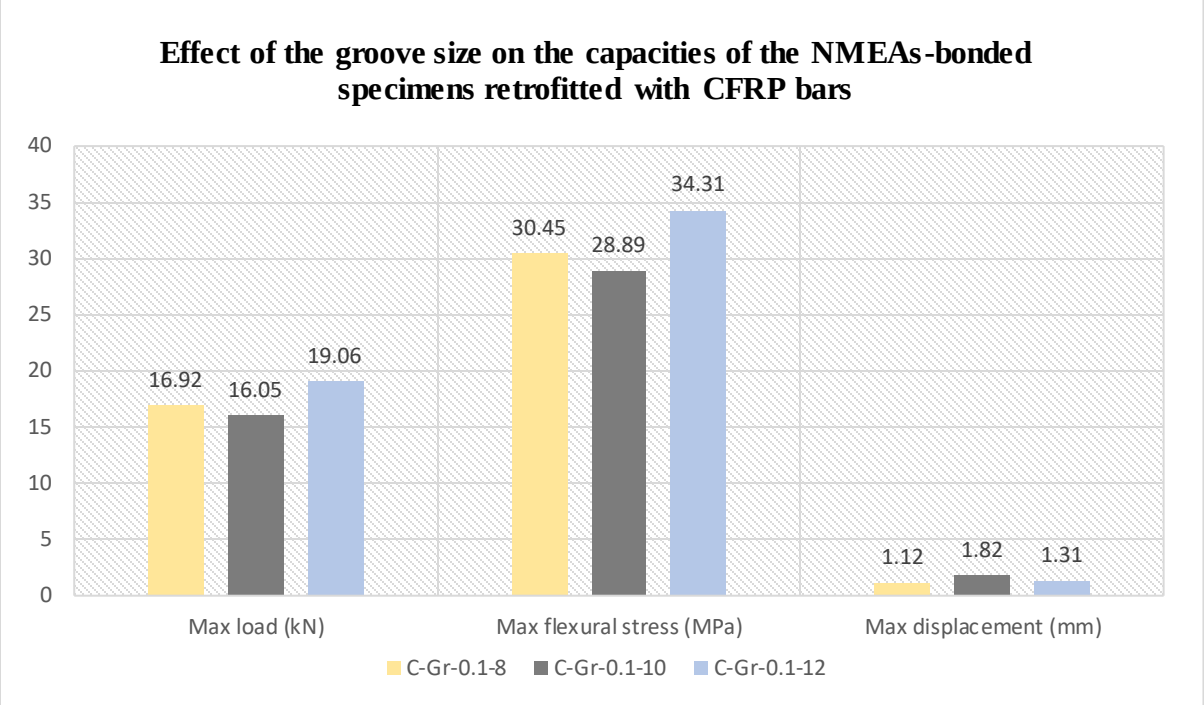

(b)

Fig. 8.1 Effect of groove size on the capacities of the CFRP-retrofitted specimens bonded with (a) NE and (b) graphite-0.1 NMEAs.

8.2.1.2 Failure modes

In the first group, the specimen C-NE-8, as shown in Fig. 8.2a, failed due to shear cracks combined with a debonding noticed in specimen B. Specimen C-NE-10 (Fig. 8.2b) also failed in pure shear without any other failure type noticed, which could be due to that, as reported by De Lorenzis and Nanni [40, 68], as the groove size increases, the thickness of the epoxy cover increases, which offers a higher resistance to splitting and eventually shifts the failure from epoxy to the surrounding concrete. Similar to what was observed in the previous specimens, the specimen C-NE-12 (A, B and C) (Fig. 8.2c), as discussed in the previous section, failed in shear followed by concrete crushing.

For the second group, specimen C-Gr-0.1-8 (Fig. 8.2d), which was retrofitted with 8 mm groove, failed in shear, as a major shear crack appeared in the concrete body with an extended tail continued to align with the adhesive line, but without passing through it. Considering 10 mm groove in specimen C-Gr-0.1-10 (Fig. 8.2e) resulted in shear failure with more sub-cracks noticed on the concrete surface, which could be due to the higher ductility. Furthermore, unlike what was noticed in specimen C-Gr-0.1-8, slight concrete peeling-off was noticed in B. For specimen C-Gr-0.1-12 (Fig. 8.2f), which was retrofitted with 12 mm groove, and as discussed

beforehand, similar failure mode to that observed in specimen C-Gr-0.1-10 was noticed, but fewer minor cracks appeared at failure. Moreover, more concrete than that happened in C-Gr-0.1-10 was detached. Therefore, it could be concluded that using smaller groove width could restrict the crack progression from breaking through adhesive line, and eventually was able to prevent the concrete peeling-off. This could be ascribed to that using smaller groove dimensions would result in less stress concentration at the interfaces. This is because of that increasing the groove dimensions means surrounding the FRP bar and bonding the concrete substrate with more adhesive, leading to higher interfacial stress concentration and weaker bonding at the interfaces.

Consequently, for the NE-bonded specimens, almost the same failure modes (i.e. pure flexure) were observed in all specimens. Thus, it can be concluded that altering the groove dimensions had insignificant influence on the failure modes, as it did not contribute in resisting the crack progression at all.

It's worthy to note that unlike what occurred in the case of using 10 and 12 mm groove dimensions, considering 8 mm grooves in the NMEAs-bonded specimens was able to curb the crack progression by preventing it from passing through the adhesive line. Moreover, no concrete peeling-off took place in the 8 mm-grooved specimens dissimilar to what happened in the other ones.

(a)

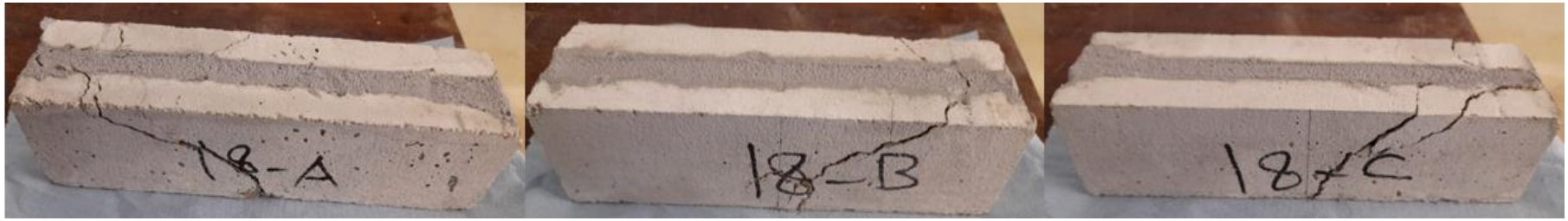

(b)

(c)

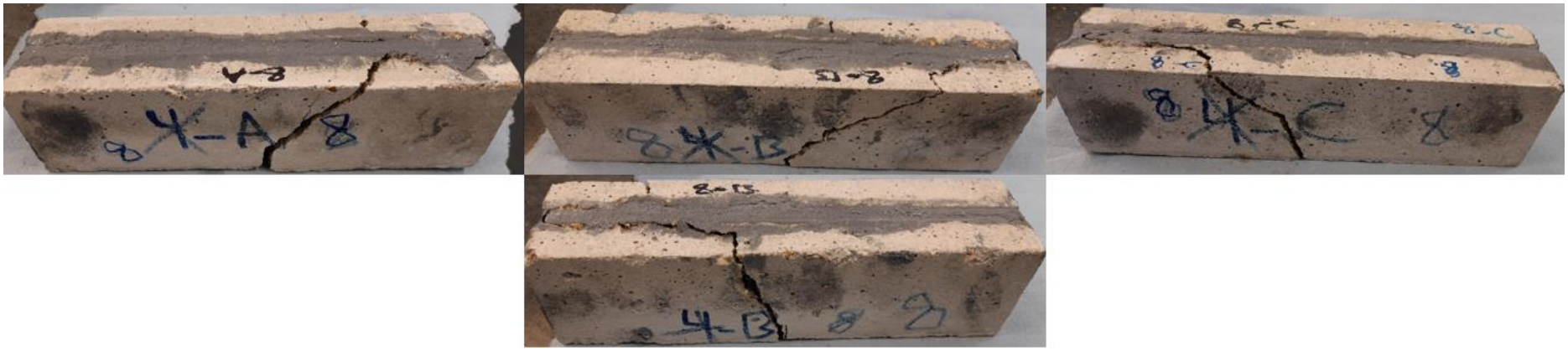

(d)

(e)

(f)

Fig. 8.2 Failure modes of specimens (a) C-NE-8, (b) C-NE-10, (c) C-NE-12, (d) C-Gr-0.1-8, (e) C-Gr-0.1-10 and (f) C-Gr-0.1-12.

8.2.2 The NE-bonded specimens retrofitted with GFRP bars

The analysis conducted in this section encompasses an evaluation effect of considering two groove sizes (i.e. 10x10 and 12x12- mm^2) on the behaviour of NE-bonded specimens retrofitted with one GFRP reinforcement bars positioned either in the groove centre (i.e. group 3, specimens G-NE-8 and 10) or on the groove edge (i.e. group 4, specimens G-NE-10- and 12-Edge), including the overall capacities, ductility response and the structural failure modes of the tested specimens.

8.2.2.1 Overall flexural capacities and ductility response

Contrary to what was observed in the CFRP-retrofitted concretes (i.e. group 1), moving from 8x8 to 10x10 mm in the GFRP-retrofitted concretes yielded a slight (about 3%) reduction in the capacity. This might be due to the difference in the mechanical properties (i.e. the tensile strength) of the bars, which could affect the behaviour, as the other components (i.e. epoxy and concrete) did not vary. However, about 43% ductility increase was achieved, which was due to the same reasons mentioned earlier. The results are presented graphically in Fig. 8.3a.

It was also remarked that increasing the groove dimensions from 10x10 to 12x12 mm in the specimens retrofitted with edge-installed GFRP reinforcement led the load-carrying capacity to decrease by about 11%, however, about 25% ductility increase was observed. This could be ascribed to the same reasons reported in the previous group of specimens. Fig. 8.3b shows the results graphically.

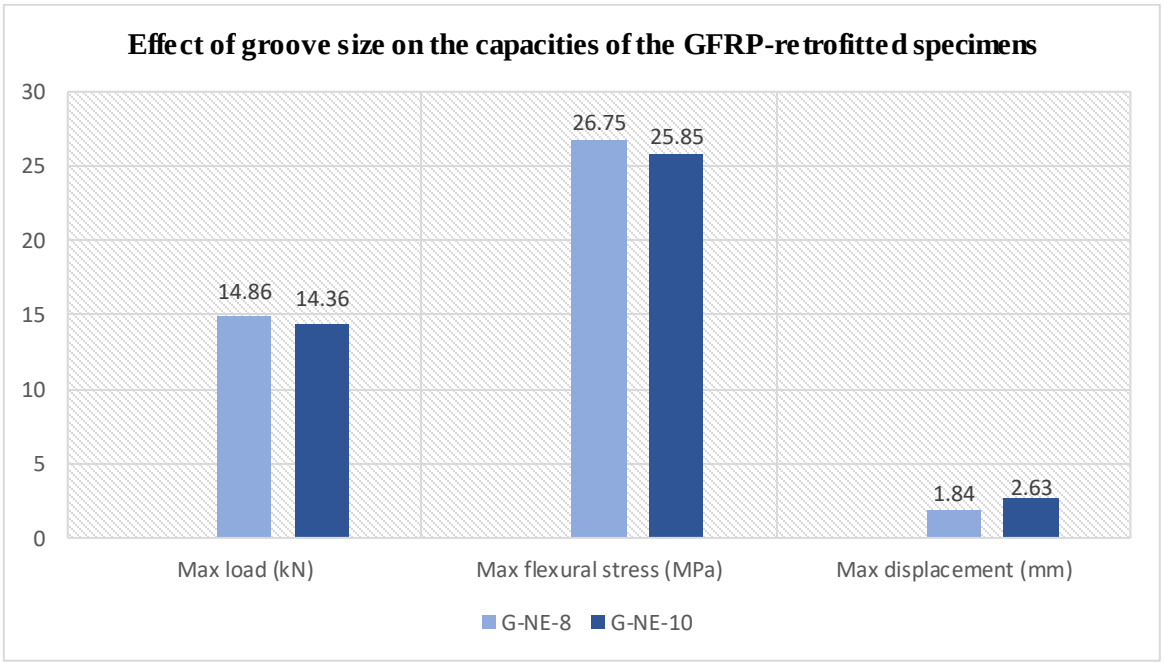

(a)

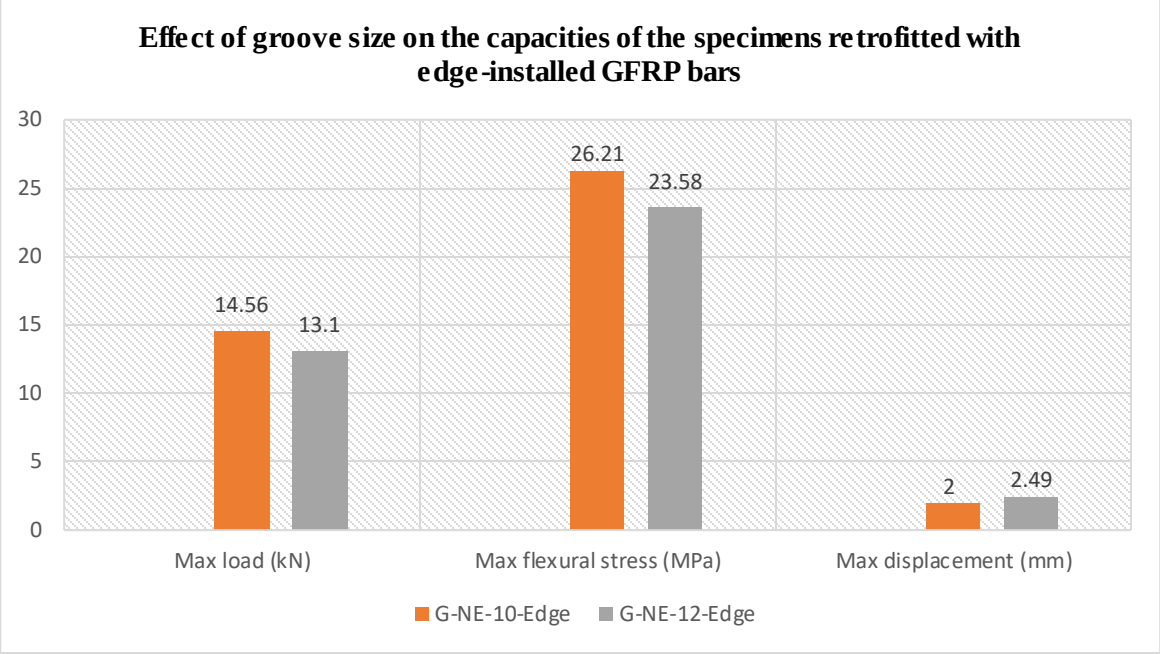

(b)

Fig. 8.3 Effect of groove size on the capacities of the specimens retrofitted with (a) centred-installed and (b) edge-installed GFRP bars.

8.2.2.2 Failure modes

For specimens in group 3, flexural failure was the dominant in specimens G-NE-8 (Fig. 8.4a). In specimen A, the flexural crack generated into concrete could break through the adhesive layer, and also kept progressing align to the GFRP-epoxy interface resulting in a partial peeling-off of the epoxy layer at the bar-epoxy interface and causing a part of concrete to detach. Specimen B failed by approximately the same manner, but the epoxy layer did not peel off. Similar observations were reported in specimen C, but the major crack that caused the failure was narrower than those appeared in the previous specimens. Specimen G-NE-10 (Fig. 8.4b), as discussed earlier, failed in a combined flexural and shear failure mode. Where specimens A and B mainly failed in flexure, while shear failure was the dominant in specimen C, leading to a partial concrete detachment followed by debonding at the bar-epoxy interface.

For the specimens retrofitted with edge-installed GFRP bars, specimens A and B of G-NE-10-Edge (Fig. 8.4c), as mentioned earlier, showed a pure flexure failure mode, while specimen C mainly failed in shear. Specimens G-NE-12-Edge (Fig. 8.4d) -A and C failed in the same manner, as a flexural crack generated in the concrete and continuing align to the epoxy line, without causing concrete detachment. Contrary to that, part of concrete was noticed to peel off in specimen B, which failed due to a major shear crack produced in the concrete body and continued to progress at the edge of the adhesive layer.

(a)

(b)

(c)

(d)

Fig. 8.4 Failure modes of specimens (a) G-NE-8, (b) G-NE-10, (c) G-NE-10-Edge and (d) G-NE-12-Edge.

8.2.3 The NE-retrofitted specimens

Investigating the effect of considering the three different groove sizes on the capacities and failure modes of the specimens retrofitted only with NE (i.e. group 5) was studied and is encompassed in this section.

8.2.3.1 Overall flexural capacities and ductility response

The specimens considered in this group showed similar trend to what was exhibited by those included in group 2. Where using 10x10 mm groove dimensions rather than 8x8 mm in the NE-retrofitted specimens yielded about 1% decrease in the load-carrying capacity, but about 44% ductility increase was observed. On the contrary, changing the groove dimensions from 8x8 mm to 12x12 mm resulted in about 20% capacity increase, but the specimens' ductility dropped by about 7%. About 21% increase in the capacity was obtained with moving from 10x10 mm to 12x12 mm groove dimensions, however, about 55% ductility reduction was detected. This was attributed to the same reasons mentioned for the specimens in group 2. The test results are shown graphically in Fig. 8.5.

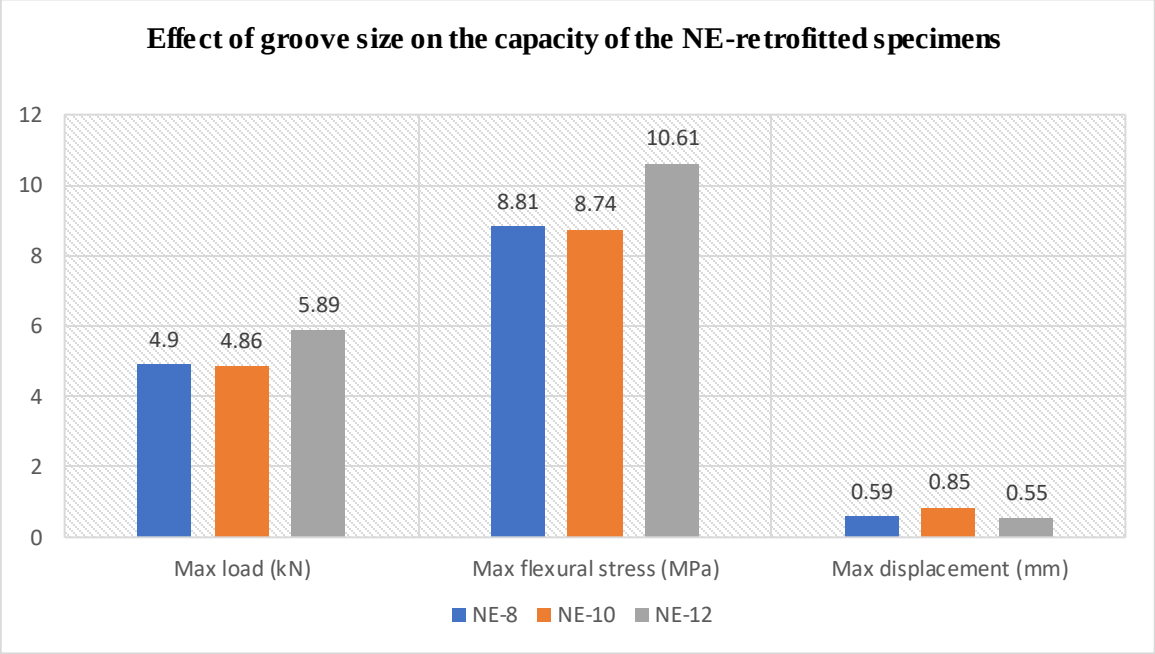

Fig. 8.5 Effect of groove size on the capacities of the NE-retrofitted specimens.

8.2.3.2 Failure modes

As shown in Fig. 8.6, almost the same modes of failure were shown by all specimens grooved with different sizes, as all of them failed in pure flexure. Thus, it can be concluded that altering the groove dimensions had insignificant influence on the failure modes, as it did not contribute in resisting the crack progression at all.

(a)

(b)

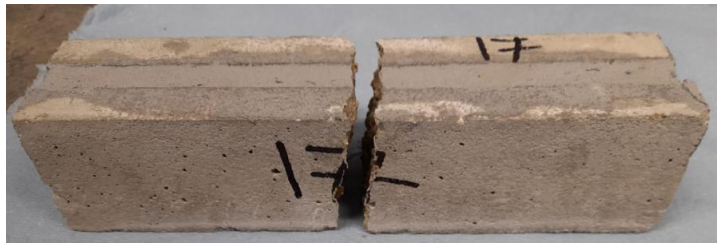

(c)

Fig. 8.6 Failure modes of specimens (a) NE-8, (b) NE-10 and (c) NE-12.

8.3 Summary

This chapter has presented a thorough investigation of the structural behaviour of NSM-FRP-retrofitted concrete prisms made with different groove sizes. Whereas the impact of changing the groove dimensions on the overall load-carrying capacities, ductility responses alongside the structural failure modes have been analysed. Valuable insights have been unveiled through the analysis of multifaceted aspects of structural performance and behaviour in specimens retrofitted using different types of FRP reinforcement bars, their positions within the grooves as well as the bonding agents used to fix those bars within the grooves. The following points summarise the main findings and conclusions of the analysis done in this chapter:

- Increasing the b/d_b ratio from 1.33 to 1.67, for the CFRP-retrofitted specimens bonded with NE, led to about 47% and 27% increase in the specimens' capacities and their ductility, respectively, while moving from 1.33 to 2.00 yielded about 14% capacity drop but a ductility increase of about 45% was achieved. Whereas about 5% decrease capacity decrease, but a ductility increases of about 63% was reported with moving from 1.33 to 1.67 in the NMEAs-bonded specimens. Further increase in the b/d_b ratio (i.e. from 1.33 to 2.00) yielded increases in both capacity and ductility by about 13% and 17%, respectively.

- Using 10- and 12-mm grooves could prevent the debonding mode, which was observed in the 8 mm-grooved specimens bonded with NE. However, the shear failure was the dominant in all specimens. All the NMEAs-bonded specimens mainly failed due to shear cracks, followed by concrete crushing observed in the 10 and 12 mm-grooved specimens.

- For the specimens retrofitted with centered-installed GFRP bars, increasing the groove size (i.e. from $1.33d_b$ to $1.67d_b$) slightly decreased the capacities, but about 30% increase in the ductility was achieved.

- Changing the groove size from $1.67d_b$ to $2.00d_b$ in the specimens retrofitted with edge-installed GFRP bars led to about 11% capacity decrease, but about 25% ductility enhancement was observed.

- Changing the groove size in the GFRP-retrofitted specimens (i.e. centered-installed) had an insignificant effect on the failure modes. While both specimens (i.e. G-10-Edge and G-12-Edge) retrofitted with edge-installed GFRP bars showed a combined shear and flexural failure modes, but a partial concrete detachment occurred in the latter specimen, which was not noticed in the former one.

Chapter 9: Conclusions and future work

9.1 Introduction

This research study has contributed to the field of Nano-modification of structural adhesives to be then considered for enhanced performance of the NSM-FRP-retrofitted concrete members, in terms of the interfacial bond behaviour and mechanical strength of retrofitted concrete. An extensive and a comprehensive experimental programme, including mechanical, physical, chemical and microstructural characterisation, was conducted for that purpose. The Nano-modification of epoxy adhesive was done through incorporating five different nanomaterials, coming from two different families, namely, carbon-based and silicon-based nanomaterials into the matrix at different wt.% concentrations. Each "recipe" had a distinct effect on the performance of the matrix. Further design parameters, in addition to the bonding agents, were adopted for the optimum retrofitting operation, such as type, position and number of NSM-FRP reinforcement bars, which were installed in grooves cut with different sizes.

This chapter presents a summary of the main research findings and primary conclusions drawn from the experimental programme conducted in this study. It also offers valuable recommendations for future research endeavours to expand and enrich the scope of this research field.

9.2 Conclusions

This thesis has provided a detailed investigation on the effect of incorporating various carbon-based (i.e. carbon nanofibres (CNF), cellulose nanocrystals and graphite Nano powder) and silicon-based nanomaterials (i.e. silica Nano powder and MMT Nano clay) into neat structural epoxy (NE) adhesive (Sikadur®-30) at 0.5, 1.0 and 1.5% by weight on its chemical, physical and microstructural properties, using spectroscopic and microscopy techniques, and the bond behaviour of the CP-adhesive-bonded joints. Moreover, a comprehensive parametric study, considering the effect of the FRP reinforcement bars, bonding agents and groove sizes, has thoroughly been carried out to investigate and to better understand the flexural behaviour and the interfacial bond characteristics of the NSM-FRP-retrofitted concrete prisms to achieve the optimum NSM-FRP retrofitting techniques.

It's noteworthy that the impact of incorporating these nanomaterials into the NE on its chemical composition was investigated using Fourier transform infrared (FTIR) spectroscopy and Raman spectroscopy. X-ray diffraction (XRD) measurements were also used to identify the

changes in the physical structure (i.e. the degree of crystallinity) that may occur in the NE with the addition of nanomaterials. Furthermore, the microstructure of the NE and NMEAs (in terms of the degree of dispersibility of the nanoparticles through the matrix) was investigated through scanning electron microscopy (SEM) analysis. A porosity analysis was also conducted across all samples. The results obtained from various tests were correlated to investigate the changes that occurred in the different properties of the matrix and the corresponding nanocomposites effectively and more critically.

It's worth mentioning that detailed conclusions and findings derived from the experimental analysis conducted for this thesis are provided in the summaries appended at the end of each result chapter (i.e. Chapters 4-8). The main conclusions can be summarised as follows:

- For the analysis of the NMEAs, the SEM images showed some particle agglomeration, which increased with increasing wt.%. An increase in the % porosity ratio of all nanocomposites over that of the NE was also observed, accompanied by a decrease in crystallinity compared to the NE. As per the FTIR spectroscopy, the chemical bonds in the NE and carbon-based NMEAs were observed to have different intensities, which were changed in the NMEAs, with the type and wt. % of the nanomaterials. No new bonds were formed by incorporating any of the nanomaterials (i.e. carbon- and silicon-based), except when adding 1.0 wt.% CNF, where a bond at 1710 cm^{-1} was observed indicating a new C=O stretching bond. As shown by Raman spectroscopy, all CNF and graphite NMEAs exhibited higher I_D/I_G values than those of the corresponding pristine materials.

- In the realm of CP-adhesive-bonded joints, the utilisation of carbon-based epoxy nanocomposites significantly enhanced the lap-shear strength (LSS) of the joints, resulting in a remarkable 165% increase in strength compared to those bonded with NE. However, strength gains plateaued at higher filler concentrations (e.g., 1.0 wt.% CNF and 1.5 wt.% of all Nano-fillers) due to the phenomenon of particle clustering. Using silicon-based nanocomposites with Nano-filler concentrations of 0.5, 1.0, or 1.5 wt.% also yielded notable strength improvements over NE, although with diminishing returns as wt.% rose. The study identified increased porosity and reduced crystallinity in nanocomposites as challenges to establishing robust interfacial bonds with the CP substrate, leading to decreased LSS attributed to reduced contact area, weakened structural integrity, and impaired load transfer capabilities. Both cohesive and adhesive failure modes predominated in joints, with

adhesively-failed regions expanding with higher Nano-filler concentrations due to particle clustering.

- The experimental retrofitting of concrete specimens revealed notable enhancements in load-carrying capacity and ductility, with the incorporation of CFRP, GFRP and BFRP reinforcement bars alongside NE. These reinforcements led to significant increases in capacity ranging from 201% to 203% and ductility improvements of 115% to 242% compared to specimens retrofitted with NE alone. Moreover, the use of FRP reinforcement bars alongside NE not only induced a more ductile failure mode but also significantly improved resistance to crack progression compared to NE-only retrofitted specimens. Furthermore, variations in the failure modes were observed with different reinforcement materials and configurations, highlighting the importance of strategic reinforcement selection for optimizing structural performance in retrofitting applications.

- For the NMEAs-bonded specimens, it was observed that the correlation between microstructural features, as observed through SEM and XRD analyses, revealed a significant impact on the mechanical behavior of NMEAs in the retrofitting system. Carbon-based NMEAs; CNF and cellulose, displayed reduced capacities compared to NE-bonded specimens due to weak interfacial bonding attributed to particle agglomeration and high % porosity. However, these NMEAs exhibited notable increases in ductility. Conversely, bonding specimens with silica-, clay- and graphite-modified epoxies resulted in capacity increases over NE-bonded specimens. Notably, while silica and clay nanocomposites enhanced ductility, higher crystallinity in graphite nanocomposites led to a reduction in ductility. Overall, silicon-based NMEAs yielded higher ultimate loads compared to carbon-based ones, although the latter showed superior ductility response. It was also found that utilizing carbon-based epoxy nanocomposites was able to prevent interfacial debonding and shifted the failure mode from shear to flexural, whereas silicon-based nanocomposites showed slight debonding at the bar-adhesive interface, accompanied by cohesive failure and minor concrete crushing.

- The impact of groove size and nanoparticle concentration on NMEAs-bonded retrofitted concrete is significant. 10 mm-grooved specimens (C-Gr-0.1-10) showed decreased capacity but increased ductility compared to NE-bonded ones. Conversely, bonding 12 mm-grooved specimens with 0.1 wt.% graphite nanocomposites (C-Gr-0.1-12) increased

capacity but reduced ductility. Graphite NMEAs maintained shear failure in both grooved specimens. Increasing nanoparticle concentration led to decreased capacities due to agglomeration within the epoxy, while ductility slightly improved. Specimens with varying wt.% of nanoparticles primarily failed in shear, except for C-Gr-0.3-12, which exhibited minor concrete crushing.

- The investigation into groove size and reinforcement configurations in retrofitted specimens elucidated key insights into capacity and ductility variations. Increasing the b/d_b ratio and adjusting groove size had discernible effects on structural performance, with capacity and ductility exhibiting distinct responses. Edge-installed GFRP bars showed promising results in enhancing ductility, albeit with slight capacity reductions. Failure modes were influenced by groove size and reinforcement placement, with shear and flexural failure modes predominating. These findings underscore the importance of optimizing reinforcement configurations to achieve desired structural outcomes in retrofitting applications.

Overall, the test results and analysis presented in this thesis have provided engineers and research community with a solid basis to specify the best practices of the NSM-FRP concrete retrofitting systems to be considered for efficient and sustainable retrofitting techniques, which will lead to stronger and more durable concrete structures and will ultimately reduce their need for maintenance and therefore reducing their repair costs.

9.3 Recommendations for future work

This study has made a substantial contribution to the domain of the Nano-modification of structural adhesives and adopt them in a novel NSM-FRP concrete retrofitting system. However, there are still other aspects that should be explored to thoroughly comprehend the efficiency of the NMEAs-bonded NSM-FRP technique for concrete retrofitting owing to this being relatively complicated and having many details to be investigated. Therefore, the following suggestions, following the findings of this study, are proposed for expanding the scope of this research:

- To conduct as comprehensive study about the new NSM-FRP retrofitting technique (by using the NMEAs) as possible, several design and retrofitting parameters have been considered for that purpose. However, since this research is the first of its type about using the NMEAs in the NSM-FRP systems, it is believed that several other parameters may be

considered to better understand the efficacy of the enhanced technique, such as using new Nano-fillers, either individually or a combination of two or more, trying out other types (i.e. Aramid FRP, AFRP) or geometries (i.e. square or rectangular strips) of FRP reinforcement in addition to studying different geometrics of grooves, to name a few.

- As confirmed in the literature, the NE-bonded NSM-FRP technique has proved its efficiency in retrofitting various concrete structures with respect to flexure, shear and torsion. This study has investigated the efficiency of the NMEAs-bonded NSM-FRP technique for flexural retrofitting. Therefore, conducting research work to explore the performance of shear and torsion retrofitting is of high importance and it's worthy to be researched.

- Applying the novel retrofitting techniques with the application of the "ideas" mentioned previously on large-scale concrete members, e.g. full-scale beams, columns or slabs, depending on the type of the structural retrofitting to be considered. This application could be expanded by considering assessing the behaviour of the retrofitted members under cyclic loads or excessive load conditions including fire and earthquake conditions.

- Following the latest NSM-FRP design guidelines provided by ACI (ACI PRC-440.2-17), an analytical formula could be generated to be utilised for the developed retrofitting system.

Limitations of the study

In accordance with the foundational premise that perfection remains an unattainable ideal, the present study, conducted in pursuit of the objectives outlined in this thesis, exhibits certain limitations/shortcomings, which are delineated, with suggested/potential solutions, as follows:

- Some of the experimental results may have error margins up to 10%, which are stemming from the inherent error margins that are from the manufacturing processes of the associated equipment and machinery.

- To provide further comprehensives and criticality to the existed outcomes, numerical simulation (i.e. using ABAQUS) might have been carried out to validate the experimental results. This was mainly due to time constraints, since this research study operated under specific timeframes, and since conducting numerical simulations can be a time-intensive endeavour, the study has not had the necessary duration to complete both experimental work and subsequent numerical simulations within the allotted timeframe. This step will, therefore, be undertaken in the future, with the aim of maintaining the highest scientific

standards by subjecting experimental findings to rigorous validation through numerical techniques.

- Some of the nanoparticles used in this study are relatively expensive, and as a result, their utilisation may not be cost-effective/financially viable, especially in the context of larger-scale or application-driven projects. However, a proposed solution of judiciously managing the utilisation of expensive nanoparticles by adhering to budget constraints and, when feasible, substituting them with more cost-effective alternatives represents a prudent and resource-efficient approach to address the identified limitation. By employing this approach, research endeavours can maintain fiscal responsibility while striving to attain research objectives. This strategy allows for the optimisation of resource allocation, ensuring that the available funds are maximally leveraged and directing them toward essential aspects of the study, where the use of expensive materials is indispensable. Additionally, the incorporation of less expensive or cost-effective materials serves to enhance the overall cost-efficiency of the research, rendering it more accessible and sustainable.

-End-

List of References

[1] M. Z. Naser, R. A. Hawileh, and J. A. Abdalla, "Fiber-reinforced polymer composites in strengthening reinforced concrete structures: A critical review," Engineering Structures, vol. 198, p. 109542, 2019.

[2] N. T. K. Al-Saadi, A. Mohammed, R. Al-Mahaidi, and J. Sanjayan, "A state-of-the-art review: Near-surface mounted FRP composites for reinforced concrete structures," Construction and Building Materials, vol. 209, pp. 748-769, 2019.

[3] Y. M. Amran, R. Alyousef, R. S. Rashid, H. Alabduljabbar, and C. C. Hung, "Properties and applications of FRP in strengthening RC structures: A review," Structures, vol. 16, pp. 208-238, Nov. 2018.

[4] A. Siddika, M. A. Al Mamun, R. Alyousef, and Y. M. Amran, "Strengthening of reinforced concrete beams by using fiber-reinforced polymer composites: A review," Journal of Building Engineering, vol. 25, p. 100798, 2019.

[5] L. C. Hollaway, "A review of the present and future utilization of FRP composites in the civil infrastructure with reference to their important in-service properties," Construction and Building Materials, vol. 24, no. 12, pp. 2419-2445, 2010.

[6] Z. E. A. Benzeguir, G. El-Saikaly, and O. Chaallal, "Size effect in RC T-beams strengthened in shear with externally bonded CFRP sheets: Experimental study," Journal of Composites for Construction, vol. 23, no. 6, p. 04019048, 2019.

[7] M. Ibrahim, T. Wakjira, and U. Ebead, "Shear strengthening of reinforced concrete deep beams using near-surface mounted hybrid carbon/glass fiber-reinforced polymer strips," Engineering Structures, vol. 210, p. 110412, 2020.

[8] J. H. Gonzalez-Libreros, C. Sabau, L. H. Sneed, C. Pellegrino, and G. Sas, "State of research on shear strengthening of RC beams with FRCM composites," Construction and Building Materials, vol. 149, pp. 444-458, 2017.

[9] C. E. Bakis et al., "Fiber-reinforced polymer composites for construction—State-of-the-art review," Journal of composites for construction, vol. 6, no. 2, pp. 73-87, 2002.

[10] S. J. E. Dias and J. A. O. Barros, "Shear strengthening of RC T-section beams with low-strength concrete using NSM CFRP laminates," Cement and Concrete Composites, vol. 33, no. 2, pp. 334-345, 2011.

[11] S. J. Dias and J. A. Barros, "Shear strengthening of RC beams with NSM CFRP laminates: Experimental research and analytical formulation," Composite Structures, vol. 99, pp. 477-490, 2013.

[12] S. J. Dias and J. A. Barros, "NSM shear strengthening technique with CFRP laminates applied in high T cross-section RC beams," Composites Part B: Engineering, vol. 114, pp. 256-267, 2017.

[13] S. S. Zhang, T. Yu, and G. M. Chen, "Reinforced concrete beams strengthened in flexure with near-surface mounted (NSM) CFRP strips: Current status and research needs," Composites Part B: Engineering, vol. 131, pp. 30-42, 2017.

[14] T. Nicolae et al., "Fibre reinforced polymer composites as internal and external reinforcements for building elements," Buletinul Institutului Politehnic din Iasi. Sectia Constructii, Arhitectura, vol. 54, no. 1, p. 7, 2008.

[15] D. Oehlers and R. Seracino, "Design of FRP and steel plated RC structures: retrofitting beams and slabs for strength, stiffness, and ductility," Elsevier, 2004.

[16] D. J. Oehlers et al., "Moment redistribution in continuous plated RC flexural members. Part 1: neutral axis depth approach and tests," Engineering structures, vol. 26, no. 14, pp. 2197-2207, 2004.

[17] R. Seracino et al., "Bond strength of near-surface mounted FRP strip-to-concrete joints," Journal of Composites for Construction, vol. 11, no. 4, pp. 401-409, 2007.

[18] F. Al-Mahmoud et al., "Strengthening of RC members with near-surface mounted CFRP rods," Composite Structures, vol. 91, no. 2, pp. 138-147, 2009.

[19] W. C. Tang et al., "Flexural strengthening of reinforced lightweight polystyrene aggregate concrete beams with near-surface mounted GFRP bars," Building and environment, vol. 41, no. 10, pp. 1381-1393, 2006.

[20] A. Carolin, H. Nordin, and B. Täljsten, "Concrete beams strengthened with near-surface mounted reinforcement of CFRP," in International Conference on FRP Composites in Civil Engineering: 12/12/2001-15/12/2001 (Vol. 2, pp. 1059-1066). Elsevier, 2001.

[21] T. Hassan and S. Rizkalla, "Investigation of bond in concrete structures strengthened with near-surface mounted carbon fiber reinforced polymer strips," Journal of Composites for Construction, vol. 7, no. 3, pp. 248-257, 2003.

[22] I. S. Liu, D. J. Oehlers, and R. Seracino, "Tests on the ductility of reinforced concrete beams retrofitted with FRP and steel near-surface mounted plates," Journal of Composites for Construction, vol. 10, no. 2, pp. 106-114, 2006.

[23] P. Mukhopadhyaya and N. Swamy, "Interface shear stress: a new design criterion for plate debonding," Journal of Composites for Construction, vol. 5, no. 1, pp. 35-43, 2001.

[24] D. M. Nguyen, T. K. Chan, and H. K. Cheong, "Brittle failure and bond development length of CFRP-concrete beams," Journal of Composites for Construction, vol. 5, no. 1, pp. 12-17, 2001.

[25] X. Huang, L. Sui, F. Xing, Y. Zhou, and Y. Wu, "Reliability assessment for flexural FRP-strengthened reinforced concrete beams based on importance sampling," Composites Part B: Engineering, vol. 156, pp. 378-398, 2019.

[26] ACI Committee 440.2R-08, "Guide for the Design and Construction of Externally Bonded FRP Systems for Strengthening Concrete Structures," American Concrete Institute, Farmington Hills, Michigan, USA, 2008.

[27] J. Y. Kang, Y. H. Park, J. S. Park, Y. J. You, and W. T. Jung, "Analytical evaluation of RC beams strengthened with near-surface mounted CFRP laminates," in 7th International symposium: fiber-reinforced polymer (FRP) reinforcement for concrete structures, 2005, pp. 779-794.

[28] A. Siddika, M. A. Al Mamun, W. Ferdous, and R. Alyousef, "Performances, challenges and opportunities in strengthening reinforced concrete structures by using FRPs–A state-of-the-art review," Engineering Failure Analysis, vol. 111, p. 104480, 2020.

[29] S. O. Asplund, "Strengthening bridge slabs with grouted reinforcement," Journal Proceedings, vol. 45, no. 1, pp. 397-406, 1949.

[30] S. J. Dias and J. A. Barros, "Performance of reinforced concrete T beams strengthened in shear with NSM CFRP laminates," Engineering Structures, vol. 32, no. 2, pp. 373-384, 2010.

[31] F. Al-Mahmoud, A. Castel, T. Q. Minh, and R. François, "Reinforced concrete beams strengthened with NSM CFRP rods in shear," Advances in Structural Engineering, vol. 18, no. 10, pp. 1563-1574, 2015.

[32] I. A. Sharaky, L. Torres, J. Comas, and C. Barris, "Flexural response of reinforced concrete (RC) beams strengthened with near surface mounted (NSM) fibre reinforced polymer (FRP) bars," Composite Structures, vol. 109, pp. 8-22, 2014.

[33] A. Rizzo and L. De Lorenzis, "Behavior and capacity of RC beams strengthened in shear with NSM FRP reinforcement," Construction and Building Materials, vol. 23, no. 4, pp. 1555-1567, 2009.

[34] S. J. Dias and J. A. Barros, "Shear strengthening of RC beams with near-surface-mounted CFRP laminates," American Concrete Institute, 2005.

[35] H. Y. Lee, W. T. Jung, and W. Chung, "Flexural strengthening of reinforced concrete beams with pre-stressed near-surface mounted CFRP systems," Composite Structures, vol. 163, pp. 1-12, 2017.

[36] L. De Lorenzis and J. G. Teng, "Near-surface mounted FRP reinforcement: An emerging technique for strengthening structures," Composites Part B: Engineering, vol. 38, no. 2, pp. 119-143, 2007.

[37] L. De Lorenzis, "Strengthening of RC structures with near surface mounted FRP rods," PhD Thesis, Department of Innovation Engineering, University of Lecce, Italy, 2002.

[38] M. Blaschko, "Bond behaviour of CFRP strips glued into slits," in Fibre-Reinforced Polymer Reinforcement for Concrete Structures: (In 2 Volumes), 2003, pp. 205-214.

[39] R. Parretti and A. Nanni, "Strengthening of RC members using near-surface mounted FRP composites: Design overview," Advances in structural engineering, vol. 7, no. 6, pp. 469-483, 2004.

[40] L. De Lorenzis and A. Nanni, "Bond between near-surface mounted fiber-reinforced polymer rods and concrete in structural strengthening," Structural Journal, vol. 99, no. 2, pp. 123-132, 2002.

[41] T. Hassan and S. Rizkalla, "Bond mechanism of NSM FRP bars for flexural strengthening of concrete structures," ACI Structural Journal, vol. 101, no. 6, pp. 830-839, 2004.

[42] Y. Yun, Y. F. Wu, and W. C. Tang, "Performance of FRP bonding systems under fatigue loading," Engineering Structures, vol. 30, no. 11, pp. 3129-3140, 2008.

[43] A. A. Islam, "Effects of NSM CFRP bars in shear strengthening of concrete members," in Structures Congress 2009: Don't Mess with Structural Engineers: Expanding Our Role, 2009, pp. 1-14.

[44] D. Galati and L. De Lorenzis, "Effect of construction details on the bond performance of NSM FRP bars in concrete," Advances in Structural Engineering, vol. 12, no. 5, pp. 683-700, 2009.

[45] L. Torres, I. A. Sharaky, C. Barris, and M. Baena, "Experimental study of the influence of adhesive properties and bond length on the bond behaviour of NSM FRP bars in concrete," Journal of Civil Engineering and Management, vol. 22, no. 6, pp. 808-817, 2016.

[46] J. R. Cruz, J. Sena-Cruz, M. Rezazadeh, S. Seręga, E. Pereira, A. Kwiecień, and B. Zając, "Bond behaviour of NSM CFRP laminate strip systems in concrete using stiff and flexible adhesives," Composite Structures, vol. 245, p. 112369, 2020.

[47] M. R. Coelho, J. M. Sena-Cruz, and L. A. Neves, "A review on the bond behavior of FRP NSM systems in concrete," Construction and Building Materials, vol. 93, pp. 1157-1169, 2015.

[48] D. Novidis, S. J. Pantazopoulou, and E. Tentolouris, "Experimental study of bond of NSM-FRP reinforcement," Construction and Building Materials, vol. 21, no. 8, pp. 1760-1770, 2007.

[49] F. Al-Mahmoud, A. Castel, R. François, and C. Tourneur, "Anchorage and tension-stiffening effect between near-surface-mounted CFRP rods and concrete," Cement and Concrete Composites, vol. 33, no. 2, pp. 346-352, 2011.

[50] S. M. Soliman, E. El-Salakawy, and B. Benmokrane, "Bond performance of near-surface-mounted FRP bars," Journal of Composites for Construction, vol. 15, no. 1, pp. 103-111, 2011.

[51] J. Gómez, L. Torres, and C. Barris, "Characterization and simulation of the bond response of NSM FRP reinforcement in concrete," Materials, vol. 13, no. 7, p. 1770, 2020.

[52] A. Merdas, B. Fiorio, and N. E. Chikh, "Aspects of bond behavior for concrete beam strengthened with carbon fibers reinforced polymers–near surface mounted," Journal of Reinforced Plastics and Composites, vol. 34, no. 6, pp. 463-478, 2015.

[53] S. S. Zhang, J. G. Teng, and T. Yu, "Bond strength model for CFRP strips near-surface mounted to concrete," Journal of Composites for Construction, vol. 18, no. 3, p. A4014003, 2014.

[54] X. Yan, B. Miller, A. Nanni, and C. E. Bakis, "Characterization of CFRP rods used as near surface mounted reinforcement," in 8th International conference on structural faults and repair, 1999, pp. 1-12.

[55] J. A. Barros and J. M. Sena-Cruz, "Bond behavior of carbon laminate strips into concrete by pullout-bending tests," 2002.

[56] J. M. Sena Cruz and J. A. Oliveira de Barros, "Bond between near-surface mounted carbon-fiber-reinforced polymer laminate strips and concrete," Journal of composites for construction, vol. 8, no. 6, pp. 519-527, 2004.

[57] L. De Lorenzis, A. Rizzo, and A. La Tegola, "A modified pull-out test for bond of near-surface mounted FRP rods in concrete," Composites Part B: Engineering, vol. 33, no. 8, pp. 589-603, 2002.

[58] M. Blaschko and K. Zilch, "Rehabilitation of concrete structures with CFRP strips glued into slits," in Proceedings of the twelfth international conference of composite materials, ICCM, 1999, vol. 12.

[59] L. De Lorenzis and A. Nanni, "Shear strengthening of reinforced concrete beams with near-surface mounted fiber-reinforced polymer rods," Structural Journal, vol. 98, no. 1, pp. 60-68, 2001.

[60] S. J. Dias and J. A. Barros, "Influence of the percentage of steel stirrups in the effectiveness of the NSM laminates shear strengthening technique," 2009.

[61] A. Mofidi, O. Chaallal, L. Cheng, and Y. Shao, "Investigation of near surface–mounted method for shear rehabilitation of reinforced concrete beams using fiber reinforced–polymer composites," Journal of Composites for Construction, vol. 20, no. 2, p. 04015048, 2016.

[62] A. Ali and T. Mezher, "Shear strengthening of RC without stirrups for deep beams with near surface mounted CFRP rods," International Journal of Engineering Research and Technology, vol. 4, no. 6, pp. 545-547, 2015.

[63] S. J. Dias and J. A. Barros, "Behaviour of RC beams shear strengthened with NSM CFRP laminates," 2008.

[64] J. A. Barros and S. J. Dias, "Near surface mounted CFRP laminates for shear strengthening of concrete beams," Cement and Concrete Composites, vol. 28, no. 3, pp. 276-292, 2006.

[65] P. Wiwatrojanagul, B. I. N. Ayudhya, and R. Sahamitmongkol, "NSM FRP shear strengthening of RC beams with internal stirrups," Science & Technology Asia, pp. 16-30, 2012.

[66] H. M. Tanarslan, "The effects of NSM CFRP reinforcements for improving the shear capacity of RC beams," Construction and Building Materials, vol. 25, no. 5, pp. 2663-2673, 2011.

[67] R. Kotynia, "Efficiency of RC T-Section beams shear strengthening with NSM FRP reinforcement," in Advances in FRP Composites in Civil Engineering, Springer, Berlin, Heidelberg, 2011, pp. 776-780.

[68] L. D. Lorenzis and A. Nanni, "Characterization of FRP rods as near-surface mounted reinforcement," Journal of Composites for Construction, vol. 5, no. 2, pp. 114-121, 2001.

[69] A. Bilotta, F. Ceroni, M. Di Ludovico, E. Nigro, M. Pecce, and G. Manfredi, "Bond efficiency of EBR and NSM FRP systems for strengthening concrete members," Journal of Composites for Construction, vol. 15, no. 5, pp. 757-772, 2011.

[70] S. J. Dias and J. A. Barros, "Experimental behaviour of RC beams shear strengthened with NSM CFRP laminates," Strain, vol. 48, no. 1, pp. 88-100, 2012.

[71] W. Sun, T. Lou, and M. Achintha, "A novel strong and durable near-surface mounted (NSM) FRP method with cost-effective fillers," Composite Structures, vol. 255, p. 112952, 2021.

[72] D. H. Lim, "Shear behaviour of RC beams strengthened with NSM and EB CFRP strips," Magazine of concrete research, vol. 62, no. 3, pp. 211-220, 2010.

[73] Y. J. Kim, A. Hmidan, and S. Yazdani, "Variable shear span-depth ratios for reinforced concrete beams strengthened with various carbon fiber-reinforced polymer configurations," ACI Structural Journal, vol. 112, no. 5, p. 635, 2015.

[74] M. N. Nurbaiah, A. H. Hanizah, A. Nursafarina, and M. N. Ashikin, "Flexural behaviour of RC beams strengthened with externally bonded (EB) FRP sheets or Near Surface Mounted (NSM) FRP rods method," in 2010 International Conference on Science and Social Research (CSSR 2010), IEEE, 2010, pp. 1232-1237.

[75] A. Bilotta, F. Ceroni, E. Nigro, and M. Pecce, "Efficiency of CFRP NSM strips and EBR plates for flexural strengthening of RC beams and loading pattern influence," Composite Structures, vol. 124, pp. 163-175, 2015.

[76] A. Khalifa, W. J. Gold, A. Nanni, and A. A. MI, "Contribution of externally bonded FRP to shear capacity of RC flexural members," Journal of composites for construction, vol. 2, no. 4, pp. 195-202, 1998.

[77] I. A. Sharaky, L. Torres, M. Baena, and C. Miàs, "An experimental study of different factors affecting the bond of NSM FRP bars in concrete," Composite Structures, vol. 99, pp. 350-365, 2013.

[78] ACI Committee 318, "Building Code Requirements for Structural Concrete (ACI 318-95) and Commentary (318R-95)," American Concrete Institute, Farmington Hills, Mich., 369 pp., 1995.

[79] ACI Committee 318 (1999). "Building Code Requirements for Structural Concrete (ACI 318-99) and Commentary (ACI 318R-99)," American Concrete Institute, Farmington Hills, Michigan, 391 pp., 1999.

[80] ACI Committee 440 (2002). "Guide for the Design and Construction of Externally Bonded FRP Systems for Strengthening Concrete Structures (ACI 440.2R-02)," American Concrete Institute, Farmington Hills, Michigan, 45 pp., 2002.

[81] A. Nanni, M. D. Ludovico, and R. Parretti, "Shear strengthening of a PC bridge girder with NSM CFRP rectangular bars," Advances in Structural Engineering, vol. 7, no. 4, pp. 297-309, 2004.

[82] M. Al-Zu'bi, M. Fan, Y. Al Rjoub, A. Ashteyat, M. J. Al-Kheetan, and L. Anguilano, "The effect of length and inclination of carbon fiber reinforced polymer laminates on shear capacity

of near-surface mounted retrofitted reinforced concrete beams," Structural Concrete, vol. 22, no. 6, pp. 3677-3691, 2021.

[83] Y. Zhang, M. Elsayed, L. V. Zhang, and M. L. Nehdi, "Flexural behavior of reinforced concrete T-section beams strengthened by NSM FRP bars," Engineering Structures, vol. 233, p. 111922, 2021.

[84] S. M. Daghash and O. E. Ozbulut, "Flexural performance evaluation of NSM basalt FRP-strengthened concrete beams using digital image correlation system," Composite Structures, vol. 176, pp. 748-756, 2017.

[85] M. Su, S. Gong, Y. Liu, and H. Peng, "Flexural behavior of RC beams strengthened with fully or partially prestressed near-surface mounted FRP strips: An experimental investigation," Engineering Structures, vol. 262, p. 114345, 2022.

[86] M. Abdallah, F. Al Mahmoud, A. Khelil, J. Mercier, and B. Almassri, "Assessment of the flexural behavior of continuous RC beams strengthened with NSM-FRP bars, experimental and analytical study," Composite Structures, vol. 242, p. 112127, 2020.

[87] H. M. Ali, M. N. Sheikh, and M. N. Hadi, "Flexural strengthening of RC beams with NSM-GFRP technique incorporating innovative anchoring system," Structures, vol. 38, pp. 251-264, 2022.

[88] M. Abdallah, F. Al Mahmoud, A. Khelil, and J. Mercier, "Efficiency of EB CFRP composites for flexural strengthening of continuous RC beams: A comparative study with NSM CFRP rods," Structures, vol. 34, pp. 1567-1588, Dec. 2021.

[89] M. Abdallah, F. Al Mahmoud, R. Boissiere, A. Khelil, and J. Mercier, "Experimental study on strengthening of RC beams with Side Near Surface Mounted technique-CFRP bars," Composite Structures, vol. 234, p. 111716, 2020.

[90] S. W. Fathuldeen and M. A. Qissab, "Behavior of RC beams strengthened with NSM CFRP strips under flexural repeated loading," Structural Engineering and Mechanics, vol. 70, no. 1, pp. 67-80, 2019.

[91] J. G. Yu, L. Cheng, S. Liu, B. Fu, and B. Li, "Inorganic adhesive based near-surface-mounted fibre reinforced polymer for strengthening of concrete structures: An overview," Structures, vol. 33, pp. 2099-2120, Oct. 2021.

[92] K. Sanginabadi, A. Yazdani, D. Mostofinejad, and C. Czaderski, "RC members externally strengthened with FRP composites by grooving methods including EBROG and EBRIG: A state-of-the-art review," Construction and Building Materials, vol. 324, p. 126662, 2022.

[93] S. M. Soliman, E. El-Salakawy, and B. Benmokrane, "Flexural behaviour of concrete beams strengthened with near surface mounted fibre reinforced polymer bars," Canadian Journal of Civil Engineering, vol. 37, no. 10, pp. 1371-1382, 2010.

[94] C. Barris, P. Sala, J. Gómez, and L. Torres, "Flexural behaviour of FRP reinforced concrete beams strengthened with NSM CFRP strips," Composite Structures, vol. 241, p. 112059, 2020.

[95] M. Al-Zu'bi, M. Fan, and L. Anguilano, "Advances in bonding agents for retrofitting concrete structures with fibre reinforced polymer materials: A review," Construction and Building Materials, vol. 330, p. 127115, 2022.

[96] I. A. Sharaky, L. Torres, M. Baena, and I. Vilanova, "Effect of different material and construction details on the bond behaviour of NSM FRP bars in concrete," Construction and Building Materials, vol. 38, pp. 890-902, 2013.

[97] M. R. Irshidat, M. H. Al-Saleh, and H. Almashagbeh, "Effect of carbon nanotubes on strengthening of RC beams retrofitted with carbon fiber/epoxy composites," Materials & Design, vol. 89, pp. 225-234, 2016.

[98] M. R. Irshidat and M. H. Al-Saleh, "Flexural strength recovery of heat-damaged RC beams using carbon nanotubes modified CFRP," Construction and Building Materials, vol. 145, pp. 474-482, 2017.

[99] M. R. Irshidat, M. H. Al-Saleh, and M. Al-Shoubaki, "Using carbon nanotubes to improve strengthening efficiency of carbon fiber/epoxy composites confined RC columns," Composite Structures, vol. 134, pp. 523-532, 2015.

[100] M. R. Irshidat and M. H. Al-Saleh, "Effect of using carbon nanotube modified epoxy on bond-slip behavior between concrete and FRP sheets," Construction and Building Materials, vol. 105, pp. 511-518, 2016.

[101] M. R. Irshidat and M. H. Al-Saleh, "Repair of heat-damaged RC columns using carbon nanotubes modified CFRP," Materials and Structures, vol. 50, pp. 1-11, 2017.

[102] N. P. Singh, V. K. Gupta, and A. P. Singh, "Graphene and carbon nanotube reinforced epoxy nanocomposites: A review," Polymer, vol. 180, p. 121724, 2019.

[103] S. Liu, V. S. Chevali, Z. Xu, D. Hui, and H. Wang, "A review of extending performance of epoxy resins using carbon nanomaterials," Composites Part B: Engineering, vol. 136, pp. 197-214, 2018.

[104] F. L. Jin, X. Li, and S. J. Park, "Synthesis and application of epoxy resins: A review," Journal of Industrial and Engineering Chemistry, vol. 29, pp. 1-11, 2015.

[105] W. Jiang, F. L. Jin, and S. J. Park, "Thermo-mechanical behaviors of epoxy resins reinforced with nano-Al2O3 particles," Journal of Industrial and Engineering Chemistry, vol. 18, no. 2, pp. 594-596, 2012.

[106] K. S. Kim, K. Y. Rhee, K. H. Lee, J. H. Byun, and S. J. Park, "Rheological behaviors and mechanical properties of graphite nanoplate/carbon nanotube-filled epoxy nanocomposites," Journal of industrial and engineering chemistry, vol. 16, no. 4, pp. 572-576, 2010.

[107] Y. L. Liu, W. W. Wei, K. Y. Hsu, and W. H. Ho, "Thermal stability of epoxy-silica hybrid materials by thermogravimetric analysis," Thermochimica Acta, vol. 412, no. 1-2, pp. 139-147, 2004.

[108] B. B. Johnsen, A. J. Kinloch, R. D. Mohammed, A. C. Taylor, and S. Sprenger, "Toughening mechanisms of nanoparticle-modified epoxy polymers," Polymer, vol. 48, no. 2, pp. 530-541, 2007.

[109] T. C. Rousakis, K. B. Kouravelou, and T. K. Karachalios, "Effects of carbon nanotube enrichment of epoxy resins on hybrid FRP-FR confinement of concrete," Composites Part B: Engineering, vol. 57, pp. 210-218, 2014.

[110] M. R. Irshidat, M. H. Al-Saleh, and M. Al-Shoubaki, "Strengthening RC columns using carbon fiber reinforced epoxy composites modified with carbon nanotubes," World Academy of Science, Engineering and Technology International Journal of Materials and Metallurgical Engineering.

[111] S. A. Morshed, A. Sinha, Q. Zhang, and J. Tatar, "Hygrothermal conditioning of wet-layup CFRP-concrete adhesive joints modified with silane coupling agent and core-shell rubber nanoparticles," Construction and Building Materials, vol. 227, p. 116531, 2019.

[112] S. A. Morshed, T. J. Young, W. M. Chirdon, Q. Zhang, and J. Tatar, "Durability of wet lay-up FRP bonded to concrete with nanomodified epoxy adhesives," The Journal of Adhesion, 2018.

[113] F. Pahlevanzadeh, R. Emadi, M. Setayeshmehr, M. Kharaziha, and S. A. Poursamar, "Antibacterial amorphous magnesium phosphate/graphene oxide for accelerating bone regeneration," Biomaterials Advances, p. 212856, 2022.

[114] S. Kujur and D. D. Pathak, "Reduced graphene oxide-immobilized iron nanoparticles Fe (0)@ rGO as heterogeneous catalyst for one-pot synthesis of series of propargylamines," Research on Chemical Intermediates, vol. 46, no. 1, pp. 369-384, 2020.

[115] M. Hosur, T. H. Mahdi, M. E. Islam, and S. Jeelani, "Mechanical and viscoelastic properties of epoxy nanocomposites reinforced with carbon nanotubes, nanoclay, and binary nanoparticles," Journal of Reinforced Plastics and Composites, vol. 36, no. 9, pp. 667-684, 2017.

[116] A. Tanvir, Y. H. El-Gawady, and M. Al-Maadeed, "Cellulose nanofibers to assist the release of healing agents in epoxy coatings," Progress in Organic Coatings, vol. 112, pp. 127-132, 2017.

[117] L. Thompson, M. Nikzad, I. Sbarski, and A. Yu, "Esterified cellulose nanocrystals for reinforced epoxy nanocomposites," Progress in Natural Science: Materials International.

[118] B. Tyagi, C. D. Chudasama, and R. V. Jasra, "Determination of structural modification in acid activated montmorillonite clay by FT-IR spectroscopy," Spectrochimica Acta Part A: Molecular and Biomolecular Spectroscopy, vol. 64, no. 2, pp. 273-278, 2006.

[119] O. Zabihi, H. Khayyam, B. L. Fox, and M. Naebe, "Enhanced thermal stability and lifetime of epoxy nanocomposites using covalently functionalized clay: experimental and modelling," New Journal of Chemistry, vol. 39, no. 3, pp. 2269-2278, 2015.

[120] K. Xu, K. Li, D. Tu, T. Zhong, and C. Xie, "Reinforcement on the mechanical-, thermal-, and water-resistance properties of the wood flour/chitosan/poly (vinyl chloride) composites by physical and chemical modification," Journal of Applied Polymer Science, vol. 131, no. 18, 2014.

[121] K. Majdzadeh-Ardakani, S. Zekriardehani, M. R. Coleman, and S. A. Jabarin, "A novel approach to improve the barrier properties of PET/clay nanocomposites," International Journal of Polymer Science, vol. 2017.

[122] S. Thomas, D. Rouxel, and D. Ponnamma, Eds., "Spectroscopy of polymer Nanocomposites," William Andrew, 2016.

[123] X. Wang, W. Xing, X. Feng, B. Yu, L. Song, and Y. Hu, "Functionalization of graphene with grafted polyphosphamide for flame retardant epoxy composites: synthesis, flammability and mechanism," Polymer Chemistry, vol. 5, no. 4, pp. 1145-1154, 2014.

[124] Z. Zhang, W. Zhang, D. Li, Y. Sun, Z. Wang, C. Hou, L. Chen, Y. Cao, and Y. Liu, "Mechanical and anticorrosive properties of graphene/epoxy resin composites coating prepared by in-situ method," International journal of molecular sciences, vol. 16, no. 1, pp. 2239-2251, 2015.

[125] N. Mahmood, M. Islam, A. Hameed, and S. Saeed, "Polyamide 6/multiwalled carbon nanotubes nanocomposites with modified morphology and thermal properties," Polymers, vol. 5, no. 4, pp. 1380-1391, 2013.

[126] A. Kumar, Y. S. Negi, N. K. Bhardwaj, and V. Choudhary, "Synthesis and characterization of cellulose nanocrystals/PVA based bionanocomposite," Advanced materials letters, vol. 4, no. 8, pp. 626-631, 2013.

[127] A. Bhattacharyya, S. Chen, and M. Zhu, "Graphene reinforced ultra-high molecular weight polyethylene with improved tensile strength and creep resistance properties," Express Polymer Letters, vol. 8, no. 2.

[128] E. Werner et al., "Hybrid polyamide/silica nanocomposites: synthesis and mechanical testing," Macromolecular Materials and Engineering, vol. 287, p. 106, 2002.

[129] M. Sadeghi et al., "Gas permeation properties of ethylene vinyl acetate–silica nanocomposite membranes," Journal of Membrane Science, vol. 322, no. 2, pp. 423-428, 2008.

[130] J. S. Tomblin, C. Yang, and P. Harter, "Investigation of thick bondline adhesive joints," Wichita State University, KS.

[131] T. Filleter et al., "Ultrahigh strength and stiffness in cross-linked hierarchical carbon nanotube bundles," Advanced Materials, vol. 23, no. 25, pp. 2855-2860, 2011.

[132] S. R. Abdullah et al., "Modified Epoxy for Fibre Reinforced Polymer Strengthening of Concrete Structures," International Journal of Integrated Engineering, vol. 12, no. 9, pp. 103-113, 2020.

[133] D. Quan, J. L. Urdániz, and A. Ivanković, "Enhancing mode-I and mode-II fracture toughness of epoxy and carbon fiber reinforced epoxy composites using multi-walled carbon nanotubes," Materials & Design, vol. 143, pp. 81-92, 2018.

[134] B. Ashrafi et al., "Enhancement of mechanical performance of epoxy/carbon fiber laminate composites using single-walled carbon nanotubes," Composites Science and Technology, vol. 71, no. 13, pp. 1569-1578, 2011.

[135] Y. Nie and T. Hübert, "Effect of carbon nanofiber (CNF) silanization on the properties of CNF/epoxy nanocomposites," Polymer International, vol. 60, no. 11, pp. 1574-1580, 2011.

[136] S. Zhao et al., "Improving dispersion and integration of single-walled carbon nanotubes in epoxy composites by using a reactive noncovalent dispersant," Journal of Polymer Science Part A: Polymer Chemistry, vol. 50, no. 21, pp. 4548-4556, 2012.

[137] S. Gantayat, D. Rout, and S. K. Swain, "Carbon nanomaterial–reinforced epoxy composites: a review," Polymer-Plastics Technology and Engineering, vol. 57, no. 1, pp. 1-16, 2018.

[138] S. X. Peng et al., "Enhanced dispersion and properties of a two-component epoxy nanocomposite using surface-modified cellulose nanocrystals," Polymer, vol. 112, pp. 359-368, 2017.

[139] L. Yue et al., "Surface-modified cellulose nanocrystals for biobased epoxy nanocomposites," Polymer, vol. 134, pp. 155-162, 2018.

[140] T. Aziz et al., "Adhesive properties of bio-based epoxy resin reinforced by cellulose nanocrystal additives," Journal of Polymer Engineering, vol. 40, no. 4, pp. 314-320, 2020.

[141] A. Allaoui, S. V. Hoa, and M. D. Pugh, "The electronic transport properties and microstructure of carbon nanofiber/epoxy composites," Composites Science and Technology, vol. 68, no. 2, pp. 410-416, 2008.

[142] L. H. Sun et al., "Preparation, characterization, and modeling of carbon nanofiber/epoxy nanocomposites," Journal of Nanomaterials, 2011.

[143] P. Jojibabu et al., "Effect of different carbon nano-fillers on rheological properties and lap shear strength of epoxy adhesive joints," Composites Part A: Applied Science and Manufacturing, vol. 82, pp. 53-64, 2016.

[144] Z. Fan and S. G. Advani, "Rheology of multiwall carbon nanotube suspensions," Journal of Rheology, vol. 51, no. 4, pp. 585-604, 2007.

[145] J. A. Kim et al., "Effects of surface modification on rheological and mechanical properties of CNT/epoxy composites," Carbon, vol. 44, no. 10, pp. 1898-1905, 2006.

[146] H. Miyagawa and L. T. Drzal, "Thermo-physical and impact properties of epoxy nanocomposites reinforced by single-wall carbon nanotubes," Polymer, vol. 45, no. 15, pp. 5163-5170, 2004.

[147] Y. Zhao and E. V. Barrera, "Asymmmetric diamino functionalization of nanotubes assisted by BOC protection and their epoxy nanocomposites," Advanced Functional Materials, vol. 20, no. 18, pp. 3039-3044, 2010.

[148] Y. Zhou et al., "Fabrication and characterization of carbon/epoxy composites mixed with multi-walled carbon nanotubes," Materials Science and Engineering: A, vol. 475, no. 1-2, pp. 157-165, 2008.

[149] F. H. Gojny et al., "Influence of different carbon nanotubes on the mechanical properties of epoxy matrix composites–a comparative study," Composites Science and Technology, vol. 65, no. 15-16, pp. 2300-2313, 2005.

[150] Y. Iwahori et al., "Mechanical properties improvements in two-phase and three-phase composites using carbon nano-fiber dispersed resin," Composites Part A: Applied Science and Manufacturing, vol. 36, no. 10, pp. 1430-1439, 2005.

[151] Y. Zhou et al., "Effect of vapor-grown carbon nanofiber on thermal and mechanical properties of epoxy," Journal of Materials Science, vol. 42, no. 17, pp. 7544-7553, 2007.

[152] R. Al-Safy, R. Al-Mahaidi, and G. P. Simon, "Thermal and mechanical characterizations of nanomaterial-modified adhesive used in bonding CFRP to concrete," The Journal of Adhesion, vol. 87, no. 7-8, pp. 842-857, 2011.

[153] J. Zhu et al., "In situ stabilized carbon nanofiber (CNF) reinforced epoxy nanocomposites," Journal of Materials Chemistry, vol. 20, no. 23, pp. 4937-4948, 2010.

[154] R. B. Ladani et al., "Multifunctional properties of epoxy nanocomposites reinforced by aligned nanoscale carbon," Materials & Design, vol. 94, pp. 554-564, 2016.

[155] P. Baruah and N. Karak, "Bio-based tough hyperbranched epoxy/graphene oxide nanocomposite with enhanced biodegradability attribute," Polymer Degradation and Stability, vol. 129, pp. 26-33, 2016.

[156] C. Bao et al., "In situ preparation of functionalized graphene oxide/epoxy nanocomposites with effective reinforcements," Journal of Materials Chemistry, vol. 21, no. 35, pp. 13290-13298, 2011.

[157] B. S. TK et al., "Microwave exfoliated reduced graphene oxide epoxy nanocomposites for high-performance applications," Polymer, vol. 55, no. 16, pp. 3614-3627, 2014.

[158] A. Kumar et al., "Graphene-like nanocarbon: An effective nanofiller for improving the mechanical and thermal properties of the polymer at low weight fractions," Composites Science and Technology, vol. 127, pp. 79-87, 2016.

[159] S. Chandrasekaran et al., "Preparation and characterization of graphite nano-platelet (GNP)/epoxy nanocomposite: Mechanical, electrical, and thermal properties," European Polymer Journal, vol. 49, no. 12, pp. 3878-3888, 2013.

[160] S. Park and D. S. Kim, "Curing behavior and physical properties of an epoxy nanocomposite with amine-functionalized graphene nanoplatelets," Composite Interfaces, vol. 23, no. 7, pp. 675-687, 2016.

[161] L. Chen et al., "Thermal properties of epoxy resin-based thermal interfacial materials by filling Ag nanoparticle-decorated graphene nanosheets," Composites Science and Technology, vol. 125, pp. 17-21, 2016.

[162] A. C. Ackermann et al., "Rheology, dispersion, and cure kinetics of epoxy filled with amine-and non-functionalized reduced graphene oxide for composite manufacturing," Journal of Applied Polymer Science, vol. 139, no. 8, p. 51664, 2022.

[163] E. Abraham et al., "Highly modified cellulose nanocrystals and formation of epoxy-nanocrystalline cellulose (CNC) nanocomposites," ACS applied materials & interfaces, vol. 8, no. 41, pp. 28086-28095, 2016.

[164] D. E. Kherroub et al., "Synthesis of polyamide-6/montmorillonite nanocomposites by direct in-situ polymerization catalyzed by exchanged clay," Oriental Journal of Chemistry, vol. 29, no. 4, p. 1429, 2013.

[165] N. Chisholm et al., "Fabrication and mechanical characterization of carbon/SiC-epoxy nanocomposites," Composite Structures, vol. 67, no. 1, pp. 115-124, 2005.

[166] F. L. Jin and S. J. Park, "Thermal properties of epoxy resin/filler hybrid composites," Polymer Degradation and Stability, vol. 97, no. 11, pp. 2148-2153, 2012.

[167] E. Huttunen-Saarivirta et al., "Characterization and corrosion protection properties of epoxy powder coatings containing nanoclays," Progress in Organic Coatings, vol. 76, no. 4, pp. 757-767, 2013.

[168] G. Bogoeva-Gaceva et al., "Parameters affecting the interface properties in carbon fibre/epoxy systems," Composites, vol. 26, no. 2, pp. 103-107, 1995.

[169] J. Guo et al., "The effects of γ-irradiation dose on chemical modification of multi-walled carbon nanotubes," Nanotechnology, vol. 16, no. 10, p. 2385, 2005.

[170] P. Jojibabu et al., "Synergetic effects of carbon nanotubes and triblock copolymer on the lap shear strength of epoxy adhesive joints," Composites Part B: Engineering, vol. 178, p. 107457, 2019.

[171] S. K. Hong et al., "Enhanced thermal and mechanical properties of carbon nanotube composites through the use of functionalized CNT-reactive polymer linkages and three-roll milling," Composites Part A: Applied Science and Manufacturing, vol. 77, pp. 142-146, 2015.

[172] S. N. Ahn et al., "Epoxy/amine-functionalized short-length vapor-grown carbon nanofiber composites," Journal of Polymer Science Part A: Polymer Chemistry, vol. 46, no. 22, pp. 7473-7482, 2008.

[173] P. C. Ma et al., "Dispersion, interfacial interaction and re-agglomeration of functionalized carbon nanotubes in epoxy composites," Carbon, vol. 48, no. 6, pp. 1824-1834, 2010.

[174] T. Ramanathan et al., "Amino-functionalized carbon nanotubes for binding to polymers and biological systems," Chemistry of Materials, vol. 17, no. 6, pp. 1290-1295, 2005.

[175] R. Wang et al., "Photocatalytic activity of heterostructures based on TiO2 and halloysite nanotubes," ACS applied materials & interfaces, vol. 3, no. 10, pp. 4154-4158, 2011.

[176] X. Wang et al., "Comparative study of three carbon additives: Carbon nanotubes, graphene, and fullerene-c60, for synthesizing enhanced polymer nanocomposites," Nanomaterials, vol. 10, no. 5, p. 838, 2020.

[177] S. H. Shengtao et al., "Characterization of exfoliated graphite prepared with the method of secondary intervening," .

[178] S. Andreev et al., "Study of fullerene aqueous dispersion prepared by a novel dialysis method: simple way to a fullerene aqueous solution," Fullerenes, Nanotubes and Carbon Nanostructures, vol. 23, no. 9, pp. 792-800, 2015.

[179] Y. Zhang et al., "Highly efficient adsorption of copper ions by a PVP-reduced graphene oxide based on a new adsorption mechanism," Nano-Micro Letters, vol. 6, no. 1, pp. 80-87, 2014.

[180] P. Galvez et al., "Effect of moisture and temperature on thermal and mechanical properties of structural polyurethane adhesive joints," Composite Structures, vol. 247, p. 112443, 2020.

[181] A. Montazeri, "The effect of functionalization on the viscoelastic behavior of multi-wall carbon nanotube/epoxy composites," Materials & Design, vol. 45, pp. 510-517, 2013.

[182] M. M. Shokrieh et al., "Stiffness prediction of graphene nanoplatelet/epoxy nanocomposites by a combined molecular dynamic–micromechanics method," Computational materials science, vol. 92, pp. 444-450, 2014.

[183] Z. Sun et al., "Crumpled graphene epoxy nanocomposites modified with polydopamine for advanced semiconductor packaging applications," Composites Science and Technology, p. 109709, 2022.

[184] S. Morimune et al., "Graphene oxide reinforced poly (vinyl alcohol) nanocomposites."

[185] L. Chen et al., "Double glass transitions and interfacial immobilized layer in in-situ-synthesized poly (vinyl alcohol)/silica nanocomposites," Macromolecules, vol. 43, no. 2, pp. 1076-1082, 2010.

[186] Z. Peng et al., "Poly (vinyl alcohol)/silica nanocomposites: morphology and thermal degradation kinetics," Journal of nanoscience and nanotechnology, vol. 6, no. 12, pp. 3934-3938, 2006.

[187] M. A. Alam et al., "Effects of SiO2 and ZnO nanoparticles on epoxy coatings and its performance investigation using thermal and nanoindentation technique," Polymers, vol. 13, no. 9, p. 1490, 2021.

[188] U. Marathe et al., "Performance Augmentation of Epoxy Adhesives with TiN Nanoparticles," ACS omega, vol. 7, no. 5, pp. 4150-4157, 2022.

[189] S. A. Sydlik et al., "Epoxy functionalized multi-walled carbon nanotubes for improved adhesives," Carbon, vol. 59, pp. 109-120, 2013.

[190] R. Moriche et al., "Thermal conductivity and lap shear strength of GNP/epoxy nanocomposites adhesives," International journal of adhesion and adhesives, vol. 68, pp. 407-410, 2016.

[191] M. Mansourian-Tabaei et al., "Lap shear strength and thermal stability of diglycidyl ether of bisphenol a/epoxy novolac adhesives with nanoreinforcing fillers," Journal of applied polymer science, vol. 131, no. 6.

[192] A. Wolf et al., "Improved adhesives containing CNT/SP1 nano fillers," The Journal of Adhesion, vol. 88, no. 4-6, pp. 435-451, 2012.

[193] P. Jongvivatsakul et al., "Enhancing bonding behavior between carbon fiber-reinforced polymer plates and concrete using carbon nanotube reinforced epoxy composites," Case Studies in Construction Materials, vol. 17, p. e01407, 2022.

[194] S. Gantayat et al., "Designing of epoxy matrix by chemically modified multiwalled carbon nanotubes," Advances in Polymer Technology, vol. 37, no. 1, pp. 176-184, 2018.

[195] M. L. Sham and J. K. Kim, "Surface functionalities of multi-wall carbon nanotubes after UV/Ozone and TETA treatments," Carbon, vol. 44, no. 4, pp. 768-777, 2006.

[196] P. C. Ma et al., "Effects of silane functionalization on the properties of carbon nanotube/epoxy nanocomposites," Composites science and technology, vol. 67, no. 14, pp. 2965-2972, 2007.

[197] Y. K. Choi et al., "Mechanical and physical properties of epoxy composites reinforced by vapor-grown carbon nanofibers," Carbon, vol. 43, no. 10, pp. 2199-2208, 2005.

[198] A. C. Ackermann et al., "Mechanical, thermal and electrical properties of epoxy nanocomposites with amine-functionalized reduced graphene oxide via plasma treatment," Journal of Composites Science, vol. 6, no. 6, p. 153, 2022.

[199] M. G. Kim et al., "Effect of CNT functionalization on crack resistance of a carbon/epoxy composite at a cryogenic temperature," Composites Part A: Applied Science and Manufacturing, vol. 43, no. 9, pp. 1620-1627, 2012.

[200] W. Liu et al., "Organoclay-modified high-performance epoxy nanocomposites," Composites Science and Technology, vol. 65, no. 2, pp. 307-316, 2005.

[201] S. Gantayat et al., "Expanded graphite as a filler for epoxy matrix composites to improve their thermal, mechanical and electrical properties," New Carbon Materials, vol. 30, no. 5, pp. 432-437, 2015.

[202] N. A. Siddiqui et al., "Mode I interlaminar fracture behavior and mechanical properties of CFRPs with nanoclay-filled epoxy matrix," Composites Part A: Applied science and manufacturing, vol. 38, no. 2, pp. 449-460, 2007.

[203] ASTM. "ASTM C39: Standard Test Method for Compressive Strength of Cylindrical Concrete Specimens." ASTM International, West Conshohocken, PA, USA, 2001.

[204] A. S. T. M. Standard, "D3163-01 Standard Test Method for Determining Strength of Adhesively Bonded Rigid Plastic Lap-Shear Joints in Shear by Tension Loading," ASTM International, West Conshohocken, PA, 2008, DOI: 10.1520/D3163-01R08.

[205] A. S. T. M. Standard, "78-02. Standard test method for flexural strength of concrete (using simple beam with third-point loading)," Annual Book of ASTM Standards, American Society for Testing and Materials, 2002.

[206] T. R. Naik, "Sustainability of the cement and concrete industries," in Sustainable Construction Materials and Technologies, CRC Press, 2020, pp. 19-25

[207] C.R. Gagg, "Cement and concrete as an engineering material: An historic appraisal and case study analysis," Engineering Failure Analysis, vol. 40, pp. 114-140, 2014.

[208] J. Michels, J. S. Cruz, R. Christen, C. Czaderski, and M. Motavalli, "Mechanical performance of cold-curing epoxy adhesives after different mixing and curing procedures," Composites Part B: Engineering, vol. 98, pp. 434-443, 2016.

[209] H. Faleh, R. Al-Mahaidi, and L. Shen, "Fabrication and characterization of nano-particles-enhanced epoxy," Composites Part B: Engineering, vol. 43, no. 8, pp. 3076-3080, 2012.

[210] V. Gavande, S. Nagappan, B. Seo, Y.S. Cho, and W.K. Lee, "Transparent nylon 6 nanofibers-reinforced epoxy matrix composites with superior mechanical and thermal properties," Polymer Testing, vol. 122, p. 108002, 2023.

[211] S.A. Morshed, T.J. Young, W.M. Chirdon, Q. Zhang, and J. Tatar, "Durability of wet lay-up FRP bonded to concrete with nanomodified epoxy adhesives," The Journal of Adhesion, vol. 96, no. 13, pp. 1141-1166, 2020.

[212] X. Shi, T.A. Nguyen, Z. Suo, Y. Liu, and R. Avci, "Effect of nanoparticles on the anticorrosion and mechanical properties of epoxy coating," Surface and Coatings Technology, vol. 204, no. 3, pp. 237-245, 2009.